



**HAL**  
open science

# Development of electron microscopy diffraction techniques for the study of two and three dimensional materials

Yannick Martin

► **To cite this version:**

Yannick Martin. Development of electron microscopy diffraction techniques for the study of two and three dimensional materials. Materials Science [cond-mat.mtrl-sci]. Université de Grenoble, 2014. English. NNT: 2014GRENY066 . tel-01442648

**HAL Id: tel-01442648**

**<https://theses.hal.science/tel-01442648>**

Submitted on 20 Jan 2017

**HAL** is a multi-disciplinary open access archive for the deposit and dissemination of scientific research documents, whether they are published or not. The documents may come from teaching and research institutions in France or abroad, or from public or private research centers.

L'archive ouverte pluridisciplinaire **HAL**, est destinée au dépôt et à la diffusion de documents scientifiques de niveau recherche, publiés ou non, émanant des établissements d'enseignement et de recherche français ou étrangers, des laboratoires publics ou privés.

**THÈSE**

Pour obtenir le grade de

**DOCTEUR DE L'UNIVERSITÉ DE GRENOBLE**

Spécialité : **Nanophysique**

Arrêté ministériel : 7 août 2006

Présentée par

**Yannick Martin**

Thèse dirigée par **Jean-Luc Rouvière**

préparée au sein du **Laboratoire d'Étude des Matériaux par Microscopies Avancées, Institut Nanoscience et Cryogénie, CEA Grenoble** et de l'**École Doctorale de Physique de Grenoble**

**Development of electron microscopy diffraction techniques for the study of two and three dimensional materials.**

Thèse soutenue publiquement le **6 octobre 2014**,  
devant le jury composé de :

**Dr. Annick LOISEAU**

Directrice de recherche, Laboratoire d'étude des microstructures, ONERA, CNRS, Rapporteur

**Pr. Adam MORAWIEC**

Professeur, Institute of Metallurgy and Materials Science, Polish Academy of Sciences, Cracovie, Pologne, Rapporteur

**Pr. Hubert RENEVIER**

Professeur, Laboratoire des Matériaux et du Génie Physique, Grenoble INP, Examineur

**Pr. Jian Min ZUO**

Professeur, Departement of Material Science and Engineering, University of Illinois at Urbana-Champaign, Examineur

**Dr. Jean-Luc ROUVIERE**

Ingenieur-Chercheur, Laboratoire d'Étude des Matériaux par Microscopies Avancées, Institut Nanoscience et Cryogénie, CEA Grenoble, Directeur de thèse

**Dr. Hanako OKUNO**

Chercheur, Laboratoire d'Étude des Matériaux par Microscopies Avancées, Institut Nanoscience et Cryogénie, CEA Grenoble, Co-Encadrant





## THÈSE

Pour obtenir le grade de

## DOCTEUR DE L'UNIVERSITÉ DE GRENOBLE

Spécialité : **Nanophysique**

Arrêté ministériel : 7 août 2006

Présentée par

**Yannick Martin**

Thèse dirigée par **Jean-Luc Rouvière**

préparée au sein du **Laboratoire d'Étude des Matériaux par Microscopies Avancées, Institut Nanoscience et Cryogénie, CEA Grenoble** et de l'**École Doctorale de Physique de Grenoble**

# Development of electron microscopy diffraction techniques for the study of two and three dimensional materials.

Thèse soutenue publiquement le **6 octobre 2014**,  
devant le jury composé de :

**Dr. Annick LOISEAU**

Directrice de recherche, Laboratoire d'étude des microstructures, ONERA, CNRS, Rapporteur

**Pr. Adam MORAWIEC**

Professeur, Institute of Metallurgy and Materials Science, Polish Academy of Sciences, Cracovie, Pologne, Rapporteur

**Pr. Hubert RENEVIER**

Professeur, Laboratoire des Matériaux et du Génie Physique, Grenoble INP, Examineur

**Pr. Jian Min ZUO**

Professeur, Department of Material Science and Engineering, University of Illinois at Urbana-Champaign, Examineur

**Dr. Jean-Luc ROUVIERE**

Ingenieur-Chercheur, Laboratoire d'Étude des Matériaux par Microscopies Avancées, Institut Nanoscience et Cryogénie, CEA Grenoble, Directeur de thèse

**Dr. Hanako OKUNO**

Chercheur, Laboratoire d'Étude des Matériaux par Microscopies Avancées, Institut Nanoscience et Cryogénie, CEA Grenoble, Co-Encadrant





---

## Acknowledgments

---

This thesis work has been done in the CEA Grenoble, Institute for Nanoscience and Cryogenics (INAC), Service of Physics of Materials and Microstructures (SP2M) in the Advanced Electron Microscopy group (LEMMA).

First of all, I would like to thank my thesis supervisor Jean-Luc for his numerous ideas and his expertise in electron microscopy, and Hanako for her good supervision and her expertise in two-dimensional materials. I would also like to thank Pascale, the head of the LEMMA group, for her support in difficult times.

I thank also my office-mates Miguel, Benedikt, Fabio, Maxime, and ex-office mates Adrien, Donatien, Eric P., Gabriel. A special thanks to Adrien who daily fights against junk food. thanks also to all the PhD and Post-docs I did not have the chance to share an office with : Bastien, Nicolas, Robert, Mathieu, Romain and I may forgot ones.

I would also like to thank all the other microscopist from the nano-characterization platform for the discussions and experiments: PH, Catherine, Martien, Nicolas Mollard, Nicolas Mante, Nicolas B., Laure, Cyril, Eric G. A special thank to Dave who has fairly good skiing skills for an Englishman.

I am also grateful to Jim Zuo for the numerous exchanges on Convergent Beam Electron Diffraction, to Vincent Favre-Nicolin for his help in Python, to Armand for the finite-element simulations.

Je tiens également à remercier mes colocataires, Mathilde, Jérémy, Chiara, Gabriel et Johan pour s'être occuper de la maisonnée (et de moi même) pendant ma période ours des cavernes de fin de thèse. Mais également mes anciens colocs Nicolas, Camille, Cédric, Sylvain, pour m'avoir supporté avant cette période, ce qui est déjà admirable.

Merci également à la famille, pour avoir essayé de comprendre le contenu de cette thèse et apporté des corrections linguistiques.

Un grand merci également aux skieurs, marcheurs, alpinistes, patineurs, kayakistes, équilibristes, casses-cous et autres bestioles en tout genre : Pauline (grillée), Pauline (aux ventouses), Pauline (double épaisseur), Flore, Philo, Cricri, Quentin, Rémi, Flo, et j'en oublie qui ont fait partie intégrante de cette thèse de par le temps nécessaire à la préparation de toutes ces sorties!



---

## Contents

---

Introduction . . . . .	1
<b>PART A Experimental techniques, studied samples and electron diffraction theory.</b> . . . . .	<b>3</b>
<b>CHAPTER A.I: Experimental techniques</b> . . . . .	<b>5</b>
A.I.1 The Transmission Electron Microscope (TEM) . . . . .	5
A.I.2 Electron diffraction techniques . . . . .	6
A.I.2.1 General considerations on electron diffraction . . . . .	6
A.I.2.2 NBED . . . . .	8
A.I.2.3 CBED . . . . .	9
A.I.2.4 PED . . . . .	11
A.I.2.5 PACBED . . . . .	11
A.I.3 Electron imaging techniques . . . . .	12
A.I.3.1 Conventional TEM. . . . .	12
A.I.3.1.1 The origin of TEM contrast. . . . .	12
A.I.3.1.2 Lenses aberrations . . . . .	13
A.I.3.1.3 Monochromated TEM . . . . .	14
A.I.3.2 STEM . . . . .	15
A.I.3.2.1 STEM image formation . . . . .	15
A.I.3.2.2 Quantitative STEM . . . . .	16
<b>CHAPTER A.II: Studied samples and context</b> . . . . .	<b>19</b>
A.II.1 Studied samples . . . . .	19
A.II.1.1 Silicon-Germanium multi-layers . . . . .	19
A.II.1.1.1 Crystal structure . . . . .	21
A.II.1.1.2 Electronic properties/Applications. . . . .	21
A.II.1.1.3 Sample preparation . . . . .	22

A.II.1.2	Graphene . . . . .	22
A.II.1.2.1	Graphene crystal structure . . . . .	23
A.II.1.2.2	Electronic properties . . . . .	23
A.II.1.2.3	Synthesis of graphene . . . . .	24
A.II.1.2.4	TEM sample preparation . . . . .	25
A.II.1.3	Other two-dimensional material . . . . .	25
A.II.1.3.1	MoS <sub>2</sub> crystal structure . . . . .	25
A.II.1.3.2	BN crystal structure . . . . .	26
A.II.1.3.3	Properties and potential applications . . . . .	27
A.II.1.3.4	TEM sample preparation . . . . .	27
A.II.2	Context and Goals of the PhD . . . . .	28
A.II.2.1	Strain measurement: the importance of TEM . . . . .	28
A.II.2.2	Two-dimensional systems: the importance of TEM characterization . . . . .	31
CHAPTER A.III:	Theory of diffraction . . . . .	35
A.III.1	The excitation error . . . . .	35
A.III.2	The projection effect . . . . .	37
A.III.3	Many-Beams dynamic Bloch waves simulation . . . . .	39
A.III.3.1	Resolution of Schrödinger equation . . . . .	40
A.III.3.2	Matrix formulation . . . . .	41
A.III.4	Two-Beams and Kinematic simulation . . . . .	42
A.III.5	Multisllice simulations . . . . .	43
PART B	Convergent Beam Electron Diffraction . . . . .	45
CHAPTER B.I:	Experimental parameters calibration using Convergent Beam Elec- tron Diffraction . . . . .	47
B.I.1	State of the art . . . . .	48
B.I.1.1	Acceleration voltage and camera length determination . . . . .	48
B.I.1.2	Sample thickness refinement . . . . .	48
B.I.1.3	Structure factor and absorption measurement . . . . .	48
B.I.2	Conditions for good experimental data . . . . .	49
B.I.2.1	Filtering . . . . .	50
B.I.2.2	Cooling . . . . .	50
B.I.3	Thickness measurement using Delille method . . . . .	52
B.I.3.1	Description of the method . . . . .	52
B.I.3.2	Application on a silicon thin lamella . . . . .	53
B.I.3.3	Comparison to EDS . . . . .	53
B.I.4	A new approach : Dynamic fitting of arbitrary profiles . . . . .	55
B.I.4.1	Sensitivity of HOLZ lines . . . . .	55
B.I.4.2	Algorithm description . . . . .	56

B.I.5	Proof of concept on simulated silicon . . . . .	58
B.I.6	Application on experimental pattern . . . . .	59
B.I.7	Discussion and further consideration . . . . .	61
B.I.8	Conclusion . . . . .	62
CHAPTER B.II: Three dimensional strain and rotation retrieval in an homogeneously deformed crystal . . . . .		63
B.II.1	The CBED strain measurement ambiguity . . . . .	64
B.II.2	Overview of the method . . . . .	65
B.II.3	Choosing the zone axis . . . . .	66
B.II.4	Simulation details . . . . .	68
B.II.4.1	Dynamic simulations . . . . .	68
B.II.4.2	Kinematic simulations . . . . .	69
B.II.5	The reference pattern . . . . .	71
B.II.5.1	Calibrating the reference pattern . . . . .	71
B.II.5.2	Detecting lines positions and angles . . . . .	71
B.II.5.3	Weighting lines . . . . .	73
B.II.5.4	Finding the Dynamical shift . . . . .	73
B.II.6	F tensor retrieval . . . . .	74
B.II.7	Results . . . . .	76
B.II.7.1	Using one direction of observation . . . . .	76
B.II.7.2	Using two directions of observation . . . . .	78
B.II.8	Discussion . . . . .	78
CHAPTER B.III: Three dimensional displacement retrieval in an heterogeneously deformed crystal . . . . .		81
B.III.1	Theoretical aspects of the method . . . . .	81
B.III.2	Algorithm presentation . . . . .	82
B.III.3	Application on simulated Silicon . . . . .	84
B.III.4	Application on an experimental Si/SiGe sample . . . . .	85
B.III.4.1	Experimental setup . . . . .	85
B.III.4.2	Descanning the beam . . . . .	86
B.III.4.3	Results . . . . .	88
B.III.5	Discussion . . . . .	92
PART C Electron diffraction of two-dimensional materials . . . . .		97
CHAPTER C.I: Study of HR-TEM contrast and diffraction of graphene . . . . .		99
C.I.1	Graphene atomic contrasts in HR-TEM images . . . . .	100
C.I.1.1	Influence of defocus and spherical aberration . . . . .	101
C.I.1.2	Influence of the number of layers . . . . .	101
C.I.1.3	Influence of the sample tilt . . . . .	102

## CONTENTS

---

C.I.1.4	Influence of three-fold astigmatism, $A_2$ . . . . .	103
C.I.2	Tilt/orientation study of few-layered material using electron diffraction. . . . .	106
C.I.2.1	Projection effect in diffraction . . . . .	107
C.I.2.2	Graphene ripples study by TEM diffraction . . . . .	109
C.I.2.3	Orientation study of MoS <sub>2</sub> by nano-diffraction . . . . .	112
CHAPTER C.II:	Thickness measurement of few-layered molybdenum disulfide and boron nitride . . . . .	117
C.II.1	Comparison of measurement methods on few-layered MoS <sub>2</sub> . . . . .	118
C.II.1.1	Determination of the crystal structure. . . . .	119
C.II.1.2	Quantitative STEM . . . . .	119
C.II.1.2.1	Experimental data . . . . .	119
C.II.1.2.2	Simulated data . . . . .	120
C.II.1.2.3	Thickness results . . . . .	122
C.II.1.3	Position Average Convergent Beam Electron Diffraction (PACBED) . . . . .	122
C.II.1.3.1	Experimental data . . . . .	122
C.II.1.3.2	Simulated data . . . . .	124
C.II.1.3.3	Thickness results . . . . .	124
C.II.1.4	Quantitative Nanobeam diffraction . . . . .	124
C.II.1.4.1	Simulated data . . . . .	124
C.II.1.4.2	Experimental data . . . . .	125
C.II.1.4.3	Thickness results . . . . .	127
C.II.1.5	Comparison of the techniques . . . . .	128
C.II.2	Thickness measurement of few-layered Boron Nitride (BN) . . . . .	129
C.II.2.1	Comparative Quantitative STEM and Nanodiffraction study . . . . .	130
C.II.2.1.1	Experimental data . . . . .	130
C.II.2.1.2	Simulation data. . . . .	131
C.II.2.1.3	Comparison of the results . . . . .	131
C.II.3	Discussion . . . . .	135
Conclusion.	. . . . .	137
Appendix . . . . .	. . . . .	139
Appendix A: Strain formalism, the deformation gradient tensor F . . . . .	. . . . .	141
Appendix B: List of python programs . . . . .	. . . . .	143
Nomenclature . . . . .	. . . . .	145
Bibliography . . . . .	. . . . .	149
List of Figures . . . . .	. . . . .	163
List of Tables . . . . .	. . . . .	167

---

## Introduction

---

In the last decade, nanomaterials has become an increasingly studied subject as shown in figure 1. They are defined as materials having a dimension smaller than 100 nm. These small dimensions increase the surface over volume ratio and gives them remarkable properties, as reduced melting point, enhanced reactivities, modified band structure, etc. Nowadays, nanomaterials are used in a wide range of fields such as energy, medicine, and are even present in our everyday life as they can be found in solar creams, sports equipment, vehicles...

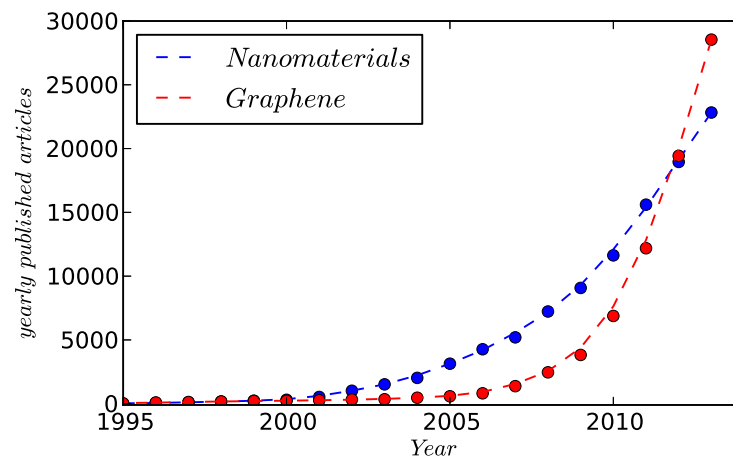


FIGURE 1 – Number of research articles containing the word “nanomaterials” or “graphene” published each year. Source : Scopus

In order to understand and control the new properties of nanomaterials, it is necessary to study them at the nanometer scale. To visualize what a nanometer is, think that a sheet of paper is about 100.000 nm thick. The study of chemical and structural properties of nanomaterials can be done using several tools, and Transmission Electron Microscopy (TEM) is one of them. By the use of an electron beam, TEM allows to obtain a magnified image or a diffraction of the specimen. This spacial resolution of last generation microscopy can reach 50 pm ( $5 \times 10^{-11}$  m) making possible for the TEM to image a single atom.

In this thesis work, TEM diffraction techniques have been developed in order to determine the structure of crystals. Python programming language has been extensively used for data treatment, for simulations and for building retrieval algorithms. Two types of sample have been

studied: (1) Silicon/Silicon-Germanium layered structures, as a reference sample for measuring strain for future application on Silicon based devices and (2) two dimensional materials, for the development of TEM techniques of few-layered materials.

The study of strain and rotation in specimen at the nanometer scale is part of this thesis. Strain is a concept that is used to describe the deviation of the crystal from its ideal state and is expressed as the spatial derivative of the displacement field inside the specimen. Studying strain at the nanoscale is essential to control the physical properties of materials,

because strain influences a lot of physical parameters such as carrier mobility, band structure, and can induce defects in the crystal structure. In microelectronics, strain is engineered on purpose to modify devices properties leading to complex three-dimensional strain field. Three-dimensional characterization of nanomaterials is therefore necessary to help engineering of new devices and nanostructures.

Another part of this thesis is the study of two-dimensional materials like Graphene, Boron Nitride or Molybdenum disulfide. The properties of such material, such as electron mobility, resistivity, mechanical properties, etc. are directly related to their atomic structure. Therefore the development of TEM techniques specific to the characterization of such materials is necessary for a correct understanding of the atomic structure of two-dimensional materials. In this thesis the correct interpretation of high resolution TEM images and the specimen thickness and orientation measurement using diffraction are discussed.

In this thesis work, several TEM microscopy techniques, such as CBED, NBED, HR-TEM, PACBED, STEM, have been used to study the specimen thickness, the three-dimensional atomic displacement, and the strain and rotation field in the sample.

The [first Part](#) of this manuscript presents these experimental techniques ([Chapter I.I](#)), the studied specimens and their scientific context ([Chapter I.II](#)) and specific points of the electron diffraction theory ([Chapter I.III](#)).

The [second Part](#) is devoted to the Convergent Beam Electron Diffraction (CBED) technique. Intensive studies of the information carried by CBED have been done during this thesis. In [Chapter II.I](#), experimental parameters measurement such as sample thickness, direction of observation, acceleration voltage and camera length is discussed. In [Chapter II.II](#), a new method to measure three-dimensional strain and rotation state in a uniformly deformed sample by the analysis of CBED lines is presented. [Chapter II.III](#) is a giving method to retrieve the three-dimensional displacement variation along the electron beam direction.

Finally the [third Part](#) studies two dimensional materials properties. Its [first Chapter](#) studies graphene HR-TEM images contrasts and diffraction and its [second Chapter](#) is focused on the thickness measurement of few-layered Molybdenum disulfide and Boron Nitride.

## Part A

# Experimental techniques, studied samples and electron diffraction theory

Transmission Electron Microscope (TEM) has been extensively used in this thesis work. This part aims to give an overview of the [experimental techniques \(Chapter I.I\)](#) and the [studied specimens \(Chapter I.II\)](#). [Diffraction theory \(Chapter I.III\)](#) is also here to give some useful precision on the theory of electron diffraction for the next parts of this thesis.

This part contains all the information needed to understand the thesis work but is not aimed to be a book on electron microscopy. The reader is hence referred to various books or scientific papers for a deeper understanding of the different developed points.



---

## Experimental techniques

---

### A.I.1 The Transmission Electron Microscope (TEM)

One of the motivations that yield to the development of Transmission Electron Microscope was the limited image resolution of visible light microscope due to the light wavelength. In 1925, [de Broglie](#) showed that electrons have wave characteristics with a wavelength that is lower than the one of visible light. [Ruska and Knoll \(1932\)](#) first proposed the term of the electron microscope.

The relativistic electron wavelength is given by the following formula:

$$\lambda = \frac{h}{\sqrt{2m_0eE \left(1 + \frac{e}{2m_0c^2}E\right)}} \quad (\text{A.I.1})$$

Where  $h$  is the Plank Constant,  $e, m_0$  the electron charge and mass,  $E$  the high voltage,  $c$  the speed of light.

The resolution that can be reached by a microscope can't be less than half the wavelength. Equation [A.I.1](#) gives for a 300kV Transmission Electron Microscope values of  $1.97 \times 10^{-3}$  nm (2 pm). In real life experiments, this value is much higher and due to aberrations induced by electron lenses as described further in section [A.I.3](#). Last generation TEMs can reach an information limit of 50 pm.

There are three main steps defining the electron path inside the TEM: illumination, interaction with the sample, and projection. Illumination and projection can be set by the microscope user to define the working mode. Today TEMs are versatile instruments that can work in different mode, HRTEM, STEM, NBED, CBED, etc. These techniques can be separated into two parts, diffraction techniques and imaging techniques. In imaging techniques, an image of the sample is given whereas for diffraction techniques, the CCD camera lies on the diffraction plane, where we have an angular representation rather than a position representation of the sample.

---

The aim of this chapter is to introduce the different TEM techniques used during this thesis. Some theoretical considerations will be given as a base for the other Chapters that will go into more details.

## A.I.2 Electron diffraction techniques

An electron diffraction technique in the TEM is a technique that can image the diffraction of the sample. The diffraction is a representation of the angular distribution of the electrons at the exit face of the sample. The diffraction contains precious information on the sample, such as the crystalline or amorphous structure, crystal lattice, orientation, strain, etc. In this section, electron diffraction techniques that have been used in this thesis are presented. Some of the techniques are not described and the reader can refer to William & Carter book ([William and Carter, 2009](#)) for a detailed and comprehensive presentation.

### A.I.2.1 General considerations on electron diffraction

Electrons interact with matter by Coulomb interaction or magnetic Lorentz interaction. The scattering of electrons can be either elastic, with no loss of energy during the scattering process or inelastic when the scattered electron has lost energy.

The scattering power of an atom is determined by its cross-section  $\sigma_{atom}(\Omega)$  which corresponds to the probability of the atom to be scattered at a solid angle  $\Omega$ . The electron atomic scattering factor (or atomic scattering amplitude)  $f_e(\mathbf{q})$  is often preferred to the cross-section because when squared, it represents the electron scattering probability that a certain momentum transfer will occur ([De Graef, 2003](#)) :

$$|f_e(\mathbf{q})|^2 = \frac{d\sigma_{atom}}{d\Omega} \quad (\text{A.I.2})$$

Where  $\mathbf{q} = \mathbf{k}' - \mathbf{k}$  is the momentum transfer vector.

In electron diffraction, the scattering factor is usually estimated using the Mott-Bethe formula ([Mott, 1930](#)). It links X-Rays and electron scattering factors following the expression:

$$f_e(\mathbf{q}) = \frac{e}{16\pi^2\epsilon_0} \left( \frac{Z - f_X(\mathbf{q})}{|\mathbf{q}|^2} \right) \quad (\text{A.I.3})$$

Where  $f_X(\mathbf{q})$  is the X-Rays scattering factor,  $Z$  the atomic number,  $e$  the electron charge and  $\epsilon_0$  the vacuum permittivity.

With the help of this formula, it is possible to have a good estimate of electron scattering factors from X-Rays scattering factors that can be found in the [international tables for crystallography](#). This formula is only an approximation and has been proved to be incorrect for low  $\mathbf{q}$  ([Peng and Cowley, 1988](#)). Other formulations of the atomic scattering factor exist ([Doyle and Turner, 1968](#); [Weickenmeier and Kohl, 1991](#)) and we refer the the reader to [Reimer and Kohl \(2008\)](#) book for a detailed description.

If we now consider the diffraction from all atoms in the crystal unit cell, then the structure factor  $F(\mathbf{q})$  is obtained :

$$F(\mathbf{q}) = \sum_i f_e^i(\mathbf{q}) \exp(-2\pi i \mathbf{q} \cdot \mathbf{r}_i) \quad (\text{A.I.4})$$

Where  $i$  is the sum over the atoms of position  $\mathbf{r}_i$  in the crystal unit cell,  $\mathbf{g}$  the scattering vector of the diffracted beam, and  $f_e^i$  the electronic atomic scattering factor of the atom  $i$ .

Since the structure factor is the same for every lattice points, the diffracted wave is given by:

$$\psi(\mathbf{q}) = \sum_j^{\text{lattices}} F(\mathbf{q}) \exp(-2\pi i \mathbf{q} \cdot \mathbf{r}_j) \quad (\text{A.I.5})$$

The sum over all the lattice sites of the crystal is called the shape factor:

$$S(\mathbf{q}) = \sum_j^{\text{lattices}} \exp(-2\pi i \mathbf{q} \cdot \mathbf{r}_j) \quad (\text{A.I.6})$$

This approach treats the specimen as superposition of single isolated atoms and neglects the changes in electronic structure due to bonding between atoms. To take in account the bonds, one have to use the density functional theory (DFT) (Hohenberg and Kohn, 1964; Soler et al., 2002).

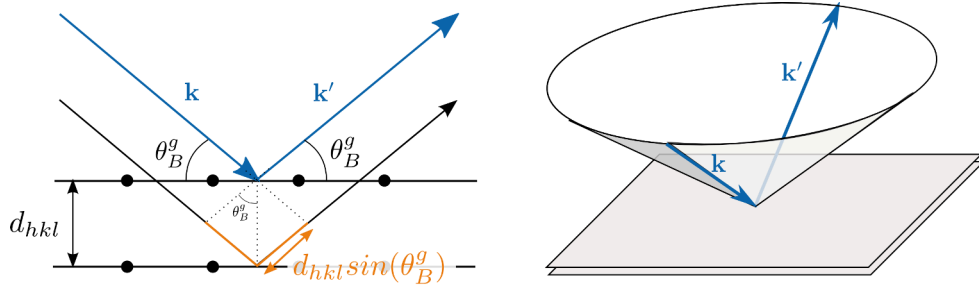


FIGURE A.I.1 – Illustration of the Bragg Law in the direct space.

The atoms ordering in crystals allows constructive and destructive interferences between diffracted beams. The Bragg law illustrated in figure A.I.1 explain these interference. In direct space, the Bragg law is given by the following equation:

$$2d_{hkl} \sin \theta_B^g = \lambda \quad (\text{A.I.7})$$

In reciprocal space, a plane wave can be represented by its wave-vector  $\mathbf{k}$  that fully characterize the direction and the wavelength. A crystal plane (hkl) is represented by its diffraction vector  $\mathbf{g}_{hkl}$ . Figure A.I.2 (b) illustrates the Bragg law in reciprocal space. If  $\mathbf{k}'$  is a diffracted vector linked to the  $\mathbf{g}$  reflection, the Bragg law can then be rewritten as :

$$\mathbf{k}' = \mathbf{k}_0 + \mathbf{g} \quad (\text{A.I.8})$$

As we consider elastic scattering, the norm of  $\mathbf{k}$  and  $\mathbf{k}'$  vectors is equal to  $\frac{1}{\lambda}$ . In perfect Bragg condition, it means that  $\mathbf{k}$  and  $\mathbf{k}'$  ends on the Ewald sphere. The vector  $\mathbf{g}$  links therefore two points of the Ewald sphere and the  $\mathbf{k} + \mathbf{k}'$  vector lies on the bisector plane of  $\mathbf{g}$  so that :

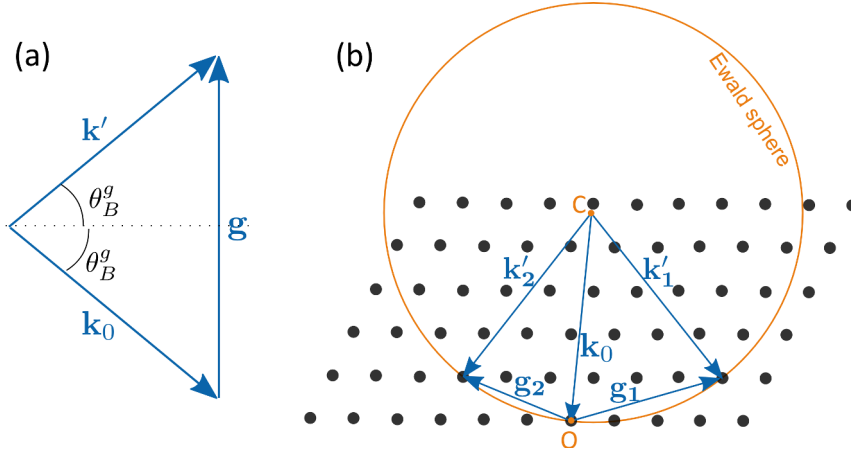


FIGURE A.I.2 – (a) Bragg Law in reciprocal space and (b) Ewald sphere construction.

$$\mathbf{g} \cdot (\mathbf{k}_0 + \mathbf{k}') = \mathbf{g} \cdot (2\mathbf{k}_0 + \mathbf{g}) = 0 \quad (\text{A.I.9})$$

This section treats the diffraction vector in perfect Bragg condition, in reality, there is often an excitation error developed in Chapter A.III.

In electron microscopy, several techniques allow to image the diffraction of a sample. In this thesis, we mainly used techniques having a small electron probe. Other techniques (TEM diffraction, SAED...) will not be described in the following sections. Small probes electron diffraction techniques can be classified in two main types: the ones that have a convergent probe (CBED) and the one that have a nearly parallel probe (NBED). Of course these techniques obey to the same physics, and this classification is purely technical. One can say that we are in Convergent Beam Diffraction when the convergent semi-angle is bigger than 10 mrad.

### A.I.2.2 NBED

NanoBeam Electron Diffraction (NBED) is a technique that allows to measure the crystal lattice parameters by looking at spots positions in the diffraction pattern. The illumination stage of the TEM is set such as the beam is rather small (few nanometers) and parallel (convergence semi-angle being a few mrad). A typical NBED pattern is shown in figure A.I.3 (a). Due to the small convergence of the beam, spots are small disks that do not overlap each other and are well separated.

The Bragg Law (equation A.I.8) explains why we see diffraction spots in a NBED pattern. The diffraction disks visible in NBED pattern give therefore information on the crystal  $\mathbf{g}$  vector and by looking to the position of the diffraction spots relatively to a reference, it is possible to retrieve the strain parameters in the plane perpendicular to the beam (Usuda et al., 2004; Beche et al., 2013). NBED can also be used in the determination of crystal structure (Alloyeau et al., 2008).

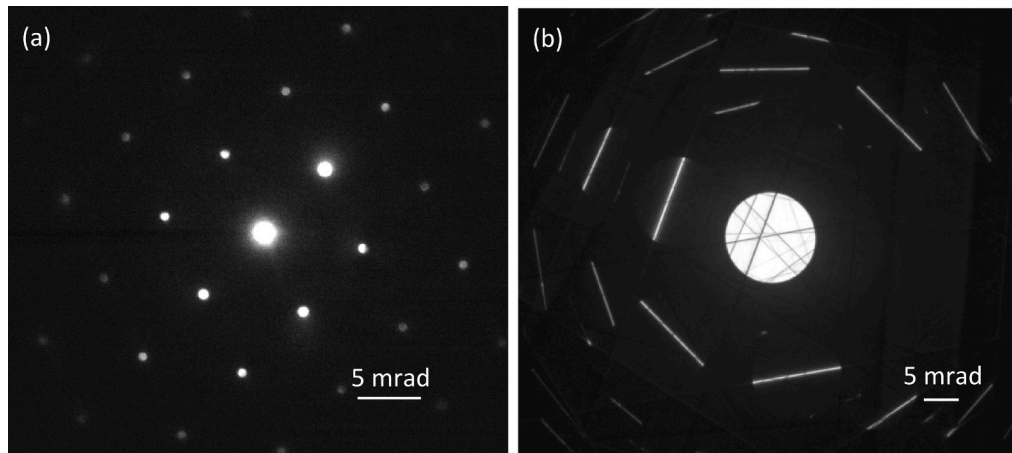


FIGURE A.I.3 – (a) Typical NBED pattern of Silicon at 200kV. (b) Typical off-axis experimental CBED pattern of Silicon at 200kV.

### A.I.2.3 CBED

In Convergent Beam Electron Diffraction (CBED), the illumination is set such as the beam is quite convergent (around 10-15 mrad) when hitting the sample. In the diffraction plane, the transmitted disk is not a spot anymore but becomes a large disk, see figure A.I.3 (b). Figure A.I.4 gives an illustration of the diffraction process in the CBED case. Inside the large diffraction disk, there is a line called excess HOLZ (High-Order Laue Zone) line, that corresponds to the intersection of beam illumination cone and Bragg condition empty cone. In the transmitted beam a negative line called deficient HOLZ line is visible and correspond to the transmitted intensity that has been diffracted. These two lines are separated in the diffraction pattern by two times the Bragg angle  $2 \times \theta_B^g$ .

CBED is a promising technique for measuring strain in crystalline material as the positions of HOLZ lines are very sensitive to small changes in the lattice parameters (Tanaka and Tsuda, 2011). Various methods to retrieve strain have been developed: based on the use of the distances between intersections of HOLZ lines (Jones et al., 1977), on the HOLZ line positions fit by using kinematic calculations including dynamical corrections (Zuo and Spence, 1991), on the use of Hough transform (Kramer et al., 2000), or on the K-line equations (Morawiec, 2007a). The broadening of HOLZ lines due to a non uniform strain along the electron beam complicates the CBED pattern analysis (Vincent et al., 1999; Clement et al., 2004). Several groups (Spessot et al., 2007; Alfonso et al., 2010) have analyzed the line broadening using finite-element modeling.

CBED patterns can also be used to measure the sample thickness (Kelly et al., 1975; Delille et al., 2000) as the profile of HOLZ lines is very dependent on the thickness.

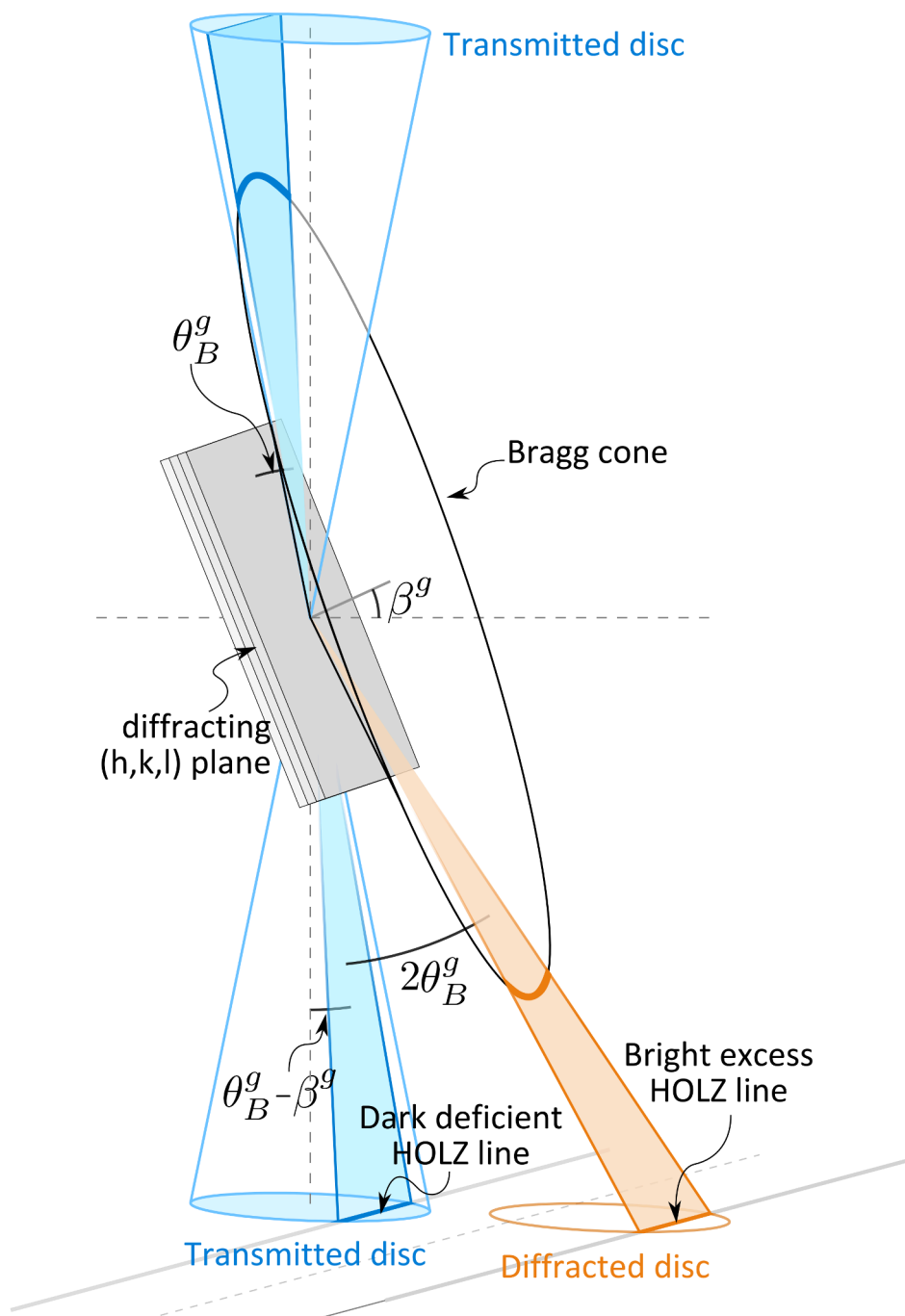


FIGURE A.I.4 – Schematic view of the formation of the CBED diffraction pattern and its HOLZ lines. The deficient and excess HOLZ lines are separated by two times the Bragg angle.

### A.I.2.4 PED

Precession Electron Diffraction (PED) is a technique that is very close to NBED and CBED, but the illumination process is set such as the beam describes an empty cone by tilting and rotating it.

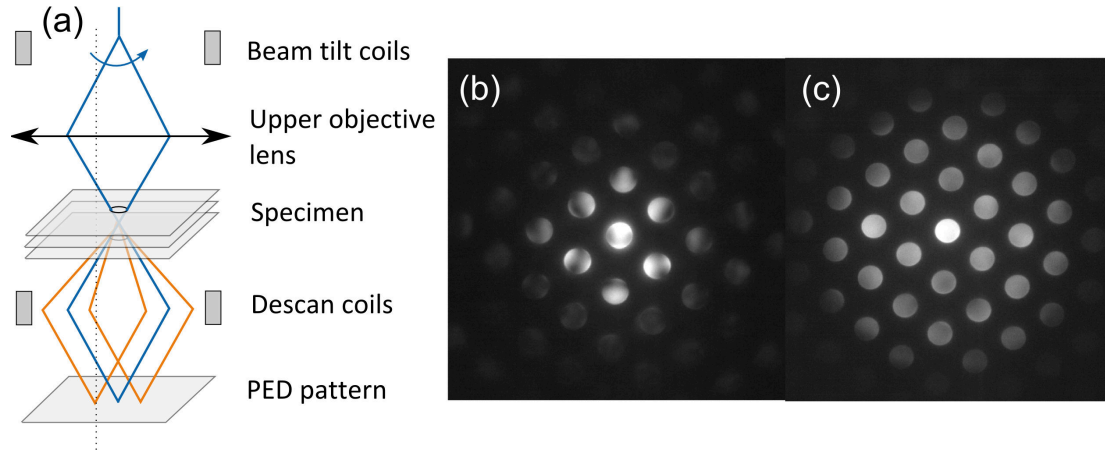


FIGURE A.I.5 – (a) Schematic ray diagram of a precession electron diffraction experiment. The beam is precessed by beam-tilt coils such as the beam never hits the sample in the zone axis (empty cone). The beam is descanned after interacting with the sample in order to retrieve a spot diffraction. A silicon diffraction pattern (b) without precession and (c) with a precession angle of  $0.5^\circ$ .

Figure A.I.5 (a) gives a ray diagram of a precession experiment. The incoming beam is tilted to form an empty illuminating cone. As the incoming beam is always tilted by the precession angle, the position of the transmitted spot describes a circle in the diffraction plane, that is why the beam is descanned, meaning that coils situated after the sample tilt the transmitted beam back to the center of the diffraction plane.

The resulting PED pattern, figure A.I.5 (c), is very similar to a NBED pattern, but as the beam was precessed, the dynamic interactions are greatly reduced. In kinematic diffraction (opposite to dynamical one) beams are only diffracted once. In Dynamical diffraction, multiple diffraction can occur inside the sample. If we consider a diffracted beam diffracted in a  $\mathbf{g}_1$  direction, it can be re-diffracted by  $\mathbf{g}_2$  and the final diffracted beam direction will be  $\mathbf{g}_1 + \mathbf{g}_2$ . The intensity of the diffracted spot is therefore redistributed, and if  $\mathbf{g}_1 + \mathbf{g}_2$  lies on a forbidden reflection, the corresponding spot will be present on the diffraction pattern because of double diffraction.

The PED technique minimizes the dynamic contrast in the diffraction spots (see [White et al., 2010](#)) and allows a better fit of the disk position ([Rouviere et al., 2013](#)).

### A.I.2.5 PACBED

Position-Averaged Convergent Beam Electron Diffraction (PACBED) uses the same illumination condition as CBED, but the diffraction patterns are averaged on a small zone (typically some unit cells) of the sample ([LeBeau et al., 2010](#)). As diffractions from large convergence

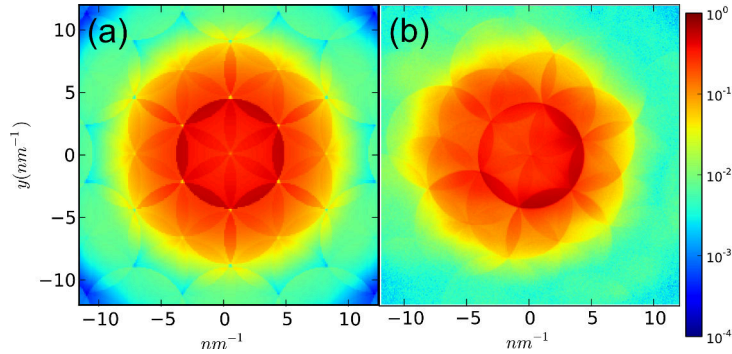


FIGURE A.I.6 – (a) simulated and (b) experimental PACBED pattern of MoS<sub>2</sub> at 80kV.

angle beams are highly dependent on the probe position in the unit cell (LeBeau et al., 2009), incoherently averaging the diffraction over few unit cells makes easier the comparison of the experimental pattern and simulated ones. The position average Figure A.I.6 shows a typical experimental PACBED pattern and its simulation (for more details on these simulations, see Chapter C.II). The specimen thickness can be determined within an error of 1 nm.

### A.I.3 Electron imaging techniques

To get an image of the sample, there are two main solutions in TEM. Either the beam illuminates a large part of the sample and the CCD camera lies on the image plane of the microscope. In this case, amplitude and phase contrast of the sample can be imaged on the CCD camera. This is the so-called TEM or CTEM (conventional Transmission Electron Microscope).

Or a small convergent beam is scanned over the sample and an annular detector integrates the diffracted beams in each scan point. In this case an image is computed from the detector signal. This is the so-called STEM (Scanning Transmission Electron Microscope).

#### A.I.3.1 Conventional TEM

##### A.I.3.1.1 The origin of TEM contrast

In the TEM mode, all electrons coming from the same point of the sample are focused in the image plane. Meaning that an image is formed by the addition of amplitudes and phases of the transmitted and several diffracted beams.

Using an aperture placed at the back-focal plane of the objective lens, it is possible to choose which beams participate to the image (figure A.I.7). In Bright-Field (BF) TEM, only the transmitted beam goes through the aperture. In this case, the thickness, the mass and the diffraction contrast contribute to the image. A thick zone, a zone with heavy atoms and a crystalline area will appear with darker contrast.

In Dark-Field (DF) TEM, the transmitted beam is blocked and only one or few diffracted beams pass through the objective aperture. The DF-image is therefore formed by diffracted

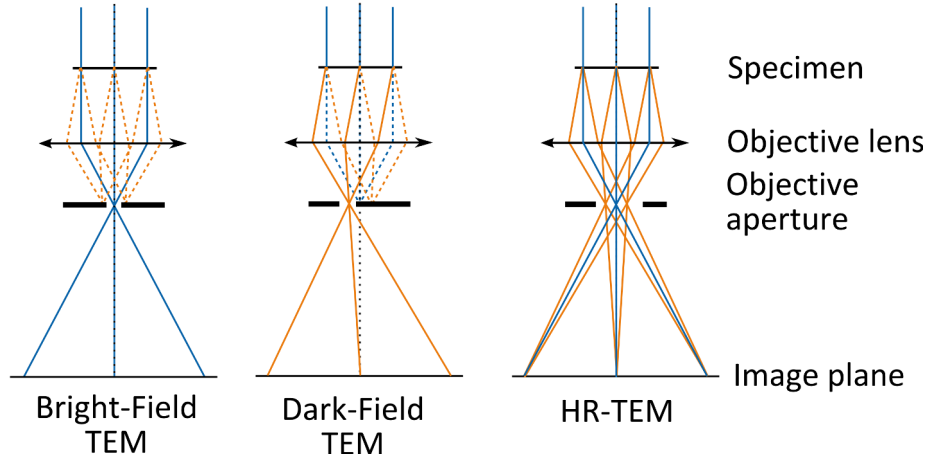


FIGURE A.I.7 – Schematic ray diagram of BF- DF- and HR-TEM.

beams and these images can contain useful information such as crystal orientation, defects, stacking faults, etc.

Finally the High Resolution TEM (HR-TEM) mode allows the transmitted and many diffracted beams to pass through the objective aperture. The image results in the interference of these beams, the phase contrast. This allows to investigate the atomic structure of the sample, if the resolution of the microscope is sufficient. It is important to note that aberrations can influence a lot the contrast in HR-TEM images, and that they have a direct impact on the resolution of the microscope.

#### A.I.3.1.2 Lenses aberrations

Unfortunately, magnetic lenses inside a TEM are not perfect, they induces aberrations. The effect of the lenses aberrations is to modulate the spacial frequencies by a complex function (Kirkland, 2010):

$$H_0(\mathbf{k}) = \exp(-i\chi(\mathbf{k})) \quad (\text{A.I.10})$$

Where  $\chi(\mathbf{k})$  is the deviation of the wavefront from an ideal spherical wavefront. Aberrations can be classified depending on their effect on the beam:

#### Spherical Aberration

If we consider perfectly symmetric lenses, the aberration only depend on the angular deviation of the beam. The spherical aberrations are given by:

$$\chi(\mathbf{k}) = \frac{2\pi}{\lambda} \left( \frac{1}{2}C_1\lambda^2\mathbf{k}^2 + \frac{1}{4}C_3\lambda^4\mathbf{k}^4 + \frac{1}{6}C_5\lambda^6\mathbf{k}^6 + \dots \right) \quad (\text{A.I.11})$$

$C_1$  is called defocus and often written  $\Delta f$  or  $df$ .  $C_3$  correspond to the third-order spherical aberration also written  $C_s$ .  $C_5$  is fifth-order spherical aberration, also called  $C_c$ .

### Astigmatism and Coma

Due to misalignment and inhomogeneity of the lenses they are not symmetric. This asymmetry induces aberration called astigmatism. The focus varies with the azimuthal angle  $\phi$ :

$$\chi(\mathbf{k}) = \frac{2\pi}{\lambda} \left( \frac{1}{2} A_1 \lambda^2 k^2 \sin(\phi - \phi_{A_1}) + \frac{1}{3} A_2 \lambda^3 k^3 \sin(3(\phi - \phi_{A_2})) + \frac{1}{3} B_2 \lambda^3 k^3 \sin(\phi - \phi_{B_2}) \right) \quad (\text{A.I.12})$$

Where  $A_1$  is the two-fold astigmatism,  $A_2$  the three-fold astigmatism,  $B_2$  the coma, and  $\phi_{A_1}$ ,  $\phi_{A_2}$  and  $\phi_{B_2}$  their azimuthal orientation.

### Chromatic aberration

The energy spread of the electron source ( $\Delta E$ ), the instabilities of the objective lens current ( $\Delta I$ ) and the instabilities of the acceleration voltage ( $\Delta V$ ) causes a variation in focal length of the lenses (the focal spread) :

$$\Delta f = C_c \sqrt{\left(\frac{\Delta E}{eV}\right)^2 + \left(\frac{\Delta V}{V}\right)^2 + \left(\frac{2\Delta I}{I}\right)^2} \quad (\text{A.I.13})$$

Where  $C_c$  is the chromatic aberration.

This focal length variation reduces the image contrast for high  $\mathbf{k}$  frequency by the temporal coherence-damping envelope

$$E_D(\mathbf{k}) = \exp\left(-\frac{(\pi\lambda\Delta f)^2 \mathbf{k}^4}{2}\right) \quad (\text{A.I.14})$$

The monochromator can be used to reduce the energy spread of the electron source to a negligible value.

Higher order and other type of aberration exists and we refer the reader to the book from [Reimer and Kohl \(2008\)](#) for detailed description on aberrations. New generation microscopes are equipped with aberration correctors that are able to reduce these aberrations.

#### A.I.3.1.3 Monochromated TEM

For imaging the graphene atomic structure, using low high voltage (80kV) is necessary because of the knock-on damage. At this operating voltage, the resolution and the information limit are limited by chromatic aberration and in order to achieve sub-angstrom resolution, it is necessary to decrease the energy spread of the incoming electron beam. To this extend, the use of a monochromator is necessary (cf. Figure [A.I.8](#)). When the beam is monochromated, the typical energy spread is about 0.2 eV.

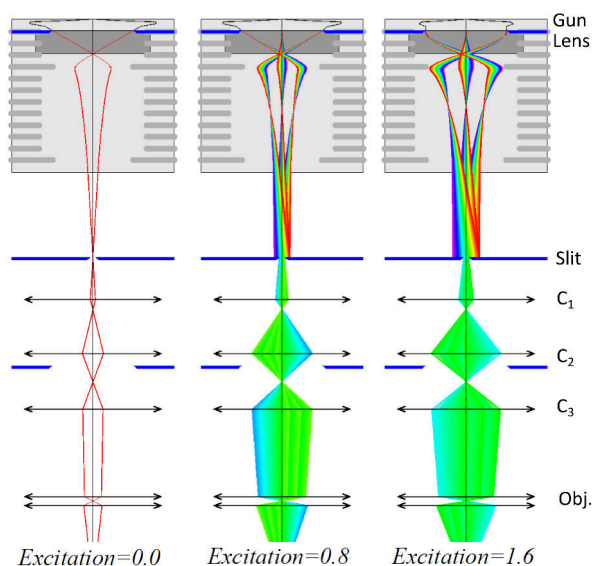


FIGURE A.I.8 – Ray-Diagram illustrating the use of the monochromator. When not excited the beam has a given energy spread, and exiting the monochromator splits the beam and a given energy width can be selected by the use of the slit. Figure taken from FEI monochromator manual.

## A.I.3.2 STEM

### A.I.3.2.1 STEM image formation

In STEM mode, a focused electron beam is scanned over the specimen as shown in figure A.I.9 (a). The image is built up pixel by pixel using the signal coming from a detector. This detector is placed in the diffraction plane and is characterized by its inner and outer radii.

There are different families of detector, according to the inner and outer collection angles. A detector that collects the unscattered (transmitted beam) and low-angle scattered signal is called a Bright-Field detector (BF). The Annular Dark-Field (ADF) detector collects low angle diffracted electrons but not the transmitted ones. And finally the High Angle Annular Dark-Field (HAADF) collects the high-angles scattered electrons. The HAADF imaging is also called Z-contrast imaging because high angle scattered electrons signal is proportional to  $Z^2$ .

The resolution in STEM mode is dependent on the size of the electron probe. The focused probe size is determined by the following factors (Michael and Williams, 1987):

- The initial Gaussian size is determined by the electron source size:  $d_g = \frac{2}{\pi} \left( \frac{I_p}{\beta} \right)^{1/2} \alpha^{-1}$  where  $\alpha$  is the convergence semi-angle,  $I_p$  is the probe current and  $\beta$  is the brightness of the source.
- The diffraction limited diameter, due to the small aperture diffraction :  $d_d = 1.22 \frac{\lambda}{\alpha}$
- The disc of minimum confusion caused by spherical aberrations:  $d_s = \frac{1}{2} C_s \alpha^3$  where  $C_s$  is the third-order spherical aberration coefficient. Other higher order aberration can influence the probe diameter.

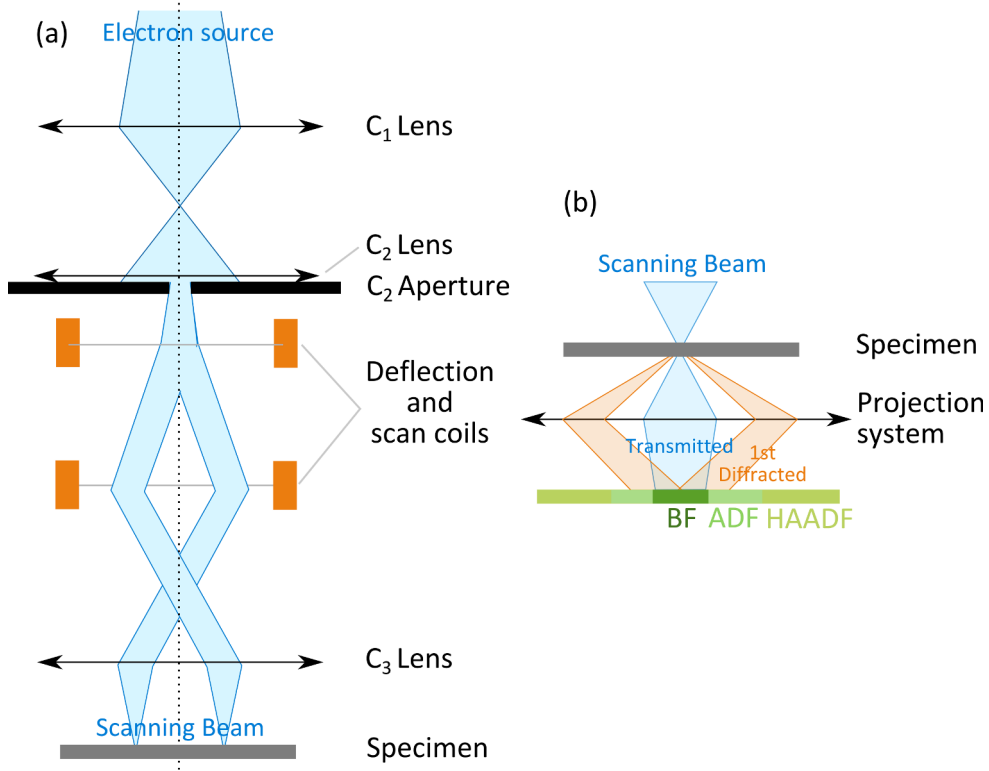


FIGURE A.I.9 – (a) Illustration of the convergent probe scanning for the formation of the STEM image. The double deflection and scan coils keep the beam parallel when it is scanned over the specimen. (b) BF- ADF- and HAADF- STEM

- The energy spread of the electron beam, causing the partial temporal coherence:  $d_{\Delta E} = C_c \frac{\Delta E}{E} \alpha$

### A.I.3.2.2 Quantitative STEM

Quantifying the information coming from the STEM detectors allows to obtain chemical information on the sample and to measure its thickness. The aim of the quantification is to know the relative proportion of the incoming electron beam which has been diffracted to the detector. The detector is scanned with the electron probe (figure A.I.10 (a)) and the signal intensity outside and inside the detector is measured. The normalized intensity is the following (Rosenauer et al., 2009):

$$I_{norm} = \frac{I_{raw} - I_{vac}}{I_{det} - I_{vac}}$$

where  $I_{raw}$  is the raw intensity of the STEM image,  $I_{vac}$  the intensity signal in the vacuum and  $I_{det}$  the mean intensity of the detector when the beam is scanned on it.

In the last part of this thesis, we will see that there are two ways of measuring the vacuum intensity signal  $I_{vac}$ , either by taking it in the detector scan image of figure A.I.10 (a) ( $I_{vac}^{DScan}$ ),

either by taking it directly in the STEM image of the vacuum ( $I_{vac}^{STEM}$ ). These methods are not strictly equivalent, although they give close results, it is preferable to use the second one (discussion is given in Chapter C.II)

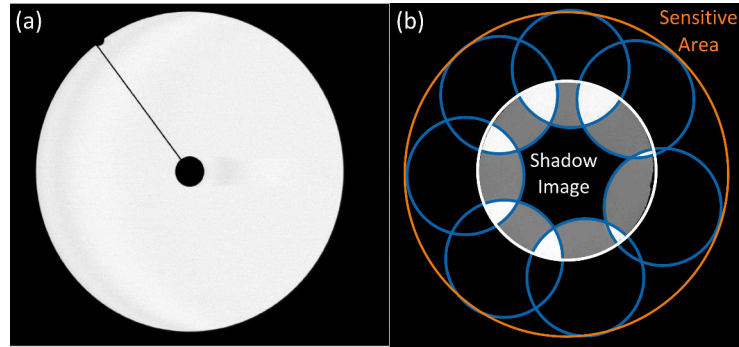


FIGURE A.I.10 – (a) Image of the DF2 detector scan. (b) Superposition of experimental patterns used to center the beam in the sensitive area of the DF2 detector

In order to compare the experimental normalized intensities with simulations, the diffraction must be carefully centered in the middle of the detector as described in figure A.I.10 (b). A delicate point is that the shadow image of the detector is not aligned with its sensitive area as described in [LeBeau and Stemmer \(2008\)](#). The diffraction should be centered on the sensitive area of the detector, meaning the edge of the scintillator crystal. Once the detector is calibrated and the diffraction correctly centered, acquired STEM images can then be directly compared to STEM simulations in order to get quantitative information on the sample.



---

## Studied samples and context

---

At the nanometer scale, the properties of materials change and these new remarkable properties need to be studied at the nanometer scale in order to understand, control, and implement them to create new materials and applications. In this thesis work, two types of materials have been studied using the TEM: The first one consisting of Silicon-Germanium layers embedded in Silicon matrix and the second one being two-dimensional materials and specifically Graphene, Molybdenum disulfide and Boron Nitride. This part will discuss the properties of such samples and describe the state of the art of their nano-scaled characterization.

### A.II.1 Studied samples

#### A.II.1.1 Silicon-Germanium multi-layers

Introducing germanium into the base layer of a transistor increases operating speed, reduces electronic noises and lowers power consumption. An example of application is the Si/SiGe heterobipolar transistor, with demonstrated frequencies beyond 100 GHz (Luy and Russer, 1994). As the strain influences the carrier mobility inside devices (Schaffler, 1997), studying the strain induced by the alternation of layers in the device is critical to understand their physical behavior.

In order to study the displacements (strain and rotations) measurement techniques, four 10nm thick Silicon-Germanium layers of different Germanium concentrations were grown by RPCVD (Reduced Pressure-Chemical Vapor Deposition, Hartmann et al. 2008) on Silicon substrate. These four layers are separated by about 30 nm and buried in 150 nanometers of Silicon. Figure A.II.1 shows a STEM HAADF image of the sample.

A SIMS (Secondary Ion Mass Spectrometry) profile has been done by Beche (2009) to measure the Germanium concentration. The composition of the layers in germanium are  $19.5 \pm 1.5\%$  for the first layer,  $29.8 \pm 2.1\%$  for the second,  $34.7 \pm 2.3\%$  for the third and  $42.5 \pm 1.7\%$  for the last one. These results will allow the modeling of the displacement field in the sample using finite element modeling.

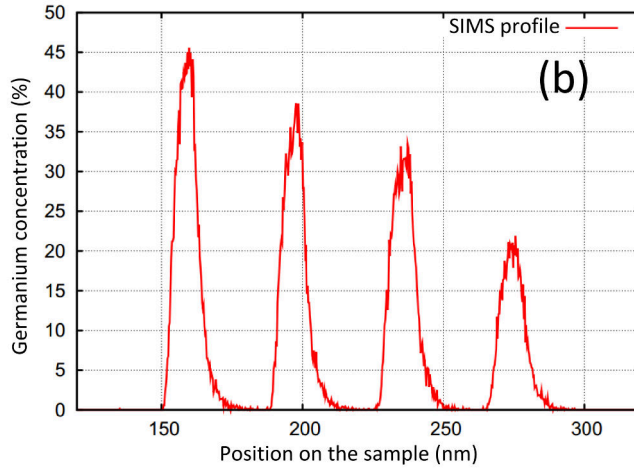
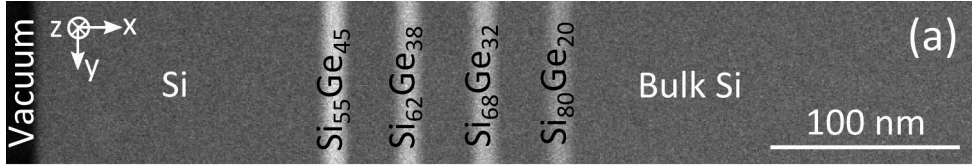


FIGURE A.II.1 – (a) HAADF STEM image of multi-layered Si-SiGe specimen. (b) SIMS profile of Germanium concentration in the SiGe layers. (b) Figure from [Beche \(2009\)](#)

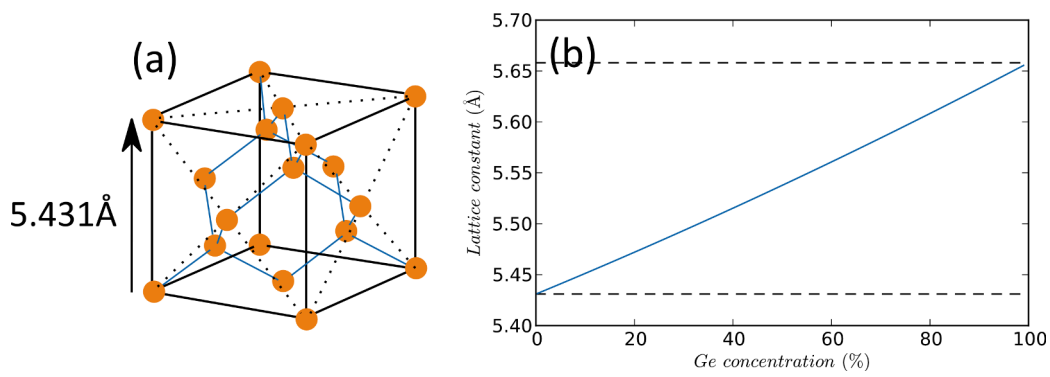


FIGURE A.II.2 – (a) Diamond structure of Silicon and Silicon-Germanium crystal. (b) Plot of the lattice parameters of SiGe alloy as a function of the Germanium concentration.

### A.II.1.1.1 Crystal structure

Silicon and Germanium crystals have both a diamond structure as given in figure A.II.2 (a). The lattice constant of Silicon is  $a_{Si} = 5.431 \text{ \AA}$ , whereas the one of germanium is  $a_{Ge} = 5.658 \text{ \AA}$  giving a lattice mismatch of 4.18% between the two structures.

The lattice parameters of SiGe random alloy is given by [Dismukes et al. \(1964\)](#):

$$a_{Si_{1-x}Ge_x} = 5.431 + 0.20x + 0.027x^2 \quad (\text{A.II.1})$$

Or by a simple ratio of lattice parameters, called Vegard's law [Denton and Ashcroft \(1991\)](#):

$$a_{Si_{1-x}Ge_x} = a_{Si}(1 - x) + a_{Ge}x \quad (\text{A.II.2})$$

### A.II.1.1.2 Electronic properties/Applications

Silicon and Germanium are both indirect band gap semiconductors, with a band gap of 1.12 eV for Silicon and 0.66 eV for Germanium. Germanium having a smaller band gap than Silicon, it is possible using SiGe alloys to tune the band gap structure within the margin of the two elements. The alloy band gap is also indirect and is given by [Krishnamurthy et al. \(1985\)](#) :

$$\begin{aligned} \Delta E_{g Si_{1-x}Ge_x} &= 1.12 - 0.41x + 0.008x^2 \text{ eV for } x < 0.85 \\ &= 1.86 - 1.12x \text{ eV for } x > 0.85 \end{aligned}$$

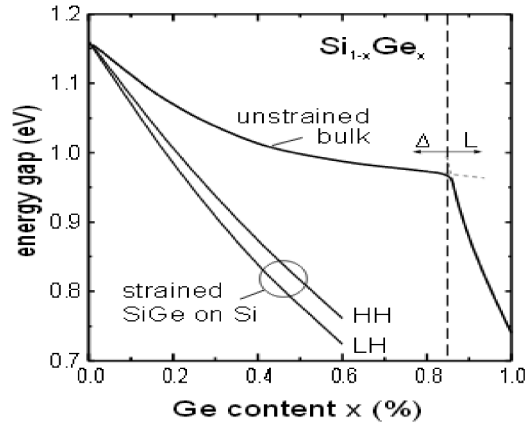


FIGURE A.II.3 – Band gap variation of  $Si_{1-x}Ge_x$  alloys with respect to the Ge concentration. The top curve gives the band gap energy for unstrained Si. The two other curves are  $Si_{1-x}Ge_x$  layers on Si substrate which leads to the splitting of valence band. Figure from [Schaffler \(1997\)](#).

This band gap structure and also numerous physical parameters of the material, such as carrier mobility are highly dependent on strain ([Schaffler, 1997](#)). Figure A.II.3 shows the band gap of strained SiGe on Si substrate compared to the unstrained one. The strain is therefore a crucial parameter and having the knowledge of the local lattice strain is important for microelectronic and semiconductor industry.

## A.II.1.1.3 Sample preparation

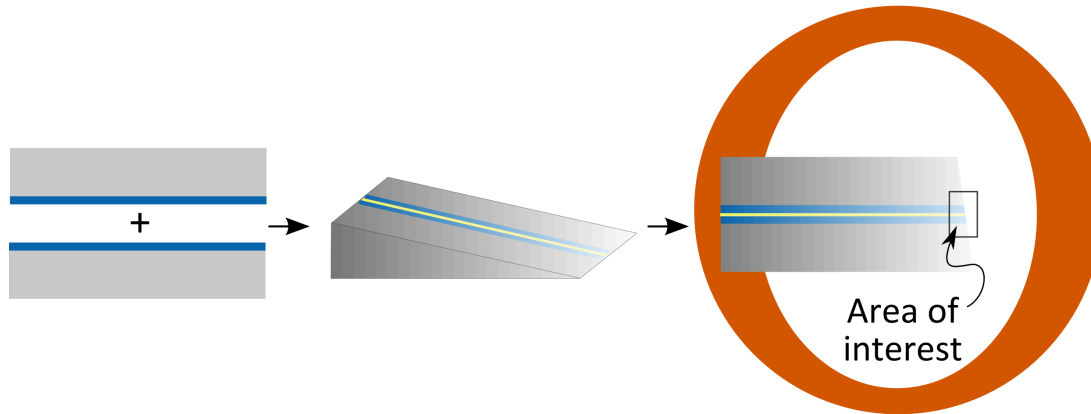


FIGURE A.II.4 – Schematic view of a wedge tripod polished sample prepared in cross-section. Figure inspired from [Ayache et al. \(2010\)](#).

To study layers deposited on a substrate, one common preparation technique is the cross-section preparation, where the layer are observed from the side (see figure A.II.4). This TEM preparation can be done several ways:

- By parallel polishing followed by ion-milling. Two pieces of sample are glued together then polished to about  $20\mu\text{m}$ . The thinning is then made by milling with Argon ions during several hours. This is the historical sample preparation method.
- FIB (Focused Ion Beam). A thin lamella of sample is extracted by focusing a Gallium Ion beam on the sample. FIB is a very versatile tool allowing to precisely select the part of the sample to be extracted.
- Wedge tripod polishing is the method giving the highest quality sample because ion milling in the two previous ones induces amorphous layers on the surface and defects in the sample. Wedge tripod polishing is similar to the parallel polishing but an angle of about  $1.5$  or  $2^\circ$  is put between the two faces. Like this, there is a very thin area of interest in the wedge shape sample, as described in figure A.II.4.

## A.II.1.2 Graphene

Graphene is a two-dimensional carbon-based material attracting the science community over the last 10 years and especially since [Novoselov et al. \(2004\)](#) were able to isolate a monolayer graphene sheet for the first time. Its two-dimensional structure gives it unique mechanical and electronic properties. Electrons inside graphene behave as mass-less electrons making it a nearly perfect electronic conductor. The mechanical properties are also outstanding, due to the high strength carbon-carbon bond. Its breaking strength is 200 times higher than steel ([Lee et al., 2008](#)). Other specificity like thermal conductivities, impermeability to gases, makes it highly attractive for numerous applications.

### A.II.1.2.1 Graphene crystal structure

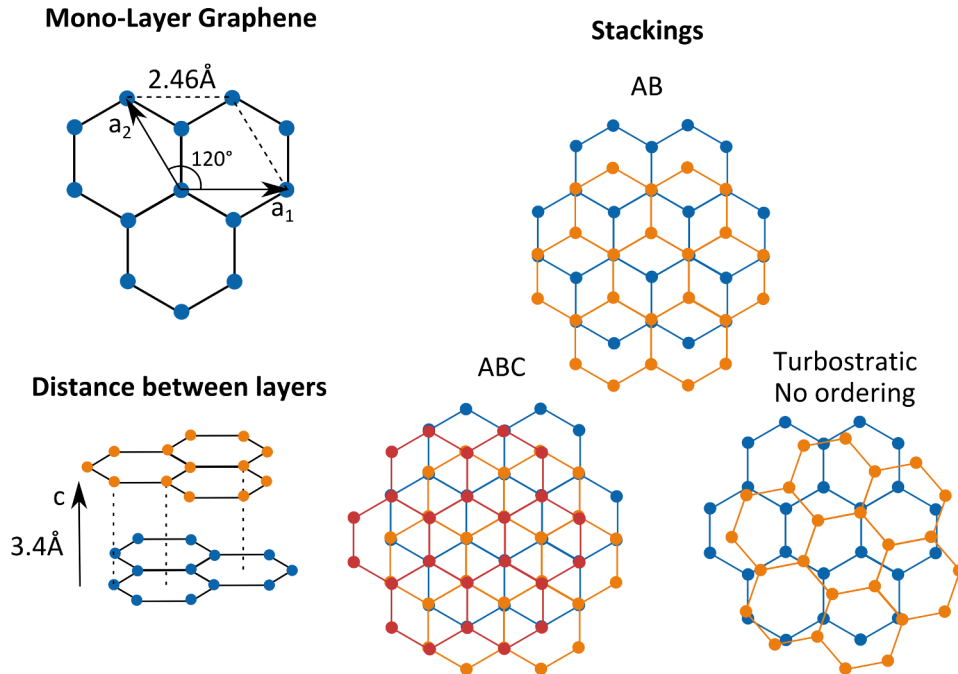


FIGURE A.II.5 – Crystal structure of graphene and graphite.

A theoretical graphene crystal is an infinite 2D layer, composed of  $sp^2$  hybridized carbon atoms. These carbon atoms are arranged in a honeycomb hexagonal lattice. The lattice constants for graphene is  $a = 1.42 \text{ \AA}$ . When more than one layer is present, layers are linked by van der Waals interactions separated by a distance  $c = 3.4 \text{ \AA}$ .

Graphite is made of several stacked Graphene layers. As illustrated by the figure A.II.5, there are three common stacking orders: AB, called Bernal stacking; ABC, called rhombohedral stacking and no stacking order, called turbostratic stacking. The most stable and therefore most studied stacking order is AB.

### A.II.1.2.2 Electronic properties

Electrical properties of graphene are different from the one of bulk graphite because of the electrons confinement and of the absence of interactions between layers. On mono-layer graphene, the band structure presented in figure A.II.6 shows that the valence and conduction bands touch each other at a single point. There are therefore few electronic states near the Fermi level and this makes graphene highly sensitive to any modification of its environment, such as external electric fields, mechanical deformations or doping.

This linear dispersion around the K point is given by the equation  $E = vk$  where  $k$  is the momentum and  $v$  the speed of light. It is called a Dirac point and Dirac electrons or holes have unusual properties compared to ordinary electron. Graphene is a way to probe quantum electrodynamics phenomena, like quantum Hall effect (Novoselov et al., 2005), non sensitivity to

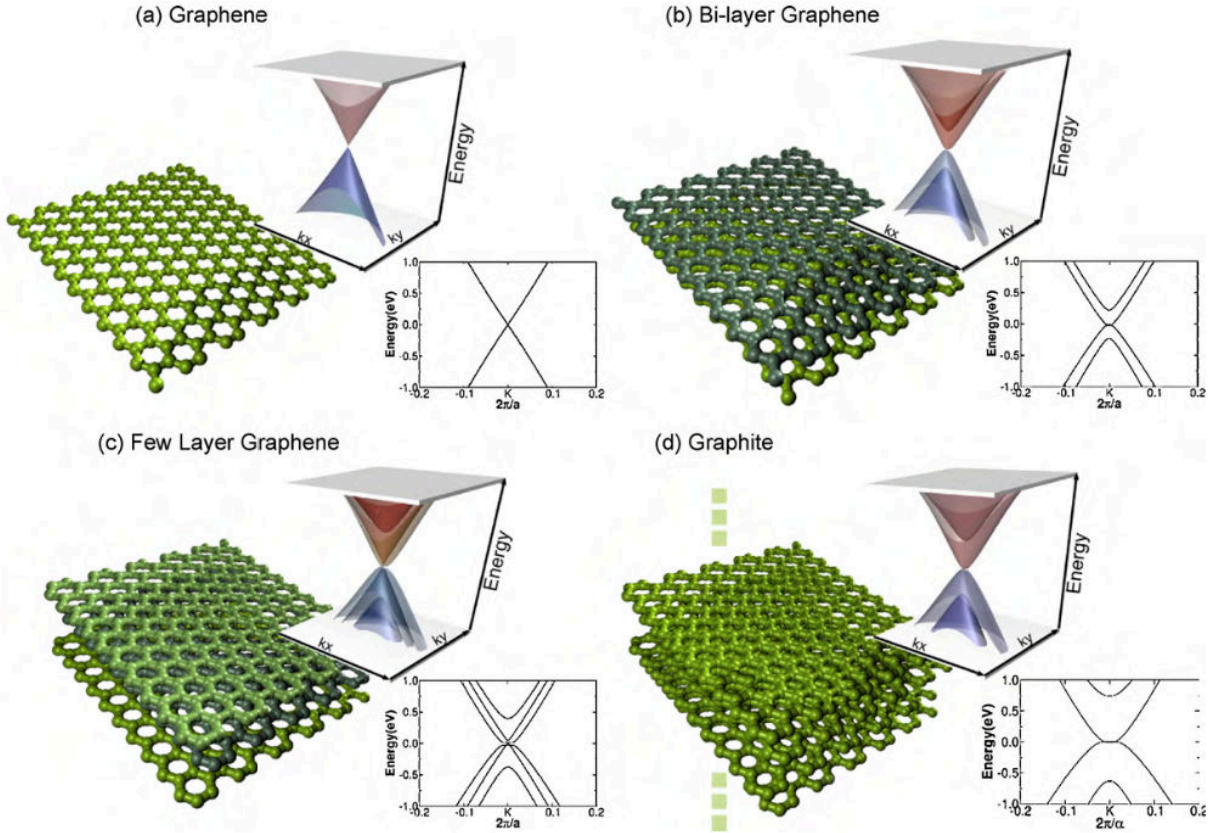


FIGURE A.II.6 – Band structure close to point K of (a) mono-layer (b) bi-layers (c) tri-layers graphene and (d) bulk graphite. The Dirac point (characteristic of relativistic fermions) is present in (a), is lost in bi-layer graphene (b) and appears again in tri-layers (c). Figure reprinted from [Terrones et al. \(2010\)](#) with permissions.

electrostatic potentials, also called Klein paradox ([Katsnelson et al., 2006](#)) or “zitterbewegung” (i.e. jittery movements of a relativistic electron) ([Rusin and Zawadzki, 2009](#)).

In recent years, many researches on graphene aim to modify graphene electronic properties in order to be appropriate for specific applications like sensors, electronic devices, energy storage, etc. We will not go further in the scope of this thesis, but for a deeper understanding of graphene electronic properties, the reader is invited to read [Castro Neto et al. \(2009\)](#) review.

### A.II.1.2.3 Synthesis of graphene

The first mono-layer of graphene was obtained in 2004 ([Novoselov et al., 2004](#)), by mechanical exfoliation (repeated peeling) of Highly Oriented Pyrolytic Graphite (HOPG). This technique allows to obtain single- and few-layered graphene flakes and opens a lot of possibilities to study the fundamental properties of graphene.

Other methods to synthesize graphene have been reported over the last decade. Chemical vapor deposition (CVD) growth over thin metal layers has been reported on Copper ([Li et al.,](#)

2009), on Nickel (Reina et al., 2009), on Iridium Coraux et al. (2008), or on Ruthenium (Sutter et al., 2008). Li et al. (2009) also developed a technique to transfer the grown graphene on another substrate by dissolving the metal foil into a iron nitrate solution.

Grain size is often defined at the nucleation step. Depending on the orientation and the density of nucleation sites, the graphene continuous films will be made of different sized domains connected by grain boundaries often consisting of alternating pentagon-heptagon defect structures (Huang et al., 2011). Synthetic graphene foils still contains many grain boundaries (Gao et al., 2010). These grain boundaries may be responsible for the difference in electrical transport often observed in CVD graphene (Avouris and Dimitrakopoulos, 2012). In order to produce electronic devices, uniformity is required at the wafer scale and that is why a lot of research projects are pushing into producing mono-crystalline graphene at large scale.

#### A.II.1.2.4 TEM sample preparation

Graphene grown by CVD on Copper surfaces can be prepared by spin coating poly(methyl methacrylate) (PMMA) on the surface of the graphene (Reina et al., 2009). The metal is then etched using ammonium persulfate, and the remaining graphene/PMMA layer is then transferred on a TEM grid. The final step is to remove the PMMA either using solvents or by annealing. Residues of amorphous carbon and etching compounds often remains on the grids and on the graphene surface.

For sample preparation of mechanically exfoliated materials, please report to the next section on MoS<sub>2</sub> and BN.

#### A.II.1.3 Other two-dimensional material

The graphene properties have been extensively studied in the past decade and they still are, but the last years have seen the rise of other single-layered materials such as MoS<sub>2</sub>, WS<sub>2</sub>, MoSe<sub>2</sub>, BN, etc. Investigations on the physical and chemical properties of these new two-dimensional structures are quite limited for now although their potential applications may overcome the graphene ones.

In the scope of this thesis, two materials were studied, Molybdenum disulfide (MoS<sub>2</sub>) and Boron Nitride (BN).

##### A.II.1.3.1 MoS<sub>2</sub> crystal structure

Molybdenum disulfide (MoS<sub>2</sub>) belongs to the transition metal dichalcogenides ( $MX_2$ ), where hexagonal layers of metal atoms M are sandwiched between two layers of chalcogen atom X (figure A.II.7). Its lattice constant is  $a = 3.15\text{\AA}$ , and the c constant depends on the stacking order. MoS<sub>2</sub> has three stacking orders: 2H, 3R and 1T. On 2H stacking, the symmetry is hexagonal and there is two layers per unit cell,  $c_{2H} = 12.30\text{\AA}$ . For 3R configuration, the symmetry is rhombohedral with three layers per unit cell,  $c_{3R} = 18.37\text{\AA}$ . For 1T stacking, the Mo atom has an octahedral coordination, and there is one layer per unit cell,  $c_{1T} = 6.15\text{\AA}$ . The interaction linking S-Mo-S layers are van der Waals interactions.

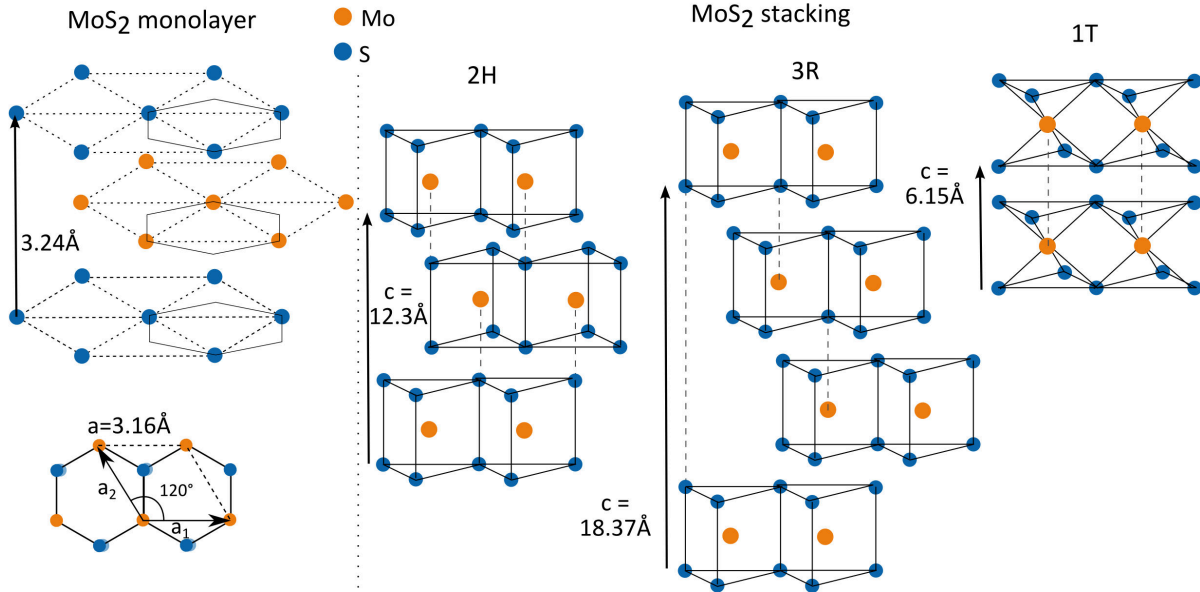


FIGURE A.II.7 – MoS<sub>2</sub> crystal structure. Mo layers are sandwiched between two S layers. 2H stacking correspond to a hexagonal symmetry, two layers per repeat unit, trigonal prismatic coordination. 3R stacking corresponds to a rhombohedral symmetry, three layers per repeat unit, trigonal prismatic coordination. And 1T stacking correspond to a tetragonal symmetry, one layer per repeat unit, octahedral coordination. Adapted from Wang et al. (2012b)

Schonfeld et al. (1983) reported that natural and synthetic MoS<sub>2</sub> can be found in the 2H or 3R polymorph, while 1T stacking is less stable and mainly observed after lithium intercalation (Wytych et al., 1999; Eda et al., 2012). However, Lin et al. (2014) observed a 1T-stacked MoS<sub>2</sub> by STEM using a heating holder between 400 and 700°C that induced a phase transition. They showed that the 1T and 2H phases could easily be converted from one to another via a transverse gliding of the S planes. This gliding was induced by the electron beam and allowed because the heating holder provided thermal activation energy for the atomic displacement. In this thesis work, MoS<sub>2</sub> was observed in room temperature so it is unlikely that the 1T phase was observed.

### A.II.1.3.2 BN crystal structure

Boron nitride has two different structures that are cubic (c-BN) and hexagonal (h-BN), like diamond and graphite for carbon atoms. As only h-BN can lead to two-dimensional layers, we focus here on the h-BN structure.

h-BN is a honeycomb atomic network. Constantinescu et al. (2013) studied the stacking in bulk and bi-layer h-BN and concludes in two stable stackings : AA' and AB. Figure A.II.8 illustrates this stacking. Other structures, namely AA, A'B,AB' described by Constantinescu et al. are less stable and are unlikely to be observed in experiments.

The lattice constant  $a$  and  $c$  are the same for bulk and bi-layer and are equals to  $a = 2.51 \text{ \AA}$  and  $c = 3.34 \text{ \AA}$ .

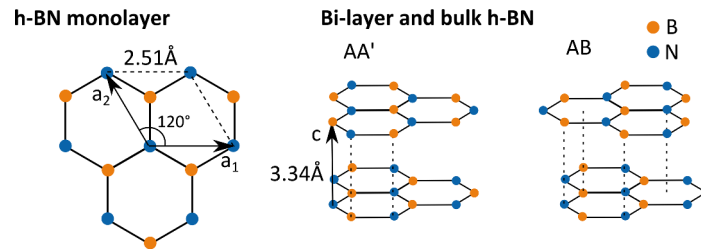


FIGURE A.II.8 – Crystal structure of hexagonal Boron Nitride (h-BN). AA' stacking correspond to B atoms on top of N atoms. AB stacking to some B or N atoms in the center of the next layer hexagon and some B atoms on top of N ones.

### A.II.1.3.3 Properties and potential applications

Unlike graphene,  $\text{MoS}_2$  is a semiconductor material that has a band gap of  $1.8\text{eV}$ . The band structure of  $\text{MoS}_2$  depends on the number of layers. Mak et al. (2010) theoretically predict the transition from indirect (bulk) to direct (lower than six layers) band gap. This transition has been measured experimentally by Splendiani et al. (2010). This transition to a direct band gap is important for the design of photonics, optoelectronics or electronic devices. Such devices have already been reported by Radisavljevic et al. (2011; 2012).

Single-layered and multi-layered h-BN is an insulating material with large band gap comprised between 4 and 8 eV. Because of his chemical and thermal stability, h-BN is a good dielectric and can be associated to conducting 2D materials to create devices. Density Functional Theory (DFT) calculations showed that a band gap on single-layer graphene can be opened when it is sandwiched between two h-BN layers (Quhe et al., 2012) or stands on h-BN layers (Slawinska et al., 2010). Dean et al. (2010) reported that the mobility of graphene on h-BN substrate is 10 times better than on  $\text{SiO}_2$  substrate.  $\text{MoS}_2$  and BN having opposite electronic properties, it is very interesting to study the possible heterostructures than could lead to other electronic structures (Ning Lu et al., 2014). Georgiou et al. (2013) demonstrate a prototype transistor based a two-dimensional  $\text{WS}_2$  barrier between two layers of graphene.

### A.II.1.3.4 TEM sample preparation

This part describes TEM sample preparation of  $\text{MoS}_2$  and BN exfoliated flakes. During this thesis,  $\text{MoS}_2$  and BN crystals have been mechanically exfoliated and transferred onto TEM grids in order to study few-layered structures. The sample preparation is quite simple and requires only few equipments. Figure A.II.9 illustrates the sample preparation.

A bulk  $\text{MoS}_2$  or BN crystal is exfoliated using adhesive tape. The choice of adhesive tape is important and there must not be too much glue on it. Then the flakes are transferred from the tape to a  $\text{SiO}_2$  substrate by gently pressing the tape on the substrate. On  $\text{MoS}_2$ , it is important not to press too much on the tape when transferring because the flakes have a high tendency to break into small parts. Once transferred on  $\text{SiO}_2$ , the remaining glue is removed with solvent (isopropanol).

The thickness of  $\text{SiO}_2$  must be chosen wisely for the single-layers to be visible by interferences (Benameur et al., 2011). Here 77nm thick silicon dioxide has been deposited on silicon wafer.

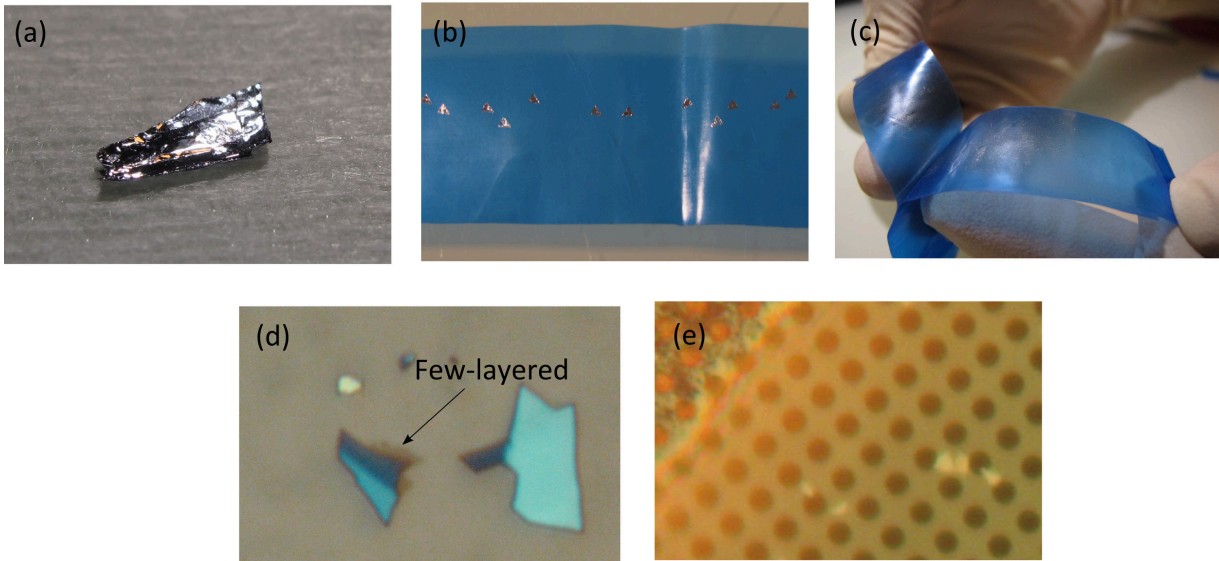


FIGURE A.II.9 – TEM sample preparation of exfoliated MoS<sub>2</sub>. (a) MoS<sub>2</sub> crystal, (b) Flakes after few exfoliation, (c) Flakes after numerous exfoliations, (d) Optical microscope image of MoS<sub>2</sub> flakes transferred on 77 nm thick SiO<sub>2</sub> substrate, (e) Optical microscope image of MoS<sub>2</sub> flakes transferred on a TEM grid.

To transfer the flakes on a TEM grid (here holey carbon film on copper grid), the grid is placed face down over the substrate containing flakes, and a small isopropanol drop is placed over the grid. There are then two possibilities. Either waiting for the drop to fully dry, put another drop and slide the grid out of the substrate. Either sliding the grid just after fringes become visible under the membrane. The first method, although it uses more isopropanol have been found to be more efficient for transferring MoS<sub>2</sub> and BN flakes.

## A.II.2 Context and Goals of the PhD

This thesis work is based on TEM techniques development. As nanotechnology is a more and more studied field, the development of new characterization techniques at the nanoscale is an essential part of this research field. In this thesis, two themes are developed, the first one on the three-dimensional strain measurement, and the second one on the study of two-dimensional materials. This section shows the motivations of the thesis work by emphasizing the importance of TEM characterization for these two specific themes.

### A.II.2.1 Strain measurement: the importance of TEM

Measuring strain at the nanoscale is essential to understand the physical properties of the matter. The aim of this section is to show the important role of TEM in the strain measurement of small sample by presenting an overview of the results from literature. The choice of techniques

is mainly dependent on the sample to be studied and on the resolution and sensitivity needed for the measurement of the strain.

For example **Raman spectroscopy** is sensitive to stress (Anastassakis et al., 1970) but is limited by the intrinsic resolution limit of visible light (less than a micrometer). The sensitivity of Raman spectroscopy can be as low as  $1 \times 10^{-4}$  using Reflectance Anisotropy Spectroscopy (Liarokapis et al., 1999).

**X-ray diffraction** is also used to retrieve the strain field in a sample. The strength of X-Ray diffraction is its very high sensibility to strain (to about  $5 \times 10^{-6}$ ) but its resolution is limited to the millimeter, unless using a synchrotron source. Techniques from synchrotron sources allows to have sub-micron resolution: Di Fonzo et al. (2000) achieved a 100 nm resolution with a  $1 \times 10^{-4}$  precision. With High-Resolution X-Ray Diffraction (HR-XRD), the spacial resolution can reach about 10 nm with a  $1 \times 10^{-5}$  precision but for periodic structures only (Gailhanou et al., 2007). The main advantage of X-Ray studies is that it is a non destructive method that does not require sample preparation, this ensures that the strain field inside the sample is not modified. But it requires synchrotron radiations that are not easily available.

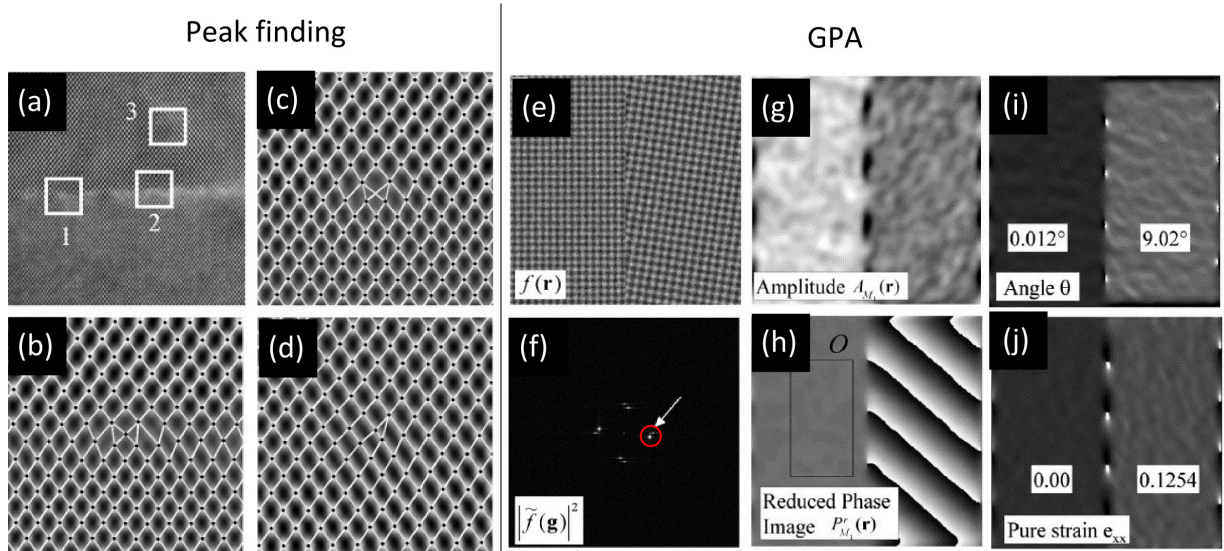


FIGURE A.II.10 – Comparison between Peak-Finding and GPA techniques. (a) HRTEM image of a CdTe/GaAs interface (see Fig. 5) (b)(c)(d) Peak-pair identification around different dislocations. (e) Real space and (f) Fourier Transformed HR-TEM image with the reciprocal space mask (red). (g) Amplitude and (h) Phase of the filtered inverse Fourier Transform. (i)(j) Retrieved shear (i) and normal (j) strain. Reprinted with permissions from Galindo et al. (2007) and Rouviere and Sarigiannidou (2005).

The **TEM** offers the highest spatial resolution for measuring strain, this spatial resolution is far below the nanometer, and last generation microscopes have a 50pm resolution.

**HR-TEM** offers a direct representation of atomic columns, and the displacement of the atomic columns can be analyzed by two different methods illustrated in Figure A.II.10. The first one is the peak finding method where the atomic columns position is found by looking at the maxima or minima positions (Bierwolf et al., 1993; Galindo et al., 2007; Rosenauer and Gerthsen,

1999). The second method called Geometrical Phase Analysis (GPA) uses the reciprocal space, by doing a Fourier Transform of the HR-TEM Image. By applying a mask in the reciprocal space around a spot, a frequency is chosen and doing an inverse Fourier Transform gives a direct space representation of this frequency, its phase is related to the displacement field inside the sample (Takeda and Suzuki, 1996; Hytch et al., 2003). The resolution of this method depends on the mask size and is around 2 nm, with a precision of  $5 \times 10^{-4}$  (Rouviere, 2008).

Using NBED, Beche et al. (2009) manage to reach a  $6 \times 10^{-4}$  precision with a spacial resolution of about 2 nm. This precision is limited by the dynamical contrast visible in NBED diffraction spots. NBED is a popular and easy to setup method for measuring two-dimensional strain in micro-electronic devices (Liu et al., 2008; Usuda et al., 2003, 2004). Recently, Rouviere et al. (2013) proposed to use PED, that removes these dynamical contrasts, and achieved to reach a resolution of  $2 \times 10^{-4}$  with a probe approaching 1 nm in diameter.

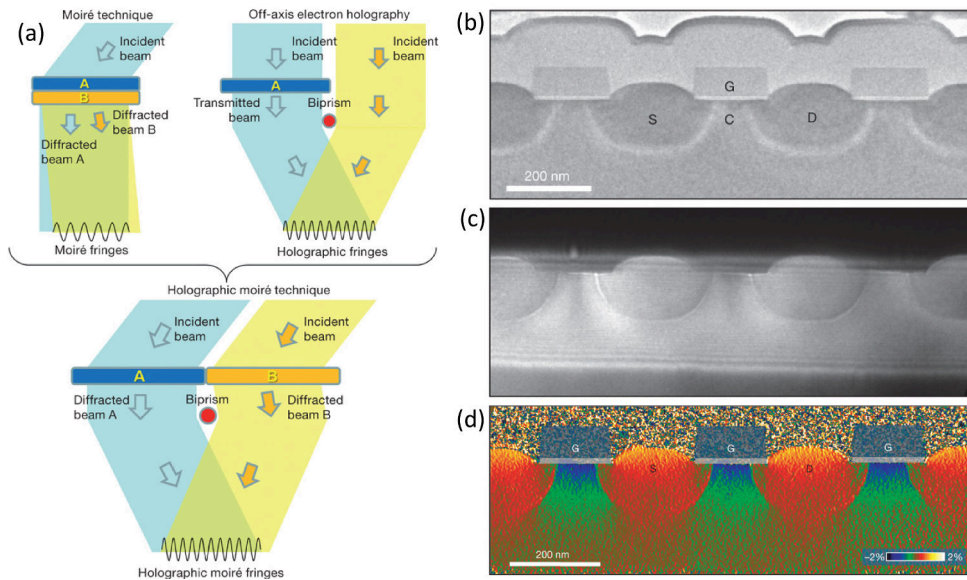


FIGURE A.II.11 – (a) Schematic drawing of the dark-field hologram formation using a biprism. (b) Bright-field image of the device (c) Dark-field hologram (d)  $\epsilon_{xx}$  deformation in the source drain direction. Adapted from Hytch et al. (2008) with permissions.

**Dark-Field Holography**, first proposed by (Hytch et al., 2008), allows to measure the strain with a precision under  $10^{-3}$  and with a resolution of 2 nm. Figure A.II.11 presents the hologram formation and some results on a Si/SiGe device. The main advantage of Dark-Field Holography is its large field of view. It is adapted to epitaxial systems because the substrate can be a reference area. It has been successfully applied to silicon devices (Cooper et al., 2010; Hytch et al., 2011) or Quantum dots (Cooper et al., 2011).

**CBED** is a powerful technique with a spacial resolution below the nanometer and a precision of  $2 \times 10^{-4}$ . Several methods have been developed to measure HOLZ lines positions (Zuo, 1992; Kramer and Mayer, 1999). The next part of this thesis is dedicated to CBED and especially CBED strain and rotations measurement.

The TEM is a very versatile tool ideal for measuring strain. By combining all these technique, a specimen can be deeply studied and very precise strain measurement results useful to understand fundamental properties of devices can be achieved.

### A.II.2.2 Two-dimensional systems: the importance of TEM characterization

Two-dimensional materials need powerful characterization tools able to determine the atomic structure, the thickness, the presence of defects or dopant atoms, etc.

One of the most powerful tool to characterize two-dimensional materials is Raman spectroscopy. Figure A.II.12 illustrates the Raman spectra of graphene as a function of number of layers. Ferrari (2007) showed that the Raman spectra are different in single-, bi-, few-layered graphene or graphite. Cancado et al. (2011) presented the possibility to reveal defects in graphene. Raman spectroscopy has become a quick and useful technique for measuring graphene thickness and evidencing the presence of types of defects, but its spatial resolution (around 500nm) is not sufficient to obtain local information on the atomic structures of defects and grain boundaries.

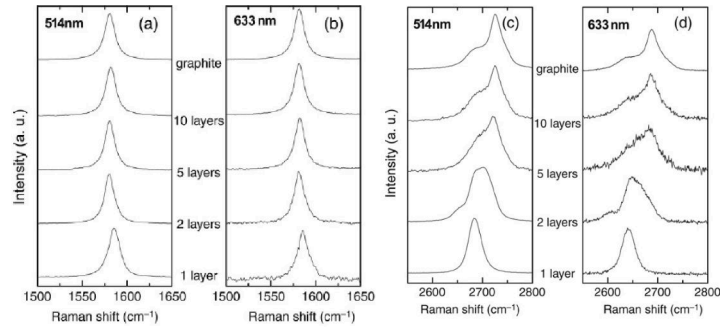


FIGURE A.II.12 – (a) and (b) Evolution of Raman G peak as a function of number of layers for 514 and 633 nm excitations, (c) and (d) Evolution of the 2D peak as a function of number of layers for 514 and 633 nm excitations. Figure from (Ferrari, 2007)

Scanning Tunneling Microscope (STM) and Atomic Force Microscope (AFM) can also be powerful tools to obtain information about the topography and the density of state of graphene at atomic resolution (Voloshina et al., 2013; Boneschanscher et al., 2012). The STM gives only very local information and complementary techniques are needed to characterize graphene at large scales.

One advantage of the TEM is that TEM can image materials from a micrometer scale to atomic scale. This wide scale range allows to study two-dimensional materials from micrometer grain structure down to atomic defects or grain boundaries.

Without the used of aberration correction and monochromator, it is possible to image graphene at low resolution and determine the grain orientation by imaging graphene from diffracted beams only (dark field). Figure A.II.13 (a,b) illustrates the study of graphene grains structure using dark-field TEM images from different diffraction spots. And the corresponding high resolution ADF-STEM image of the grain boundaries. It is also possible, using diffraction, to determine if the observed layer is single- or bi-layered. As given in figure A.II.13 (c), the diffraction from

single-layer graphene shows a higher intensity for the first ring of spots whereas the second ring is stronger in bi-layers graphene.

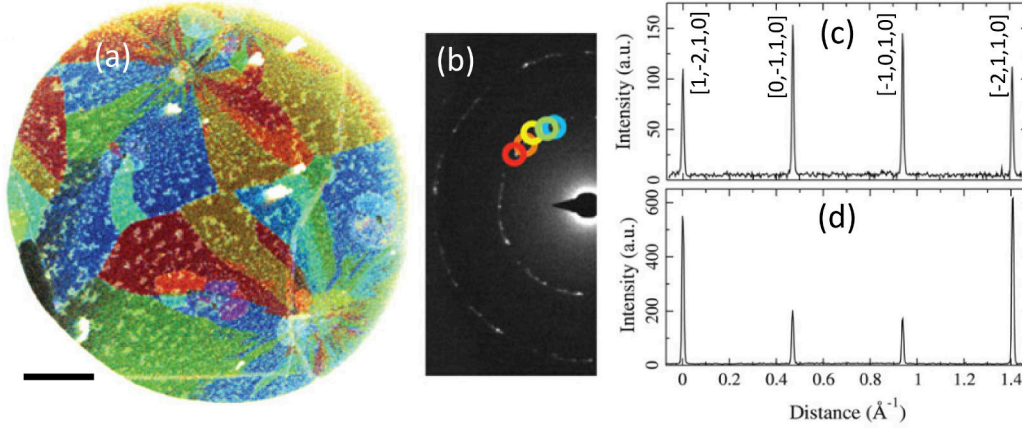


FIGURE A.II.13 – (a) Color-coded images of single-layer graphene grains regions using several different aperture locations showed in (b). Scale bar is 500 nm (a)(b) Reprinted from [Huang et al. \(2011\)](#) and (c)(d) reprinted from [Meyer et al. \(2007\)](#) with permissions.

Recently, TEM have brought essential characterization to graphene research. Two factors make difficult the observation of atomically resolved graphene in the TEM. Firstly because graphene is only a one atom thick layer of a low atomic number material and therefore a weak electron scatterer. Correcting the aberrations in electron optics is hence crucial to maximize atomic contrast. And secondly because the knock-on damages due to highly accelerated electrons forces the use of a high tension lower than 90 kV for the observation of graphene. A lower voltage leads a higher wavelength and therefore to a lower resolution.

In addition, lowering the focal spread  $\Delta f$  (equation A.I.13) is essential for the interaction with a mono-layer (that does not contain atomic columns). To minimize this focal spread, one can lower the energy spread  $\Delta E$  by the use of monochromator or cold FEG, or lower the chromatic aberration  $C_c$  by the use of an image corrector.

Thanks to the recent development of the TEM instrument, like aberration correction or monochromator that allows to lower the focal spread, it is now possible to resolve a unique carbon atom at 80kV. Recent work ([Kaiser et al., 2011](#)) even showed the possibility to image single carbon atoms at 20kV. These monochromated and aberration-corrected TEM made possible to image the vacancies and the dopant atoms in graphene. [Meyer et al. \(2011\)](#) compared High-Resolution TEM images of nitrogen substitutions in graphene and h-BN layers and density functional theory based on TEM simulation. The substitution of a light atom (here C or B) by a light atom (N) is visible due to modifications of the electronic structure around the defect. [Wang et al. \(2012a\)](#) also imaged transition-metal atoms embedded in vacancies.

STEM is also a great technique that is sensitive to the atomic number. Using an aberration corrected microscope optimized for low voltage operation, [Krivanek et al. \(2010\)](#) evidenced single atoms substitution in mono-layered Boron-Nitride (see Figure A.II.14). They found three types of substitutions: Carbon substituting for Boron, Carbon substituting for Nitrogen, and Oxy-

gen substituting for Nitrogen and confirmed them using simulation based on density-functional theory.

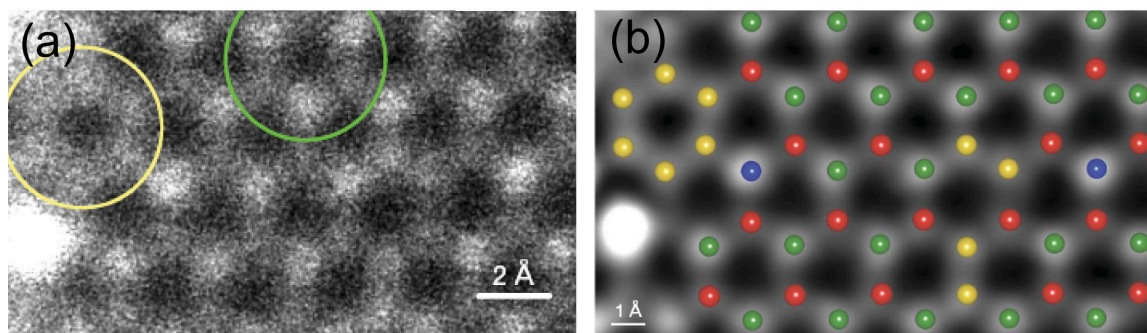


FIGURE A.II.14 – (a) as-recorded ADF-STEM image of monolayer BN at 60kV. (b) Atomic structure determined by the intensity atoms and simulated using density-functional theory. Figure adapted from [Krivanek et al. \(2010\)](#) with permissions.

With the willing of tuning the properties of two-dimensional material through chemical or structural modifications, the TEM is one of the few techniques that are able to directly image the structure, and tell if the modifications are the expected ones. In this context, the development of new techniques in the TEM is essential to improve the TEM abilities and to push the limits of the nano-characterization even further.



---

Theory of diffraction

---

**A.III.1 The excitation error**

Following the Bragg equation A.I.2, when a crystal is perfectly in zone axis, there should not be any diffraction spots because there is only a few chances that the Ewald sphere crosses exactly a lattice point. However in experimental patterns, there are plenty of diffraction spots. This is because TEM samples are relatively thin and in consequence there is intensity even when the Bragg law is not exactly satisfied. A deviation parameter  $\mathbf{s}_{\mathbf{g}}$  is therefore introduced in equation A.I.8:

$$\mathbf{k}' = \mathbf{k}_0 + \mathbf{g} + \mathbf{s}_{\mathbf{g}} = \mathbf{k}_0 + \mathbf{g}_{eff} \quad (\text{A.III.1})$$

Where  $\mathbf{g}_{eff}$  is the effective diffraction vector and  $\mathbf{s}_{\mathbf{g}}$  is a vector parallel to the specimen foil normal  $\mathbf{n}$  and its associated value  $s_g$  is defined by  $\mathbf{s}_{\mathbf{g}} = s_g \mathbf{n}$ . By convention,  $s_g$  is negative when the reciprocal lattice point is outside the Ewald sphere, and positive when it is inside.

In figure A.III.1, we make a difference between the variable  $s_g$ , and  $S_{\mathbf{g}}$  which is the value of  $s_g$  at the Ewald sphere intersection point for an incident beam parallel to the optical axis.  $s_g$  gives the deviation from Bragg condition for any incoming beam. If  $s_g = 0$  the beam is in perfect Bragg condition.  $S_{\mathbf{g}}$  represents how far from the Bragg condition is the diffracted beam for an incident beam parallel to the optical axis.

The conservation of energy implies  $|\mathbf{k}_0| = |\mathbf{k}'|$ , i.e.  $\mathbf{k}_0^2 = (\mathbf{k}_0 + \mathbf{g} + \mathbf{s}_{\mathbf{g}})^2$ . If we consider  $s_g$  by neglecting the second order term in  $s_g^2$  we obtain:

$$s_g = \frac{\mathbf{k}_0^2 - (\mathbf{k}_0 + \mathbf{g})^2}{-2(\mathbf{k}_0 + \mathbf{g}) \cdot \mathbf{n}} \quad (\text{A.III.2})$$

if we suppose  $\mathbf{n}$  parallel to  $\mathbf{k}_0$  and  $|\mathbf{g}| \ll |\mathbf{k}_0|$ , the deviation parameter takes the following expression :

$$s_g = \frac{\mathbf{k}_0^2 - (\mathbf{k}_0 + \mathbf{g})^2}{2|\mathbf{k}_0|} \quad (\text{A.III.3})$$

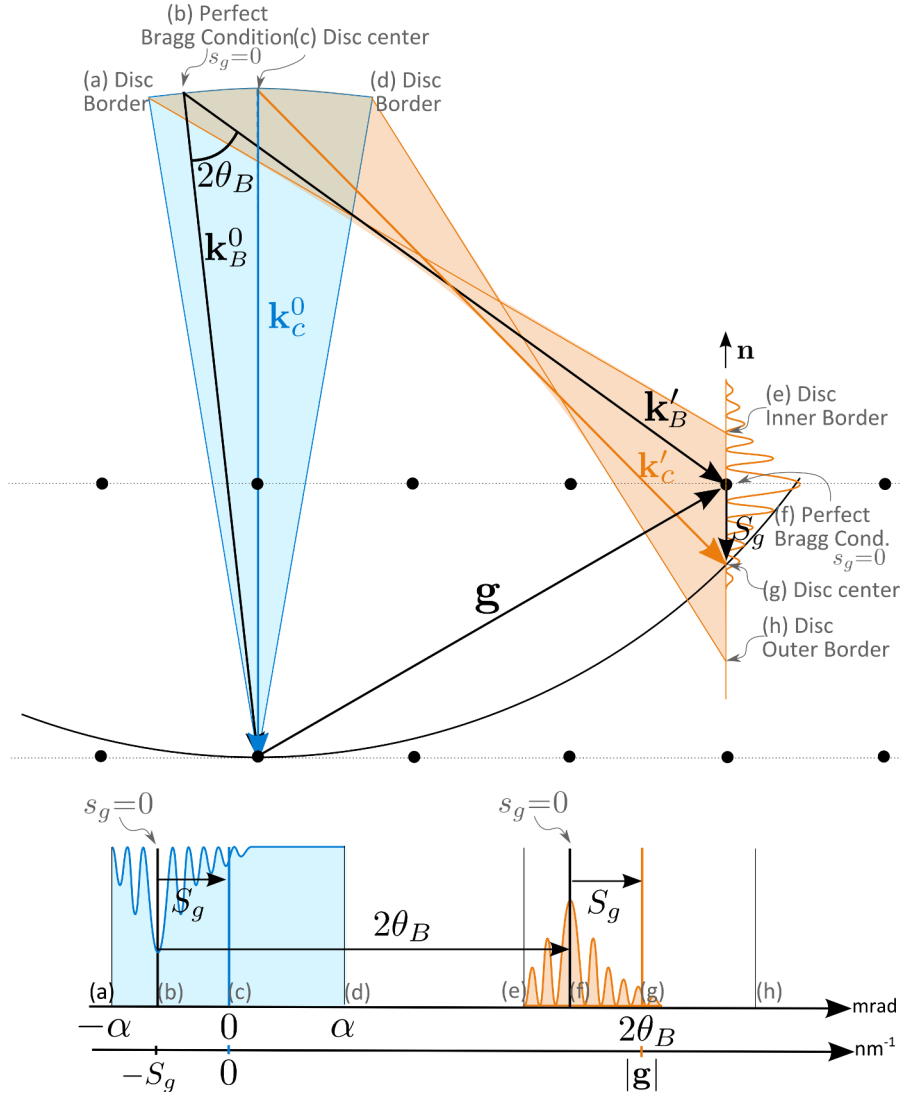


FIGURE A.III.1 – Schematic representation of excitation error ( $S_g$ ) in a CBED pattern. Excitation error leads to an HOLZ line that is not centered in the transmitted and diffracted beams.

The intensity variation of the diffracted beam as a function of the deviation parameter is given, in a kinematic approach (see next section), by:

$$I_g(s_{\mathbf{g}}) = \left(\frac{\pi}{\xi_g}\right)^2 \frac{\sin^2(\pi t s_{\mathbf{g}})}{(\pi s_{\mathbf{g}})^2} \quad (\text{A.III.4})$$

where  $t$  is the sample thickness, and  $\xi_g$  is the extinction distance of the diffracted beam  $g$ .

This equation leads to the relrod representation in figure A.III.1. The intensity of the spot is represented by a relrod, centered on the reciprocal lattice point and parallel to the foil normal. Remember that, if the beam is not convergent (in NBED for example), the only allowed incident beam is  $\mathbf{k}_c^0$ , the one parallel to the optical axis, and therefore the intensity of the spot is given by:

$$I_g = \left(\frac{\pi}{\xi_g}\right)^2 \frac{\sin^2(\pi t S_{\mathbf{g}})}{(\pi S_{\mathbf{g}})^2} \quad (\text{A.III.5})$$

### A.III.2 The projection effect

In a diffraction pattern, the distance between the transmitted beam and the diffracted beam  $\mathbf{g}$  is generally not equal to  $|\mathbf{g}|$ . In a standard situation, this difference is very small, but for two-dimensional materials, this difference can be very large when the sample is tilted. This is what we call the “projection effect” hereafter.

Figure A.III.2 gives the geometric construction of the diffraction when a two-dimensional sample is tilted. The angle between diffracted and transmitted beams is  $2\theta_{eff}$  and from geometrical consideration, the relation between  $\theta_{eff}$  and  $\mathbf{g}_{eff}$  is:

$$\theta_{eff} = \arcsin\left(\frac{|\mathbf{g}_{eff}|}{2|\mathbf{k}_0|}\right) \quad (\text{A.III.6})$$

In figure A.III.2,  $z$  is the optical axis and  $x$  is parallel to  $\mathbf{g}$  when the sample is not tilted. The Ewald sphere equation is given by:

$$x^2 + (z - k_0)^2 = k_0^2 \quad (\text{A.III.7})$$

Or, by using the  $\theta$  parameter, where  $\theta$  varies between 0 and  $\pi$ :

$$\begin{cases} x = k_0 \sin(2\theta) \\ z = -k_0 \cos(2\theta) + k_0 \end{cases} \quad (\text{A.III.8})$$

When the sample is tilted by  $\phi_{tilt}$  (figure A.III.2), the equation of the relrod line is given by:

$$x \cos \phi_{tilt} + z \sin \phi_{tilt} = g \quad (\text{A.III.9})$$

For a given value of  $\phi_{tilt}$ , the diffraction angle  $2\theta_{eff}$  is obtained by calculating the intersection of the relrod and the Ewald sphere, resulting in the following equation:

$$2\theta_{eff}(\phi_{tilt}) = \arcsin\left(\frac{g}{k_0} - \sin \phi_{tilt}\right) + \phi_{tilt} \quad (\text{A.III.10})$$

In order to quantify the projection effect, we define the projection factor as the ratio:

$$pf(\phi_{tilt}) = \frac{2\theta_{eff}(\phi_{tilt})}{2\theta_B} = \frac{\arcsin\left(\frac{g}{k_0} - \sin \phi_{tilt}\right) + \phi_{tilt}}{2 \arcsin\left(\frac{g}{2k_0}\right)} \quad (\text{A.III.11})$$

If  $\phi_{tilt} = 0$ , i.e. the sample is not tilted, then  $2\theta_{eff}(0) = \arcsin\left(\frac{g}{k_0}\right)$ . The Bragg angle expression is  $2\theta_B = 2 \arcsin\left(\frac{g}{2k_0}\right)$ . So even when not tilted, the effective diffraction angle is close

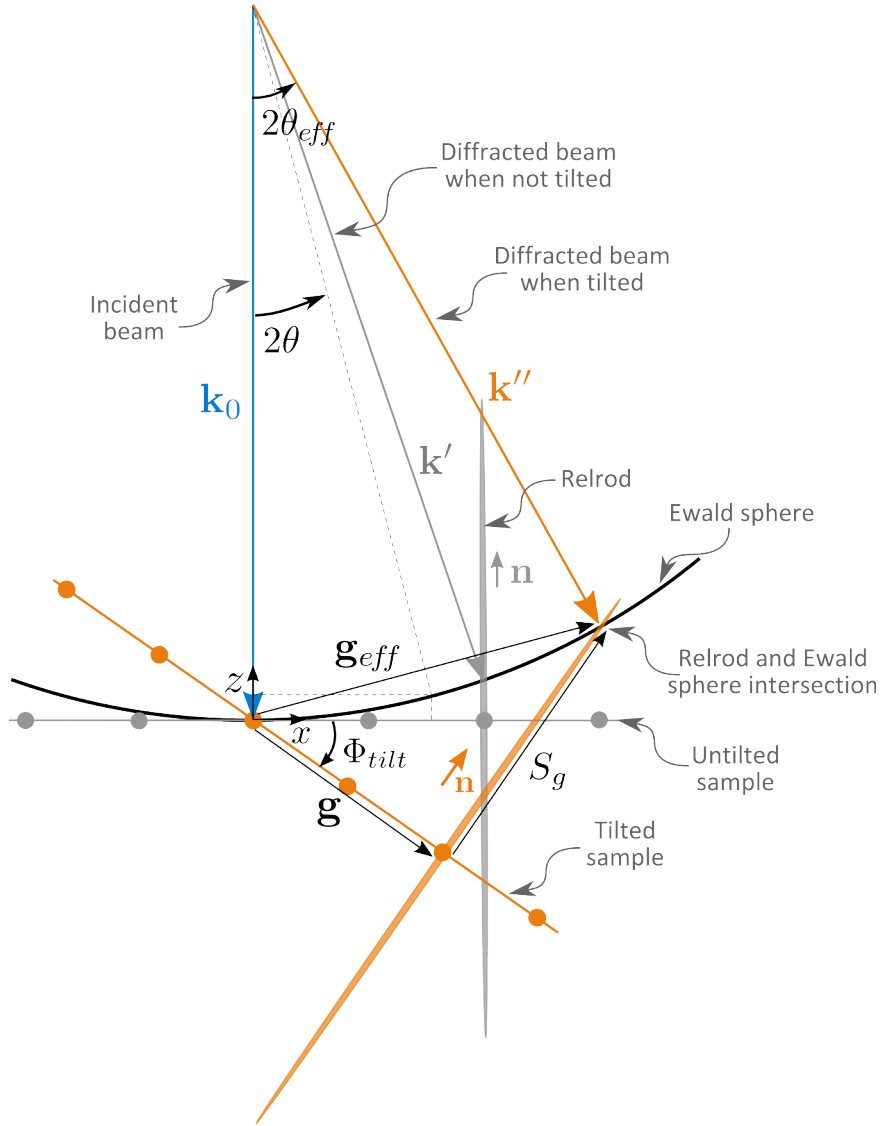


FIGURE A.III.2 – Schematic representation of the projection effect observed when tilting a monolayered sample. The relrod in the case of a monolayer sample is very elongated, this allows to have intensity for the spot even when the tilt angle  $\phi_{tilt}$  is large.

but different from Bragg angle. For Silicon at 200 kV,  $pf_{(200)}(0) = 10^{-5}$  and  $pf_{(600)}(0) = 9.10^{-5}$ . This projection effect is less than the experimental precision.

For graphene at 80kV for  $\phi_{tilt} = 0$ , the projection factors  $pf_{(100)}(0) = 5.10^{-5}$  and  $pf_{(300)}(0) = 4.10^{-4}$  begins to be not negligible.

For standard TEM lamella, the thickness being important, the relrods are short. Therefore when tilting the sample, the intensity of the spots quickly vanishes and it is not possible to measure the projection factor. For a single-layer graphene, experiments showed that even with a  $45^\circ$  tilt, the diffraction spots were still visible. Because of the long relrods of two-dimensional

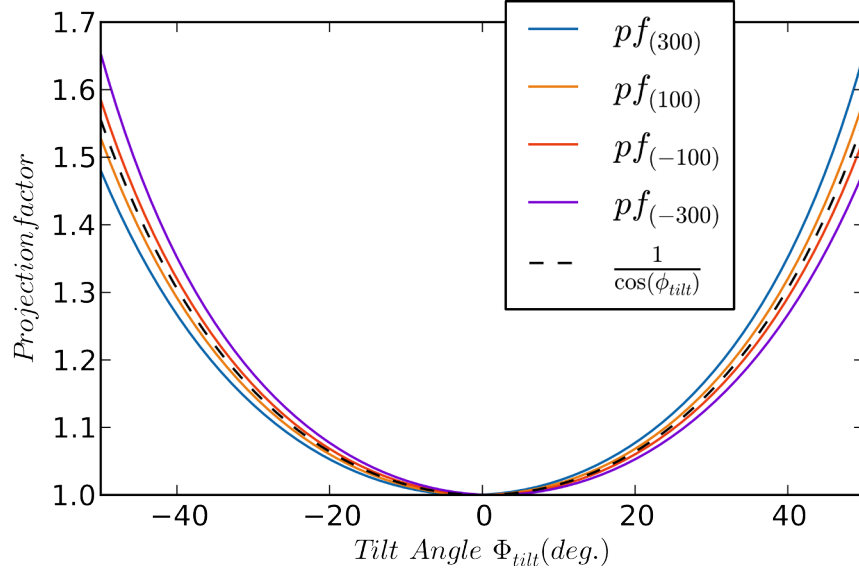


FIGURE A.III.3 – Projection factor as a function of the sample tilt angle ( $\phi_{tilt}$ ) for different diffraction vectors  $\mathbf{g}$  of graphene at 80kV. Solid lines correspond to the exact values calculated from equations A.III.7 and A.III.9, dashed line is the approximate expression from equation A.III.12.

materials, the projection factor due to the sample tilt can reach important values (see figure A.III.3).

As shown in figure A.III.3, the projection factor depends on the considered reflection. In order to quantify the tilt of a few-layered samples an approximated value of the projection factor is taken by ignoring the excitation error at zero tilt (i.e. for a mono layer, considering that the Ewald sphere is flat):

$$pf(\phi_{tilt}) \approx \frac{1}{\cos(\phi_{tilt})} \quad (\text{A.III.12})$$

Figure A.III.3 gives the projection factor (1) from the intersection between the relrod and the Ewald sphere (equation A.III.11) and (2) from the flat sphere approximation (equation A.III.12). The approximate value is very useful because it does not depend on the diffraction vector and also because it behaves as a mean value of spot displacements. It will be used in this thesis to quantify the tilt of a sample (see Chapter C.I).

### A.III.3 Many-Beams dynamic Bloch waves simulation

The aim of this section is to give the theoretical expressions that will be used in the further parts of this thesis for the simulation of electron diffraction patterns. Many-beams Bloch waves simulation is a method that is based on the Bloch wave theory of dynamical electron diffraction (Bethe, 1928). This method can be expressed in a matrix form and therefore is easy to implement in a computer algorithm, although it needs a lot of computing time. A Python software

(Appendix B) has been written using this method to simulate the CBED patterns in this thesis work.

### A.III.3.1 Resolution of Schrödinger equation

The dynamic simulation of diffraction pattern using Bloch waves is also called the general matrix method. It is based on time independent Schrödinger equation:

$$\frac{-\hbar^2}{8\pi^2m}\nabla^2\psi(\mathbf{r}) + eV(\mathbf{r})\psi(\mathbf{r}) = \frac{\hbar^2k_0^2}{2m}\psi(\mathbf{r}) \quad (\text{A.III.13})$$

Where  $U(\mathbf{r}) = \frac{2me}{\hbar^2}V(\mathbf{r})$  and  $V(\mathbf{r})$  is the crystal potential. The crystal potential can be expanded as Fourier Series:

$$\begin{aligned} U(\mathbf{r}) &= \frac{2me}{\hbar^2}V(\mathbf{r}) \\ &= \frac{2me}{\hbar^2}V_0 + \sum_{g \neq 0} \frac{2me}{\hbar^2}V_g \exp(2i\pi\mathbf{g}\cdot\mathbf{r}) \\ &= U_0 + \sum_{g \neq 0} U_g \exp(2i\pi\mathbf{g}\cdot\mathbf{r}) \\ &= U_0 + U' \end{aligned} \quad (\text{A.III.14})$$

We can then consider a wave vector  $\mathbf{k}$ , representing the wave vector at the crystal entrance. Due to the mean crystal potential, the electrons accelerate when entering the crystal:

$$k^2 = k_0^2 + U_0 \quad (\text{A.III.15})$$

The Schrödinger equation can then be rewritten using the Fourier Series of the potential:

$$\nabla^2\psi(\mathbf{r}) + 4\pi\mathbf{k}^2\psi(\mathbf{r}) = -4\pi^2U'(\mathbf{r})\psi(\mathbf{r}) \quad (\text{A.III.16})$$

To solve this equation, [Bethe \(1928\)](#) used a superposition of Bloch waves. These Bloch waves propagate in the crystal in the following form:

$$\psi(\mathbf{r}) = \sum_g \varepsilon^g b(\mathbf{k}^{(j)}, \mathbf{r}) \quad (\text{A.III.17})$$

Where  $b(\mathbf{k}^{(j)}, \mathbf{r})$  is a Bloch wave associated to the wave vector  $\mathbf{k}^{(j)}$ . Each Bloch wave can be expressed as a superposition of plane waves:

$$b(\mathbf{k}^{(j)}, \mathbf{r}) = \sum_g C_g^j \exp\left(2i\pi\left(\mathbf{k}^{(j)} + \mathbf{g}\right)\cdot\mathbf{r}\right) \quad (\text{A.III.18})$$

Where  $C_g(\mathbf{k}^{(j)})$  is the coefficient, for Bloch wave number  $j$ , associated to the  $\mathbf{g}$  reflection in the reciprocal space.

By putting equation A.III.18 in the Schrödinger equation A.III.16, this leads to the electron dispersion equation:

$$\left[ \mathbf{k}^2 - \left| \mathbf{k}^{(j)} + \mathbf{g} \right|^2 \right] C_g^j + \sum_{h \neq g} U_{g-h} C_g^{(j)} = 0 \quad (\text{A.III.19})$$

To solve this equation, the continuity of the tangential component of the incident wave vector  $\mathbf{k}_0$  and the wave vector  $\mathbf{k}$  inside the crystal has to be taken into account. Each Bloch wave vector  $\mathbf{k}^{(j)}$  must also have the same tangential component as the incident wave vector:

$$\mathbf{k}^{(j)} = \mathbf{k}_t = \mathbf{k}_{0t} \quad (\text{A.III.20})$$

This means that the Bloch wave vector can vary only by its normal component to the surface.

$$\mathbf{k}^{(j)} = \mathbf{k} + \gamma^{(j)} \cdot \mathbf{n} \quad (\text{A.III.21})$$

where  $\mathbf{n}$  is the normal to the crystal surface.

Equation A.III.19 can then be rewritten in the form:

$$\left[ \mathbf{k}^2 - |\mathbf{k} + \mathbf{g}|^2 + \gamma^{(j)2} \right] C_g^j + \sum_{h \neq g} U_{g-h} C_g^{(j)} = 2 [(\mathbf{k} + \mathbf{g}) \cdot \mathbf{n}] \gamma^{(j)} C_g^{(j)} \quad (\text{A.III.22})$$

Neglecting the back-scattered electrons, the term in  $\gamma^{(j)2}$  can be neglected. Introducing the deviation parameter  $\mathbf{S}_g$ , the equation A.III.22 can be rewritten:

$$2\mathbf{k} \cdot \mathbf{S}_g C_g^j + \sum_{h \neq g} U_{g-h} C_g^{(j)} = 2 [(\mathbf{k} + \mathbf{g}) \cdot \mathbf{n}] \gamma^{(j)} C_g^{(j)} \quad (\text{A.III.23})$$

Equation A.III.23 is a sum over an infinite number of diffraction vector. However, most of the beams do not contribute to the final diffraction because they are far away from Bragg condition. This is equivalent to say that, for a given  $\mathbf{h}$  diffraction, the deviation parameter, and therefore  $2\mathbf{k} \cdot \mathbf{S}_h$  is very large. This leads to  $C_h^{(j)} = 0$  for these reflections.

### A.III.3.2 Matrix formulation

$C_h^{(j)} = 0$  for most of crystal reflections. We can consider only  $N$  reflections. Equation A.III.23 can be reformulated in  $N \times N$  matrix form:

$$\mathbf{A} \mathbf{C}^j = \mathbf{B} \mathbf{I} \gamma^{(j)} \mathbf{C}^j \quad (\text{A.III.24})$$

where  $\mathbf{I}$  is the identity matrix,  $\mathbf{C}^j$  is a column vector made with  $C_g^{(j)}$  values, and  $\mathbf{A}$  and  $\mathbf{B}$  are defined by:

$$\mathbf{A} = \begin{pmatrix} 2\mathbf{k} \cdot \mathbf{S}_{g_1} & U_{g_1-g_2} & \cdots & U_{g_1-g_N} \\ U_{g_2-g_1} & 2\mathbf{k} \cdot \mathbf{S}_{g_2} & \ddots & \vdots \\ \vdots & \ddots & \ddots & U_{g_{N-1}-g_N} \\ U_{g_N-g_1} & \cdots & U_{g_N-g_{N-1}} & 2\mathbf{k} \cdot \mathbf{S}_{g_N} \end{pmatrix} \quad (\text{A.III.25})$$

and

$$\mathbf{B} = \begin{pmatrix} 2(\mathbf{k} + \mathbf{g}_1) \cdot \mathbf{n} & 0 & \cdots & 0 \\ 0 & 2(\mathbf{k} + \mathbf{g}_2) \cdot \mathbf{n} & \ddots & \vdots \\ \vdots & \ddots & \ddots & 0 \\ 0 & \cdots & 0 & 2(\mathbf{k} + \mathbf{g}_N) \cdot \mathbf{n} \end{pmatrix} \quad (\text{A.III.26})$$

Solving the equation [A.III.24](#) is equivalent to determinate the eigenvalues and eigenvectors of the matrix  $\mathbf{D} = \mathbf{B}^{-1}\mathbf{A}$ :

$$\mathbf{D}\mathbf{C} = \mathbf{C}\mathbf{\Gamma} \quad (\text{A.III.27})$$

where

$$\mathbf{D} = \mathbf{B}^{-1}\mathbf{A} = \begin{pmatrix} \frac{\mathbf{k} \cdot \mathbf{S}_{g_1}}{(\mathbf{k} + \mathbf{g}_1) \cdot \mathbf{n}} & \frac{U_{g_1 - g_2}}{(\mathbf{k} + \mathbf{g}_1) \cdot \mathbf{n}} & \cdots & \frac{U_{g_1 - g_N}}{(\mathbf{k} + \mathbf{g}_1) \cdot \mathbf{n}} \\ \frac{U_{g_2 - g_1}}{(\mathbf{k} + \mathbf{g}_2) \cdot \mathbf{n}} & \ddots & \ddots & \vdots \\ \vdots & \ddots & \ddots & \frac{U_{g_{N-1} - g_N}}{(\mathbf{k} + \mathbf{g}_{N-1}) \cdot \mathbf{n}} \\ \frac{U_{g_N - g_1}}{(\mathbf{k} + \mathbf{g}_N) \cdot \mathbf{n}} & \cdots & \frac{U_{g_N - g_{N-1}}}{(\mathbf{k} + \mathbf{g}_N) \cdot \mathbf{n}} & \frac{\mathbf{k} \cdot \mathbf{S}_{g_N}}{(\mathbf{k} + \mathbf{g}_N) \cdot \mathbf{n}} \end{pmatrix} \quad (\text{A.III.28})$$

$$\mathbf{C} = \begin{pmatrix} C_{g_1}^{(1)} & \cdots & C_{g_1}^{(N)} \\ \cdots & \ddots & \cdots \\ C_{g_N}^{(1)} & \cdots & C_{g_N}^{(N)} \end{pmatrix} \quad (\text{A.III.29})$$

and

$$\mathbf{\Gamma} = \begin{pmatrix} \gamma^{(1)} & 0 & \cdots & 0 \\ 0 & \ddots & \ddots & \vdots \\ \vdots & \ddots & \ddots & 0 \\ 0 & \cdots & 0 & \gamma^{(N)} \end{pmatrix}$$

To simulate a convergent beam pattern, the matrix given in equation [A.III.27](#) should be resolved by considering an addition of incoming plane waves  $\mathbf{k}_0$ , with different orientations describing the illumination cone.

#### A.III.4 Two-Beams and Kinematic simulation

Despite being very realistic, the general matrix method is very consuming in terms of computing time. For faster calculation and even to make possible the convergence of an algorithm in a reasonable amount of time, a two-beam approach can be used by considering only two beams, the transmitted one, and the diffracted one. This hypothesis will not allow dynamical diffraction between beams. Equation [A.III.24](#) becomes:

$$\begin{pmatrix} -2k_n\gamma & U_{-g} \\ U_g & 2\mathbf{k} \cdot \mathbf{S}_g - 2k_n\gamma \end{pmatrix} \begin{pmatrix} C_0 \\ C_g \end{pmatrix} = 0 \quad (\text{A.III.30})$$

By solving this simple equation, the intensity profile of the line can be extracted giving (Spence and Zuo, 1992):

$$I_g(s_g) = \frac{|U_g|^2 \sin^2 \left( \frac{\pi t}{k_n} \sqrt{k^2 s_g^2 + |U_g|} \right)}{k^2 s_g^2 + |U_g|^2} \quad (\text{A.III.31})$$

$$= \frac{|U_g|^2 \sin^2(\pi t \Delta\gamma)}{(k_n \Delta\gamma)^2} \quad (\text{A.III.32})$$

Where  $\Delta\gamma$  is the gap between the dispersion surfaces defined by:

$$\Delta\gamma = \frac{\sqrt{k^2 s_g^2 + |U_g|}}{k_n} \quad (\text{A.III.33})$$

In the kinematic regime, the term  $|U_g|$  in the  $\Delta\gamma$  expression is neglected and the equation A.III.4 is obtain:

$$I_g(s_g) = |U_g|^2 \frac{\sin^2(\pi t s_g)}{(\pi s_g)^2} \quad (\text{A.III.34})$$

This equation has the advantage of being a Fourier Transform as given in Chapter B.III. This is very efficient in computing time.

## A.III.5 Multislice simulations

In addition to the matrix approach, the simulation method called Multislice is based on the propagation of electron waves inside the sample.

Following Dyck (1980), the atomic potentials can be treated as a small perturbation and the traveling wave in the specimen can be split in two parts, a plane wave traveling along  $z$  direction and the wave traveling in the other directions :

$$\left[ \nabla_{xy}^2 + \frac{4\pi i}{\lambda} \frac{\partial}{\partial z} + \frac{2meV(\mathbf{r})}{\hbar} \right] \psi(\mathbf{r}) = 0 \quad (\text{A.III.35})$$

Where  $m = \gamma m_0$  is the relativistic mass of the electron,  $\nabla^2$  the Laplace operator,  $\hbar = h/2\pi$  the reduced plank constant and  $V(\mathbf{r})$  the diffusing potential distribution in the sample.

Figure A.III.4 shows the principle of the multislice simulations. A thick specimen is cut into thin slices. The atomic potential inside each slide is then projected on top of it. The electron wave propagating in the sample can therefore be treated as an alternation of transmission and propagation processes. For the transmission step, the propagation term in equation A.III.35 is neglected and the equation becomes:

$$\frac{\partial \psi(\mathbf{r})}{\partial z} = -i \frac{2me\lambda V(\mathbf{r})}{h^2} \psi(\mathbf{r}) \quad (\text{A.III.36})$$

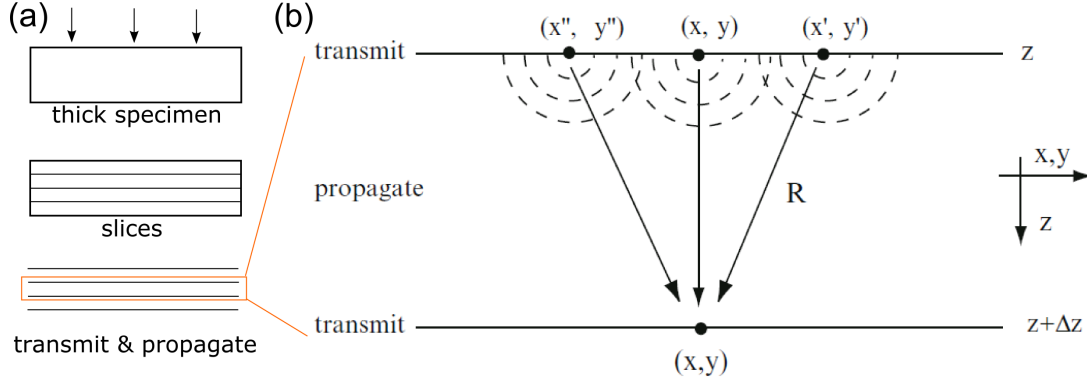


FIGURE A.III.4 – Illustration of the Multislice simulation. (a) Decomposition of a thick specimen, in slices of thickness  $\Delta z$  and each slice is then considered as a transmission followed by a propagation.

For the propagation term, there is no more voltage term and the equation A.III.35 simply becomes:

$$\frac{\partial \psi(\mathbf{r})}{\partial z} = \nabla_{xy}^2 \psi(\mathbf{r}) \quad (\text{A.III.37})$$

We refer the reader to Kirkland (2010) book for the resolution of these equations. The final multislice equation can be expressed as:

$$\psi(x, y, z + \Delta z) = p(x, y, \Delta z) \otimes [t(x, y, z) \psi(x, y, z)] \quad (\text{A.III.38})$$

With  $t(x, y, z)$  the transmission function solution of A.III.36 given by:

$$t(x, y, z) = \exp \left[ i\sigma \int_z^{z+\Delta z} V(x, y, z) dz \right] \quad (\text{A.III.39})$$

where  $\sigma = 2me\lambda/h^2$  is the interaction parameter relative to the electron/matter interaction strength.

And with  $p(x, y, \Delta z)$  the propagator function solution of equation A.III.37 given by

$$p(x, y, \Delta z) = \frac{1}{i\lambda\Delta z} \exp \left( \frac{i\pi}{\lambda\Delta z} (x^2 + y^2) \right)$$

In this thesis work, multislice simulations from Kirkland (2010) code have been used to simulate PACBED and NBED pattern, and to simulate diffraction pattern for STEM signal intensity quantification.

# Part B

## Convergent Beam Electron Diffraction

Convergent Beam Electron Diffraction (CBED) patterns contain large amount of information on the sample geometry. These information are carried by the HOLZ lines that comes from the intersection of convergent beam illumination cone and Bragg condition empty cone. HOLZ lines contain information on the sample thickness, on the structure factor, on the direction of observation, on the electron acceleration voltage, on the camera length and on the displacement field, or strain and rotation of the sample. This part aims to demonstrate how to extract all the information on the specimen that is contained in CBED patterns.

Chapter [B.I](#) deals with the measurement of experimental parameters such as the sample thickness, the direction of observation, the acceleration voltage and the camera length using a single CBED pattern from a perfect crystal. Chapter [B.II](#) is a three-dimensional study of the strain and rotation state in a uniformly deformed sample and Chapter [B.III](#) presents a displacement field retrieval method based on the study of HOLZ line broadening in a multi-layered SiGe sample in a Si matrix.



---

## Experimental parameters calibration using Convergent Beam Electron Diffraction

---

Convergent Beam Electron Diffraction (CBED) is a powerful technique that produces electron diffraction containing information on both sample structure and microscope illumination conditions. This technique can be used on crystals and allows several parameters, such as strain, rotation, thickness, acceleration voltage etc., to be determined.

In this chapter, the focus will be put on what we call experimental parameters, meaning all the parameters that have to be determined prior to do a deeper study of the sample. The measurement of experimental parameters such as sample thickness, structure factor, direction of observation, acceleration voltage and camera length is discussed. Measuring precisely these parameters is crucial for the measurement of strain and rotations which is developed in the next chapters.

The study of a crystal of a known relaxed structure (like perfect silicon) is necessary in order to extract these parameters from experimental patterns. In the present chapter, different techniques from literature are introduced, conditions for obtaining good experimental CBED patterns are given and a new method for determining the experimental parameters is presented.

---

## B.I.1 State of the art

This section presents the state of the art of experimental parameters measurement from CBED patterns. Its aim is to give an overview of the different techniques used to retrieve experimental parameters.

### B.I.1.1 Acceleration voltage and camera length determination

Jones et al. (1977) used the intersections between ZOLZ lines to determine the acceleration voltage on silicon and germanium, the reported precision was 0.7%. Zuo (1992) also used the same principle by comparing the distances between HOLZ line intersections on a filtered CBED pattern. He reported a precision of 15 eV at 100kV (0.015%). Kramer et al. (2000) reported a precision of 20 eV at 120kV (0.015%) using Hough transform to detect the HOLZ lines position.

Camera Length and Acceleration voltage are usually the first parameters to be determined, and they are determined from a known crystal structure. Once they are known, other parameters can be retrieved such as the sample thickness.

### B.I.1.2 Sample thickness refinement

One crucial experimental parameter that has to be determined in a TEM experiment is the sample thickness. The sample thickness can be measured by various methods such as the “ $t/\lambda$ ” method using plasmon loss spectra (Egerton, 1986) or quantitative STEM (Rosenauer et al., 2009) or using the projection of an interface viewed from different angles.

In CBED, Kelly et al. (1975) proposed a famous method that uses the spacing of intensity oscillations of an HOLZ line in a CBED pattern. Based on the two beam theory, the thickness can be determined by using the following equation:

$$\left(\frac{S_i}{n_i}\right)^2 + \left(\frac{1}{n_i}\right)^2 \left(\frac{1}{\xi_g}\right)^2 = \frac{1}{t^2} \quad (\text{B.I.1})$$

Where  $S_i$  is the deviation of the  $i$ th minimum from the exact Bragg position,  $\xi_g$  the extinction distance,  $n_i$  an integer number, and  $t$  the specimen thickness.

By plotting  $\left(\frac{S_i}{n_i}\right)^2$  versus  $\left(\frac{1}{n_i}\right)^2$ ,  $\frac{1}{t^2}$  and therefore the sample thickness can be deduced. An accuracy of 2% can be reached using this method. The main drawback is that multi-beam interaction and anomalous absorption can lead to errors in the measurement that can reach up to 10% (Ecob, 1986).

### B.I.1.3 Structure factor and absorption measurement

#### Two-beams calculation

Delille et al. (2000) proposed a refinement of Kelly method that is also based on the two beam theory. The limitation of Kelly method is that only the minima positions are measured

and the information carried by intensity is not used. Delille method is based on the rocking curve intensity function  $|\phi_g|^2$ , given by:

$$|\phi_g|^2 = \sin^2 \beta (\sin^2 (\pi \Delta k t) + \sinh^2 (\pi \Delta k' t)) \exp \left( \frac{-2\pi t}{\xi'_0} \right) \quad (\text{B.I.2})$$

Where  $\beta = \tan^{-1} \left( \frac{1}{s\xi_g} \right)$  and  $\Delta k' = \frac{\sqrt{1+(s\xi_g)^2}}{\xi'_g}$ , with  $\xi'_g$  and  $\xi'_0$  being anomalous absorption distances.

The thickness and extinction distances are calculated through a minimization of the difference between the experimental and the calculated HOLZ line intensity profile. The precision of this method is given to be 0.2% on thickness and 2% on extinction distance. This method does not take in account potential multi-beam interactions but is fast, as it is based on a simple analytical equation that takes in account both extinction distance and anomalous absorption.

This method has been used in the scope of this thesis and the obtained results are given in section B.I.4.

### Multi-beams calculation

Zuo and Spence (1991) developed an automated refinement program of crystal thickness, structure factor, and absorption coefficients. This program is based on multi-beam equation A.III.27 described in Chapter A.III. Using 33 reflections, they studied a line profile crossing the 002 and 004 reflection on a MgO crystal. There have been able to retrieve the following 5 parameters by minimizing the difference between the calculated line profile and the experimental one :

$$U_{200}, U'_{200}, U_{400}, U'_{400} \text{ and } t$$

The precision of this method is about 0.5% on thickness and 2% on structure factors.

All the above methods suppose the high tension and the camera length to be previously measured. These parameters are not refined in the retrieval algorithm. In this chapter, a new method based on multi-beam calculations and allowing to measure simultaneously the acceleration voltage, the convergence angle, the sample thickness and the direction of observation is presented.

## B.I.2 Conditions for good experimental data

High quality CBED patterns are necessary in order to accurately determine the experimental parameters. One basic but important point is that the CBED pattern must be in focus, with a correct setting of the diffraction stigmator. In these conditions, the transmitted beam is a perfect circle of an uniform intensity, containing deficient HOLZ lines. Two other points should be noted in order to improve the pattern sharpness: filtering and cooling.

### B.I.2.1 Filtering

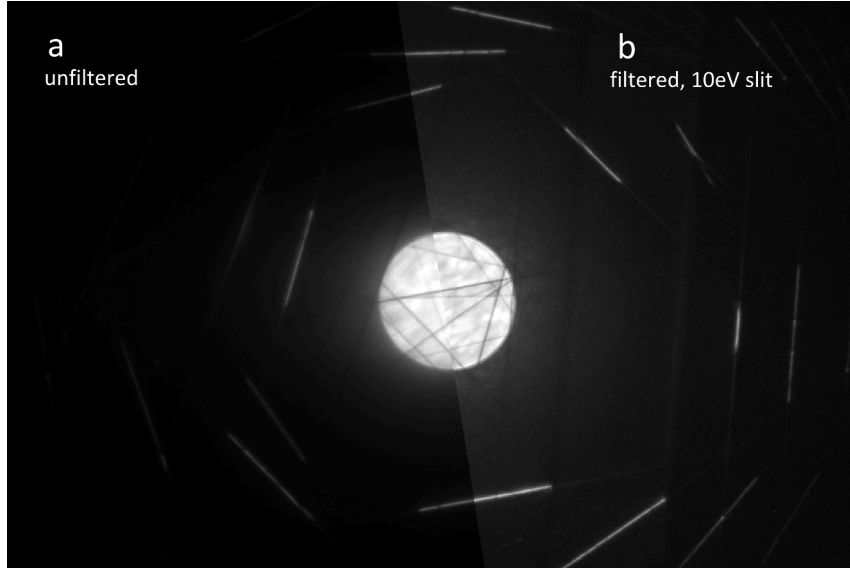


FIGURE B.I.1 – (a) unfiltered and (b) filtered (using 10eV slit) CBED pattern taken under the same conditions, 200kV on silicon (slightly out of focus). Filtered image exhibit sharper HOLZ lines and less diffuse background.

Using an electron energy filter will result in a much better diffraction, as inelastic scattering creates a diffuse background on CBED pattern. Figure B.I.1 shows two CBED patterns, one unfiltered and one filtered with a 10 eV slit. The filtered pattern is sharper and has more details and less diffuse background. To filter the pattern, it is sufficient to put a large slit (10-15 eV) over the zero loss value of the spectra in order to avoid the inelastically scattered electrons. Using a smaller slit will result in stability issues, as the energy filter tends to drift over time.

### B.I.2.2 Cooling

During this thesis, a Gatan double tilt cooling holder (see figure B.I.3) has been used in order to study the influence of temperature on CBED patterns. Figure B.I.2 shows the resulting CBED pattern taken at 0°C and -150°C with the same acquisition and illumination conditions. One can see that weak HOLZ lines are much more visible in the cooled CBED pattern and the excess lines are also more contrasted. This improvement is quite similar to the improvement of filtering the pattern, according to Lu et al. (2003), “the quality of CBED patterns taken at low temperatures without energy filtering was found to be qualitatively similar to that of CBED patterns taken at room temperature with energy filtering”.

Figure B.I.3 gives the [1,-1,-5] HOLZ line profile as a function of the temperature of the sample. The intensity of the line is multiplied by 3 between 0°C and -150°C and the line oscillations become also more visible. With decreasing temperature, the thermal vibration is reduced, and therefore the Bragg condition is better respected and the lines are sharper.

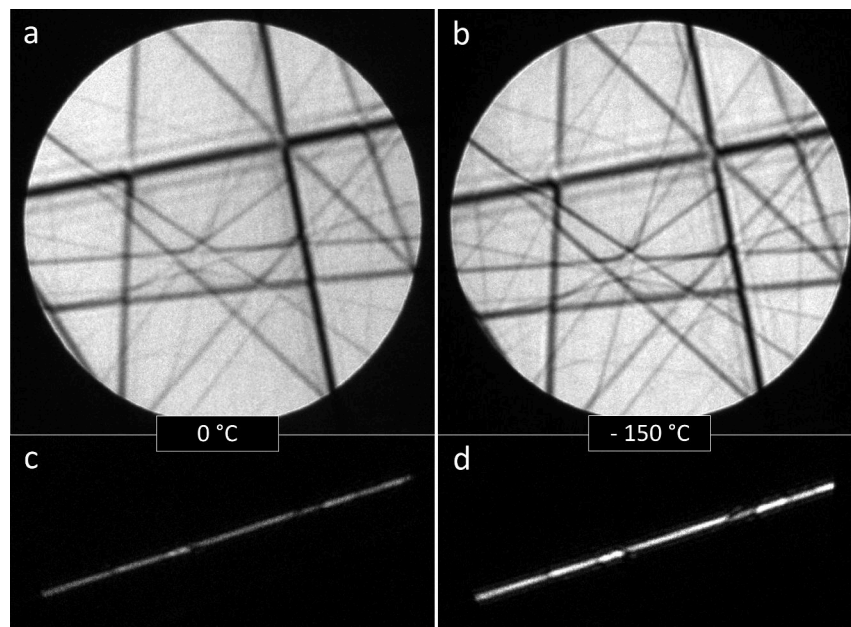


FIGURE B.I.2 – (a) 0°C and (b) -150°C filtered CBED pattern, from perfect Silicon at 200kV with the same acquisition time. Weak HOLZ lines are clearly visible in the cooled sample. (c) and (d) represent one excess HOLZ line and shows a better contrast of the line in the cooled case. The color scale is the same for all pictures.

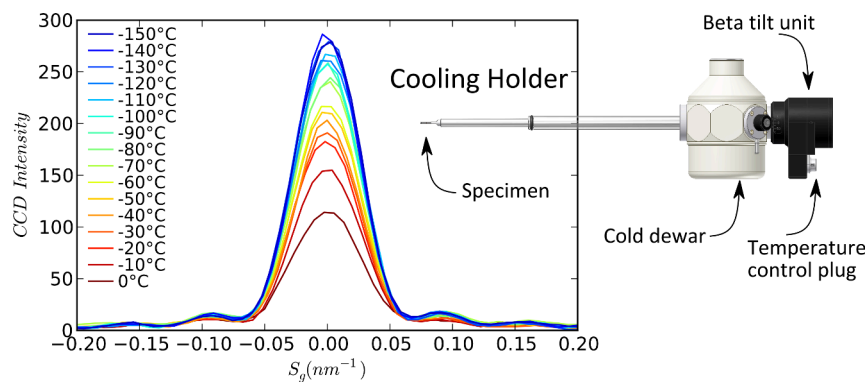


FIGURE B.I.3 – Effect of cooling on the profile of [1,-1,-5] HOLZ line (perfect Silicon, 200kV). Holder illustration taken from Gatan datasheet. Acquisition and illumination conditions are the same for all the profiles.

For future works on CBED patterns, cooling the sample could be a good method to obtain a better precision on the detection of the HOLZ lines.

## B.I.3 Thickness measurement using Delille method

### B.I.3.1 Description of the method

The method allows the retrieval of sample thickness and extinction distance. It is based on equation B.I.2. To apply this method, one must be in two beam condition, meaning that the sample must be tilted and one significant HOLZ line (for example the (004) of Silicon) must be in Bragg condition inside the transmitted beam.

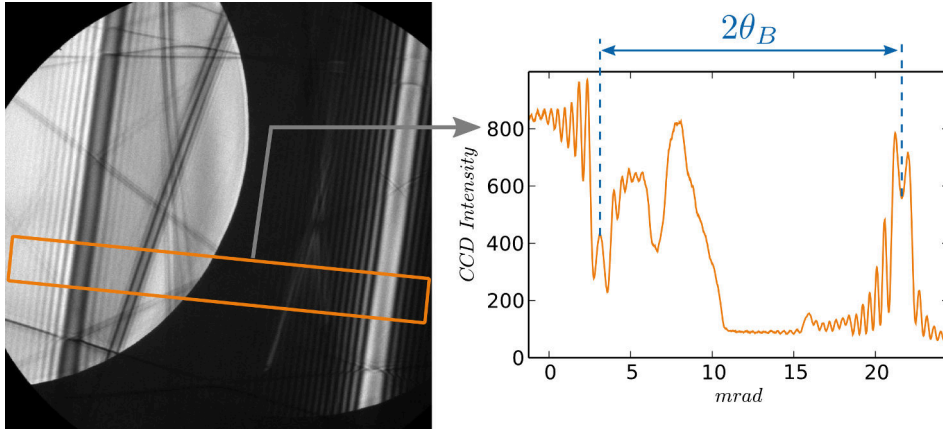


FIGURE B.I.4 – Calibration of the camera length using deficient and excess silicon (004) HOLZ line on a filtered CBED pattern. The distance between deficient and excess HOLZ lines is given by twice the Bragg angle.

To apply the method, the camera length must be calibrated. A typical filtered CBED diffraction and the camera length calibration is presented in figure B.I.4. The distance between the deficient and excess HOLZ line is measured and this distance corresponds to twice the Bragg angle ( $\theta_B$ ) of the considered reflection. To precisely measure this distance, the template matching technique can be used (see next chapter). Here we supposed the acceleration voltage to be in its nominal value (200kV), but it should be better to previously apply one of the methods described in section B.I.1.1 to precisely determine the voltage.

Once the camera length is known, the profile of the excess HOLZ line only is extracted. As illustrated in figure B.I.5, a constant and slope background have been removed, this procedure was not described in the paper by Delille *et al.*, but was necessary to remove the contribution of the background (maybe due to amorphous Silicon on surface due to FIB preparation, or remaining diffuse scattering). The Gaussian background has then been subtracted “to cope with the non-zero intensity of the experimental minimums”.

When the different backgrounds have been removed from the experimental curve, the simplex downhill algorithm is used to minimize the two parameters, thickness ( $t$ ) and extinction distance

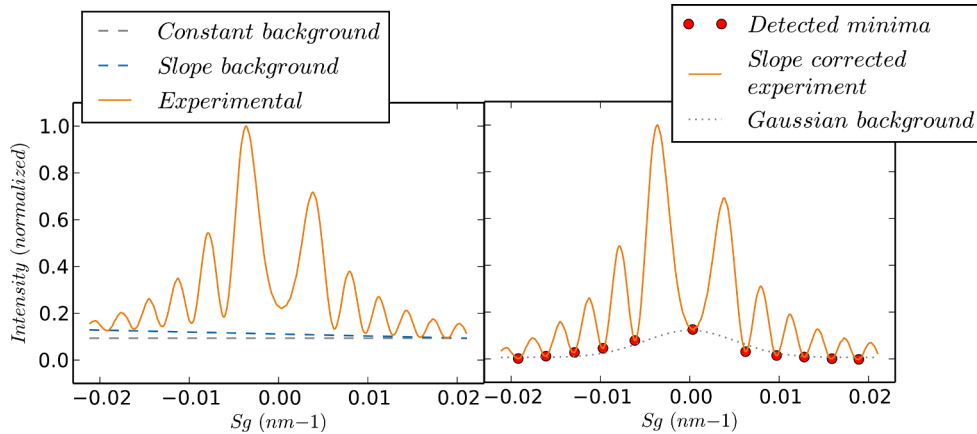


FIGURE B.I.5 – Profile of 004 silicon excess HOLZ line at 200kV. The constant and slope background is removed and the minima are detected to fit the Gaussian background.

( $\xi_g$ ), using the equation B.I.2. Using a minimization function based on intensity squared difference or a minimization function based on intensity gradient squared difference gives similar results.

### B.I.3.2 Application on a silicon thin lamella

This method has been applied to a Silicon sample prepared by Focused Ion Beam (FIB). The sample is made of steps of different thicknesses (see figure B.I.6) which are not uniform, the bottom side being thinner. The thickness and the extinction distance have been measured in several points on the sample. The retrieved rocking curve is well match for every points except when the line is asymmetric, like the first profile given in figure B.I.6. On these asymmetric profiles the fit may not be very accurate, although it seems to give good oscillations spacing. The asymmetry of the line could be due to small residual strain in the sample (Benedetti et al., 2008).

Delille et al. reported a precision of 0.2%. Here due to background and asymmetric issue on some profiles, the error is estimated to be around 1%.

### B.I.3.3 Comparison to EDS

These thickness measurements in CBED have been done as a reference thickness to be compared to a new Energy Dispersive Spectroscopy (EDS) technique in the Scanning Electron Microscope (SEM). This new method is being developed in the laboratory by Eric Robin.

Figure B.I.7 presents the thickness obtained with EDS compared to the one obtained with CBED. EDS measurement leads to a systematic thicker sample (about 30nm thicker). This difference is not in the error range of the CBED measurement that should be few nanometers. The explanation can be that the thickness measured by CBED is only the crystalline thickness of the sample, as the amorphous part does not participate in the HOLZ line profile or position. The EDS technique being a method inspired by the  $\zeta$ -Factors method from Watanabe and Williams

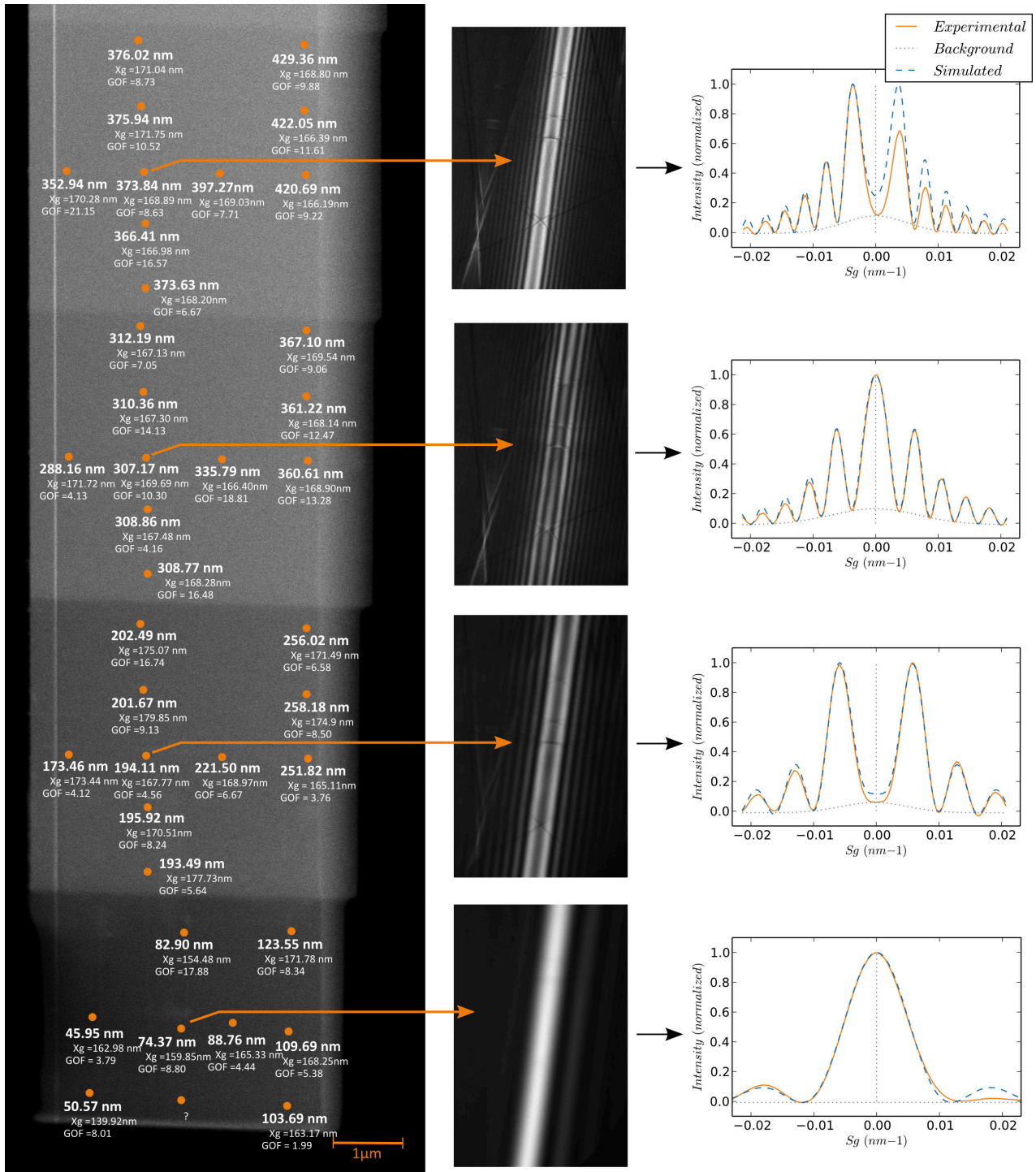


FIGURE B.I.6 – Results of the CBED thickness and structure factor measurement using [Delille et al. \(2000\)](#) method. Sample is Silicon prepared by FIB, with different thickness steps. Diffractions have been taken in FEI Titan 80-300 at 200kV.

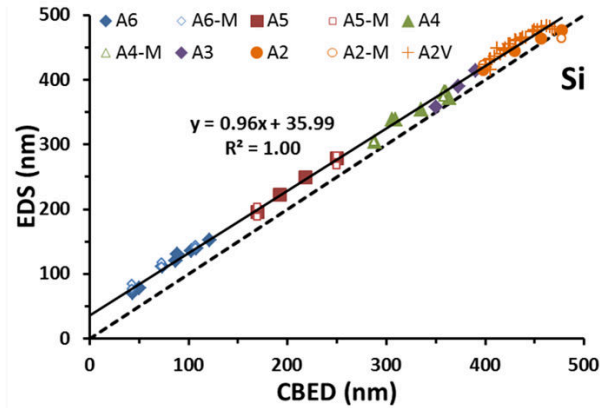


FIGURE B.I.7 – Comparison of results between CBED thickness measurement from B.I.3.2 and EDS measurement in a SEM. A systematic shift of the thickness is observed that could be due to presence of amorphous Silicon from FIB preparation that is not measured by CBED.

(2006). It measures the total thickness of the sample and as the sample is FIB prepared, there should be amorphous layer due to ion milling damage (Ayache et al., 2010) that could explain this 30nm difference between the two measures.

## B.I.4 A new approach : Dynamic fitting of arbitrary profiles

A new approach of experimental parameters fitting is given in this section. We have seen previously that usually the measurements are done in two separate steps: (1) Calibration of camera length and acceleration voltage, (2) determination of thickness and/or structure factor. Here we propose a new method that allows to measure the acceleration voltage, camera length, the direction of observation and the thickness all in once. In this method the structure factors are supposed to be known.

Dynamic multi-beam simulations are used to fit the parameters in the experimental pattern. As it would be too long to simulate the entire diffraction pattern, a series of profiles are taken in the experimental pattern, and these profiles are compared to simulated ones. The followings parts give the equations, the description of algorithm, proof of concept and an application on experimental silicon diffraction pattern.

### B.I.4.1 Sensitivity of HOLZ lines

As seen in the first chapter, HOLZ lines in the CBED pattern are sensitive to a lot of parameters. In order to understand why thickness, direction of observation, acceleration voltage and camera length can be determined for a CBED pattern, let's recall the equation of line position in CBED pattern :

$$l_{Kin}^g = \frac{\sqrt{g_x^2 + g_y^2}}{2} - \frac{g_z}{g} \sqrt{k^2 - \frac{g^2}{4}} \quad (\text{B.I.3})$$

Where  $l_{Kin}^g$  is the kinematic position of an HOLZ line in the CBED pattern,  $(x, y, z)$  are the microscope axes,  $\mathbf{g}$  the diffraction vector,  $\mathbf{k}$  the wave-vector.

And the equation of a line profile (in case of uniform deformation) :

$$I_g(s_g) = \left(\frac{\pi}{\xi_g}\right)^2 \frac{\sin^2(\pi t s_g)}{(\pi s_g)^2} \quad (\text{B.I.4})$$

Where  $I_g$  is the line profile,  $S_g$  the deviation from Bragg condition,  $t$  the sample thickness,  $\xi_g$  the extinction distance.

Equation B.I.3 shows that HOLZ lines are sensitive to  $k$ , meaning sensitive to acceleration voltage. They are sensitive to the projection of  $\mathbf{g}$  along the microscope axes, meaning that they are sensitive to the direction of observation of the sample. And their position is given in  $nm^{-1}$  meaning that the position on the CCD in pixel is dependent on the camera length.

The next equation (B.I.4) shows that the profile of the lines is sensitive to the thickness  $t$  of the sample and to the extinction distance  $\xi_g$ , meaning the structure factor.

These equations are simple kinematic equations that illustrate the influence of experimental parameters on the CBED pattern. They do not take in account the dynamical behavior of the diffraction, that is why in the following we will use the multi-beam dynamical equation given in Chapter A.III to fit the experimental data.

### B.I.4.2 Algorithm description

The algorithm is based on the downhill simplex algorithm (Nelder and Mead, 1965) and is illustrated in figure B.I.8. The downhill simplex algorithm needs several steps to converge (some hundreds), so simulating the whole CBED using the multi-beam dynamical equation given in equation A.III.27 would take too much computing time (few days on a desktop computer). In order to reduce this computing time,  $N$  arbitrary profiles, crossing the center of the CBED disk were used. Here the lines are crossing the center for practical reasons but they could have been anywhere in the CBED pattern.

The parameters that can be fitted by the algorithm are the following:

$t$	<i>sample thickness</i>
$E$	<i>acceleration voltage</i>
$\alpha_{cv}$	<i>convergence semi - angle</i>
$u, v$	<i>DO (direction of oritation) [u, v, w]</i> <i>with <math>w = \sqrt{1 - u^2 - v^2}</math></i>

The structure factor is supposed to be known, and if not, it can be found before applying the algorithm, following (Zuo and Spence, 1991) or (Delille et al., 2000).

The camera length is not a direct fit parameter, but it is easy to retrieve its value. The equivalent fit parameter is the convergence semi-angle. The extracted profiles have a length  $D$  in

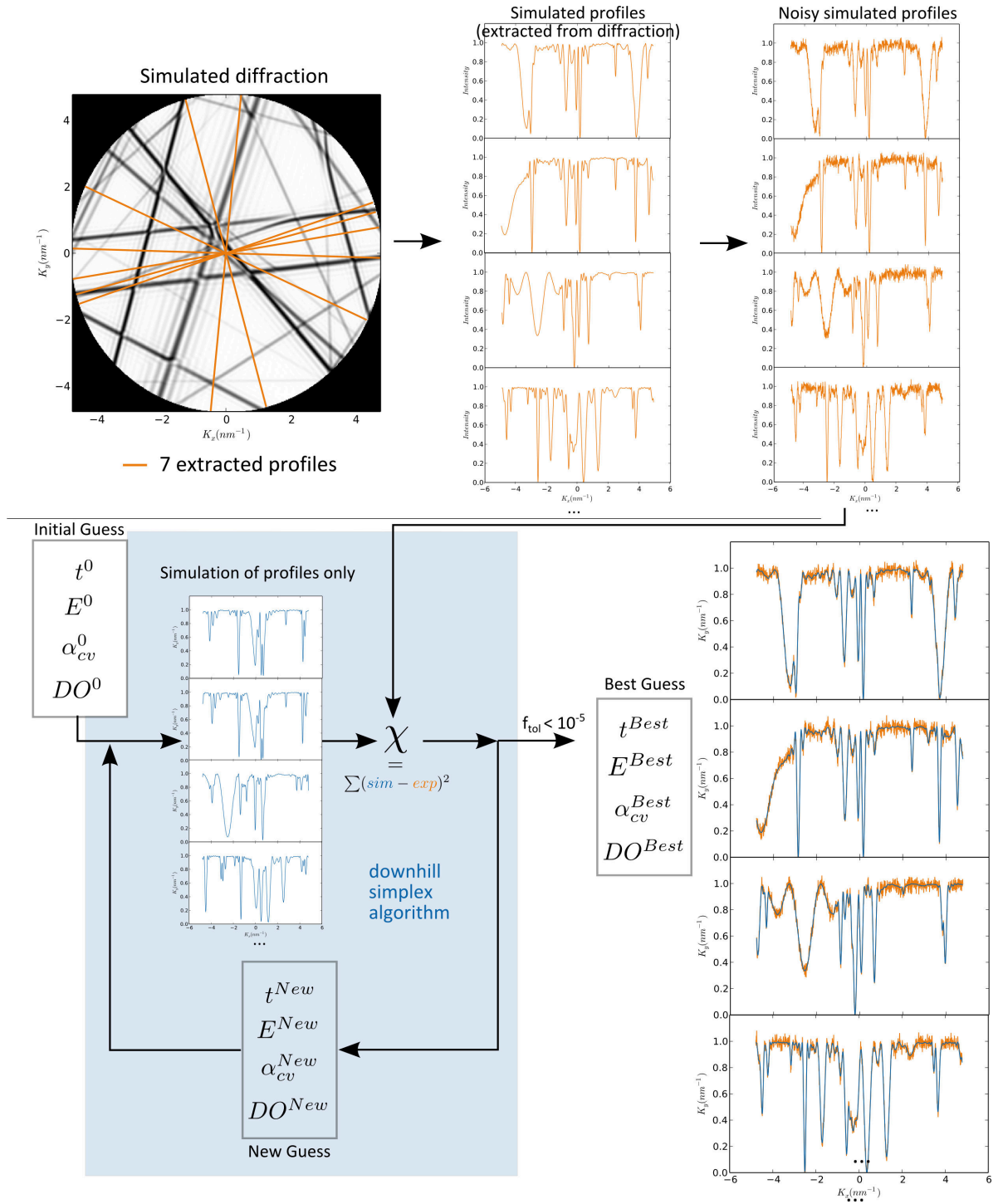


FIGURE B.I.8 – Description of the experimental parameters retrieval algorithm. Here 7 profiles crossing the center of the  $1k \times 1k$  CBED disk have been simulated, and noise has been added to them. The algorithm is a downhill simplex algorithm that minimizes 5 parameters ( $t, \lambda, \alpha_{cv}, u, v$ ) using the minimization function given in B.I.7.

---

pixel that is the diameter of the CBED disk. These profiles go from  $-\alpha_{cv}$  to  $\alpha_{cv}$  and therefore, the camera length ( $CL$ ) in  $mrad/pix$  is the following:

$$CL_{mrad/pix} = \frac{2\alpha_{cv}}{D} \quad (\text{B.I.5})$$

Or equivalently in  $nm^{-1}/pix$  :

$$CL_{nm^{-1}/pix} = \frac{2\alpha_{cv}\lambda}{D} \quad (\text{B.I.6})$$

Where  $\lambda$  is the wavelength.

A rough value of every parameter must be given to the algorithm as starting parameters.  $E^0$  can be the nominal wavelength,  $\alpha_{cv}^0$  the convergence semi-angle given by the microscope interface,  $t^0$  an estimate value (the initial value  $t^0$  is not critical as it changes only the line profile) and  $DO^0$  ( $u^0v^0$ ) must have been approximately determined using for example JEMS software (Stadelmann, 1987).

From these initial values, the algorithm will simulate profiles and compare them to experimental ones. The minimization function  $\chi$  being the squared difference:

$$\chi(t, \lambda, \alpha_{cv}, u, v) = \sum_{profiles=1}^N (simulated(t, \lambda, \alpha_{cv}, u, v) - experimental) \quad (\text{B.I.7})$$

The algorithm stops when the relative error acceptable for convergence ( $f_{tol}$ ) equals to  $10^{-5}$ . The downhill simplex algorithm can be stuck into local minima, but if the initial values are not too far away from the real values, it should converge to the right solution.

## B.I.5 Proof of concept on simulated silicon

A proof of concept of the experimental parameters retrieval has been done using simulations.

A  $1k \times 1k$  diffraction pattern of perfect Silicon at 200kV has been simulated and 7 profiles (see top of figure B.I.8) have been extracted. These profiles have been chosen parallel to some HOLZ lines and crossing the center of the CBED disk for simplification reasons, but it could be virtually any profiles as long as the  $k_x$  and  $k_y$  values of the profiles are known. The simulated parameters were the following:

$$\begin{aligned} t &= 180 \text{ nm} \\ E &= 200 \text{ kV} \\ \alpha_{cv} &= 12 \text{ mrad} \\ [u, v, w] &= [0.56041, 0.82727, 0.03939] \end{aligned}$$

In order to reproduce errors that could be induced by experimental data, random noise has been added to these lines in order to reproduce the CCD noise levels observed in experimental patterns. In addition a random error between  $\pm 0.5^\circ$  in all the profiles direction have been

simulated in order to reproduce the error an user can make while matching the experimental and simulated patterns. Without any noise and random error in orientation of the pattern, the retrieved values are the exact same as the original ones.

20 different retrievals of the extracted profiles (with different random noises and different angles errors in profile) have been made. The initial value for the retrieval has been chosen randomly in the following intervals:

$$\begin{aligned} t^0 &= [150, 210] \text{ nm} \\ E^0 &= [195, 205] \text{ kV} \\ \alpha_{cv}^0 &= [11, 13] \text{ mrad} \\ [u, v, w]^0 &= [0.56041, 0.82727, 0.03939] \pm 2 \text{ mrad} \end{aligned}$$

The mean values and the standard deviations of the 20 retrievals are the following:

$$\begin{aligned} t^{Best} &= 179.94 \pm 0.25 \text{ nm} \\ E^{Best} &= 200.017 \text{ kV} \pm 56 \text{ V} \\ \alpha_{cv}^{Best} &= 12.000382 \pm 3.72 \times 10^{-3} \text{ mrad} \\ [u, v, w]^{Best} &= [0.56041, 0.82727, 0.03939] \pm 2.82 \times 10^{-3} \text{ mrad} \end{aligned}$$

The accuracy on thickness (0.15%) is similar to the one obtained by [Delille et al. \(2000\)](#). The precision on the high tension (56V) is a bit worse than the 20V reported by [Kramer et al. \(2000\)](#). The precision on the convergence angle is very good and the direction of observation is fitted to precision lower than  $3 \times 10^{-3}$  mrad (in this case, this represents a quarter of a pixel).

## B.I.6 Application on experimental pattern

The experimental parameters retrieval algorithm has been applied to an experimental pattern, taken on perfect silicon, at a nominal voltage of 200 kV. The diffraction pattern was filtered using a 15eV slit but it was not cooled down so the dynamic simulations have to take into account the temperature of the sample. This is done by applying a Debye Waller correction in the Silicon structure factor ([Gao and Peng, 1999](#)).

The rough direction of observation has been retrieved using JEMS software and is [441,651,31]. The following initial parameters have been taken:

$$\begin{aligned} t^0 &= 150 \text{ nm} \\ E^0 &= 200 \text{ kV} \\ \alpha_{cv}^0 &= 10 \text{ mrad} \\ [u, v, w]^0 &= [0.56041, 0.82727, 0.03939] \end{aligned}$$

Figure [B.I.9](#) gives the result of the fitting. The position and profiles of the HOLZ lines are well retrieved by the algorithm. The retrieved values are :

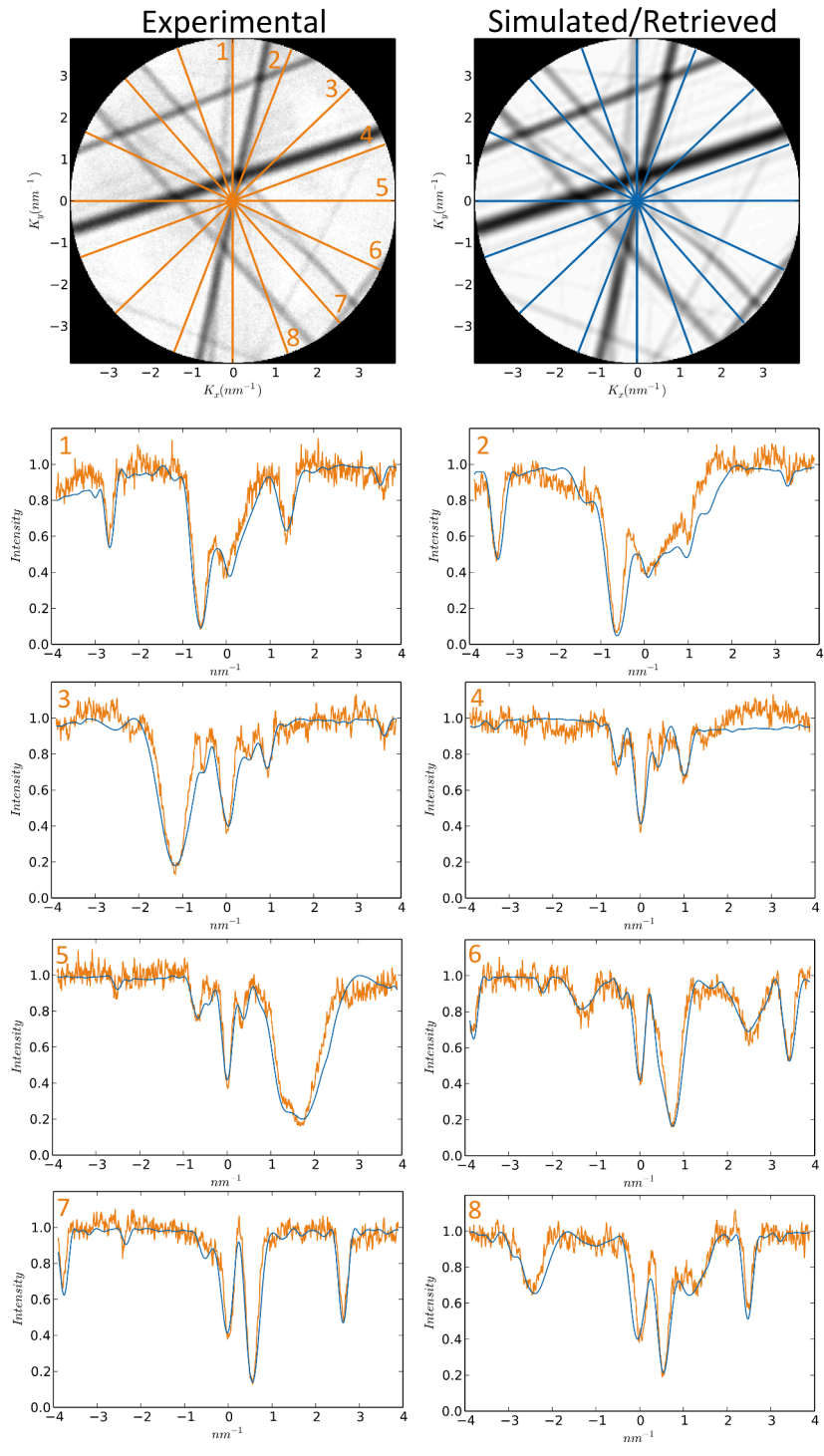


FIGURE B.I.9 – Fit of the experimental parameters on a 200kV CBED pattern of Silicon (taken with a FEI Titan 80-300). On top is the experimental and the retrieved simulated pattern, the lines represents the selected profiles that are used for the fit. Below, experimental and retrieved simulated profiles are given.

$$\begin{aligned}
 t^{Best} &= 93.74 \text{ nm} \pm 0.2\% \\
 E^{Best} &= 202.406 \text{ kV} \pm 60V \\
 \alpha_{cv}^{Best} &= 9.6883 \pm 4 \times 10^{-3} \text{ mrad} \\
 [u, v, w]^{Best} &= [0.559845, 0.827639, 0.03982] \pm 4 \times 10^{-3} \text{ mrad}
 \end{aligned}$$

## B.I.7 Discussion and further consideration

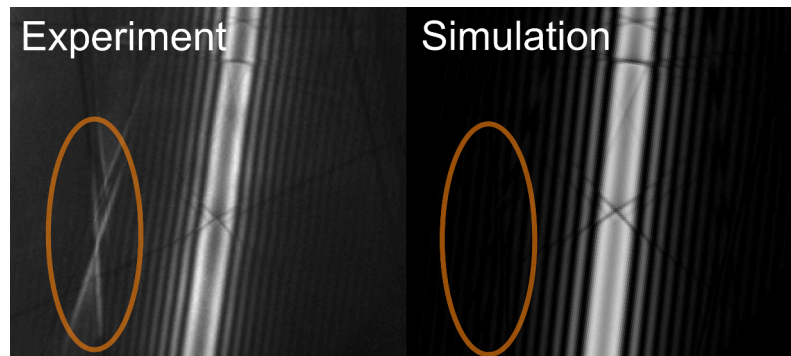


FIGURE B.I.10 – Example of interactions between excess lines that are not visible in the simulation. The simulation has been done in the same zone axis, with an acceleration voltage of 200kV on silicon. The coherent CBED approach has been used in order to add the phases (and not the intensities) when two excess disks are overlapping.

The proof of concept and the application of the method on silicon showed the great possibility of this technique. One main advantage of this algorithm is that it uses dynamical equations to fit the parameters allowing to fit the direction of observation without using a corrected voltage as proposed by [Lin et al. \(1989\)](#). Some points need nevertheless to be developed. For example, here the rotation of the experimental pattern in the CCD plane has been fitted manually. This rotation could easily be added as a parameter to be fitted by the algorithm. This algorithm could also be extended to the measure of structure factors and could also use the information carried by excess HOLZ lines.

HOLZ lines contain all the necessary information to determine the structure factor. [Delille et al. \(2000\)](#) described a way to measure the structure factor of one unique line (004 in silicon), [Zuo and Spence \(1991\)](#) measured the structure factor of two lines (002 and 004 in MgO). Here as we take the whole pattern profile, and we are not in two beam conditions, the structure factor of several lines should be taken in account. In addition Zuo and Delille used excess lines to measure the structure factor, and preliminary tries showed that the noise in the transmitted pattern will make difficult the measurement of the structure factor in our case. Including excess HOLZ lines could then be a solution allowing to measure the structure factor.

Applying this algorithm to excess line would allow an even more precise retrieval as excess HOLZ lines are less noisy than deficient ones. But there are some difficulties that have to be taken

---

into account: the first difficulty is that some of the interactions appearing in the experimental pattern are not present in the simulation. Figure B.I.10 shows an example of interaction between two HOLZ lines that are not directly excited by the transmitted beam but that appears on the experimental pattern, maybe due to a three beam interaction with the 004 line. The second difficulty is that the camera length should be big enough in order to minimize the CCD transfer function. To see the diffracted beams, there are then two solutions, keep the same camera length and take several diffraction shifted patterns, or lower the camera length and include the CCD MTF. In the last case, the precision of the measure may be reduced.

## B.I.8 Conclusion

In conclusion, the presented method is an easy way to retrieve 4 experimental parameters in a CBED pattern in one common fit: acceleration voltage, convergence angle, sample thickness, and sample direction of observation. The precision of the measure is good compared to other CBED techniques. The precision is 0.2% on thickness, 60V on acceleration voltage, and  $4 \times 10^{-3}$  mrad on convergence angle and direction of observation. This method supposes a known structure factor. It would be possible to measure the structure factor by including excess HOLZ lines, but it will need some efforts to get around the difficulties given in the previous section.

Of course this method is limited by the CBED principle itself. The measurements have to be carried out on a crystal (the measured thickness will be the crystalline thickness, and will ignore amorphous layers) and will not be possible on very thin samples (below 50nm). See Chapter C.II for thickness measurement techniques of thinner materials.

---

**Three dimensional strain and rotation retrieval in an  
homogeneously deformed crystal**

---

Most of the electron microscopy methods analyze the strain in the plane perpendicular to the electron beam, and can thus retrieve at best 4 parameters of the deformation gradient tensor. CBED is one of the few TEM techniques that can provide three-dimensional information thanks to the presence of HOLZ lines that are associated to inclined planes. Nevertheless, it is important to notice that the strain determination from CBED pattern can be ambiguous ([Morawiec, 2005](#)), because it is a two-dimensional pattern carrying three-dimensional information.

In this chapter, a strain and rotation measurement method has been developed in order to remove the diagonal terms ambiguity. This method has been validated on Bloch waves dynamic simulations, from one and two different directions of observation.

## B.II.1 The CBED strain measurement ambiguity

CBED patterns must be analyzed cautiously because ambiguities can arise and not all the 9 components of the deformation gradient tensor can be retrieved. [Morawiec \(2005\)](#) gave a detailed description of these ambiguities. He concluded that it is not possible to get reliable information on the  $xz$  and  $yz$  shear strains ( $z$  being the beam axis). Moreover, there is an ambiguity on a linear combination of the diagonal components of the strain tensor. It means that only 6 independent parameters of the deformation gradient tensor can be determined.

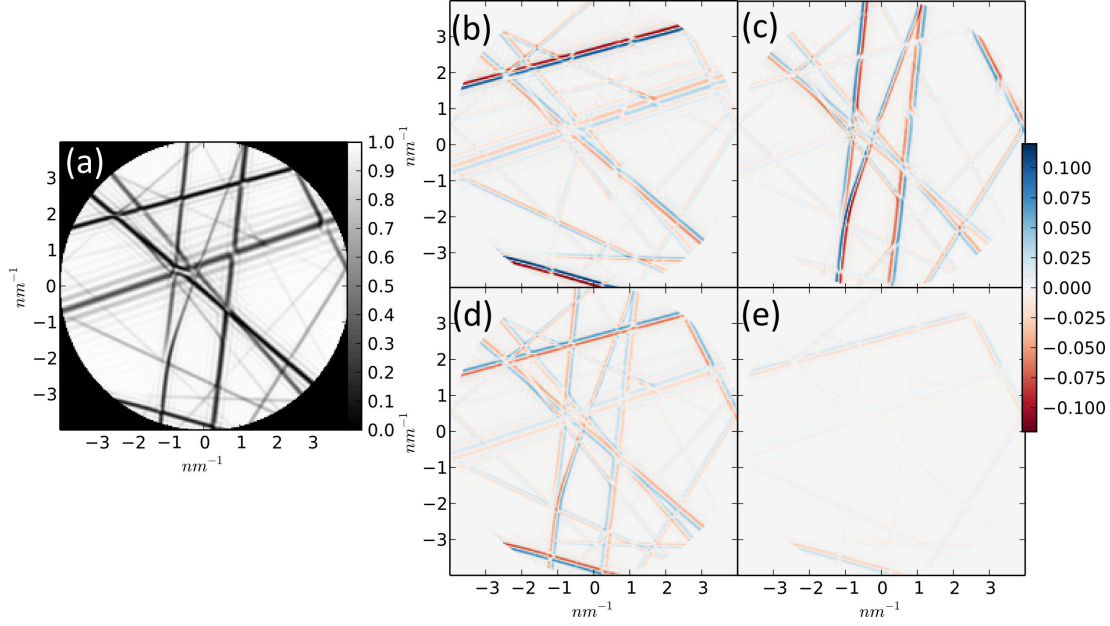


FIGURE B.II.1 – (a) Reference CBED dynamically simulated pattern of perfect silicon. (b)(c)(d)(e) Difference between the reference CBED pattern and a deformed silicon pattern. The deformation given in the microscope CCD basis ( $XYZ$ ,  $Z$  being the beam axis) is (b)  $\varepsilon_{XX} = 5 \times 10^{-4}$ , (c)  $\varepsilon_{YY} = 5 \times 10^{-4}$ , (d)  $\varepsilon_{ZZ} = 5 \times 10^{-4}$ , (e)  $\varepsilon_{XX} = 5 \times 10^{-4}$ ,  $\varepsilon_{YY} = 5 \times 10^{-4}$  and  $\varepsilon_{ZZ} = 8.7 \times 10^{-4}$ . In (b)(c)(d), the small strain clearly displaces the HOLZ lines, but in (e) the linear combination (1,1,1.74) of the normal strain components gives a nearly similar pattern as the undeformed case.

The diagonal terms ambiguity is illustrated in figure B.II.1. The linear combination of  $\varepsilon_{XX}, \varepsilon_{YY}, \varepsilon_{ZZ}$  in the ratio (1,1,1.74) gives CBED patterns very similar to the unstrained ones. This ratio depends on magnitudes of reciprocal lattice vectors and on the magnitude of the wave vector. [Morawiec \(2005\)](#) found a ratio of (1,1,2.014) for a 120kV silicon pattern and predicted a decreases of 0.004 per 1kV. This is coherent with the 1.74 value found here. In Electron BackScatter Diffraction (EBSD), the ambiguity on the diagonal component is also present, and the full strain tensor is recovered by applying a traction free condition on the surface of the sample ([Maurice et al., 2012](#)).

In the following, a strain and rotation measurement method which removes the diagonal terms ambiguity is presented. It does not make any assumption on the lattice or strain state ([Toda et al., 2000](#); [Wittmann et al., 1998](#)). This is made possible by the use of both deficient and

excess HOLZ lines. 7 of the 9 parameters of the deformation gradient tensor  $\mathbf{F}$  can be fitted from a single zone axis, this allows to retrieve also the volume of the lattice with only one zone axis. The retrieval algorithm uses template matching for line measurement and a reference diffraction pattern from which HOLZ lines displacement are determined. Here, only sharp HOLZ lines are considered, that is to say a uniform strain along the beam direction is assumed.

## B.II.2 Overview of the method

The method presented in this chapter analyzes off-axis CBED pattern similar to the one presented figure A.I.3 (b). Such patterns are obtained in high voltage TEMs by observing rather thick crystals. Acceleration voltages are between 80kV and 400kV and crystal must have a thickness in between 100 to 400nm. The convergence of the beam, 12 mrad, is chosen such that the transmitted spot is a large disk but with no overlap of the diffracted disks. The crystal is oriented along a high index direction in order to reduce the dynamical contrasts.

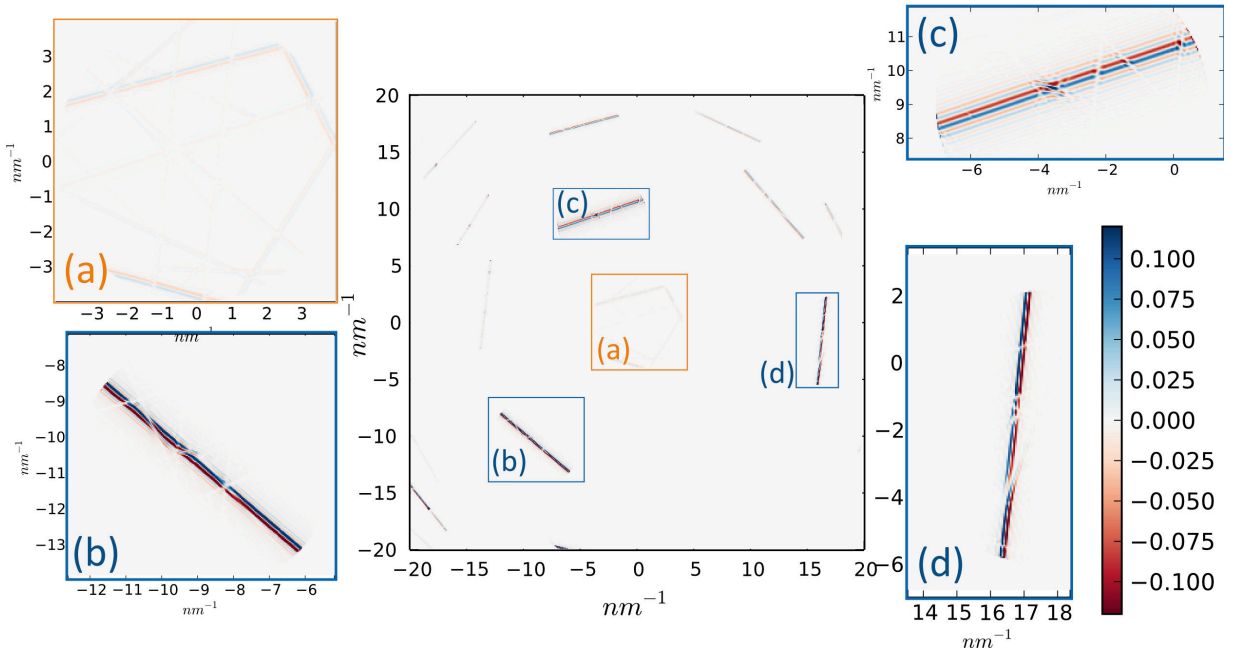


FIGURE B.II.2 – Difference between a reference dynamically simulated CBED pattern and a deformed one. Deformation is set as for figure B.II.1 (e) :  $\varepsilon_{XX} = 5 \times 10^{-4}$ ,  $\varepsilon_{YY} = 5 \times 10^{-4}$  and  $\varepsilon_{ZZ} = 8.7 \times 10^{-4}$ . In the transmitted beam, the deformation is nearly not visible, whereas in the diffracted beams, the displacement of excess line is clearly present and measurable. This is an illustration of the additional information carried by the excess HOLZ lines.

The analyzed CBED patterns are composed of a transmitted disk containing sharp dark HOLZ lines and the associated excess, i.e. bright, HOLZ lines. The dark or deficient HOLZ lines of the transmitted beam correspond to directions of the incident beam that are in Bragg angle condition for a family of crystallographic planes characterized by the vector  $\mathbf{g}$ . The excess

---

HOLZ lines correspond to the electrons diffracted in Bragg angle condition i.e. diffracted in the direction  $\mathbf{k} + \mathbf{g}$ ,  $\mathbf{k}$  being the incident beam direction of the convergent beam that is in Bragg condition. So each deficient HOLZ line of the transmitted beam has an associated excess HOLZ line, parallel, of the same length and separated by the distance  $|\mathbf{g}|$ . In angle, the HOLZ lines are separated by twice the Bragg angle, i.e.  $2\theta_B$ . (see figure A.III.1)

Small changes in the lattice parameters of the initial crystal will produce translations and/or rotations of the HOLZ lines and variation of the distance between HOLZ lines pair, this is why positioning accurately the HOLZ lines gives a precise measure of the lattice parameters. For practical reasons, mainly the limited size of the CCD cameras, generally only the deficient HOLZ lines are analyzed. In the presented method, on the contrary, both the deficient and excess HOLZ lines are analyzed to determine the lattice parameters or equivalently the deformations, or the rotations and the strains.

Here the deformation is written using the deformation gradient tensor  $\mathbf{F}$  convention, this convention is described in Appendix A. This tensor is expressed by reference to an undistorted crystal. The method itself, involves several steps: (1) the acquisition of a series of local off-axis CBED pattern acquired in a crystalline material that is supposed to be deformed (2) the acquisition of a reference CBED pattern obtained in the same condition but in a region with no deformation, this reference pattern can belong to the previous series or can be acquired independently, (3) the determination of the main experimental and numerical parameters by comparing the reference CBED pattern to dynamical simulations as presented in the previous chapter (4) the retrieval of the deformations in each local CBED patterns.

The method has been tested on a series of simulated CBED patterns and a reference experimental CBED pattern has been acquired to verify the possibility of having adapted experimental data.

### B.II.3 Choosing the zone axis

Choosing wisely the zone axis of the CBED pattern is very important for applying successfully the excess line method. Figure B.II.3 gives the representation of the inner and outer limits of Ewald spheres for two zone axes  $[1,1,0]$  and  $[651,441,31]$  of perfect silicon.

#### Low index zone axes

The zone axis  $[1,1,0]$  is an example of low index zone axis. It is an axis from where the crystal presents symmetries. These symmetries will lead to symmetries in the diffraction pattern and to the presence of dense atomic planes. These dense atomic planes are strong scatterers and therefore, they have strong dynamic interaction with each others. The excess line method being based on kinematic simulation, we want to avoid a strong dynamic scattering.

These planes are classified by Laue Zone, defined by the dot product of the zone axis and the diffracting plane. A HOLZ layer  $n$ , is defined by the equation:

$$n = [h, k, l] \cdot [u, v, w]$$

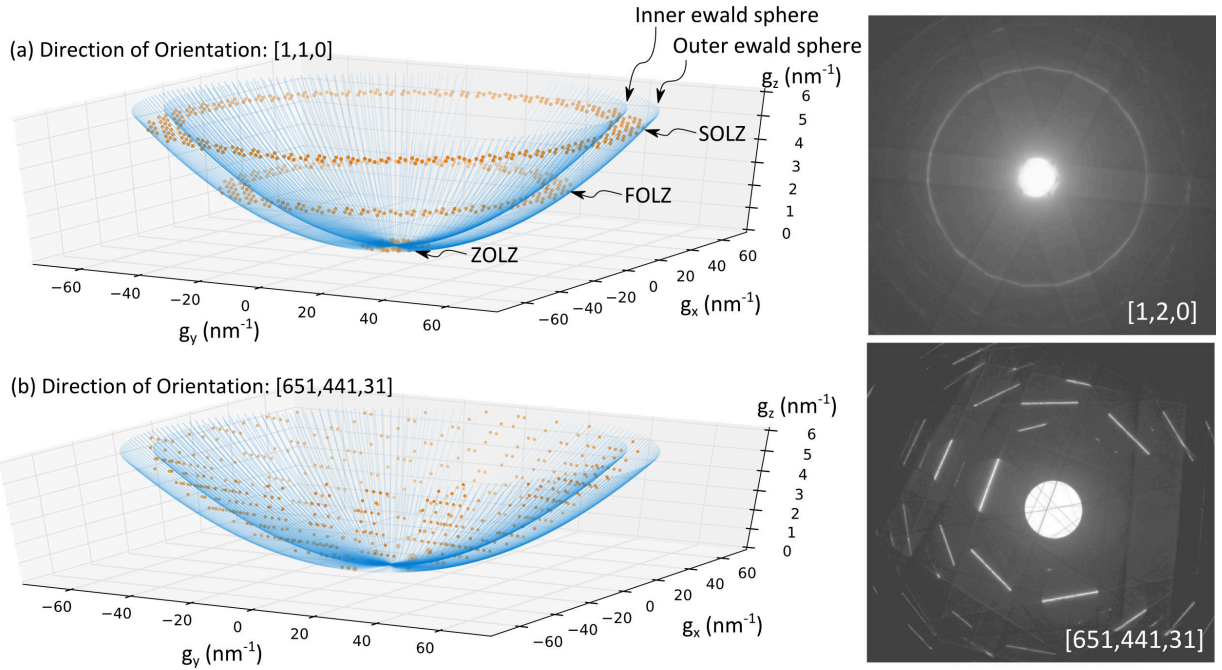


FIGURE B.II.3 – (a) on-axis  $[1,1,0]$  or (b) off-axis  $[651,441,31]$  reciprocal space of Silicon, showing the diffracting planes in CBED condition (inner and outer Ewald spheres limits are plotted here). On the right, two experimental Silicon patterns from a low and high index zone axis.

where  $[u, v, w]$  is the zone axis and  $[h, k, l]$  the plane index. Diffracting  $hkl$  planes that are in the ZOLZ are parallel to the beam ( $[h, k, l] \cdot [u, v, w] = 0$ ).

The diffraction spots are therefore grouped by Laue Zones, forming circles around the transmitted disk. Such low index axes are very useful for determining the crystal symmetry (Morniroli et al., 2012).

### High index zone axes

The zone axis  $[651,441,31]$  is an example of high index zone axis. In high index zone axes, the crystal presents less symmetry. The diffracting spots are much more separated on the diffraction pattern than for the low index zone axis case. The HOLZ lines positions are therefore easier to fit. The classical definition of the Laue Zone is less relevant in this type of zone axes. We prefer using the normalized dot product to represent the z component of the diffraction vector:

$$\arcsin\left(\frac{g_z}{g}\right) = \frac{[h, k, l] \cdot [u, v, w]}{|[h, k, l]| |[u, v, w]|}$$

The excess line method requires high index zone axes, because of the spacing of HOLZ lines on the diffraction pattern and because the dynamic effects are reduced.

## B.II.4 Simulation details

In order to develop, test and validate the proposed method, dynamical simulations of a 180nm thick silicon at 200kV observed along a  $[651, 441, 31]$  direction and presenting different states of uniform deformations have been done. A high index zone axis  $10^\circ$  away from the  $[110]$  zone axis was taken in order to reduce dynamical effects and to have well separated HOLZ lines in the transmitted beam. It was chosen in order to reproduce the experimental CBED reference pattern. Dynamical simulations are also used in the accurate fitting of the acceleration voltage and sample thickness. Kinematic simulations are used in the fitting of the  $\mathbf{F}$  tensor.

### B.II.4.1 Dynamic simulations

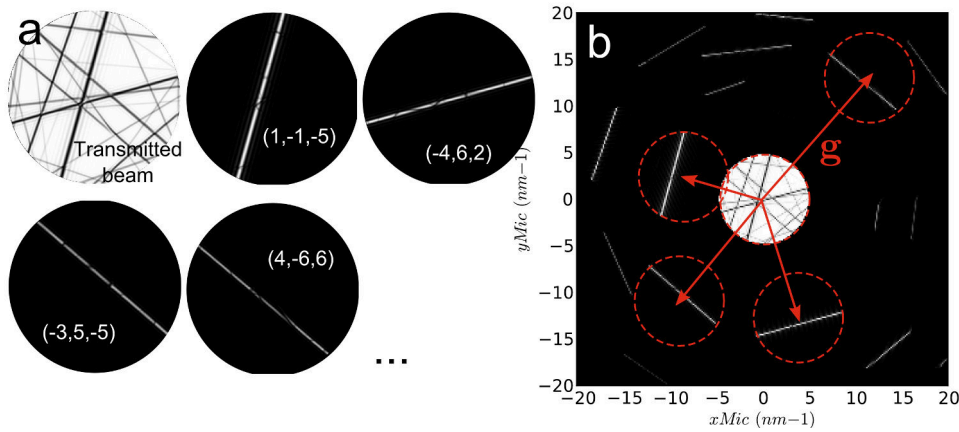


FIGURE B.II.4 – (a) Dynamically simulated CBED disks using the Bloch Waves method. The top left disk is the transmitted disk, the others represent different diffracted disks whose diffraction vector is given in parentheses. Each disk is stored in a  $1k \times 1k$  image. (b) Reconstruction of the whole dynamic CBED pattern by shifting each beam by  $\mathbf{g}$ .

Dynamical CBED patterns have been simulated with an home made python software using the Bloch Waves method presented in Chapter A.III. For each pixel in the transmitted beam, the software resolve a  $N \times N$  matrix,  $N$  being the number of diffraction planes. In order to select the diffracting crystal planes to be included in the simulation, all the planes that are inside the Laue circles defined by 1.3 times the convergence angle are taken. The value 1.3 helps to take into account possible strong reflections that are near the Bragg condition. Usually around 15 to 20 diffracted beams are visible on experimental patterns. To be sure to include them in the simulations and in order to limit the computing time, the planes are classified considering their interaction strength (i.e. their structure factor) and the 30 planes having the highest interaction strength are considered in the simulations.

This method gives a set of images, the first corresponding to the transmitted beam, and the others corresponding to the diffracted beams (see figure B.II.4). In order to obtain the whole diffraction pattern, each diffracted beam  $\mathbf{g}$  is shifted by  $2\theta_B^g$  or  $\mathbf{g}$  where  $\theta_B^g$  is the Bragg angle

of the diffracted beam  $g$ . To be sure of the accuracy of our software, these dynamical CBED patterns were compared to the ones calculated by the JEMS software (Stadelmann, 1987).

### B.II.4.2 Kinematic simulations

In the fitting subroutine in order to retrieve the local strain and rotation of the sample in a reasonable amount of time, kinematic simulations are used. For a comparison, a  $1k \times 1k$  simulation takes about 15 minutes for dynamic simulations, while the kinematic simulation only takes a few seconds.

Each point of the central CBED disk corresponds to a different incident beam direction  $(k_x, k_y, k_z)$  which has a constant energy i.e. constant wavelength  $\lambda$ :  $k = \sqrt{k_x^2 + k_y^2 + k_z^2} = 1/\lambda$ . It is thus natural to calibrate the CBED pattern in  $nm^{-1}$  and use the tangential components  $(k_x, k_y)$  as the local variables of the CBED pattern. The pixel size in  $nm^{-1}$  defined a scale (in  $nm^{-1}/pixel$ ) of the CBED image which is linked to the camera length (CL) of the microscope. HOLZ lines are associated by pairs: one deficient line in the central disk and one excess line in the diffracted beam that are separated by the distance  $\mathbf{g}$  (Bragg law). The equation of a given  $\mathbf{g}=(g_x, g_y, g_z)$  HOLZ 'line' is obtained by putting the excitation error  $S_g$  equals to zero, which leads to:

$$\mathbf{k} \cdot \mathbf{g} = -\frac{g^2}{2} = k_x g_x + k_y g_y + \sqrt{k^2 - k_x^2 - k_y^2} g_z \quad (\text{B.II.1})$$

In CBED, as the tangential components are small compared to  $k$ , this equation represents in good approximation a straight line whose normal is given by  $\mathbf{g}_t = (g_x, g_y)$  and whose distance  $l_{Kin}^g$  along  $\mathbf{g}_t$  to the origin is given by:

$$l_{Kin}^g = \frac{\sqrt{g_x^2 + g_y^2}}{2} - \frac{g_z}{g} \sqrt{k^2 - \frac{g^2}{4}} \quad (\text{B.II.2})$$

So a given HOLZ line position is characterized by its distance  $l_{Kin}^g$  to the origin and the angle  $\varphi_g$  (see figure B.II.5) defined by:

$$\varphi_{Kin}^g = \text{atan2}(g_y, g_x) \quad (\text{B.II.3})$$

Here  $\text{atan2}$  is the arc-tangent function with two arguments in order to return the appropriate quadrant of the angle.

The kinematic simulations are made in three steps: (i) determination of excess HOLZ lines intensity profiles, (ii) transmitted beam reconstruction and (iii) excess HOLZ lines reconstruction.

#### (i) Determination of excess HOLZ lines intensity profiles

The kinematic intensity profile, also known as rocking curve, of a sharp excess HOLZ line (uniform strain along the beam), is given by:

$$I_g(s_g) = \left(\frac{\pi}{\xi_g}\right)^2 \frac{\sin^2(\pi t s_g)}{(\pi s_g)^2} \quad (\text{B.II.4})$$

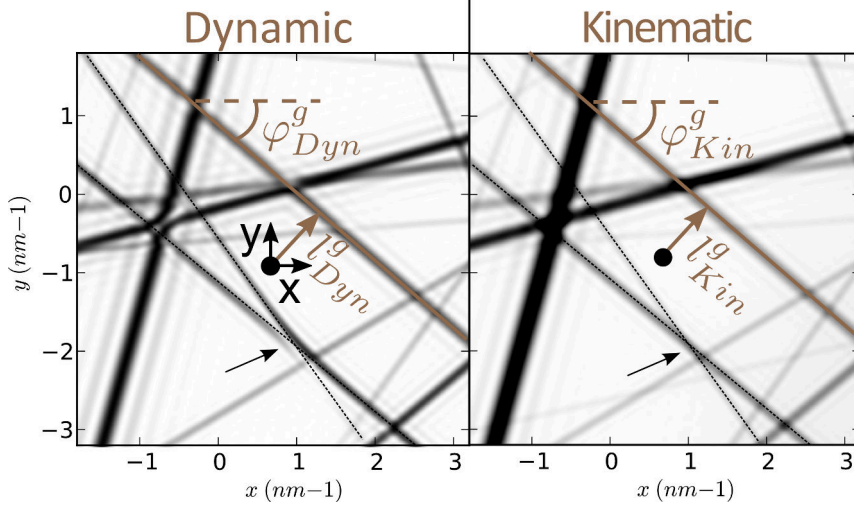


FIGURE B.II.5 – Comparison between Kinematic and Dynamic simulation. The dispersion surface and changes of intensity between lines (black arrow) are only visible in dynamically simulated pattern. Perfect silicon, high voltage 200kV, zone axis [651,441,31], thickness 180nm. Kinematic simulation is a very good approximation in high index zone axes.

where  $t$  is the sample thickness,  $s_g$  is the deviation parameter given by equation A.III.2 and  $\xi_g$  is the extinction length of the diffracted beam  $g$ .

### (ii) Transmitted beam reconstruction

Each HOLZ line is placed in the CBED disk according to its distance  $l_{Kin}^g$  to the center of the disk (equation B.I.3) and its orientation (eq. B.II.3) and subtracted from the transmitted beam:

$$I_{transmitted} = I_0 - \sum_{g=1}^N I_g \quad (\text{B.II.5})$$

It is well known that due to dynamical interactions these kinematic equations do not give the exact locations of HOLZ lines and that dynamical HOLZ line shifts (DS) have to be introduced in the kinematic simulations:

$$l_{Dyn}^g = l_{Kin}^g + DS^g \quad (\text{B.II.6})$$

where  $DS^g$  is the dynamical shift of the  $\mathbf{g}$  HOLZ line and  $l_{Dyn}^g$  its dynamically corrected distance to the center.

As explained in the next section, the dynamic HOLZ line shifts will be introduced by fitting HOLZ lines in the reference pattern. We checked that for small deformations, these  $DS^g$  do not change when small deformations are introduced.

### (iii) Excess HOLZ lines reconstruction

The excess HOLZ lines are placed on the diffraction pattern shifted by  $\mathbf{g}$  with respect to the transmitted beam.

An example of simulated patterns is shown in figure B.II.5. Taking into account the dynamical HOLZ shift correction the kinematic simulation reproduces very well the dynamical simulation. Mainly, only the interactions between two or several HOLZ lines, which give rise to the dispersion surface effect (Spence and Zuo, 1992), are not included in the kinematically simulated pattern. However this will have few effects on the results, as described below.

## B.II.5 The reference pattern

### B.II.5.1 Calibrating the reference pattern

The reference pattern is at the heart of the experimental parameters calibration. It allows to get the values of the camera length (CL), direction of observation (DO), rotation of the pattern around DO, indexation of the HOLZ lines, sample thickness ( $t$ ), acceleration voltage ( $V$ ).

The first step is to determine approximately the experimental parameters. The acceleration voltage is firstly simply read from the microscope interface. Then by comparing the reference pattern to kinematic or dynamical simulations, the direction of observation, the HOLZ line indexes and an estimation of the sample thickness can be determined. Here, the JEMS software was used to determine the direction of observation. The direction of observation is defined as the beam direction at the center of the transmitted disk, this beam direction being expressed in the crystallographic basis.

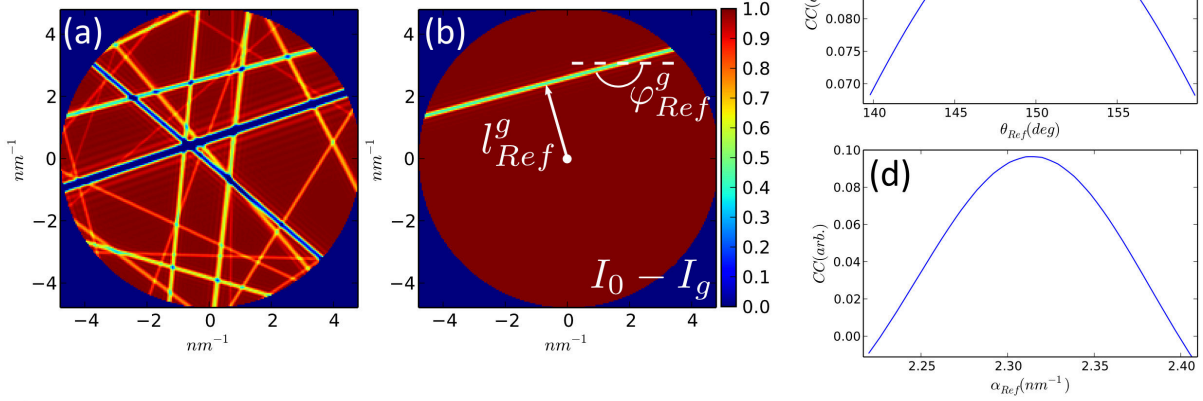
Once the initial experimental parameters have been determined, it is possible to retrieve more accurate values using the method given in Chapter B.I. Previous publications showed that the accurate determinations of  $t$  (Zuo and Spence, 1991; Delille et al., 2000) and  $V$  (Kramer et al., 2000) are critical and detailed how to measure them accurately.

### B.II.5.2 Detecting lines positions and angles

As introduced before, each HOLZ line pair is characterized by 3 parameters:  $l^g$ ,  $\varphi^g$  and  $g$  (figure B.II.6) and by its profile. The retrieval of the 3 parameters characterizing each HOLZ line pair is obtained by using the method of template matching described in figure B.II.6, instead of using the now more traditional Hough transform method (Kramer and Mayer, 1999).

For a given CBED pattern, the positions of HOLZ lines (either excess or deficient) are determined by maximizing the cross-correlation coefficients between the analyzed CBED pattern and a series of simulated templates. For a given HOLZ line, the templates have the same profile as given by equation B.I.4. They differ by the distance to the origin ( $l^g$ ) and by their orientation ( $\varphi^g$ ) for the deficient template, and by the distance to the deficient line ( $\mathbf{g}$ ) for the excess template. B.II.6 gives for instance one template for a transmitted line, given by  $I_0 - I_g$ , and one template for the corresponding diffracted line given by  $I_g$ .

### Deficient HOLZ line position fit



### Exces HOLZ line position fit

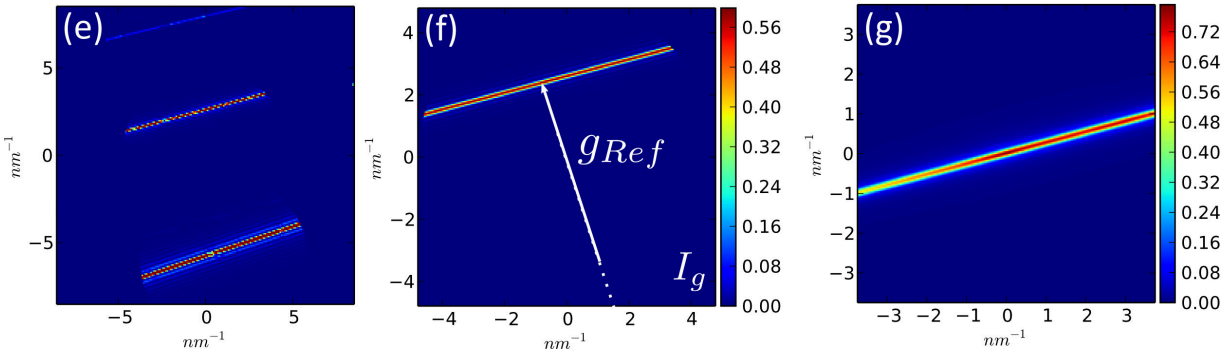


FIGURE B.II.6 – (a)(e) Experimental (a) transmitted and (e) diffracted beams. Templates used for fitting (b) transmitted [2,-2,-8] HOLZ line and (f) excess [2,-2,-8] HOLZ line. For each  $\mathbf{g}$  reflection, For a given HOLZ line, the templates have the same profile as given by equation B.I.3. It varies with the distance to the origin ( $l^g$ ) and the orientation ( $\varphi^g$ ) for the transmitted template, and with the distance to the deficient line ( $\mathbf{g}$ ) for the excess template. (c)(d) Correlation Coefficients as a function of the deficient line parameters. (g) Correlation Coefficient as a function of the line displacement.

For These figures shows the reflection [2,-2,-8], but other reflections gives similar results.

It is important to note that the length of the HOLZ line changes with the position of the HOLZ line within the disk, i.e. the template method includes the length of the HOLZ line in its fitting, which is not the case when the Hough transform is used. Using the template matching algorithm of OpenCV library (Bradski, 2000) and the L-BFGS-B minimization algorithm (Byrd et al., 1995), the combination of  $l^g$  and  $\varphi^g$  that gives the best match is retrieved. Once the excess and deficient lines have been accurately positioned, the norm of the diffraction vector  $\mathbf{g}$  is simply calculated.

A precision of 0.2 degree on HOLZ line orientation ( $\varphi^g$ ) have been reached. The precision on HOLZ line position ( $l^g$ ) is about  $2 \times 10^{-3} \text{ nm}^{-1}$  (meaning in angle about  $3 \times 10^{-4}$  degree).

The advantage of this fitting algorithm is that it takes into account not only the positions of the lines within the disk but also their profiles and length within the transmitted or diffracted disks. In addition, this fitting method can be applied not only to sharp HOLZ lines but also to HOLZ lines that have been broadened by a non uniform strain distribution along the beam direction (Clement et al., 2004). The direct application of this method on broad HOLZ lines has not been done in the scope of this thesis, but Chapter 3 discusses this splitting of HOLZ lines.

### B.II.5.3 Weighting lines

For each  $\mathbf{g}$  HOLZ line, a weight  $w^g$  is calculated in the transmitted beam in order to give more or less power to the HOLZ lines:

$$w^g = C_{wo}^g - C_{all} \quad (\text{B.II.7})$$

where  $C_{all}$  is the correlation coefficient between the reference pattern and the simulated pattern containing all HOLZ lines, and  $C_{wo}^g$  the correlation coefficient between the reference pattern and the simulated pattern without the given line.

This weight is very useful, as it will give far less importance to a weak line or to a line that is near the edge of the disk and consequently has a shorter length. It will be applied to all further calculation, when there is a need to compare experimental and simulated patterns. Table B.II.1 gives the weights obtained for the [651,441,31] direction.

### B.II.5.4 Finding the Dynamical shift

The kinematic simulation can take into account the dynamical shift for each HOLZ line. The kinematically calculated positions  $l_{Kin}^g$  given by B.I.3 can be dynamically corrected by adding a correction term  $DS^g$ . This approach is similar to the one implemented by Kramer et al. (2000), i.e. each  $\mathbf{g}$  HOLZ lines will have its own dynamical shift (DSg) that is determined on the reference pattern :

$$l_{Dyn}^g = l_{Kin}^g + DS^g \quad (\text{B.II.8})$$

For each line,  $DS^g$  is given to be the difference between  $l_{Ref}^g$ , the fitted line positions in the reference pattern and  $l_{Kin}^g$ , the kinematically calculated line position:

$$DS^g = l_{Ref}^g - l_{Kin}^g \quad (\text{B.II.9})$$

$g$ ( $hkl$ )	$w^g$ (arb.unit)	$DS^g$ ( $\text{nm}^{-1}$ )	$g$ ( $hkl$ )	$w^g$ (arb.unit)	$DS^g$ ( $\text{m}^{-1}$ )
(-4 6 2)	1.00	0.27	( 6 -8 -6)	0,05	-0.5
( 1 -1 -5)	0.85	0.43	( 4 -6 10)	0,05	-2.45
( 2 -2 -8)	0.77	-0.87	(-1 1 9)	0,04	-0.07
(-3 5 -5)	0.47	0.39	(-4 6 10)	0,03	-1.35
( 4 -6 6)	0.34	-1.29	(-6 10 -4)	0,02	0.17
(-4 6 6)	0.29	-1.40	(-1 1 11)	0,02	-0.33
( 5 -7 -1)	0.17	-1.05	( 0 0 12)	0,02	-0.41
( 5 -7 1)	0.15	-1.31	( -1 3 -11)	0,02	-0.38
( 5 -7 -3)	0.08	-0.2	( 3 -3 -11)	0,01	1
( -2 4 -10)	0.08	0.7	( 0 2 -14)	0,01	0.19

TABLE B.II.1 – HOLZ line weight ( $w^g$ ) and dynamic shifts ( $DS^g$ ) fitted on a reference dynamic simulation pattern. Perfect 180nm thick silicon in [651,441,31] zone axis at 200kV. For each line, the normalized correlation weight is given. Zero weight lines have been removed from the table. Negative sign in the shift is a movement toward the center of the CBED disk.

The Table B.II.1 gives dynamic shifts of some HOLZ lines of the dynamically simulated reference pattern. We check on the simulations that these DS do not change when a small deformation is introduced. As this method works by reference and measures the variations of HOLZ line positions with deformation, these DSs will disappear when using relative HOLZ line positions and they are therefore not necessary in the retrieval of the  $\mathbf{F}$  tensor.

The positioning in the reference pattern is used to determine the dynamical HOLZ shifts (DS) as explained below. The positions in the other CBED of the series are used in the  $\mathbf{F}$  tensor retrieval as explain in the next section.

## B.II.6 F tensor retrieval

The values of the  $\mathbf{F}$ -tensor will be determined from the variations of the HOLZ lines positions and new variables relative to the reference pattern are introduced:

- The position shift ( $\Delta l^g$ ) of transmitted HOLZ line :  $\Delta l^g = l^g - l_{ref}^g$
- The angle variation ( $\Delta \varphi^g$ ) of transmitted HOLZ lines, which has to take care of discontinuities of  $\varphi^g$  around 0 and  $2\pi$  :

$$\begin{aligned} \Delta \varphi^g &= \varphi^g \% 2\pi - \varphi_{ref}^g \% 2\pi && \text{if } \varphi_{ref}^g \% 2\pi \text{ is in } \left[ \frac{\pi}{2}; \frac{3\pi}{2} \right] \\ \Delta \varphi^g &= (\varphi^g + \pi) \% 2\pi - (\varphi_{ref}^g + \pi) \% 2\pi && \text{otherwise} \end{aligned} \quad (\text{B.II.10})$$

- The variation of distance between the HOLZ line pair gives directly the variation of  $g$  :  $\Delta g = g - g_{ref}$

The  $\Delta g$  parameter is the essential parameter in this method, because it can only be obtained by looking at the excess HOLZ lines. It is therefore the independent parameter that adds the necessary information to the proposed method.

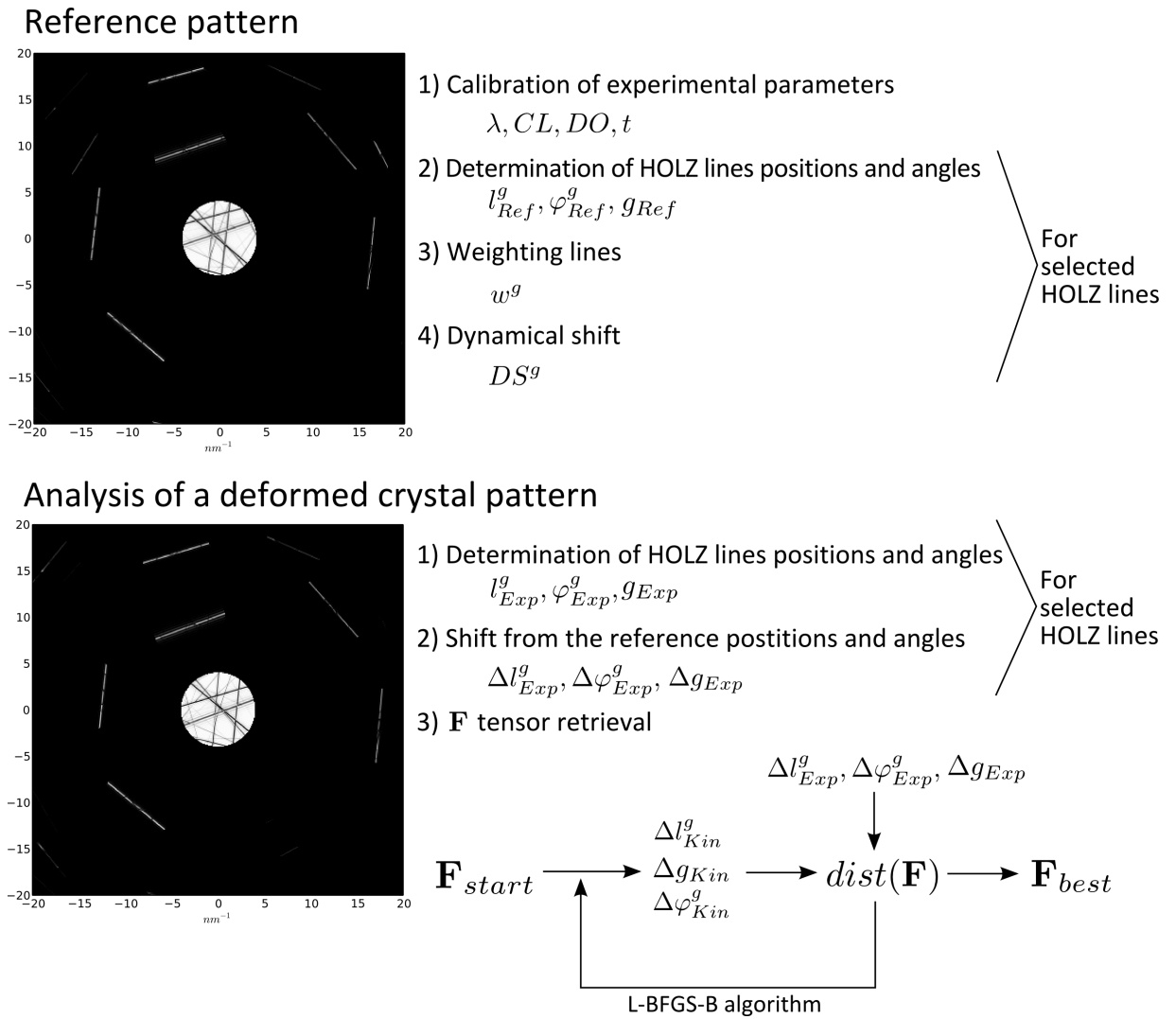


FIGURE B.II.7 – Schematic view of the **F**-tensor retrieval. The calibration of the reference pattern is detailed in section B.II.5, the F-tensor retrieval in section B.II.6.

---

In the previous experimental positioning of HOLZ lines all these new variables ( $\Delta l_{Exp}^g$ ,  $\Delta \varphi_{Exp}^g$ ,  $\Delta g_{Exp}$ ) have been determined. The components of the  $\mathbf{F}$  tensor are then retrieved by fitting these experimental variations with kinematic simulations. So for a given F-tensor, the kinematic variations of the HOLZ line positions ( $\Delta l_{Kin}^g$ ,  $\Delta \varphi_{Kin}^g$ ,  $\Delta g_{Kin}$ ) are determined using the kinematic equations B.II.2 and B.II.3. Then by varying the 9 components of the  $\mathbf{F}$  tensor, the algorithm minimizes the distance between these calculated and experimental variations; more precisely it is the  $dist(\mathbf{F})$  function that is minimized.

$$dist(F) = \sum_{g=1}^N w^g \left\{ \left( \Delta l_{Kin}^g - \Delta l_{Exp}^g \right)^2 + \left( \Delta g_{Kin} - \Delta g_{Exp} \right)^2 + C_\varphi \left( \Delta \varphi_{Kin}^g - \Delta \varphi_{Exp}^g \right)^2 \right\} \quad (\text{B.II.11})$$

Here the summation is over the  $N$  selected HOLZ lines,  $w^g$  is the correlation weight of the line as defined in section B.II.5.3, and  $C_\varphi$  is a scaling coefficient to give  $\varphi^g$  more or less importance (here  $C_\varphi = 5$ ).

The  $\mathbf{F}$  tensor parameters retrieval is made in python (Appendix B) by the L-BFGS-B algorithm (Byrd et al., 1995). This algorithm has the advantage to use the gradient information but does not require to calculate it. It is also a bound constrained optimization (meaning that the parameters must be in a given interval). On this study, the interval has been set between  $-5 \times 10^{-2}$  and  $5 \times 10^{-2}$  for every  $\mathbf{F}$  parameters. To address the local minima issue, the L-BFGS-B algorithm is launched multiple times (on the order of one hundred times for a good retrieval) where the starting points are chosen randomly in the interval.

## B.II.7 Results

To evaluate the possibilities of this method, several series of simulated deformed silicon crystals have been studied: firstly, a series of 20 deformed crystals observed along one DO, then the same deformed crystals observed along two DOs. Using multiple DOs has been considered by Maier et al. (1996), and has also been implemented by Morawiec (2007b) and applied by Brunetti et al. (2010). For the one DO case, the results of the minimization are presented in the ( $x$ ,  $y$ ,  $z$ ) basis linked to the CCD camera. For the two DOs case a crystallographic ( $X$ ,  $Y$ ,  $Z$ ) basis in between the two DOs, is chosen:

$$X = [0, 0, 1]; \quad Y = [1, -1, 0]; \quad Z = [1, 1, 0] \quad (\text{B.II.12})$$

### B.II.7.1 Using one direction of observation

The retrieval procedure has been applied to dynamic simulations of strained silicon observed along the  $[651, 441, 31]$  zone axis with strains varying between 0 and  $2 \times 10^{-2}$ . The simulated CBED patterns were images of  $7k \times 7k$  pixels (equivalent to a  $1k \times 1k$  transmitted disk). The pixel size was equal to  $0.01 \text{ nm}^{-1}/\text{pix}$ . Our minimization results show that two parameters  $f_{zx}$  and  $f_{zy}$  have no effects on the positions of the HOLZ lines: changing them freely in a reasonable

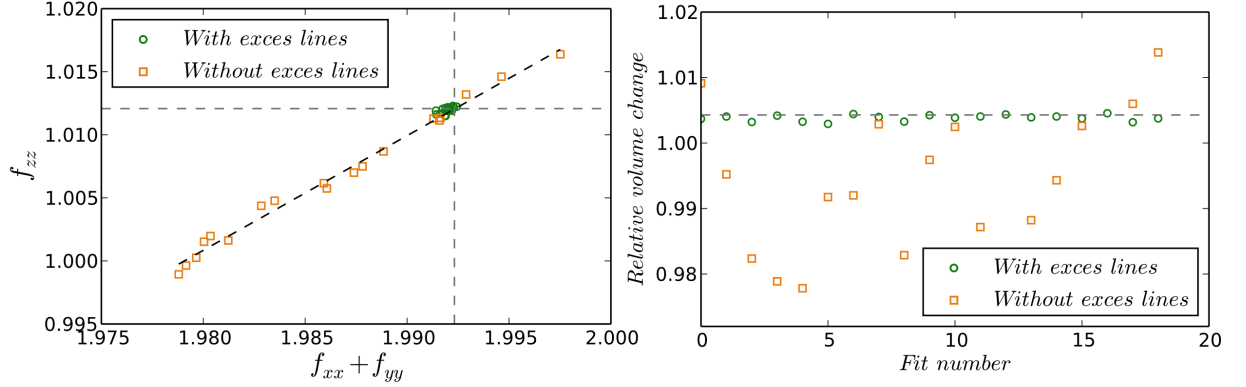


FIGURE B.II.8 – Scatter plot of 20 independent retrievals of the same deformation state (same simulated pattern). Dashed lines shows the original simulated parameters. Adding excess line is solving the ambiguity on  $f_{xx}$ ,  $f_{yy}$  and  $f_{zz}$  components. It also allows to retrieve the lattice volume with a precision of about  $10^{-3}$ (relative to the reference volume)

range of  $\pm 1 \times 10^{-2}$  does not change significantly  $\text{dist}(\mathbf{F})$  (eq. B.II.11), and therefore the positions of the lines are not affected by these two parameters. This effect has been double checked on dynamic simulations. That is why only 7 parameters of the  $\mathbf{F}$  tensor can be retrieved. The standard deviation between retrieved parameters and simulated ones are:

$$\Delta \mathbf{F} = \begin{pmatrix} 2 \times 10^{-4} & 4 \times 10^{-4} & 1 \times 10^{-5} \\ 4 \times 10^{-4} & 3 \times 10^{-4} & 1 \times 10^{-5} \\ & & 3 \times 10^{-4} \end{pmatrix}_{CCD} \quad (\text{B.II.13})$$

Figure B.II.8 shows the result of 20 independent retrievals of the same deformation states without using the excess HOLZ lines. There is an almost linear dependence of the retrieved  $f_{zz}$  over  $f_{xx} + f_{yy}$ . Thus, the fitting without the excess HOLZ line does not allow to retrieve unique values of the  $\mathbf{F}$  tensor diagonal terms, i.e.the volume of the lattice cannot be determined.

The Figure B.II.9 shows the results on twenty simulated deformations when the excess lines are added to the retrieval. Adding excess line removes the ambiguity on the diagonal terms, and it is now possible to retrieve the diagonal terms  $\mathbf{F}$  tensor and therefore the volume of the lattice. In total, 7 parameters of the  $\mathbf{F}$  tensor can then be retrieved with one DO. The precision on the volume is about  $10^{-3}$ .

To understand why the two parameters  $f_{zx}$  and  $f_{zy}$  cannot be retrieved when only one DO is used, it is useful to consider the decomposition of the  $\mathbf{F}$  tensor in terms of rotation  $\mathbf{R}$  and strain:

$$\mathbf{F} = \mathbf{R} + \epsilon = \begin{pmatrix} 1 & -R_z & R_y \\ R_z & 1 & -R_x \\ -R_y & R_x & 1 \end{pmatrix} + \begin{pmatrix} \epsilon_{xx} & \epsilon_{xy} & \epsilon_{xz} \\ \epsilon_{xy} & \epsilon_{yy} & \epsilon_{yz} \\ \epsilon_{xz} & \epsilon_{yz} & \epsilon_{zz} \end{pmatrix} \quad (\text{B.II.14})$$

where  $R_v$  represents a pure rotation around the  $v$  axis.

The effect of the  $\epsilon_{xz}$  (resp.  $\epsilon_{yz}$ ) shear strain is the same on the CBED pattern as a pure rotation  $R_y$  (resp.  $-R_x$ ). The addition of the two effects,  $f_{zx} = \epsilon_{xz} + R_y$  (resp.  $f_{yz} = \epsilon_{yz} - R_x$ ), can therefore be retrieved. But determining the difference between the two effects,  $f_{zx} = \epsilon_{xz} - R_y$

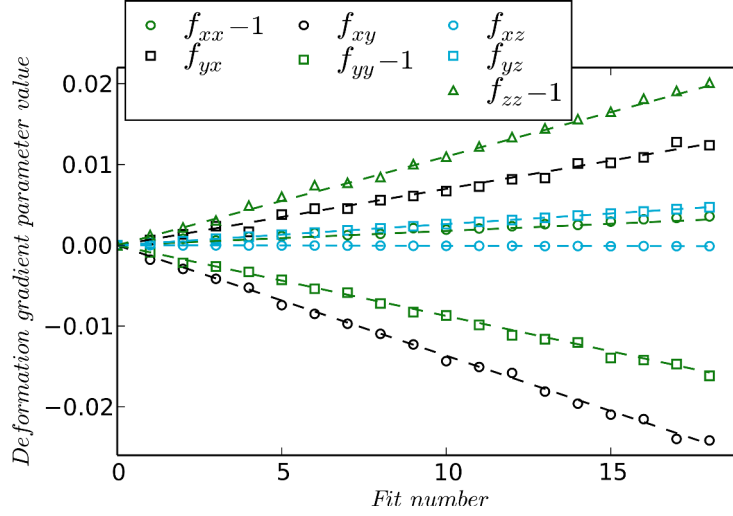


FIGURE B.II.9 – Algorithm retrieval results obtained from 20 dynamically simulated patterns, with different strains and rotation state. Dashed lines are the input values, symbols the fitted one. Both excess and deficient HOLZ lines were used. The zone axis is  $[651,441,31]$  on silicon at 200kV. 7 parameters of the distortion matrix are well retrieved.

(resp.  $f_{zy} = \varepsilon_{yz} + R_x$ ) would involve to be able to separate the contribution of shear strain and pure rotation, which is not possible because they produce an effect that is not measurable even in a simulated the CBED pattern. To remove the 2 ambiguities on  $f_{zx}$  and  $f_{zy}$ , it is necessary to use a second DO.

### B.II.7.2 Using two directions of observation

When using two DOs, it is possible to retrieve all the nine parameters of the  $\mathbf{F}$  tensor. Figure B.II.10 shows the results of the analysis of twenty simulated deformed crystals (identical to the one DO case) observed along two DOs,  $[651,441,31]$  and  $[441,651,31]$  which make an angle of about  $22^\circ$ . As can be seen in Fig. 7, all the 9 parameters of the  $\mathbf{F}$  tensor are well retrieved when using these two DOs,

The standard deviations between retrieved parameters and starting ones are:

$$\Delta \mathbf{F} = \begin{pmatrix} 2 \times 10^{-4} & 1 \times 10^{-4} & 1 \times 10^{-4} \\ 1 \times 10^{-4} & 2 \times 10^{-4} & 2 \times 10^{-4} \\ 3 \times 10^{-4} & 5 \times 10^{-4} & 1 \times 10^{-3} \end{pmatrix}_{XYZ} \quad (\text{B.II.15})$$

## B.II.8 Discussion

Section B.II.7.1 clearly shows the advantage of using the excess HOLZ lines: without the excess lines an ambiguity on the sum of  $f_{xx}$ ,  $f_{yy}$ , and  $f_{zz}$ , i.e. the volume of the crystal cell remains and its only by using the excess HOLZ lines that this ambiguity is removed. Of

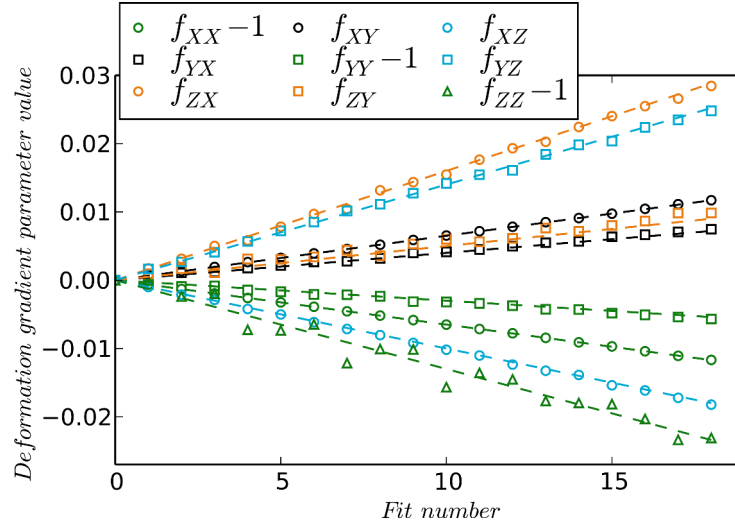


FIGURE B.II.10 – Results obtained from dynamic simulations, with two zone axes : [651,441,31] and [441,651,31] (on silicon at 200kV). Dashed lines are the input values, symbols the fitted one. The result are given in the XYZ basis described previously. The 9 parameters of the distortion matrix are retrieved, the precision is very good on all parameters except on  $f_{ZZ}$  whose sensitivity is low.

course adding the excess lines adds new constraints on the  $\mathbf{F}$  tensor: the excess line variations directly measure the variations of  $\mathbf{g}$ . However our simulations tend to show that one direction of observation is not enough to retrieve the 9 components of  $\mathbf{F}$  and one should not try to recover the 6 components of the strain tensor without considering the 3 components of the rotation: as explained in section 6.1 a small rotation  $R_y$  can have the same effect as a small shear  $\varepsilon_{xz}$ .

The results about ambiguities are based on a set of numerical simulations of a particular direction of observation. It is so not a thorough demonstration and not a general result. For instance, one direction of observation exhibiting fewer HOLZ line or too noisy experimental data could give not enough input data to retrieve 7 parameters. However we think that the chosen direction of observation is not so special and that it is reasonable to say that equivalent results, certainly with slightly different error bars could be obtained in another direction of observation or experimentally.

Adding the second direction made possible the retrieval of  $f_{ZX}$  and  $f_{ZY}$ , and their standard deviations is smaller than  $5 \times 10^{-4}$ . However, the standard deviations of some components of the  $\mathbf{F}$  tensor increase surprisingly when going from the one to the two directions case. For instance  $\Delta F_{XZ}$  and  $\Delta F_{YZ}$  are one order of magnitude higher in the two directions case. This is because  $\mathbf{F}$  has been expressed in 2 different bases. If, for the 2 DOs case  $\mathbf{F}$  is expressed in a basis linked to one of the DO (i.e. the (x,y,z) basis), one obtains  $\Delta F_{xz}$  and  $\Delta F_{yz}$  around  $1 \times 10^{-5}$  instead of  $\Delta F_{XZ} = 1 \times 10^{-4}$  or  $\Delta F_{YZ} = 2 \times 10^{-4}$ .  $\Delta F_{XZ}$  and  $\Delta F_{YZ}$  have higher values in the (X,Y,Z) coordinates because these components incorporate uncertainties that were included in other directions in the (x, y, z) basis.

As can be seen in (B.II.15)  $\Delta F_{ZZ}$  is also high: there is also a general lack of precision along Z, the average beam direction of the two DOs case. The fact that there is only a  $10^\circ$  angle between Z and the two DOs can explain this low sensitivity along Z.

---

In this chapter the excess line method has been explained and applied to series of simulated CBED patterns of different deformed Si crystal to demonstrate its feasibility and evaluate its possibilities. Of course the next step will be to apply it to experimental data. Experimental data could be acquired in two ways. Either a global CBED pattern, containing both excess and deficient HOLZ lines could be acquired; but with the traditional  $2k \times 2k$  CCD cameras the pixel size in  $nm^{-1}$  could then be too small and the CBED patterns could have too coarse details. Or, as the method works by comparison to a reference pattern and measures variations of the HOLZ lines positions in a series of patterns, several shifted CBED patterns could be acquired at a given position of the crystal, each CBED pattern would be zoomed on either the transmitted disk or on some excess HOLZ lines. Of course this second way would extend the acquisition time but would give HOLZ lines with more defined profiles.

As the method works by difference relatively to a reference pattern the method should not be very sensitive to some experimental imperfection like camera distortions.

The power of this method is to be able to include broadening or splitting of the HOLZ lines, a fact that often happens in strained thin lamella (Clement et al., 2004). Here the method has only been applied to non split lines, the following chapter will treat more in detail the broadening of the HOLZ lines and retrieve the three-dimensional strain variations.

---

## Three dimensional displacement retrieval in an heterogeneously deformed crystal

---

In this Chapter, the focus is put on the study of the displacement field inside the sample. In the previous Chapter, we considered that the strain was uniform along the beam direction ( $z$ ), here the variation of the displacement along the beam direction is studied. When the strain is not uniform along  $z$ , the Bragg condition also changes along the beam direction. This induces a broadening of the HOLZ lines observed in previous work.

This broadening of HOLZ lines has been studied by [Houdellier et al. \(2006\)](#), [Benedetti et al. \(2008\)](#) and [Beche \(2009\)](#). [Spessot et al. \(2007\)](#) also made an extensive study of the three-dimensional displacement inside the sample based on Finite Element modeling. In this Chapter, a method to retrieve the displacement field inside the sample directly from several HOLZ lines profiles is presented. This method is applied to the multi-layered Si-SiGe sample presented in Part I. The displacement retrieval has been done without making any hypothesis on the deformation state and using two directions of observation.

### B.III.1 Theoretical aspects of the method

The kinematic scattered wave  $\phi_{g,t}$  for a rocking curve associated to a given  $\mathbf{g}$  reflection is given by (see Chapter [A.III](#) and [Vincent et al., 1988](#)):

$$\phi_{g,t}(s_g) = \frac{i\pi}{\xi_g} \int_0^t \exp(-2i\pi(s_g z + \mathbf{g} \cdot \mathbf{u}(z))) dz \quad (\text{B.III.1})$$

Where  $\mathbf{g}$  is the diffraction vector,  $s_g$  is the deviation parameter,  $t$  the sample thickness (along the beam direction),  $\mathbf{u}$  the displacement vector, and  $\xi_g$  the extinction distance of the diffracted beam  $\mathbf{g}$ .

The rocking curves splitting and position are carrying many helpful information for the reconstruction of the three dimensional displacement. The profile of HOLZ lines is dependent on the atomic displacement by the dot product  $\mathbf{g} \cdot \mathbf{u}$  in equation [B.III.1](#). It means that if only

---

one split HOLZ line is studied, it is only possible to retrieve the component of the displacement vector that is along the corresponding diffraction vector. By studying the profile of several HOLZ lines in the CBED pattern, more information can be retrieved. We will see that to retrieve the whole three-dimensional displacement field, the use of two CBED patterns from two directions of orientation is compulsory.

The equation B.III.1 can be seen as an integral over the whole  $z$  space multiplied by a window function  $\Pi_t(z)$ :

$$\phi_{g,t}(s_g) = \frac{i\pi}{\xi_g} \int_{-\infty}^{+\infty} \exp(-2i\pi \mathbf{g} \cdot \mathbf{u}(z)) \times \Pi_t(z) \times \exp(-2i\pi s_g z) dz \quad (\text{B.III.2})$$

Where  $\Pi_t(z) = 1$  when  $0 \leq z \leq t$ ,  $\Pi_t(z) = 0$  otherwise.

Equation B.III.2 can be seen as a Fourier Transform of the phase factor  $\exp(-2i\pi(\mathbf{g} \cdot \mathbf{u}))$  multiplied by the window function  $\Pi_t(z)$ . This Fourier Transform is useful to perform fast computation of the rocking curve intensity :

$$I_{g,t}(s_g) = |\phi_{g,t} \phi_{g,t}^*| = \mathcal{FT}(\exp(-2i\pi \mathbf{g} \cdot \mathbf{u}(z)) \times \Pi_t(z)) \quad (\text{B.III.3})$$

$$\text{with } \Pi_t(\mathbf{z}) = \begin{cases} 1 & \forall z \in [0, t], \\ 0 & \forall z \notin [0, t] \end{cases}$$

Where  $\mathcal{FT}$  is the Fourier Transform.

Thickness plays a role in the HOLZ lines oscillations, by the window function  $\Pi_t(z)$  in equation B.III.3. Using method presented in Chapter B.I to know precisely the thickness will help to precisely determine the displacement vector  $\mathbf{u}(z)$ .

It is important to note that regarding the equation B.III.3, the following  $\mathbf{u}(z)$  solutions are equivalent (Vincent et al., 1999):

- Phase is defined modulo  $2\pi$
- Adding a constant to  $\mathbf{u}(z)$  does not change the rocking curve shape.
- As  $\phi_{g,t}^*$  and  $\phi_{g,t}$  plays the same role,  $\mathbf{u}(z)$  and  $-\mathbf{u}(-z)$  lead to the same rocking curve. This is equivalent to a physical inversion of the TEM specimen.

## B.III.2 Algorithm presentation

A Monte Carlo based algorithm that is able to retrieve the displacement vector from splitting of HOLZ lines has been set-up. Figure B.III.1 gives a schematic view of the algorithm. The algorithm can use several rocking curves to retrieve the displacement. It minimizes the difference between the experimental rocking curves and the ones simulated by equation B.III.3.

The displacement vector  $\mathbf{u}(z)$  has three components  $u_x(z)$ ,  $u_y(z)$  and  $u_z(z)$ . Each component is parametrized by Fourier Series to which a slope term is added:

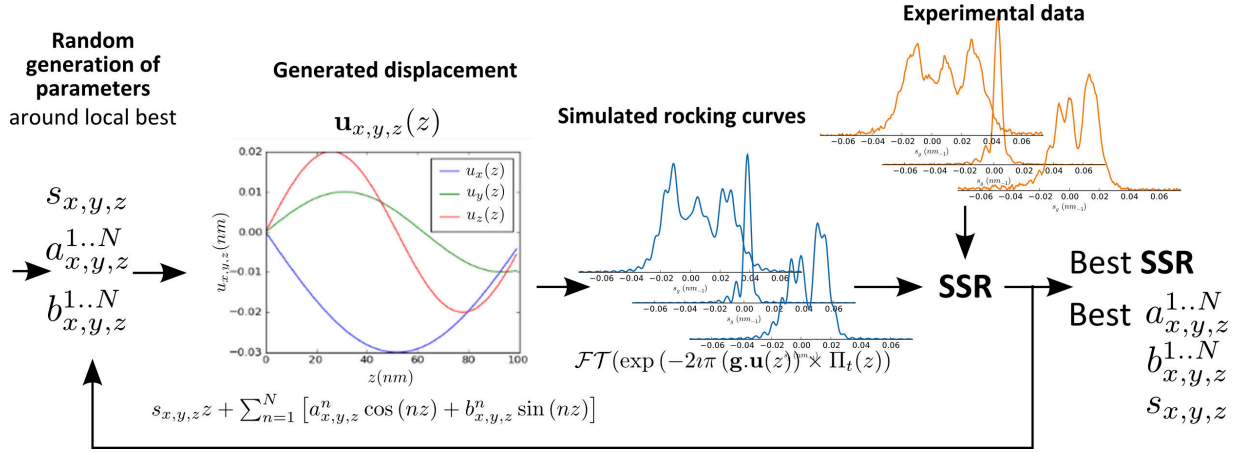


FIGURE B.III.1 – Schematic view of the Monte Carlo algorithm displacement retrieval.

$$\begin{aligned}
 u_x(z) &= s_x z + \sum_{n=1}^N [a_x^n \cos(nz) + b_x^n \sin(nz)] \\
 u_y(z) &= s_y z + \sum_{n=1}^N [a_y^n \cos(nz) + b_y^n \sin(nz)] \\
 u_z(z) &= s_z z + \sum_{n=1}^N [a_z^n \cos(nz) + b_z^n \sin(nz)]
 \end{aligned} \tag{B.III.4}$$

The number of parameters must not be too high for a good retrieval and it has been found that taking  $N=6$  parameters gives a good algorithm convergence.

Once the parameters are given, the algorithm simulates corresponding rocking curves of the given  $\mathbf{g}$  reflections. These rocking curves are simulated using equation B.III.3. Then the simulated rocking curves are compared to the experimental ones. The comparison takes in account the shape and the intensity of the rocking curve, the intensity being normalized to the beam intensity in the transmitted beam. The minimizing function is defined by the Sum of Squared Residuals (SSR) :

$$SSR(a_{x,y,z}^{1..N}, b_{x,y,z}^{1..N}) = \sum_{i=0}^{n_{HOLZ}} (I_g^{exp} - I_g^{simu}(a_{x,y,z}^{1..N}, b_{x,y,z}^{1..N}))^2 \tag{B.III.5}$$

The algorithm is based on a Monte Carlo minimization, meaning that it randomly changes the parameters trying to minimize the difference. The Monte Carlo algorithm first randomly changes the initial parameters within defined bounds. If the new solution is better, it starts from this solution and randomly changes the parameters within the same bounds. The best found solution is always the starting point of the new random generation. After a defined number of tries (here 300) the algorithm restart from the initial parameters. This is called a run, after each run, the algorithm stores the best SSR and best parameters. Each run is totally independent.

After a defined number of run (here 1000), the algorithm stops and returns the best parameters of the best run.

To refine the parameters, it is useful to launch the algorithm several times by reducing the random bounds (i.e. reducing the step) starting from the best previous point. The algorithm finally returns the  $s_{x,y,z}$ ,  $a_{x,y,z}^{1..N}$  and  $b_{x,y,z}^{1..N}$  parameters corresponding to the best SSR. The resulting  $\mathbf{u}(z)$  displacement vector is then the retrieved solution. At the end, there is no proof that the algorithm converge to the right solution, but it always converged to the correct solution for all simulated data used in this work.

### B.III.3 Application on simulated Silicon

As a proof of concept, and in order to study the good convergence, the algorithm has been applied to simulated Silicon. An arbitrary displacement in a Silicon sample has been generated, and the associated rocking curves were simulated using equation B.III.3. Two cases have been studied:

- One unique direction of observation: [21,14,1], and 7 associated rocking curves.
- Two directions of observation: [21,14,1] and [17,27,1]. 7 rocking curves for the first one and 4 rocking curves for the last one.

Simulations		Direction of observation			
		[21,14,1]		[17,27,1]	
Case 1	[21,14,1] direction only	[5,-7,-1]	[4,-6,6]	[-7,5,-7]	[10,-6,0]
Case 2	[21,14,1] and [17,27,1] directions	[5,-7,-3]	[-4,6,6]	[-7,5,-5]	[10,-6,4]
		[6,-8,-6]	[-2,4,-10]		
		[-4,6,10]			

TABLE B.III.1 – Direction of observation and diffracting planes used for the simulation of silicon rocking curves.

The diffracting planes have been chosen to be the one observed in experimental Silicon CBED diffraction and are summarized in table B.III.1.

In order to speed up the retrieval, the algorithm finds the best three first Fourier coefficients ( $a_x^0, a_y^0, a_z^0$ ), then continues with the second ones, and adds another three Fourier coefficients each time the best fit is found. The previous Fourier coefficients are free to change when adding the next parameters. This allows to guide the algorithm through the solution. In this case, we choose to limit the number of Fourier coefficient to 6 (6  $a_{x,y,z}$  and 6  $b_{x,y,z}$ ).

Figure B.III.2 shows the result of the retrieval. For both cases, the algorithm as been tested eight times in the same conditions to verify it's good convergence. One can see that in the case 1 (only one direction of orientation) the lack of information along the beam direction does not allow the algorithm to find a unique solution. Theoretically, it would be possible to retrieve the three-dimensional displacement by using at least three non-collinear diffraction vectors, but as the diffracting planes are nearly parallel to the beam axis, the solution is underdetermined. From

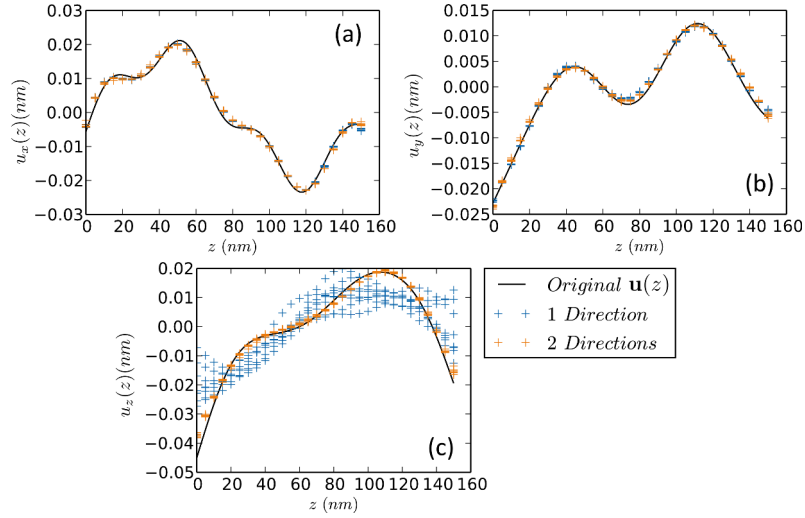


FIGURE B.III.2 – (a)  $u_x(z)$ , (b)  $u_y(z)$ , (c)  $u_z(z)$  displacement retrieval by the Monte Carlo algorithm, using 7 simulated rocking curves from  $[21,14,1]$  zone axis for 1 direction of observation, and 4 additional simulated rocking curves from  $[17,27,1]$  for the second direction. For each case, the result of 8 similar minimizations is shown. The use of the second zone axis allows the algorithm to find the displacement in the  $z$  direction.

only one CBED diffraction pattern, it is therefore possible to retrieve only the two-dimensional displacement in the plane perpendicular to the beam.

In the second case (two direction of orientation), the three-dimensional displacement is well retrieved by the algorithm due to the new information coming from the additional direction of orientation. For both cases, as the retrieved displacement is defined to a constant and as  $\mathbf{u}(z)$  and  $-\mathbf{u}(-z)$  are equivalent, the  $\mathbf{u}$  displacements have been average to zero and either  $\mathbf{u}(z)$  or  $-\mathbf{u}(-z)$  have been plotted.

## B.III.4 Application on an experimental Si/SiGe sample

### B.III.4.1 Experimental setup

The Monte Carlo algorithm has been tested on an tripod polished Si substrate, containing four Si-Ge layers of different compositions. The sample has been plasma cleaned during 1 minute ( $\text{H}_2\text{O}_2$ ) before insertion into the microscope. The CBED patterns were taken at 200kV with a C2 aperture of 30 $\mu\text{m}$ , on a Probe Corrected FEI Titan. To improve the HOLZ lines contrast, a cryogenic holder was used with a working temperature of  $-120^\circ\text{C}$ .

To be in a high index direction of orientation (i.e. low symmetry), the sample has been tilted approximately  $10^\circ$  from the  $[110]$  polishing axis, as parallel to the Si/SiGe interface as possible. Nevertheless, the interface appears slightly tilted of about 2 degrees.

Due to the lattice mismatch between the two materials, the bulk Silicon is deformed near the layers. As the sample has two free surfaces, it relaxes on these directions, that is the direction

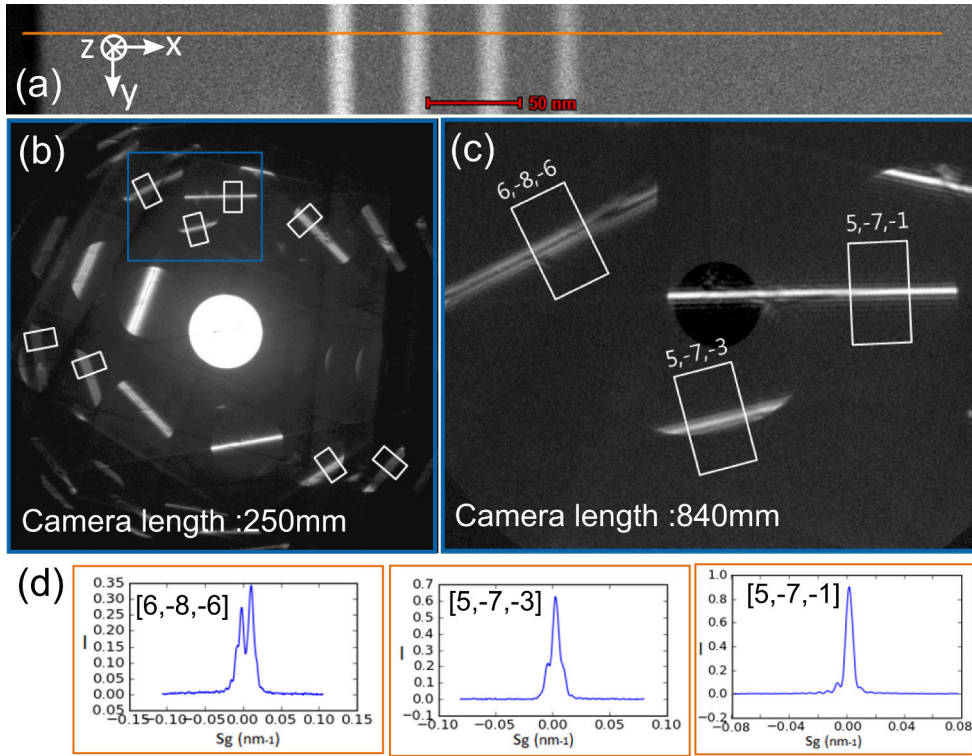


FIGURE B.III.3 – Extraction of experimental HOLZ line profiles. (a) STEM image of the Si-Ge layers in the bulk Si. 120 diffractions were taken along the 500 nm orange line. (b) Overview of the CBED pattern at a camera length of 250mm. The direction of orientation is  $[22,14,1]$ . The 7 profiles corresponds to the 7 lines given in table B.III.1. (c) Diffraction taken at a camera length of 840mm. The profile of three HOLZ lines (d) are extracted from this diffraction.

of the beam. The strain is therefore not uniform along the beam direction and the HOLZ lines splits. It is possible to retrieve the displacement by fitting this splitting.

Figure B.III.3 gives view of the sample, the acquisition procedure and details on the HOLZ lines profile extraction. A line scan perpendicular to the layers has been done in order to visualize the displacement as a function of the distance to the structures. It is important to note that, to have good resolution on excess rocking curves, four shifted diffractions were taken at a high camera length value (840 mm) and HOLZ lines profiles were extracted from these four 840 mm diffractions.

### B.III.4.2 Descanning the beam

When acquiring series of diffraction, the beam is scanned on the sample using STEM deflectors. If the pivot points of the microscope are well aligned, then the beam should stay parallel to the optical axis while scanning. On the FEI Titan 80-300 at 200kV, although the microscope has been aligned as well as possible, there was still a residual tilt when the beam was scanned. If the scan amplitude is low, then this residual tilt is negligible, but as in this case the scan is

about half a micrometer, the tilt becomes clearly visible and will affect the zero position of the extracted HOLZ lines profiles.

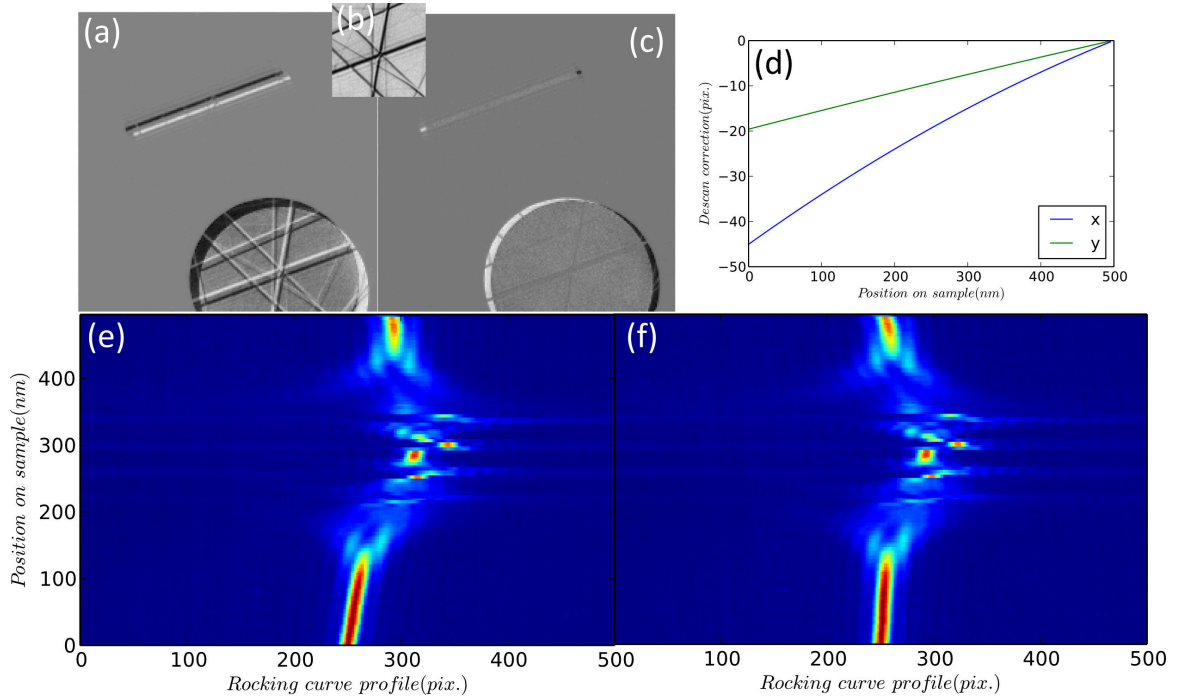


FIGURE B.III.4 – (a) Difference between two diffraction separated by 500nm in perfect silicon. HOLZ lines moves due to the slightly misaligned pivot point. (b) Template of the center of transmitted beam, used to match HOLZ lines position (c) Difference between descan corrected diffractions, the HOLZ lines are exactly in the same place after the descan correction using template matching. (e) original extracted profiles (f) descan corrected profiles.

In order to remove the tilt of the beam when scanning, a numerical correction was applied to the acquired series. Figure B.III.4 shows the principle of the descan correction. First of all, a series of diffraction are taken of perfect silicon in the same condition as the Si/SiGe experimental data. By making this, we know that any displacement of the lines is due to a microscope misalignment and not a physical property of the sample. Figure B.III.4 (a) is the difference between the two extreme diffraction patterns of the 500 nm acquisition line. We can see that the tilt due to the beam shift is rather important.

In order to correct the beam position, a template (Figure B.III.4 (b)) was taken in the transmitted beam of the last diffraction, and matched in all the other diffraction. Figure B.III.4 (c) shows the difference between the two extreme diffraction after correcting the position according to the template matching result. Correcting the descan ensures that a change in the lines positions will be due to strain. Note that it is not the beam that is centered but the lines that are matched, because we want to measure zero displacement as it should be the case on this perfect silicon. Figure B.III.4 (d) shows the result of the HOLZ line shifting as a function of the scan position.

Figure B.III.4 (e) and (f) shows the uncorrected and descan corrected extracted profile of a HOLZ line in the Si/SiGe sample.

### B.III.4.3 Results

The same two directions of orientation and the same eleven experimental profiles as in the simulation case were used to retrieve the experimental displacement (see table B.III.1). Along the orange line in figure B.III.3, 120 series of diffraction were taken at a camera length of 840mm. From each series, eleven profiles are extracted and the displacement retrieval algorithm is launch using these eleven experimental profiles. Figure B.III.5 shows the 120 profiles of the 11 experimental and simulated HOLZ lines.

The rocking curves are really well retrieved in all the series, except near the interfaces and inside the Si-Ge layers where the goodness of fit, i.e. the value of the Sum of Squared Residual function, is high. This is due to the fact that the simulation considers only pure Silicon, and the scattering factor of Si-Ge is different from the one of pure Silicon. In addition, around the interfaces, the slight inclination of the sample makes a superposition of Si and SiGe layers over few nanometers. As the HOLZ line profile is not calculated when the beam goes through two different crystals, the algorithm failed to find a correct value of the displacement. We therefore considered the retrieved values inside and just aside the layers were not accurate given the high value of the SSR function. The results in the following will not be plotted because it complicates the display and interpretation of the correct results.

Figure B.III.6 shows the retrieved displacement projected on the (x,z) plane, z being the beam axis and x the direction of the line profile. Due to the presence of SiGe layers that have a higher lattice parameter, the Si substrate relaxes mainly in the z direction. The maximum amplitude of the displacement is around 0.8 nm. We can see that the presence of a SiGe layer is “sensed” by the Silicon up to 50 nm away from the interface. The magnitude of the displacement vector is indeed increasing from 50nm to the Si/SiGe interfaces.

Retrieved and simulated  $u_x$   $u_y$  and  $u_z$  displacements are shown in figure B.III.7. The displacements being retrieved to a constant, to represent the 120 retrievals, a mean value of zero for the each displacement has been taken. In addition,  $-\mathbf{u}(-z)$  and  $\mathbf{u}(z)$  being also equivalent, a template matching between each neighbor has been done in order to choose between  $-\mathbf{u}(-z)$  and  $\mathbf{u}(z)$  and ensure the continuity of the retrieve displacement. The highest component of the retrieved displacement field is the z component, this agrees with the fact that the sample is relaxing in the z direction because of the free surfaces.

Finite element simulation of the Si/SiGe multi-layered structure has been done (Beche, 2009), considering that the y direction (direction perpendicular to the SiGe layers) is infinite and that there can not be any displacement in this direction. Figure B.III.7 shows the results of these simulations. Figure B.III.7 (a) and (b) shows the  $u_x$  displacement. In the simulation, the  $u_x$  displacement induced by the SiGe layers is “shifting” everything in the x direction because the surface at  $x = 0$  was let free. As discussed before, the displacement in the experimental case is sensitive to a constant, and therefore this shift is not detected. It could be included if we measure the  $\varepsilon_{xx}$  component, but here  $\varepsilon_{xx}$  was not part of the retrieval. We discuss this point in the next section.

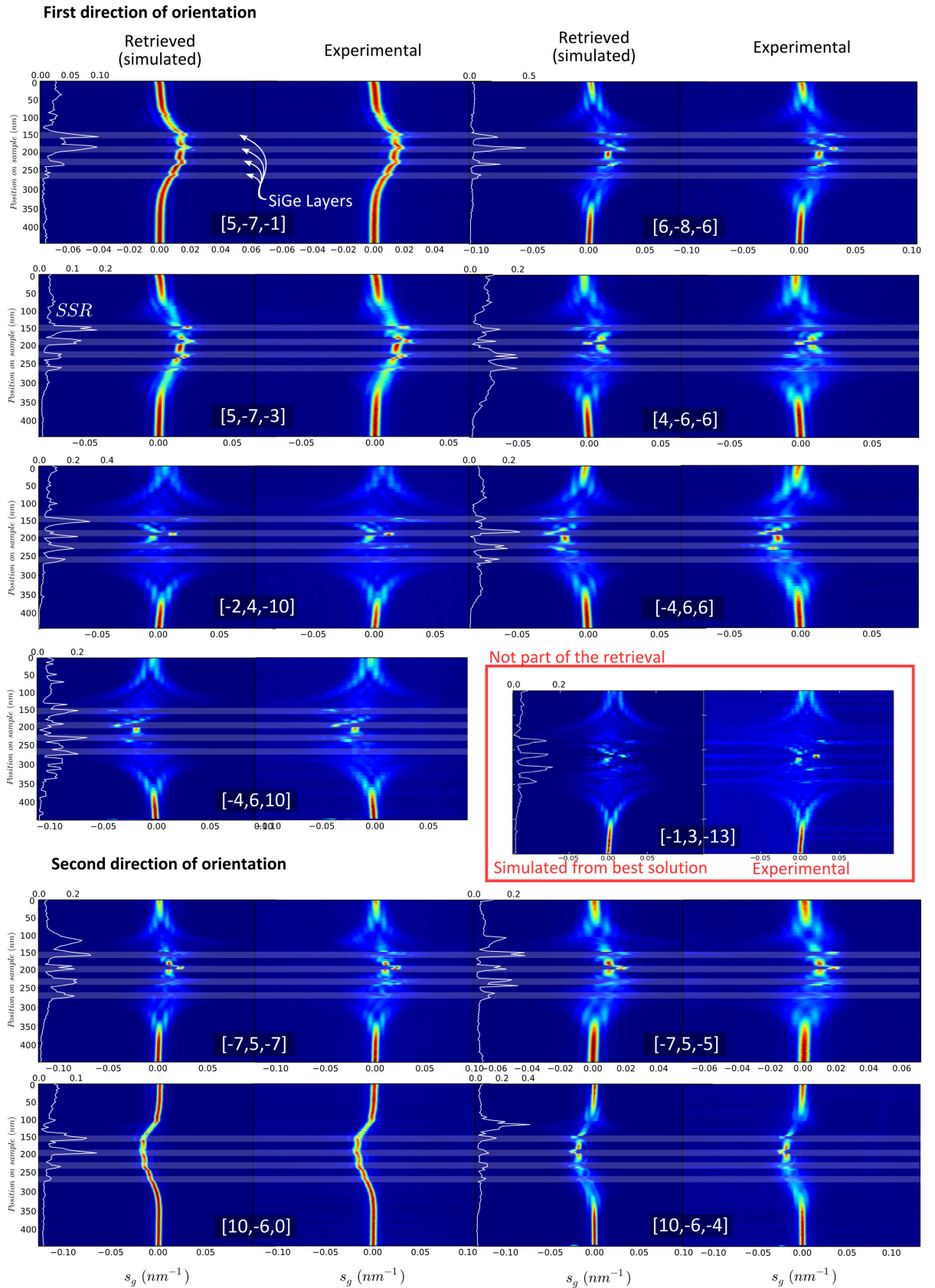


FIGURE B.III.5 – Experimental HOLZ lines profiles used in the algorithm retrieval and the corresponding retrieved simulated profiles for the best  $\mathbf{u}(z)$  solution. The red boxed HOLZ line  $[-1,3,-13]$  was not part of the retrieval and has been simulated afterward using the best  $\mathbf{u}(z)$  solution. There is a nearly perfect agreement of the lines profiles except inside the SiGe layers.

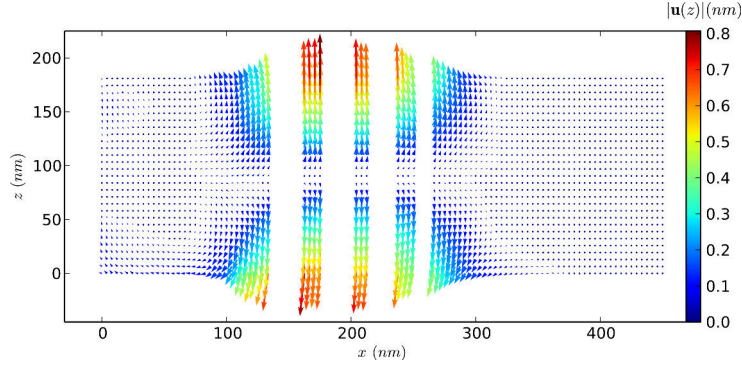


FIGURE B.III.6 – Projected retrieved displacement on the  $(x,z)$  plane. The displacement scale has been exaggerated to better visualize the displacement.

The specimen inversion equivalence is also visible in the retrieval, and for  $x$  position lower than  $200 \text{ nm}$ , the retrieved  $u_x$  displacement is mistaken because there is an inversion of the displacement compared to the simulated case. This inversion was corrected simply by taking  $-u_x(-z)$  as a solution. But without the simulations, it would not have been possible to see that there was an inversion problem.

as shown in figure B.III.7 (c)(d), the algorithm retrieved a non zero value for  $u_y$  displacement, whereas it should be zero given the symmetry of the sample. One explanation can be that the sample upper and lower surfaces are not strictly parallel because it is a  $2^\circ$  tripod polished specimen. It could be interesting to simulate using finite element modeling if this angle between surfaces could induce such a displacement. Finally the  $u_z$  displacement is from about 20% over-estimated. This is not explained for now, but it might be an ambiguity with the  $u_y$  displacement, that may also explain the non zero value of this displacement.

The displacement field also gives information on the strain tensor, which contains derivatives of the displacement vector. But in this experiment, there is missing information. Firstly, as  $\mathbf{u}(z)$  is defined to a constant for each retrieval (in the  $x$  direction), the mean value is set to zero (to ensure the continuity of the displacement along  $x$ ). Therefore it is senseless to try to make a derivative with respect to the  $x$  direction. In addition, here, there is no information on the  $y$  direction, and even if there was, the constant problem will be the same, and no derivative with respect to  $y$  would be possible. It is therefore only possible to do the derivative of  $\mathbf{u}(z)$  with respect to the  $z$  direction. The available information are therefore:

$$\frac{\delta u_x}{\delta z}, \frac{\delta u_y}{\delta z} \text{ and } \varepsilon_{zz} = \frac{\delta u_z}{\delta z}$$

Figure B.III.8 shows the derivative of the  $u_x(z)$ ,  $u_y(z)$  and  $u_z(z)$  displacement with respect to  $z$  for experiment and simulated data. As showed in figure B.III.7 (e), the  $u_z$  is close to a linear slope in between the layers, meaning that the  $\varepsilon_{zz}$  strain is nearly constant in the  $z$  direction. In fact, the sample seems to relax about  $10 \text{ nm}$  under the surface on the simulation even if this behavior is less clear in the experimental retrieval. The  $\frac{\delta u_x}{\delta z}$  value agrees very well with the simulation by correcting the inversion problem discussed above. The boxed area in figure B.III.8 shows a place where the algorithm failed to describe well the displacement.

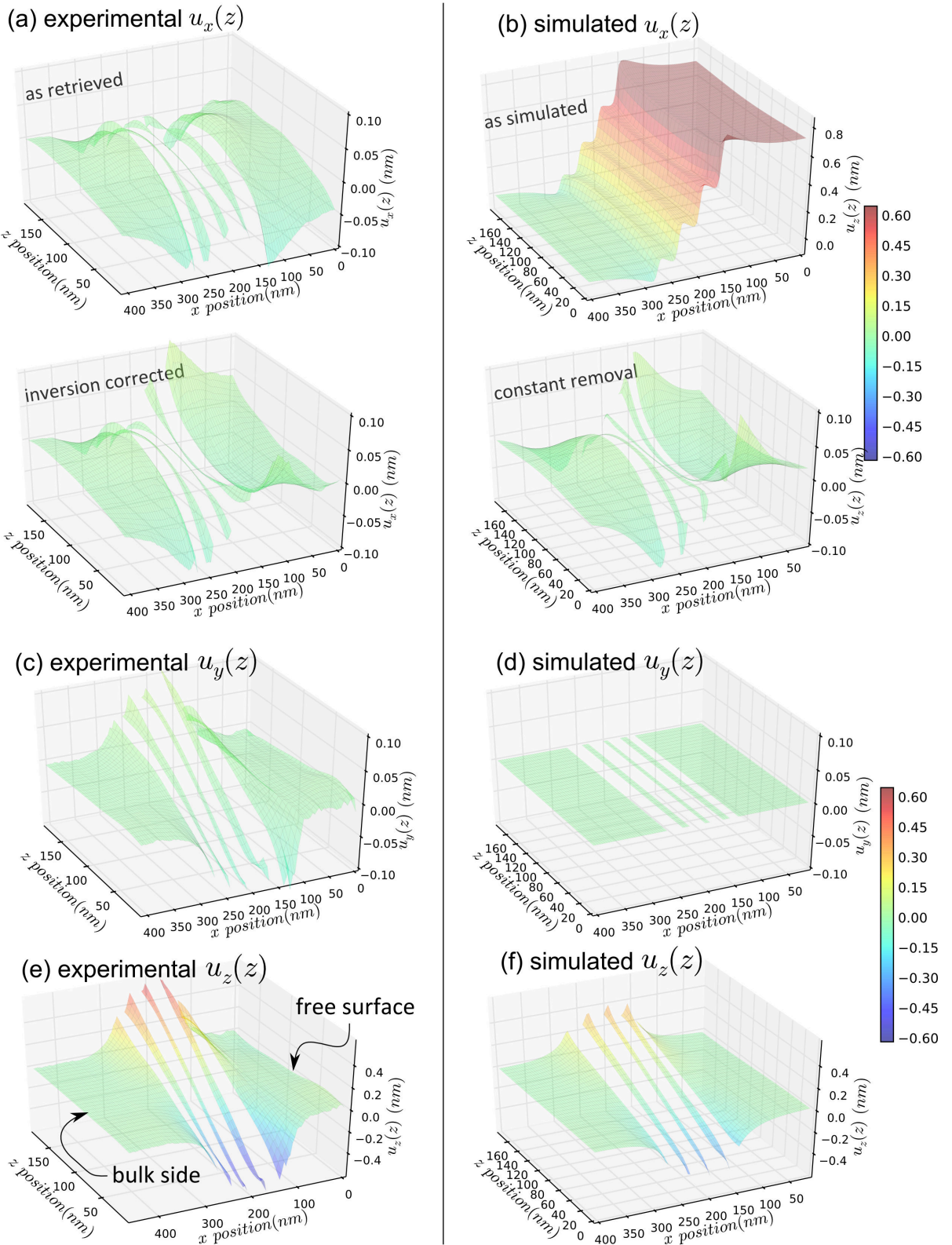


FIGURE B.III.7 – Retrieved (a)  $u_x(x, z)$  (c)  $u_y(x, z)$  and (e)  $u_z(x, z)$  displacements compared to (b)(d)(f) simulated ones. Results from SiGe layers have been removed because of the high SSR values in experimental retrieval. One can clearly see that the main displacement comes from the  $z$  relaxation of the sample. The measured displacements agrees pretty well with the simulated ones, with an about 20% scaling for  $u_z(z)$  and a non zero value for  $u_y(z)$ .

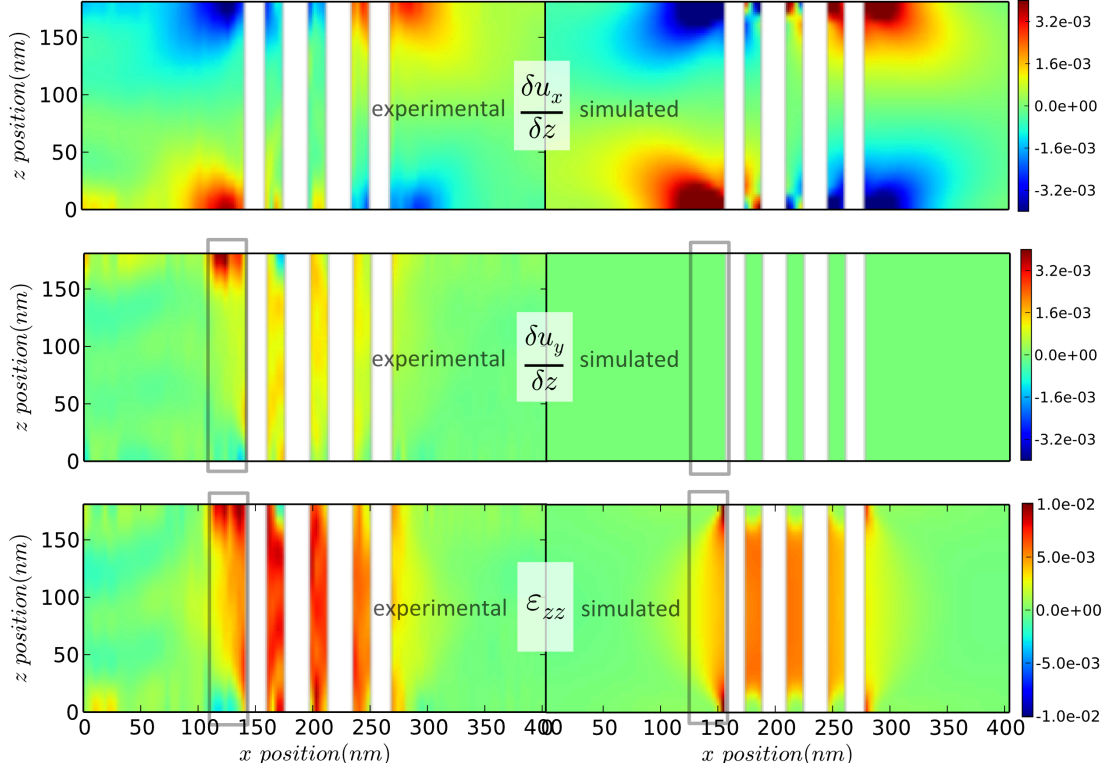


FIGURE B.III.8 – Derivative of the  $u_x(z)$ ,  $u_y(z)$  and  $u_z(z)$  displacement with respect to  $z$  for experimental and simulated case.  $\frac{\delta u_x}{\delta z}$  is in a good agreement with simulation when corrected for inversion as explained in figure B.III.7.  $\frac{\delta u_z}{\delta z}$  is overestimated on the experimental measurement.

## B.III.5 Discussion

The presented method to retrieve the variation of the displacement along the beam direction gives consistent results outside the SiGe layers. The retrieved displacement is qualitatively correct, but if we rely on the simulated displacements, it is not quantitatively exact. The experimental retrieval of  $u_z$  is overestimated by about 20%, underestimated by also 20% for  $u_x$  and there is a  $u_y$  displacement whereas the simulation considered symmetric conditions in the  $y$  direction. Nevertheless as the tripod specimen does not have parallel faces, the symmetry in the  $y$  direction is removed and induces  $u_y$  displacement. This may also induced changes in the  $u_z$  and  $u_x$  displacements.

The descans procedure is very important as it can induce large errors on the displacement measurement. So either the microscope is perfectly aligned and there is no move of the HOLZ line when scanning the beam on a perfect undeformed sample, or correcting this movement using template matching must be done before going further in the deformation analysis.

This method fits the displacement inside the sample, but is limited in terms of information on the displacement because each retrieval is defined to a constant. Therefore if we identify to the  $\mathbf{F}$  tensor used in the previous chapter and defined in Appendix A, it is possible to retrieve  $F_{xz}$ ,  $F_{yz}$  and  $F_{zz}$ . All the other components being derivative with respect to  $x$  and  $y$  cannot be

retrieved using this method. This under-determination is due to the fact the equation B.III.1 studies the variation of  $\mathbf{u}$  along  $z$ . To include the other  $\mathbf{F}$  parameters it could be useful to add the technique presented in Chapter B.II, i.e. to add the transmitted HOLZ lines to the fitting procedure. This could induce difficulties because split HOLZ lines are more difficult to see in the transmitted beam but could be a very powerful method to fully characterize three-dimensional displacement in the whole sample.



---

## Conclusion on Convergent Beam Electron Diffraction

---

CBED contains an amazing number of information on the sample geometry. Chapter [B.I](#) showed that CBED can measure the sample thickness, the direction of observation, the acceleration voltage and the camera length on a single CBED pattern from a perfect crystal. Chapter [B.II](#) and [B.III](#) showed that the HOLZ lines in the CBED pattern contains information on the deformation in the plane perpendicular to the beam but contains also information along the beam direction like only few other electron diffraction techniques. This information along the  $z$  axis is carried by two things:

- The position of excess and deficient HOLZ lines that comes from planes which are not strictly parallel to the beam direction.
- The broadening of HOLZ lines due to the variation of the displacement along the beam direction

In this thesis work, the two effects have been studied separately. Chapter [B.II](#) studying the position shift of HOLZ lines induced by a three-dimensional strain and rotation and Chapter [B.III](#) studying the broadening of HOLZ lines induced by a displacement variation along the beam direction.

The ultimate measurement procedure would include all these effects in one retrieval algorithm, allowing the study of the three-dimensional displacement field inside the sample. Developing this method would need another thesis work but could be a real breakthrough in the strain measurement of TEM samples.

However, the presented method has several drawbacks. The main drawback of the method is certainly its lack of generality. Only deformation in a unique crystal (Si) having different deformation states has been analyzed, and we faced to SiGe crystal, another parameter (the Germanium concentration) have to be included in the simulations. This method is only valid for an uniform sample composition, and if the composition changes along the beam direction (for example if the beam crosses an interface) the algorithm will fail retrieving the displacement field. Complexity is the second drawback of the method. If researchers are only interested in the analysis of strain in a 2D plane, a technique like the PED ([Rouviere et al., 2013](#)) is certainly a better adapted technique. In addition CBED is limited to relatively thick crystals of relatively good quality, thicker than 100nm in silicon, unless the LARBED (Large Angle Rocking Beam Electron Diffraction) method developed by [Koch \(2011\)](#) is applied.



## Part C

# Electron diffraction of two-dimensional materials

Two-dimensional materials have properties that are way different from the bulk ones. These unique properties have attracted a lot of scientific interests especially since [Novoselov et al. \(2004\)](#) succeeded to isolate a monolayer graphene sheet for the first time. Hence, developing characterization tools to reveal the atomic structure of graphene and other two-dimensional materials is essential to understand and control its properties and ultimately use them in new devices or materials. With its high field of view and high resolution abilities, the TEM is an ideal tool to characterize two-dimensional materials. Nevertheless their characterization is a big challenge in the TEM because two-dimensional materials are consisting of only one or few atomic layers.

In this part, three different materials are studied: Graphene, Boron Nitride and Molybdenum disulfide. The [first Chapter](#) of this part discusses the delicate interpretation of the contrast in HR-TEM images and the two-dimensional specimen orientation using electron diffraction. The [second Chapter](#) is a study of TEM thickness measurement of few-layered Molybdenum disulfide and Boron Nitride.



---

## Study of HR-TEM contrast and diffraction of graphene

---

Properties of graphene such as electron mobility and resistivity are directly related to its atomic structure. Researchers are willing to reveal the detailed atomic structure of graphene and graphene based materials in order to understand and control their intrinsic properties. Direct imaging of real atomic structure of graphene is thus an important issue in many analytical techniques. The TEM techniques would be an ideal characterization tool for the graphene-based materials science, which provides a large area of observation together with extremely high resolution local structural analysis. However, TEM atomic resolution imaging is still a big challenge because graphene is consisting of only one atom thick layer of carbon. To produce a TEM atomic scale image of the graphene, high spacial and energy resolutions are required under low accelerating voltage to avoid beam damage. Recently achieving the required conditions for TEM atomic scale imaging has become possible thanks to aberration corrector and monochromator.

Although it is now possible, using the state of the art TEMs, to visualize the atomic structure of graphene, the interpretation of images is quite complex. The TEM images are not directly giving the atomic position because the contrast of an atom appears positive or negative, depending on the transfer function defined by several parameters such as the defocus and the aberrations. These images should be interpretable with the help of simulations to compare with real experimental conditions. Nevertheless, we often face to difficulties of interpretation on the atomic positions of graphene because of some additional unexpected parameters. Therefore, detailed study on the effect of different parameters on the image is crucial for a correct understanding of atomic structures.

In addition to HR-TEM images, electron diffraction can easily be taken in the TEM to study the reciprocal space of graphene, to determine the stacking structures or to study the specimen orientation. With diffraction, no contrast interpretation is needed, but one have to be careful to the projection effect describe in Chapter [A.III](#).

This chapter contains two different sections, the first one stating on the delicate interpretation of atomic contrasts of graphene atoms in HR-TEM images. In this first section, two important parameters, three-fold astigmatism and incident angle, are studied and their influence on the image contrast are demonstrated associated with the image simulations. The other section

---

describes a study of the tilt or orientation of a two-dimensional specimen by using the projection effect in electron diffraction.

### C.I.1 Graphene atomic contrasts in HR-TEM images

HR-TEM images are delicate to interpret because the contrast is a complex interaction of phases and intensities of diffracted and transmitted beams. And because graphene is a one atom thick layer of a low atomic number material, it is a weak electron scatterer and therefore the contrast of graphene atoms is also weak. This contrast depends on numerous parameters of the electron beam such as focus spread, lenses aberrations, defocus and even sample orientation. Understanding the behavior of HR-TEM contrast is essential to understand graphene structure and be able to determine the atomic positions, and therefore study defects or interfaces.

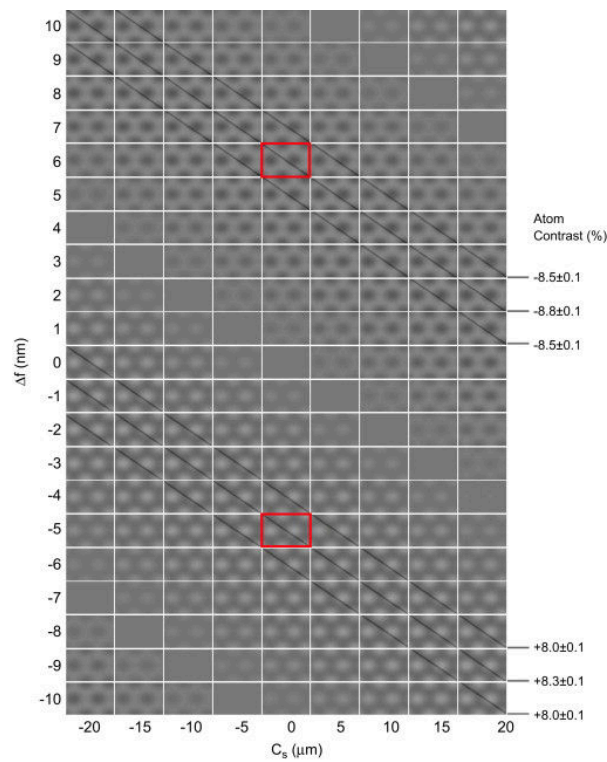


FIGURE C.I.1 – Calculated HRTEM images of graphene at 80 kV, with  $C_c=1.41$  mm and measured focus spread. The highest dark and bright atom contrasts are obtained for a set of  $C_s$  and  $\Delta f$  values marked by the middle diagonals. The two images marked by the red rectangles are in the center of the highest-contrast diagonal representing optimum contrast values. Figure reprinted from [Lee et al. \(2012\)](#) with permission.  $\approx 17nm$

### C.I.1.1 Influence of defocus and spherical aberration

The defocus is one of the main microscope parameters that influence the HRTEM image contrast because unfocussing the beam changes drastically the illumination conditions, but the behavior of the HRTEM image in regards to the focus can be complex. Figure C.I.1 shows for example the influence of third-order spherical aberration ( $C_s$ ) and defocus on the HR-TEM contrast of a graphene mono-layer. This figure illustrates the importance of knowing the beam properties for analyzing the atomic positions of graphene.

This figure from Lee et al. (2012) shows that the atom position is not always on the dark or bright intensity, for certain combinations of spherical aberration and defocus values, the atom will either lie on the dark spot or on the bright one. Some combinations will result to a very low contrast and the graphene sheet won't be visible anymore. By simulating the HR-TEM images for different  $C_s$  and  $\Delta f$  values, Lee et al. (2012) calculated an optimum image contrast.

In addition, using an image corrected microscope, it is possible to compensate for the  $C_s$  aberration by adjusting the value of the spherical aberration coefficient (Chang et al., 2006).

### C.I.1.2 Influence of the number of layers

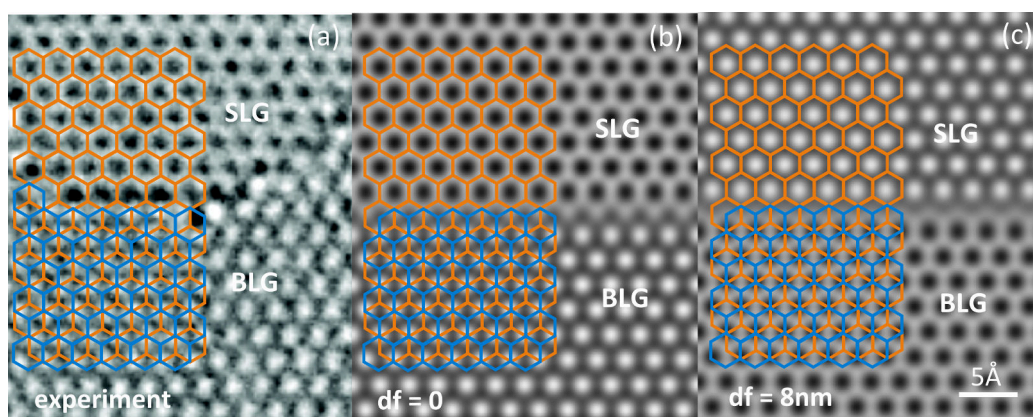


FIGURE C.I.2 – (a) Step from a single-layer (SLG) to a bilayer (BLG) with overlay of the graphene lattice (orange) and the second layer (blue), offset in the AB stacking of graphite. In the bilayer region, white dots appear where two carbon atoms align in the projection. (b)(c) Simulated HR-TEM images of a step from SLG to BLG for two different defocus. Changing the defocus invert the contrast, and SLG looks like BLG. (a) Adapted with permission from Meyer et al. (2008). Copyright 2008 American Chemical Society.

It is easily understandable that the number of layers in a graphene membrane influences the HR-TEM contrast. Nevertheless, the contrast of graphene layers is not trivial. Figure C.I.2 (a) is an experimental image showing the difference of contrast at a step between single- and bi-layer graphene Meyer et al. (2008). The AB stacked bilayer region has a different contrast that the single-layer region. But one have to be careful because as shown in figure C.I.2, (b) and (c) the contrast of single-layer graphene can be similar to the one of bi-layered graphene at a different

defocus. So this HR-TEM image tells us that there is a step, but electron diffraction should be taken to identify whether the graphene is single or bi-layered (Meyer et al., 2007).

### C.I.1.3 Influence of the sample tilt

The sample orientation can also have an influence on the contrast of graphene HR-TEM images. For few-layered graphene membranes Wang et al. (2012c) have been able to reconstruct the surface topography by comparing the contrast variation of experimental image to simulated ones. A small tilt of the surface normal shifts the phase of the electron waves and lead to changes in the image contrast. This change can be important as there even can be a contrast inversion as visible in figure C.I.3.

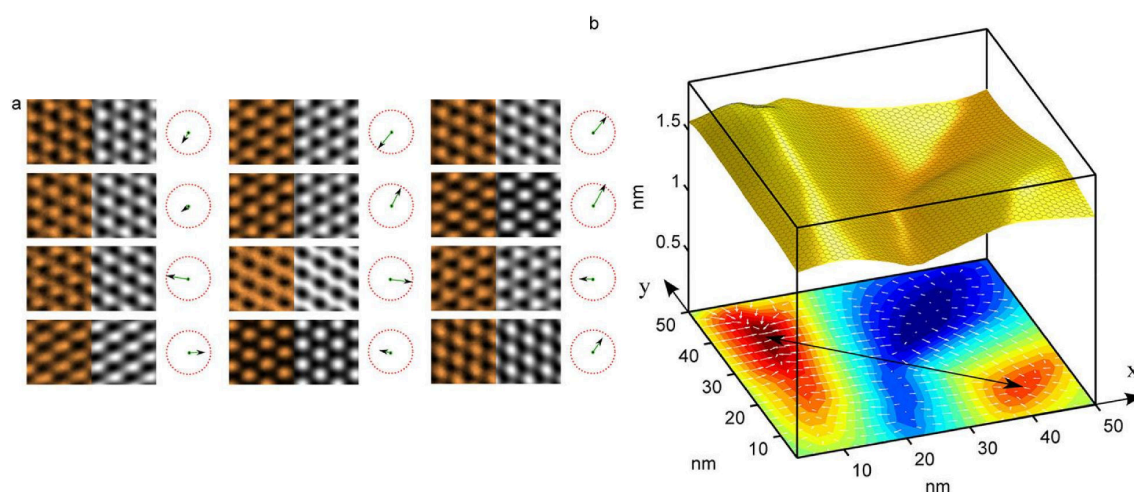


FIGURE C.I.3 – (a) Unfiltered experimental HRTEM image (orange) and simulated images (white) used to reconstruct the surface topography of few-layered graphene presented in (b). The arrows represent the tilt direction. Reprinted with permission from Wang et al. (2012c) . Copyright 2012 American Chemical Society.

TEM simulations are usually carried out using with an independent atomic model, assuming the potential to be the sum of individual atomic potentials. Here, Wang et al. simulated the images using density functional theory (DFT) calculations (Soler et al., 2002). This method allows to accurately reproduce the projected total potential by modeling the bonding effects between atoms. In order to simulate such images, the lenses aberrations must be perfectly known to have a correct quantification of the tilt. For this ripples study, Wang et al. did not give the uncertainties of the aberration measurement although it is a crucial point and their effect on the HR-TEM image. In section C.I.1.4, the effect of aberration will be discussed.

It is also important to note that their study has been done for few-layered graphene only (around 10 layers). Here the obtained local tilt was about  $7^\circ$ . The tilt of a mono-layer graphene does not have such influence on the HR-TEM image. Figure C.I.4 gives filtered HR-TEM images of graphene for a  $0^\circ$ ,  $10^\circ$  and  $30^\circ$  tilt. No such contrast variation was observed for a tilt that was even higher than the maximum measured one in the case of Wang et al. study. For mono-layered

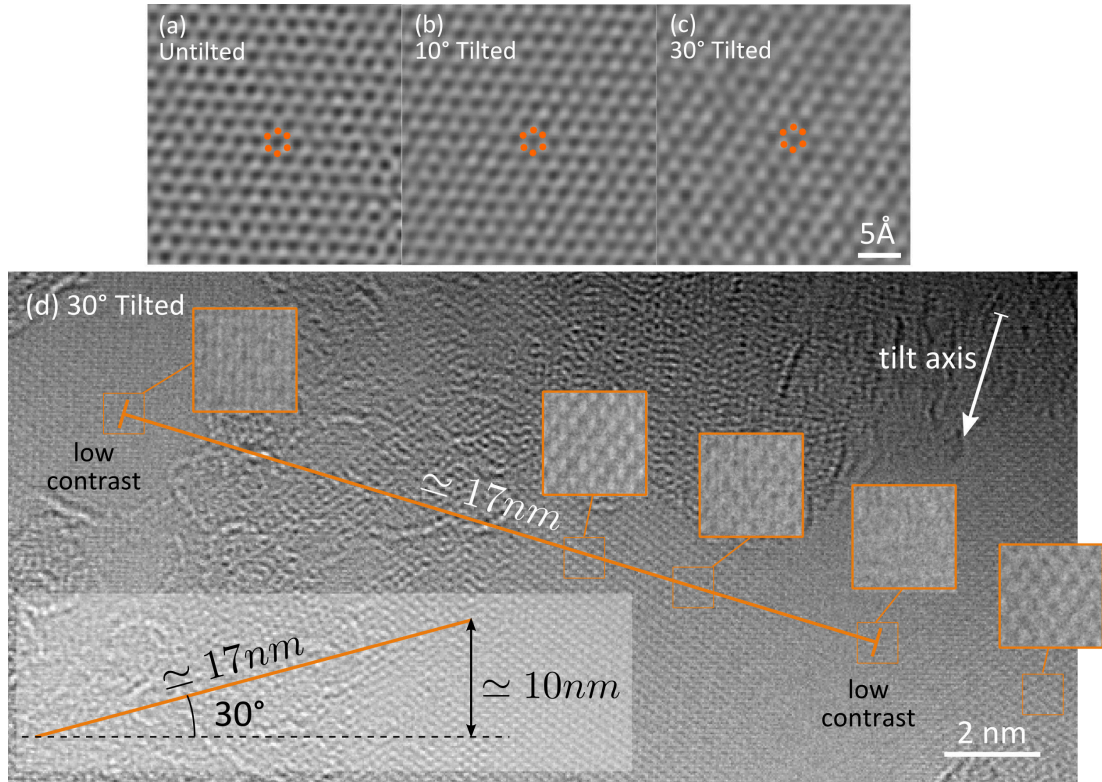


FIGURE C.I.4 – Filtered HR-TEM images of (a) untitled, (b) 10° tilted and (c) 30° tilted graphene mono-layer at 80kV. For single-layer graphene, the contrast variation induced by the tilt is far less important than in the “few-layered” case of Wang et al.. (d) HR-TEM image of 30° tilted graphene. Orange line represents the distance between zero contrast areas. The schematic drawing shows that these zero contrast areas are separated by about 10nm in the beam direction.

samples, it would be difficult to quantify small tilt variation (less than 10°) by studying the contrast of the image. In addition, the number of layers of the sample must be perfectly known to carry such simulations. Thickness measurement of few-layered samples will be discussed in chapter C.II.

Figure C.I.4 (d) shows a HR-TEM image of a 30° tilted graphene. On this image, one can see the variation of contrast from left to right due to the change in focus (the layer is not parallel to the beam axis). Knowing the tilt of the graphene layer (30°), the distance between two zero contrast areas gives the equivalent defocus between the zero contrast areas. This defocus is estimated to be 10nm which is coherent with the results of Figure C.I.1 where two zero contrast areas are separated by  $\Delta f = 11\text{nm}$ .

#### C.I.1.4 Influence of three-fold astigmatism, $A_2$

During this thesis, CVD grown graphene was observed in the last generation double-corrected and monochromated FEI Titan Ultimate. The aim of this section is to show the delicate inter-

pretation of TEM images. Figure C.I.5 shows a HR-TEM image of a mono-layer graphene grain boundary. The two graphene sheets are rotated by about  $30^\circ$ .

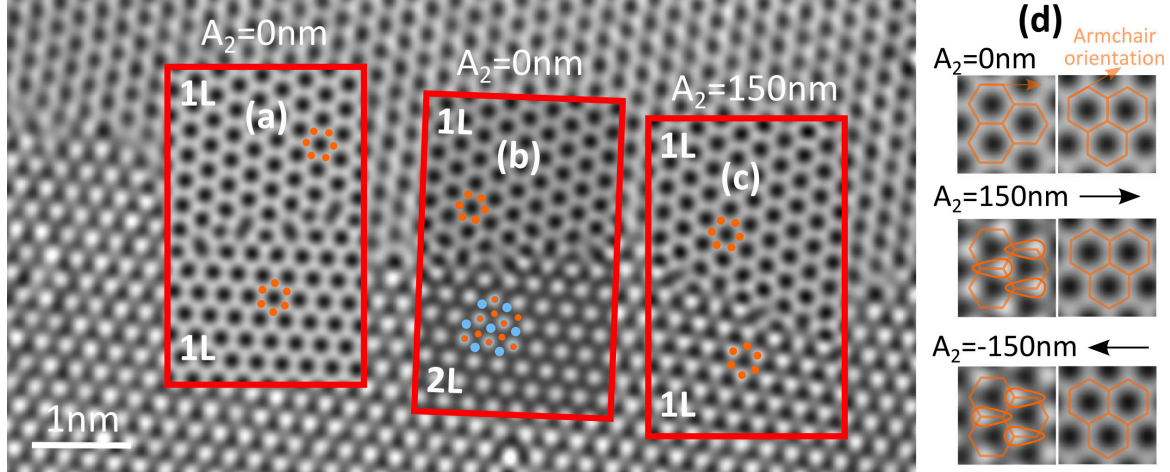


FIGURE C.I.5 – HR-TEM image of graphene grain boundary at 80kV. (a) Simulated single layer-graphene grain boundary,  $C_3 = 15\mu\text{m}$  and  $C_5 = 5\text{mm}$ ,  $defocus = 0\text{nm}$ , defocus spread 1.4nm, high tension 80kV. (b) Grain boundary between single- and bi-Layer graphene under the same conditions. (c) single-layer graphene with a 150nm three-fold astigmatism. (d) Influence of the lattice orientation and of the direction of  $A_2$  aberration.

Insets superimposed to this image are simulated with different aberration conditions and different number of layers. The simulations have been performed using Kirkland code (Kirkland, 2010). The  $C_s$  has been taken equals to  $15\mu\text{m}$ ,  $C_c$  to  $5\text{mm}$ , and other aberrations equals to zero except third inset where  $A_2$  is 150nm.

Figure C.I.5 (a) shows the simulated images of the grain boundary considering a monolayer at each side of the boundary. The contrast of the top part is close to the one of the experimental image, but on the bottom part, the contrast does not correspond to the simulated image anymore.

One could interpret the experimental contrast by the presence of AB stacking bi-layer graphene at the bottom part. Figure C.I.5 (b) is showing such case. The contrast given by the bi-layer graphene is in agreement with the experimental case. So a misleading interpretation of this image could conclude in a grain boundary between a mono-layered graphene and a bi-layered graphene.

In fact, on both side of the boundary, it is a single-layer graphene, but there was a residual  $A_2$  aberration. As shown in figure C.I.5 (d), when the the  $A_2$  aberration is in the direction of the C-C bonding (i.e. in the armchair direction), it induces a contrast modification and one of the two atoms of this bond appears with a stronger contrast leading to a triangular shaped contrast in the armchair direction. The contrast is not inverted, the atoms stays white in this case. Figure C.I.6 also shows an illustration of the  $A_2$  aberration effect on the HR-TEM contrast. A flower defect structure inside graphene appears with a  $30^\circ$  rotation. Depending on the orientation, either the graphene layer, either the flower appears with triangular shaped contrast along the armchair direction. This can induce misleading interpretation of the flower defect as its shape seems to be different, and as one could interpret that there is a contrast inversion and therefore a change in atom positions. Simulations of Figure C.I.6 shows that for every case (no three-

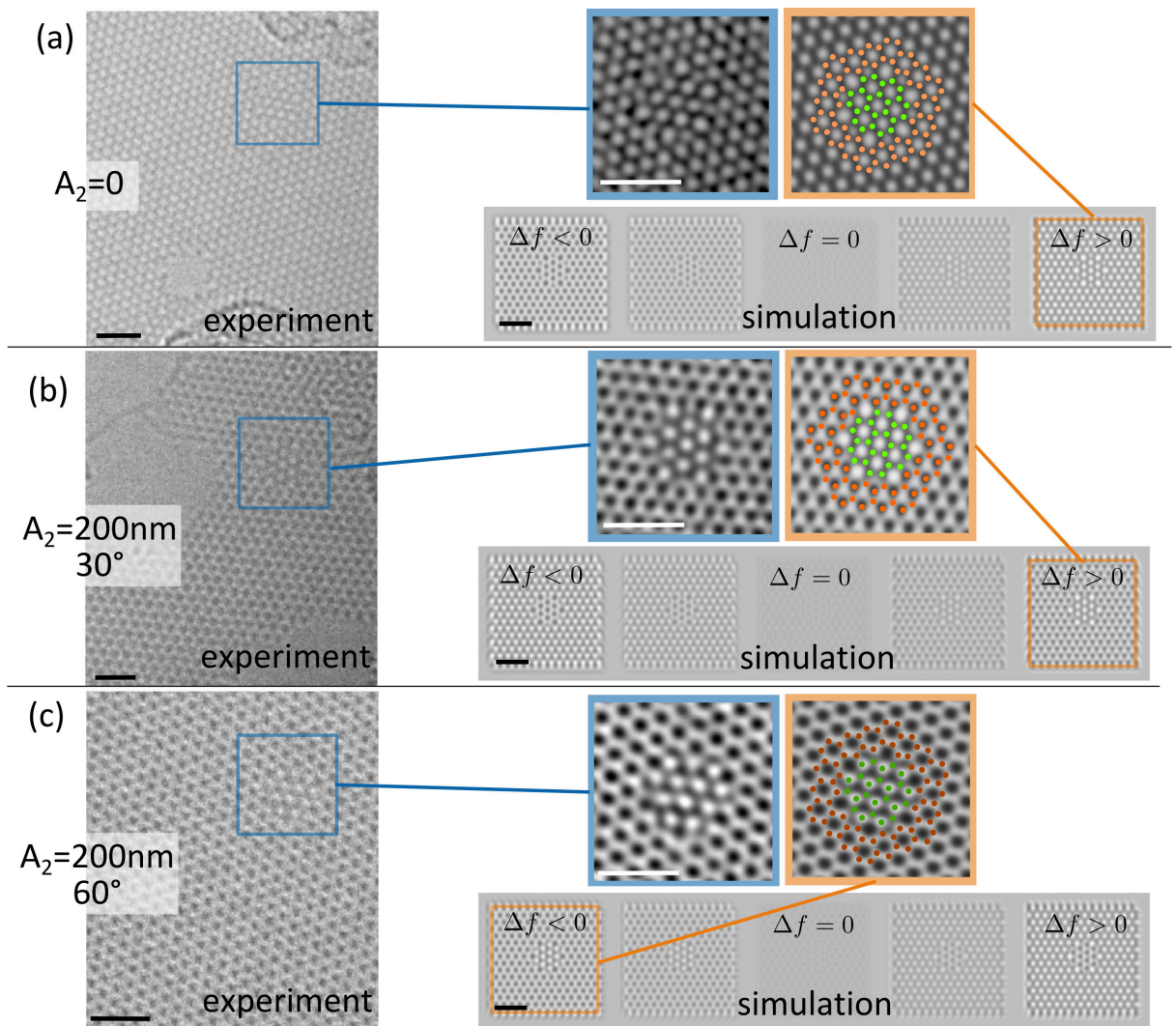


FIGURE C.I.6 – Experimental and simulated flower defect in graphene. Orange and green points showing atoms positions have been superposed to the simulation image, evidencing the effect of  $A_2$  aberration. (a) With no  $A_2$  astigmatism. On the experimental image, the atoms are black. (b) With  $A_2 = 200nm$  with an angle of  $30^\circ$ , the atoms outside the flower have black triangular shapes. (c) With  $A_2 = 200nm$  with an angle of  $60^\circ$ , the atoms inside the flower have a triangular shape. On this image, the defocus is changed and is negative, atoms are white. Simulation have been carried out using JEMS software(Stadelmann, 1987). Scale bars are 1nm.

fold astigmatism, 30° three-fold astigmatism, or 60° three-fold astigmatism) there is no contrast inversion: atoms are white for negative defocus and black for a positive defocus.

The value of 200nm measured for  $A_2$  may appear large, but when working in positive or negative  $C_s$  condition, the uncertainty given by the CEOS aberration corrector is around 100nm, therefore even by the use of aberration corrector, it is still difficult to precisely measure and control the three-fold astigmatism.

Controlling the  $A_2$  astigmatism is therefore necessary in order to be able to determine the atomic position in a HR-TEM image. If this aberration is not known, HR-TEM images can be misinterpreted. Here, the presence of grain boundaries allowed us to see the different contrast depending on graphene orientation, but on perfect graphene with only one orientation, the presence of  $A_2$  astigmatism can lead to errors in the interpretation of the contrast (black of white atoms).

## C.I.2 Tilt/orientation study of few-layered material using electron diffraction

The motivations of this section are to better understand the physics behind two-dimensional crystal diffraction. The understanding of the diffraction will allow to characterize the layer orientation by looking at the diffraction spots position.

As stated in Section A.III.2 of Chapter A.III, the diffraction physics can be represented in the reciprocal space by relrods. These relrods comes from the three-dimensional Fourier Transform of the atoms positions. As the specimen is large in the plane perpendicular to the sample normal, and thin (atomically thin in the case of graphene) in the sample normal direction, they are shaped like rods with the long direction parallel to the surface normal.

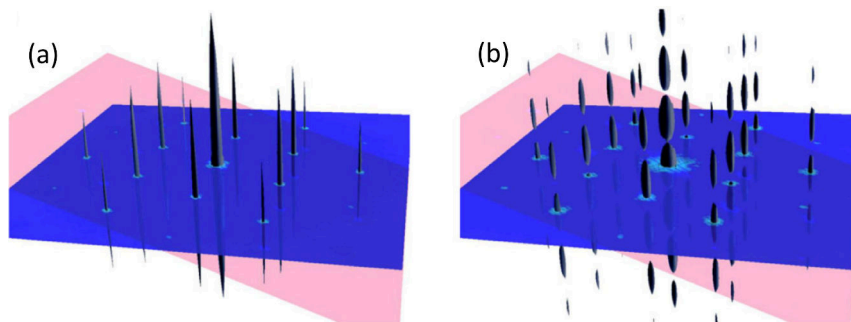


FIGURE C.I.7 – Illustration of the reciprocal space of single- and double-layer graphene. (a) For single-layer graphene, intensities in reciprocal space are continuous relrods (b) For two-layer graphene, the intensity along the relrods is discontinuous. Figure printed from Meyer et al. (2007) with permissions.

Electron diffraction of two-dimensional materials is very specific compared to the diffraction of bulk materials. Indeed, the Fourier transform of bulk materials give discontinuous relrod, relatively short. HOLZ lines in CBED patterns presented in Part II illustrate these oscillations of the relrod. In bulk materials, when the sample is tilted, the intensity of a spot quickly vanishes

because of the short relrods. On the contrary, the relrods of few-layered material being much more elongated, a tilt, even important will not have much effect on the spot diffracted intensity.

Figure C.I.7 gives an illustration of relrods for two cases: single-layer graphene and bi-layers graphene. In the case of bi-layers graphene, the relrods are still discontinuous and the diffraction spots are vanishing at certain angles. In the case of mono-layered graphene, the relrods are continuous, and therefore the intensities of diffraction spots vary only weakly with the tilt angle.

The strength of studying diffraction is that there is no need to interpret the HR-TEM image contrast and the risk of error is reduced. For example it is very easy to determine if the graphene is mono-layer or bi-layer (Meyer et al., 2007), whereas using image the contrast can be misleading. Using diffraction it is also possible to study the sample tilt orientation by looking at the spot positions and diffraction effects.

### C.I.2.1 Projection effect in diffraction

Diffraction spots are often thought as a perfect representation of the reciprocal lattice. But in electron microscopy the spot distance to the transmitted beam does not always represent the Bragg angle, due to the excitation error (see Chapter A.III). The excitation error always expressed along the surface normal direction induces a hereafter called “projection effect”.

This projection effect has been observed experimentally on a perfect graphene sheet. The diffractions were taken in TEM mode with a slightly convergent beam. The illuminated area was large, about one micrometer, and make of only one graphene grain (i.e. one unique crystalline direction). Figure C.I.9 gives a TEM image of the sample, showing the illuminated area used for taking the diffraction of the tilted sample.

As given by equation A.III.12, the projection effect can be approximated by the following expression:

$$g_{eff} \approx \frac{g}{\cos(\phi_{tilt})} \quad (C.I.1)$$

The previous formula only states for a diffraction vector that is perpendicular to the tilt axis. If the tilt axis is in any other direction, the effect of the projection will be less important. If  $\mathbf{u}_\perp$  is the projection equation is expressed by:

$$g_{eff} \approx g + \frac{|\mathbf{g} \cdot \mathbf{u}_\perp|}{\cos(\phi_{tilt})} \quad (C.I.2)$$

The projection factor (i.e. the stretching factor of the spot distance to the diffraction center) is simply given by :

$$P_\phi(\mathbf{g}) = \frac{g_{eff}}{g} \approx 1 + \frac{|\mathbf{g} \cdot \mathbf{u}_\perp|}{\cos(\phi_{tilt}) |\mathbf{g}|} \quad (C.I.3)$$

Figure C.I.8 (a) gives a superposition of two diffraction, a diffraction from an untilted sample, and a diffraction from a 36° tilted sample. One can see that for spots that are perpendicular to the tilt axis, the displacement is important and the spot is more diffuse (the broadening of the spot is explained in the next section). On the contrary, the spots that are close to the tilt axis are only fewly affected by the tilt. Figure C.I.8 (b) and (c) give the analysis of the distances between

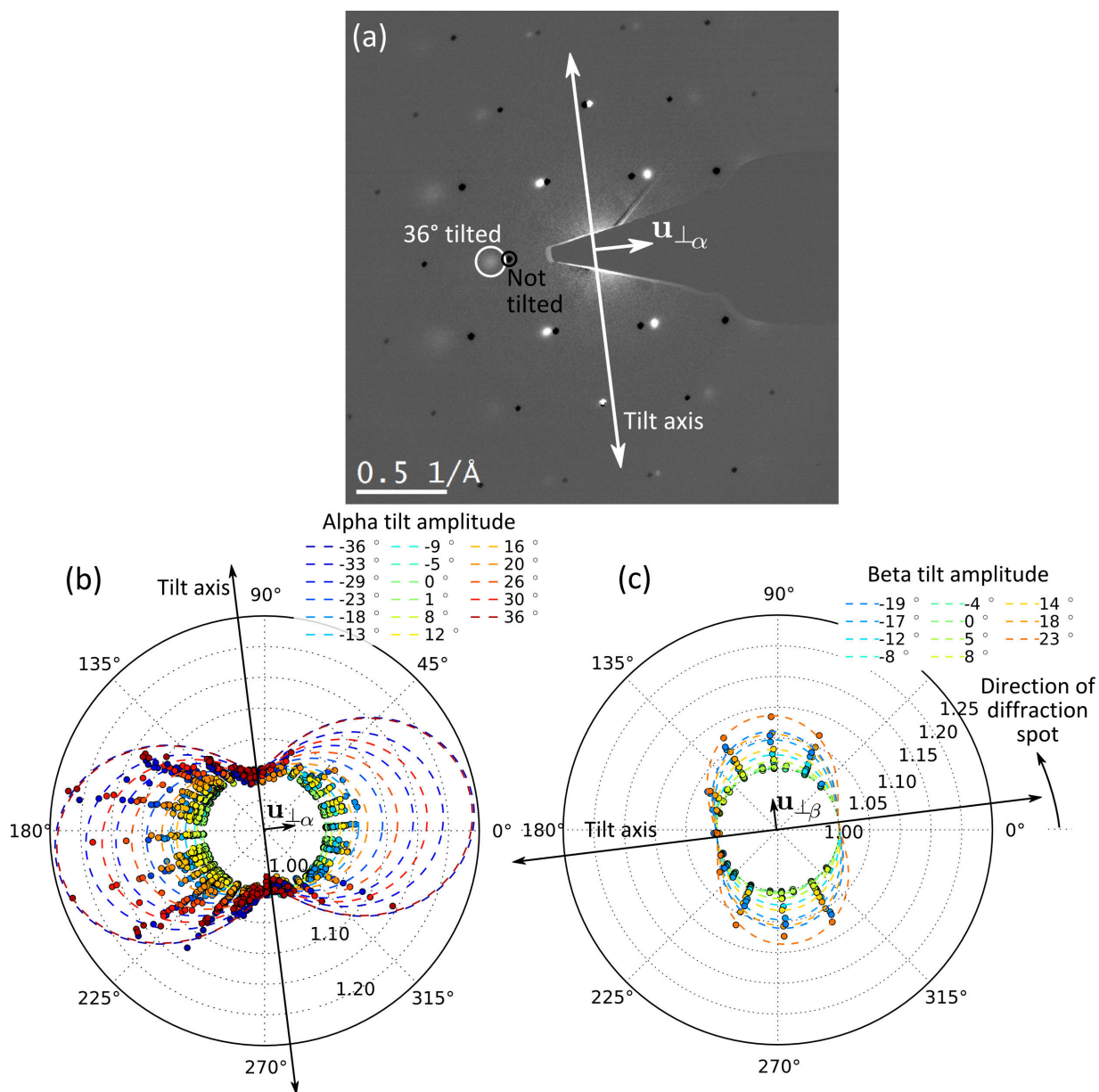


FIGURE C.I.8 – Measurement of the projection effect in graphene. (a) Difference between a 36° tilted and an untilted graphene diffraction. (b)(c) Polar representation of the projection factor as given in equation C.I.3 by tilting using the (b) alpha (c) beta axis. The experimental projection factor is given by colored dots and the theoretical one is given in dashed lines. The projection is visible for the spots having a component perpendicular to the tilt axis. The spots lying on the tilt axis does not move.

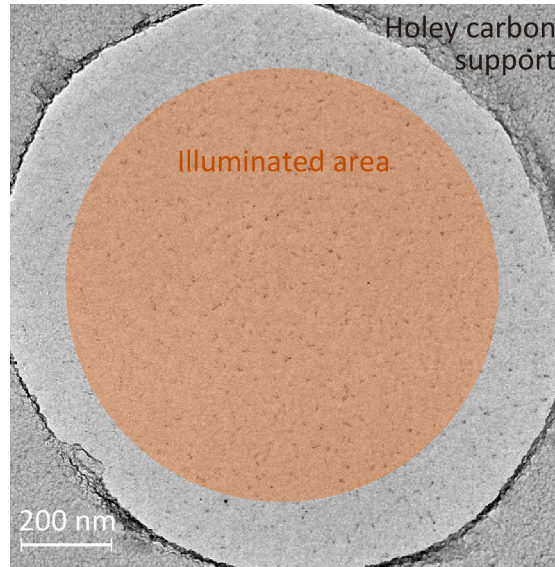


FIGURE C.I.9 – TEM image of the sample used to evidence the projection effect. Observed sample is made from free standing graphene sheet of one unique grain grown by CVD.

diffraction spots for different tilting angle and two different tilt axes. The two tilt axes ( $\alpha$  and  $\beta$ ) are perpendicular to each other. The experimental projection factor is given by colored dots and the theoretical one is given in dashed lines. In all the diffraction, the spots that are perpendicular to the tilt axis keeps a projection factor of 1, whereas the other follows the projection formula given in equation C.I.2.

This behavior of diffraction spot when tilting few-layered sample, despite being simple, is quite puzzling. The sample itself does not change, the spaces between atoms and the reciprocal space vectors does not change, but the diffraction spots moves and their distance to the center increases. One have to be careful not to interpret this projection as a compressive strain, there is not strain in the sample in this case. This phenomena make difficult the measurement of strain in few-layered samples because strain and rotation could have the same effect on spot positions.

### C.I.2.2 Graphene ripples study by TEM diffraction

On figure C.I.8 (a), the spots that have a component perpendicular to the tilt axis are broadened. By strictly following the theory given in Chapter A.III, the diffraction spot size should not increase when the sample is tilted. This broadening has first been observed by Meyer et al. (2007).

Figure C.I.10 (a) gives the broadening of a spot perpendicular to the tilt axis. Figure C.I.10 (b) and (c) is a schematic drawing of the reciprocal space showing the diffracted vectors for a flat and a rough sample. When the sample is flat, the relrod is continuous and thin, when tilting the sample, the part of the relrod that is probed is further (the excitation error is larger), but as the relrod is thin, this tilt does not increase the spot size. When the sample is rough, there is numerous surface normal at different places of the sample. These different normals will induce

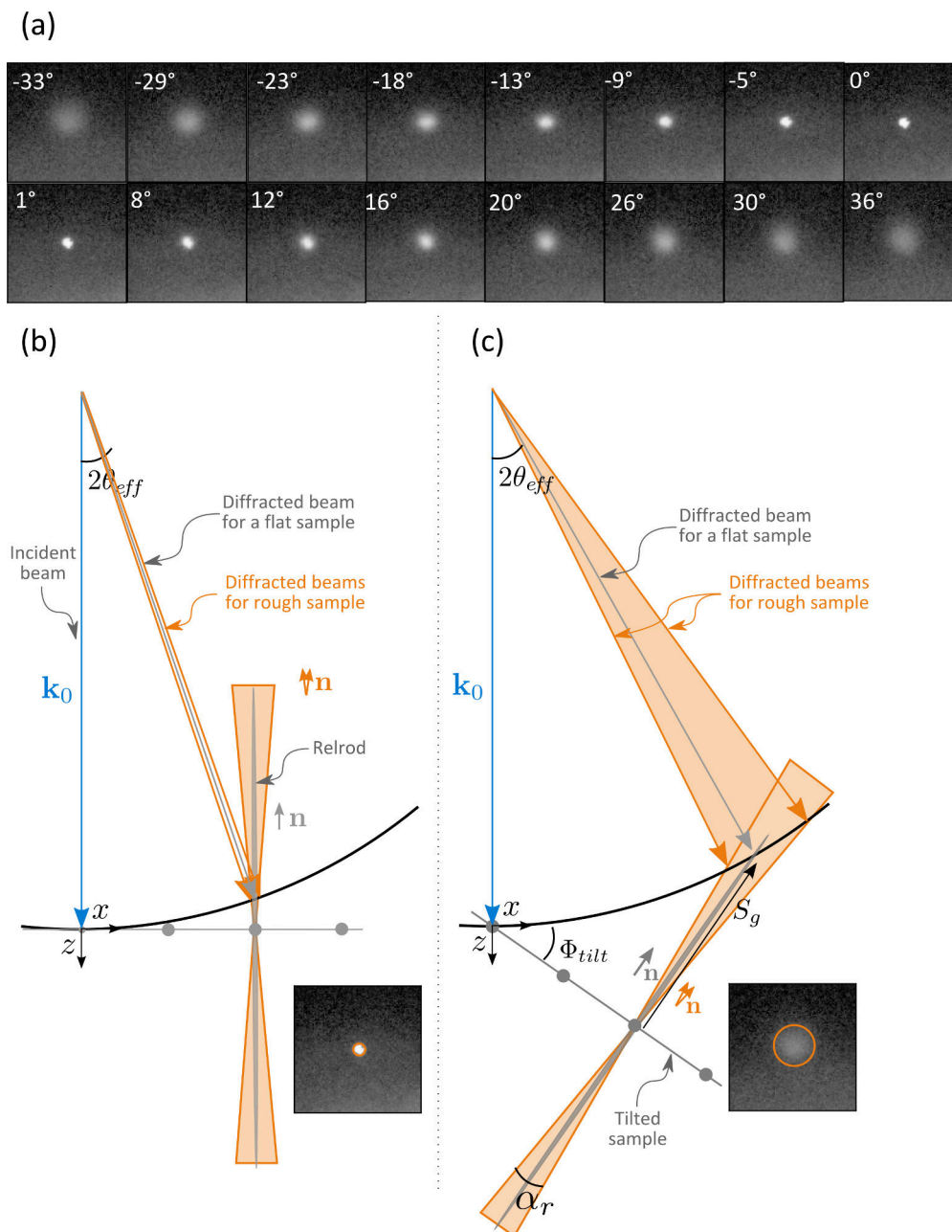


FIGURE C.I.10 – (a) Experimental broadening with tilt amplitude of a diffraction spot perpendicular to the tilt axis. (b) Reciprocal space drawing of diffracted beam for an untilted specimen. The roughness of the sample has a small influence on the spot diameter. (c) Same drawing with a tilted sample. The broadening of the spot is much more important because the excitation error is bigger.

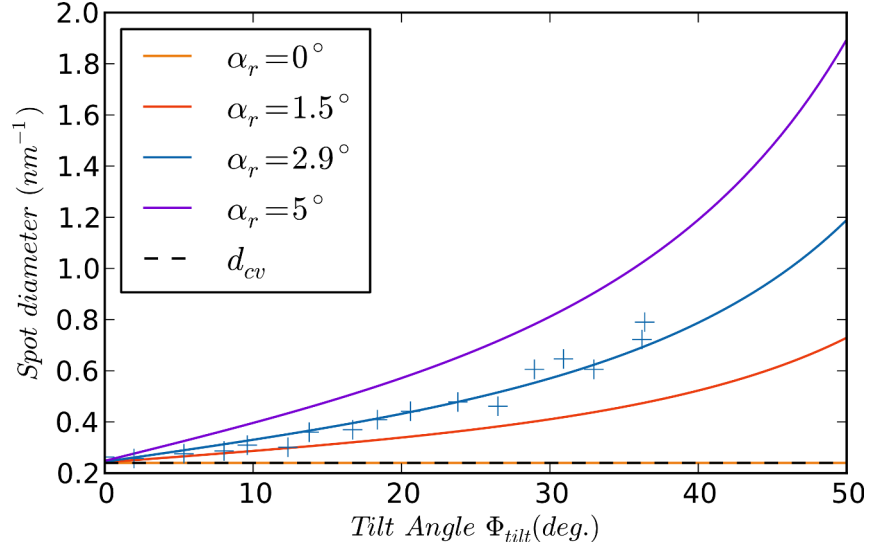


FIGURE C.I.11 – Broadening of the (100) graphene diffraction spot with sample tilt as a function of the sample roughness. The blue crosses are experimental FWHM of the (100) diffraction spot perpendicular to the tilt axis.

different directions in the relrods. When the sample is not tilted, these different directions fewly influence the spot diameter, because the excitation error is small, but when the sample is tilted, the relrods are well separated and lead to diffraction vector that are different and then to a broadening of the spot.

To quantify the broadening of the diffraction spots it is necessary to go back to the equations A.III.7 and A.III.9. What is interesting in this case is the intersection point of the Ewald sphere and the different relrods. If  $\alpha_r$  is the roughness of the sample (the maximum angle between surface normals) then the extremum relrods equation is of the following form:

$$z - g \sin(\phi_{tilt}) = \tan\left(\frac{\pi}{2} - \phi_{tilt} \pm \frac{\alpha_r}{2}\right) (x - g \cos(\phi_{tilt})) \quad (\text{C.I.4})$$

The intersection points with the Ewald sphere defined by equation A.III.7 are calculated numerically and the corresponding  $g_{eff}^{-\alpha_r/2}$  and  $g_{eff}^{+\alpha_r/2}$  are calculated. The spot diameter is given as the difference between the two extreme effective diffraction vectors:

$$d_{spot} = \left| g_{eff}^{-\alpha_r/2} - g_{eff}^{+\alpha_r/2} \right| + d_{cv}$$

where  $d_{cv}$  is the diameter of the spot due to the convergence of the beam.

Figure C.I.11 gives the result of simulated spot diameter for different tilt angle and sample roughness. The experimental diffraction spot FWHM are also plotted. Using the above formula, we can see that the spot broadening is not linear with the tilt angle.

The retrieved value of the specimen roughness is  $2.9^\circ$ . If the distribution of surface normal orientations is Gaussian, as the FWHM was taken as the spot diameter, this roughness value is also a FWHM value of the roughness. This result is close to the one claimed by Meyer et al.,

### C.I.2.3. Orientation study of MoS<sub>2</sub> by nano-diffraction

which was 5°. Meyer et al. nevertheless did not explain how they end up with such value, and only drew a linear fit of the spot broadening.

The presented method to determine the roughness of a mono-layer is quite easy to set-up and does not need an aberration corrected microscope as the illuminated area is on the order of the micrometer. Nevertheless no local information on the sample oscillation could be retrieved from this study. It is only a statistical analysis of the sample oscillation under the wide electron beam. To obtain local information on the sample tilt, it is necessary to take local diffractions, and this is done in the next section on a few-layered MoS<sub>2</sub>.

### C.I.2.3 Orientation study of MoS<sub>2</sub> by nano-diffraction

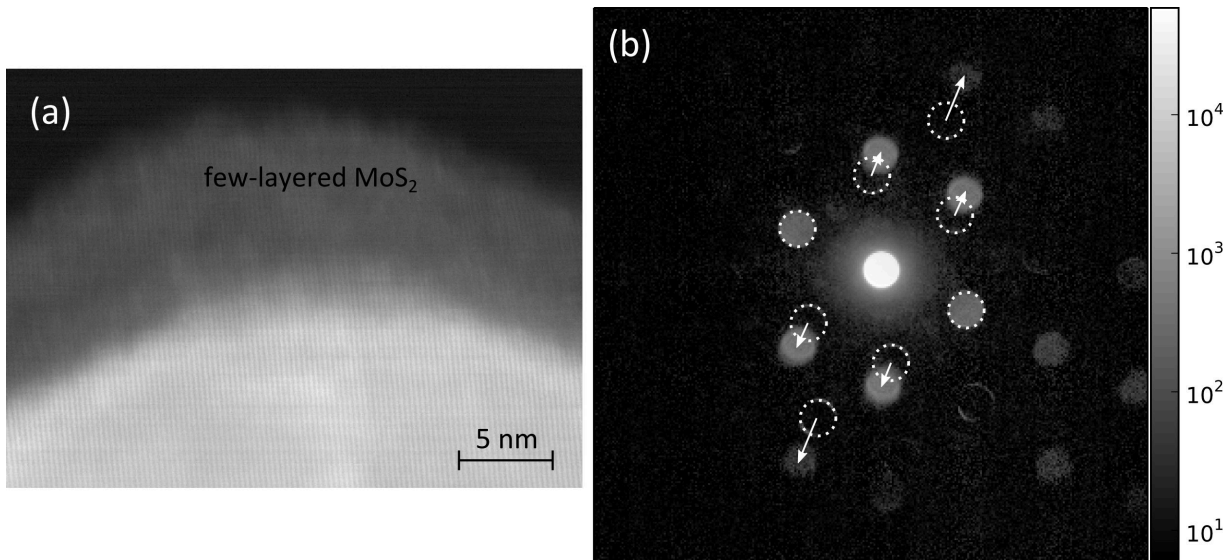


FIGURE C.I.12 – (a) STEM image of the few-layered MoS<sub>2</sub> attached to a thicker zone, (b) One diffraction coming from the MoS<sub>2</sub> thin layer showing the stretching of the diffraction. Dotted circles correspond to the spot positions in the thick zone.

Local ripple study of mechanically exfoliated MoS<sub>2</sub> has been done using nanobeam electron diffraction. It has been done in STEM mode and nanodiffractions were taken by using a small 10  $\mu\text{m}$  C2 aperture. Figure C.I.12 shows the STEM image and one typical diffraction coming from the few-layered area. The diffraction is clearly stretched compared to the diffraction in the bulk MoS<sub>2</sub>, meaning that there is either a tilt of the sample, either a strain, either both of it. In the following, we will quantify the tilt of the thin layer considering that the main contribution to the spot displacement comes from tilt (i.e. the sample is relaxed by tilting, which is the most probable case).

To study the displacement of the spots, we used a template matching algorithm similar to the one presented in Chapter B.II using the OpenCV library (Bradski, 2000). The template was an average of 25 vacuum transmitted spot, meaning a nearly perfect disk (Figure C.I.13). The cross-correlation function was then treated in python to detect maxima. The maxima positions

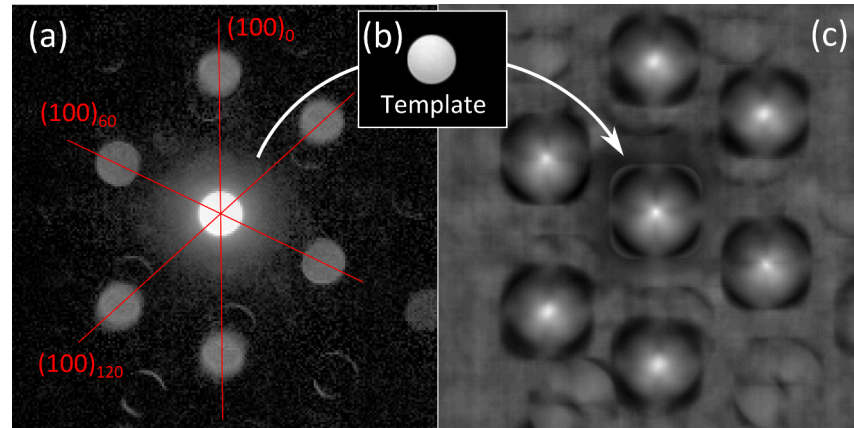


FIGURE C.I.13 – Template matching to determine the spot positions. (a) Original diffraction (b) Template is made of 25 average transmitted spot in the vacuum (c) Resulting cross correlation function.  $(100)_{0,60,120}$  shows the two equivalent  $(100)$  spots in the same direction.

of the  $(100)$  spots were detected with a sub-pixel precision by using the center of mass around the maxima. The maxima positions were compared to the position of the bulk sample and a stretching coefficient is extracted. The stretching coefficients of the distance of the spot to the transmitted beam are relative to the one of the bulk. This stretching coefficients are plotted in figure C.I.14 (a).

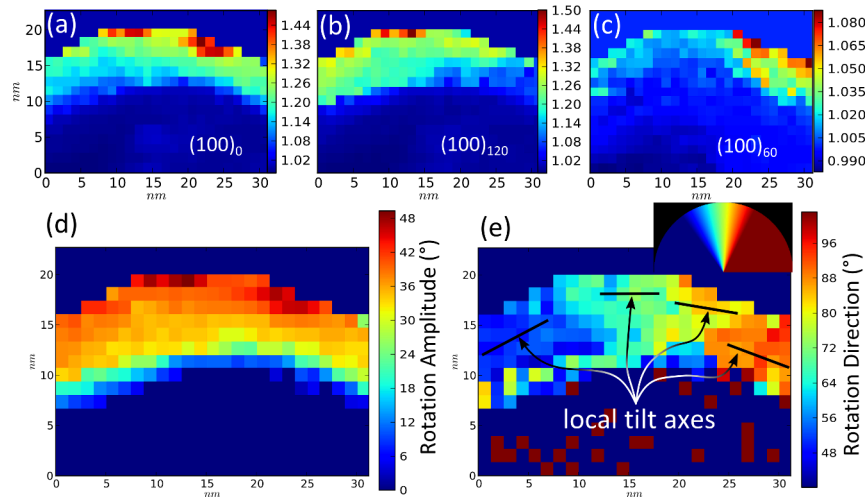


FIGURE C.I.14 – Average stretching coefficient of the (a)  $(100)_0$ , (b)  $(100)_{60}$ , (c)  $(100)_{120}$  spots in  $\text{MoS}_2$ , as defined in figure C.I.13. The spots does not move in the bulk, there is no rotation, but in the few-layered  $\text{MoS}_2$ , the stretching of  $(100)_0$  and  $(100)_{120}$  spots can reach 150% of the original distance. (d)(e) Retrieval from the stretching coefficients of (d) the tilt amplitude and (e) the tilt direction. The tilt direction is defined as perpendicular to the tilt axis.

The stretching of the (100)<sub>0</sub> and (100)<sub>120</sub> spots can reach 1.5 times the original distance. The (100)<sub>60</sub> spots are nearly not affected, except in the top-right corner of the sample, where the stretching can reach 1.08. This stretching of the spots has then been analyzed in term of rotation of the sample. The rotation is defined by two parameters: the rotation direction and the amplitude of the rotation. To retrieve these two parameter from the stretching coefficients, an minimization algorithm have been made in python using the projection formula given in equation A.III.12 (Appendix B).

The results of the minimization are given in figure C.I.14 (d) and (e). There is no visible rotation on the bulk (although the method is not sensitive to few degrees rotations) and the rotation of the few-layered MoS<sub>2</sub> is progressive from the bulk to the vacuum. It can reach more than 45° at the free surface. The tilt direction is given in figure C.I.14 (e). One can see that the tilt axis is parallel to the sample borders.

This local analysis of the orientation can only be done on few-layered materials. Indeed, for bulk materials, the relrods are too short, and the diffraction spots are not visible when the sample is rotated. For example, the few-layered MoS<sub>2</sub> studied here allowed the diffraction spots to stay visible with a 45° rotation. This technique is a powerful method to quantify the rotation of layers in two-dimensional materials.

## Discussion

In this chapter, we have seen that the HR-TEM contrast of few-layered graphene is delicate to interpret. The contrast depends on the number of layers, on the defocus, on aberrations such as third-order spherical aberration ( $C_s$ ) or three-fold astigmatism ( $A_2$ ), or even on the sample orientation. This complex image formation often requires the comparison of the experimental observation with simulations. Even by comparing with simulation, there still can be some ambiguities, for example to differentiate a single-layer graphene from a bi-layer one. And the image aberrations could lead to incorrect interpretation of the HR-TEM contrast. Nevertheless when the HR-TEM contrast is understood, the simulations will allow in many cases the determination of the atomic positions from the HR-TEM images. These atomic positions can then be used to understand the formation of defects, grain boundaries, vacancies or to study the doping of graphene.

Using diffraction, we have seen that it is possible to study the tilt or orientation of a specimen by using the projection effect. Due to the long relrod in the reciprocal space of single-layered materials, the same diffracted planes are kept when tilting the sample. When tilting, the reciprocal lattice distance does not move but the angular direction of the effective diffraction vector increases. As the HR-TEM image is formed by interference between these diffracted vectors, the image is also affected by the projection. Figure C.I.15 shows an experimental HR-TEM image and the analysis of the projected graphene lattice for a tilted and a non tilted specimen. The HR-TEM image shows exactly the same projection behavior as the diffraction, and the projected distances between atoms are decreased when tilting the sample. It could therefore be possible to study the oscillations of graphene by looking at the projected lattice, but the sensitivity of such technique would be low, of the order of 10°.

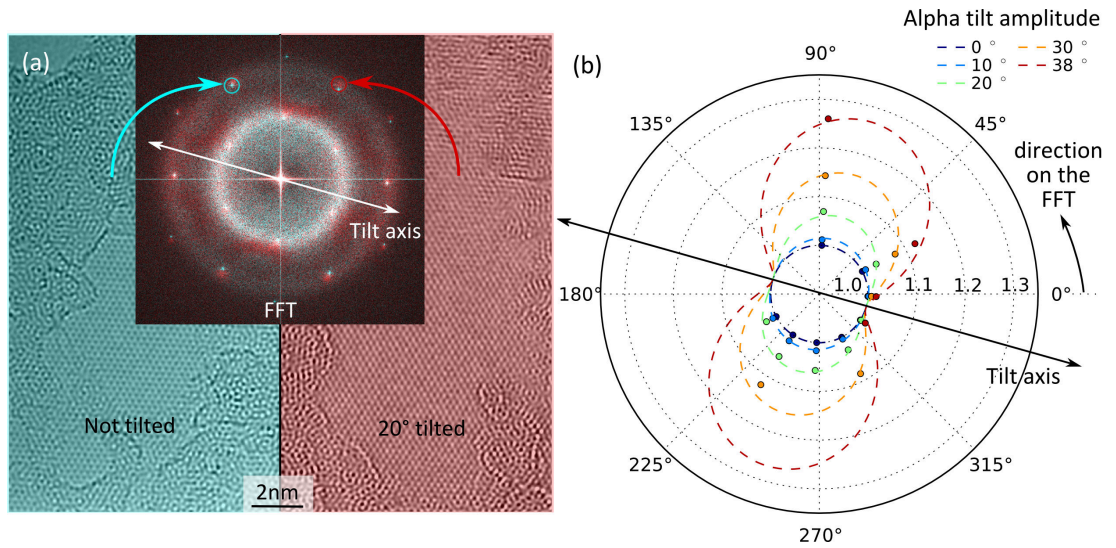


FIGURE C.I.15 – (a) Effect of the alpha tilt on a HR-TEM image of graphene. Untilted graphene is shown in blue, 20° tilted in red. The FFT is a superposition of unilted and 20° tilted FFT. Due to projection effects, the FFT spots are further in tilted graphene. (b) Projection factor for series of tilts. The FFT spot perpendicular to the tilt axis move away whereas the ones parallel to the tilt axis stays in the same place.

Moreover, it is difficult to make the difference between strain and rotation when dealing with two-dimensional samples. Indeed, for both diffractions and HR-TEM images, the rotation has the same effect as a compressive strain in the direction perpendicular to the tilt axis. Both rotation and compressive strain will reduce the distances between atoms and increase the diffraction vectors norms. Hence, when analyzing strain in an HR-TEM image of a two-dimensional material, one has to be sure that there is no orientation change in the sample.

To increase the sensitivity of roughness measurement, one could imagine tilting the sample and doing local diffraction. Because the excitation error  $S_g$  will be large and a small variation of the surface normal would induce a quite important spot movement. It could then be possible to measure the local sample orientation quite precisely. Difficulties of such an experiment could be the low intensity of diffraction spots in NBED due to the low scattering amplitude of graphene.



---

## Thickness measurement of few-layered molybdenum disulfide and boron nitride

---

Accurate measurement of the sample thickness is critical for many applications in TEM. For example, quantitative comparison between experiment and image simulation needs a precise determination of the thickness.

Chapter B.I discuss sample thickness measurement using CBED, this is an accurate method for determining the thickness of thick specimens (over 50nm). But for two-dimensional materials, this method is not suitable because HOLZ lines oscillations become larger when the thickness decreases. The electron energy loss spectroscopy (EELS) log-ratio method presented in Chapter B.I (Egerton, 1986) is also a very applied method, and it can determine the thickness with a precision of  $\pm 10\%$  (Ecob, 1986). But for thin samples (<20nm) surface plasmons decreases the accuracy of the method (Egerton, 1986), unless the bulk- and surface-losses are separated (Mkhoyan et al., 2007). This correction of surface effect can be as large as 30nm in some material (LeBeau et al., 2008), limiting the precision of the measurement for few-layered materials.

The thickness of two-dimensional materials is often less than 10 atomic layers, i.e. less than 10 nm. That is why, in this chapter, the thickness will be not be given in nanometers but in number of atomic layers. Among thickness measurement techniques, two of them are suitable for measuring such very thin samples : PACBED and Quantitative STEM. These methods are described in the experimental techniques chapter A.I and are applied to MoS<sub>2</sub> and BN samples. We also introduce another thickness measurement method, similar to PACBED, but using a less convergent electron probe, we called it Quantitative Nanobeam Diffraction.

This chapter will discuss these thickness measurement methods and compare them together applying them to few-layered exfoliated molybdenum disulfide and boron nitride. To perform these analysis, extensive use of multislice simulations and data analysis have been realized. For the multislice simulation of diffraction, the free software from Kirkland (2010) has been used. For the data analysis, homemade scripts in python were written (see Appendix B).

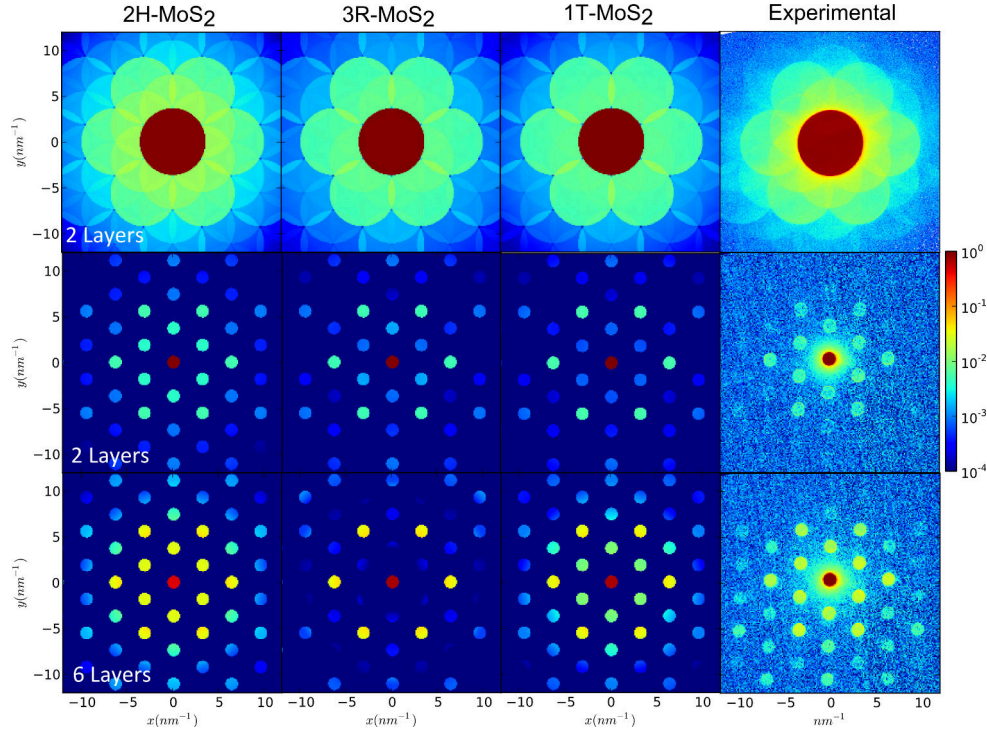


FIGURE C.II.1 – Determination of  $\text{MoS}_2$  crystal structure from PACBED and NBED diffraction patterns. On the left, simulation of bi-layer MoS carried out using Kirkland (2010) code. On the right, experimental diffraction taken at 80kV, on a FEI Titan Ultimate, using a 125msec integration time. Convergence angle is 2.9 mrad for nanobeam and 14.9 mrad for PACBED. Color scale is logarithmic.

### C.II.1 Comparison of measurement methods on few-layered $\text{MoS}_2$

For all the techniques (PACBED, Quantitative STEM, and Quantitative Nanobeam Diffraction), the intensity signal is not linear compared to the sample thickness. This is due to dynamic electron diffraction (Rosenauer et al., 2009) and it is therefore necessary to compare experimental results with simulations.

LeBeau and Stemmer (2008) have used an approach based on multislice frozen phonon model calculations (Loane et al., 1991), here we used the same calculation method based on Kirkland code (Kirkland, 2010). This code has been automatized in python (Appendix B) to simulate several thicknesses and illumination conditions. In order to quantify the thermal motion of atoms, the Debye-Waller factors have been taken from Gao and Peng (1999). LeBeau and Stemmer (2008) shows an agreement of the frozen phonon calculation with the Bloch waves matrix method for thin specimens (under 20nm), so Bloch waves could also be used to simulate the electron diffraction.

The frozen phonon approximation assumes that there is no movement of the atom when the electron goes through the sample. The traveling time of the electron in the specimen being much smaller than the thermal oscillation period of the atoms, this approximation is close to the reality

and an incoherent average of 10 configurations have been taken here to simulate the different diffractions.

### C.II.1.1 Determination of the crystal structure

Before any attempt of measuring the thickness of the sample, it is necessary to know the crystal structure of the sample. The crystal structure will indeed influence the intensities of diffraction spots. For determining the stacking order, 2H- $\text{MoS}_2$ , 3R- $\text{MoS}_2$ , and 1T- $\text{MoS}_2$  have been simulated. The crystal structures of the few-layered  $\text{MoS}_2$  were built using Vesta software (Momma and Izumi, 2011), the crystal data have been taken from the American Mineralogist Structure Database (AMCSD) for 2H- and 3R- $\text{MoS}_2$ . For 1T- $\text{MoS}_2$ , the structure has been built in Vesta from the description given in Lin et al. (2014).

Figure C.II.1 gives the results of these simulations. In order to compare PACBED and nanobeam diffraction techniques, the simulations have been carried out for two different convergence angles: 2.9 mrad and 14.9 mrad.

In simulated patterns, we can see that in 2H- $\text{MoS}_2$ , the first spot of the diffraction pattern (100) is as intense as the second spot (110). In 3R and 1T structures, the first spot is much weaker. This is both visible in PACBED and nano-beam patterns but it is clearly easier to see in nano-beam diffraction patterns.

By comparing to the experimental pattern taken in the same conditions, we can say that the exfoliated  $\text{MoS}_2$  we are studying is a 2H -  $\text{MoS}_2$ , which is the most stable crystal structure for  $\text{MoS}_2$ .

### C.II.1.2 Quantitative STEM

#### C.II.1.2.1 Experimental data

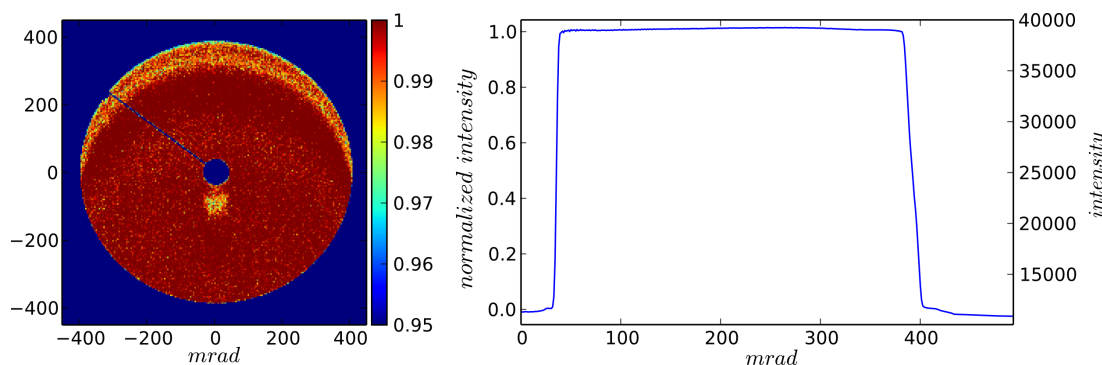


FIGURE C.II.2 – (a) Normalized sensitivity of FEI Titan Ultimate DF2 detector. (b) Rotational average of the normalized detector intensity. The scale in mrad corresponds to a camera length of 0.5m.

Quantitative STEM method has been applied to mechanically exfoliated 2H- $\text{MoS}_2$  in order to measure the thickness of the crystal near the edge of an exfoliated sheet. The FEI Titan

Ultimate at 80kV with the DF2 detector was used. Figure C.II.2 shows the image of the detector scan, normalized to the mean intensity. This detector scan has been rotational average to find the detector sensitivity as a function of the scattering angle. Here the vacuum intensity of the detector is close to 11000 and the intensity when the beam is on the detector is close to 40000.

The beam convergence angle is 14.9 mrad. The camera length has been chosen to be 500mm, and at this camera length, the shadow image radius is 20 mrad and the sensitive area of the detector starts from 36 mrad and ends at 390 mrad.

### C.II.1.2.2 Simulated data

The diffraction from large convergence angle beams are highly dependent on the probe position in the unit cell, i.e. there is High Resolution in the STEM images. This high resolution complicates the quantitative analysis, because it depends on the probe aberrations. Therefore the simulated diffractions have been averaged on one unit cell in order to measure the thickness of the sample. This is strictly equivalent to the PACBED approach. The experimental data have also been averaged to remove the atomic resolution contrast.

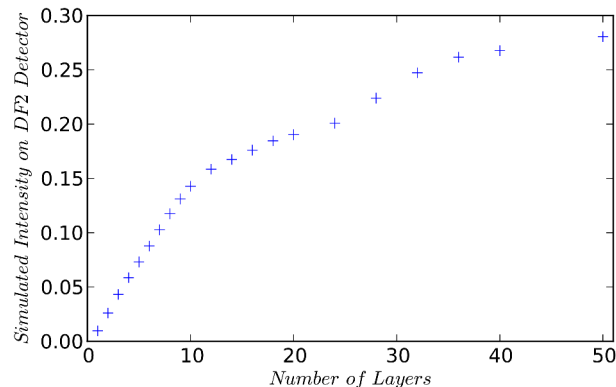


FIGURE C.II.3 – Simulated normalized intensity on the DF2 detector of few-layered 2H-MoS<sub>2</sub>. For this simulation, the inner radius on the detector is 36 mrad and the outer one is 300 mrad.

Simulations of 2H-MoS<sub>2</sub> diffraction have been done for several layers: every layer from 1 to 10 layers, every two layers from 10 to 26, and every four layers from 26 to 50 layers. Figure C.II.3 give the normalized intensity on the detector as a function of the number of layers. This figure was obtained by multiplying the simulated diffraction by the detector sensitivity given in figure C.II.2.

The outer detector radius for the simulation has been taken to be 300 mrad, which is inferior to the experimental outer-radius of the DF2 (390mrad). Nevertheless, it has been tested that, for such thin specimens, taking a higher outer-radius (and therefore simulating with a better real-space resolution, i.e. increasing the simulation time) does not change the intensity on the detector. [LeBeau and Stemmer \(2008\)](#) took 240 mrad outer radius for simulation with 400 mrad experimental radius and draw the same conclusions.

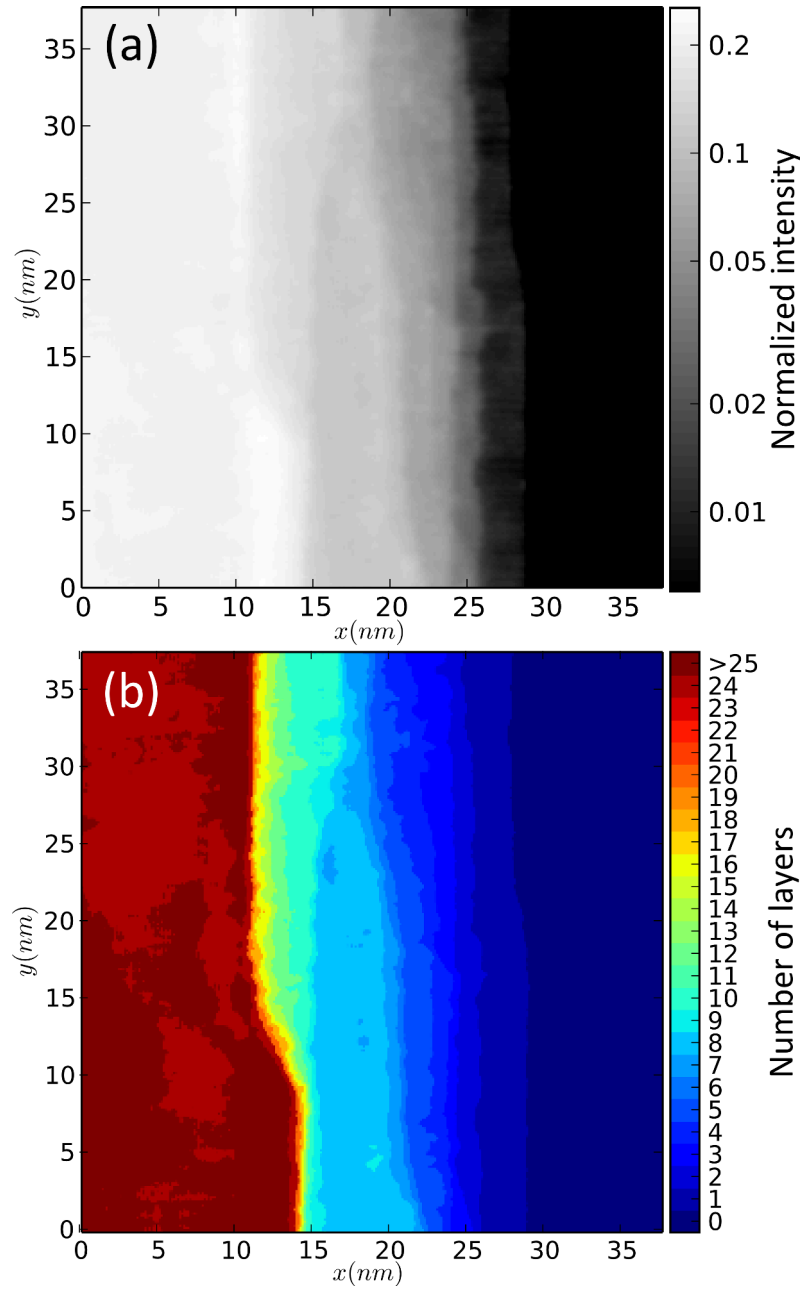


FIGURE C.II.4 – (a) Normalized DF2 HR-STEM image of exfoliated 2H-MoS<sub>2</sub> (b) Retrieved thickness, the atomic resolution have been averaged using a Gaussian blur of the size of the crystal cell.

### C.II.1.2.3 Thickness results

When combining the normalized experimental image with the simulated intensities given in figure C.II.3, the thickness of the sample can be retrieved. Figure C.II.4 shows the number of layer determination on the edge of an exfoliated MoS<sub>2</sub> sheet. It shows that quantitative STEM is sensitive to one layer of MoS<sub>2</sub> and can make a difference between vacuum, one layer, two layers, etc. To remove the atomic contrast appearing in the original STEM image of figure C.II.4, a Gaussian blur of the size of the crystal cell has been applied.

In order to be sensitive to the mono-layer, a particular attention has to be paid to the vacuum intensity of the detector. As described in Part I, the vacuum intensity ( $I_{vac}$ ) of the detector can be measured in two ways. The first one is to measure it on the detector scan and in this case, the measured intensity was  $I_{vac}^{DScan} = 10937$ . The other one is to measure it in the STEM image of vacuum, and the intensity was  $I_{vac}^{STEM} = 10977$ . The difference between the two intensities  $I_{vac}^{STEM} - I_{vac}^{DScan} = 40$  is to be compared to the STEM image noise in the vacuum. The standard deviation of the STEM signal in the vacuum is  $\Delta I_{vac} = 24$ . It is lower than the error made by measuring the vacuum intensity level on the detector scan. It is therefore better to use the vacuum intensity extracted from the STEM image, nevertheless in any case the measurement is precise enough to detect a mono-layer (with  $I_{mono}^{MoS_2} = 270$  calculated intensity value) and distinguish between mono- and bi-layers (with a  $I_{bi}^{MoS_2} = 780$  calculated intensity value).

The difference between the two vacuum intensities may be explained in our case by the fluctuation of incoming beam intensity due to the presence of a monochromator in the microscope. Taking the vacuum intensity in the STEM image will be even more important when measuring thickness of lighter materials as Boron Nitride.

## C.II.1.3 Position Average Convergent Beam Electron Diffraction (PACBED)

### C.II.1.3.1 Experimental data

LeBeau et al. (2010) demonstrated the possibility of measuring the sample thickness with a precision of  $\pm 1$  nm in bulk crystals (from 8 to 100 nm). Here we show that it is even possible to measure with a one layer precision in a few-layered 2H-MoS<sub>2</sub> crystal. Figure C.II.5 shows PACBED diffraction taken in the same region than the previous Quantitative STEM study. The diffraction has been plotted in log color scale for a better visualization of the diffracted spots. A mono-layer diffraction using a linear color scale is nearly not visible.

In order to center the diffraction pattern, the sample was tilted as precisely as possible. But it was difficult to perfectly align the sample and therefore, after orienting the sample as close as possible to the zone axis, the beam was slightly tilted to center the diffraction intensity around the transmitted spot. This sensitivity to the specimen orientation allows to measure tilts as small as 0.5 mrad (LeBeau et al., 2010). The measured convergence angle is 14.9 mrad using the 50  $\mu$ m C2 aperture. The acceleration voltage is 80kV and the camera length 500mm. The patterns are energy filtered using a 10eV slit to get the cleanest diffraction possible (see Chapter B.I). The beam is spatially averaged by scanning it during the CCD acquisition over a window of  $2 \times 2nm$ .

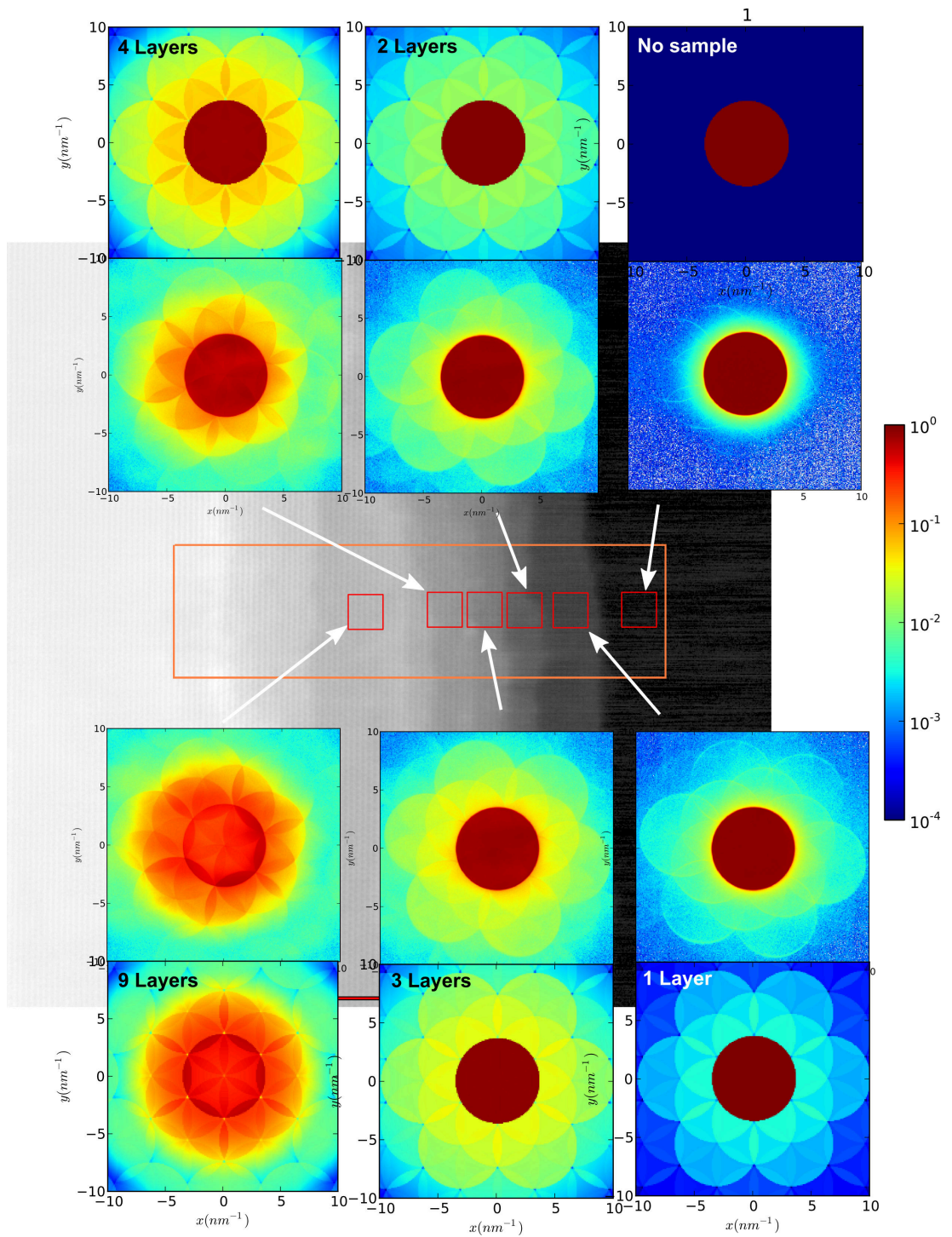


FIGURE C.II.5 – Log scale color plot of experimental PACBED pattern and their corresponding simulated patterns. The intensity is normalized to the intensity of the beam in the vacuum.

### C.II.1.3.2 Simulated data

The simulated patterns are exactly the same than the one used for the Quantitative STEM, the difference is that Quantitative STEM is measuring the average intensity of high angle diffracted beams, while PACBED measures the intensity of the diffracted spots close to the transmitted beam.

### C.II.1.3.3 Thickness results

On Figure C.II.5 we can see that the patterns are very sensitive to the changes in thickness and it is possible to determine the thickness to a mono-layer precision even simply by comparing visually the simulated pattern with the experimental ones. This method is really convenient to obtain a quick measurement of the sample thickness. It has the advantage of staying in the same illumination conditions as for the STEM mode. Nevertheless, if a filtered pattern is required, the HAADF detector can not be used. The camera length on the energy filter CCD being high, the inner angle of the HAADF detector would be too large. That is why we used a DF detector to make the Quantitative STEM study.

## C.II.1.4 Quantitative Nanobeam diffraction

PACBED patterns are easy to obtain because there is no need to change the acquisition conditions between STEM imaging and PACBED diffraction. However they do need to be spatially averaged by scanning the beam during the acquisition, this scanning takes control of the microscope STEM scan coils and it is therefore not possible (with the FEI software) to automatize the acquisition of data (for example to do a line scan). Instead of averaging the pattern by scanning the beam, we changed the C2 aperture to a small one (10  $\mu\text{m}$ ). This reduces the convergence angle of the beam, and increases the size of the beam. Therefore, there is no need anymore to scan the beam to obtain a position average because the size of the beam becomes larger than the unit cell and the data collection can be automatized using the STEM scan coils.

Changing only the C2 aperture allows to acquire less convergent diffraction patterns with no need of averaging over the unit cell. These diffractions can then be compared with simulation, as done with PACBED diffraction. We called this technique Quantitative Nanobeam diffraction.

### C.II.1.4.1 Simulated data

The simulated data is very similar to the PACBED one, but the convergence angle is reduced to 2.9 mrad with the change of C2 aperture. The other simulation parameters stay the same and the unit cell averaged diffraction is also taken.

In order to quantify the intensity of the diffraction spots, the intensity inside the disk is taken for the six equivalent spots (six because we are looking to an hexagonal specimen) and averaged. For simulation, each one of the six equivalent spots have strictly equal intensities, but averaging over the six spots can have an importance on experimental patterns.

Figure C.II.6 shows the intensities of the (100), (110), (200) and (300) spots for 2H-MoS<sub>2</sub> crystal. The variation of the intensities are not at all linear with the thickness. The intensity of

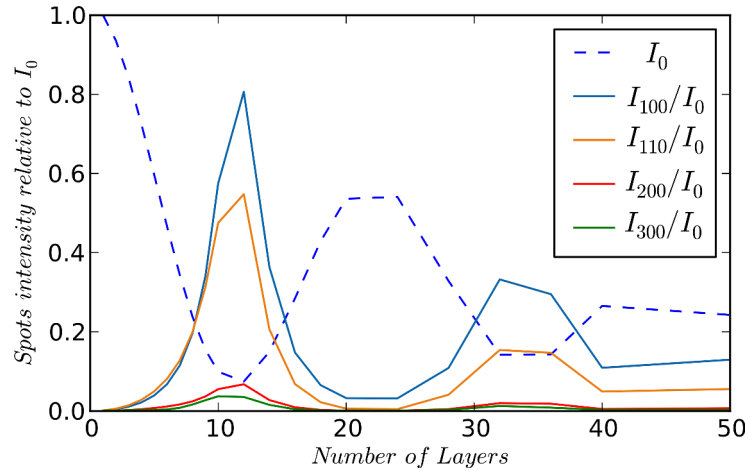


FIGURE C.II.6 – Transmitted and diffracted spots intensities in as a function of the sample thickness for 2H-MoS<sub>2</sub>. The transmitted spot intensity is given relative to the vacuum beam intensity, and the diffracted spot intensities are given relative to the transmitted spot intensity. Simulations have been done at 80kV with a 2.9 mrad convergence angle.

the transmitted spot decreases from 1 (vacuum) to less than 0.1 for 12 layers. The diffraction spots follows the reverse evolution, with increasing intensities until 12 layers. Then the transmitted spot starts to increase again until a maximum around 22 layers. The relative intensity of diffracted spot decreases again. This behavior will complicate the analysis of the thickness for thicknesses around 20-25 layers, but will make the diffraction quite sensitive to changes in thin zones.

#### C.II.1.4.2 Experimental data

The experimental data is a set of diffraction pattern taken in the same zone as PACBED and STEM image in the orange scan area visible in figure C.II.5. From this dataset, the spots intensities are extracted and presented in figure C.II.7.

To quantify the intensity of the spot, a square is drawn inside it and the spot intensity is an average of the intensity inside the square (see figure C.II.7). The background diffraction was taken in a vacuum zone near the sample. A correction is applied to subtract the background created by the Modulation Transfer Function of the CCD camera: Around the transmitted spot, there is a diffuse intensity well visible in the log scale plot. This intensity is removed by subtracting the background square to the diffraction square.

It is also possible to see on the background diffraction small disks around the diffracted spots positions: Due to the small aperture, the probe has the shape of an Airy disk, and this allows to probe with slight intensity the sample that is near the probe position, that is why there is a this small disk around the spot. The square taken for extracting the intensity does not include these disks.

Figure C.II.7 shows the spots intensity map from the set of diffractions. Going right to left in the STEM image is an increase of thickness. The transmitted spot intensity decreases from right to left, except for the last 5 nm, where it increases again. This is exactly the behavior of the

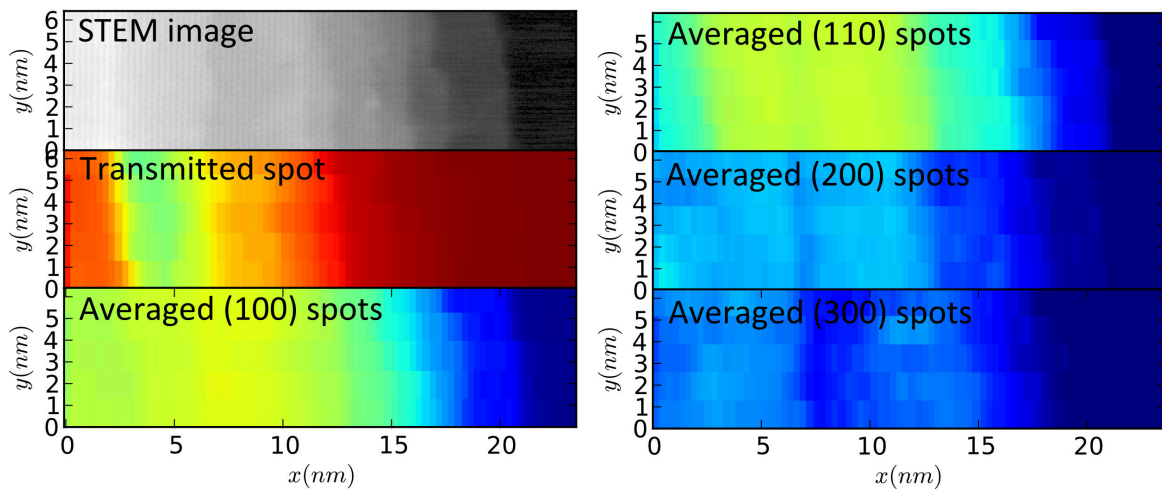
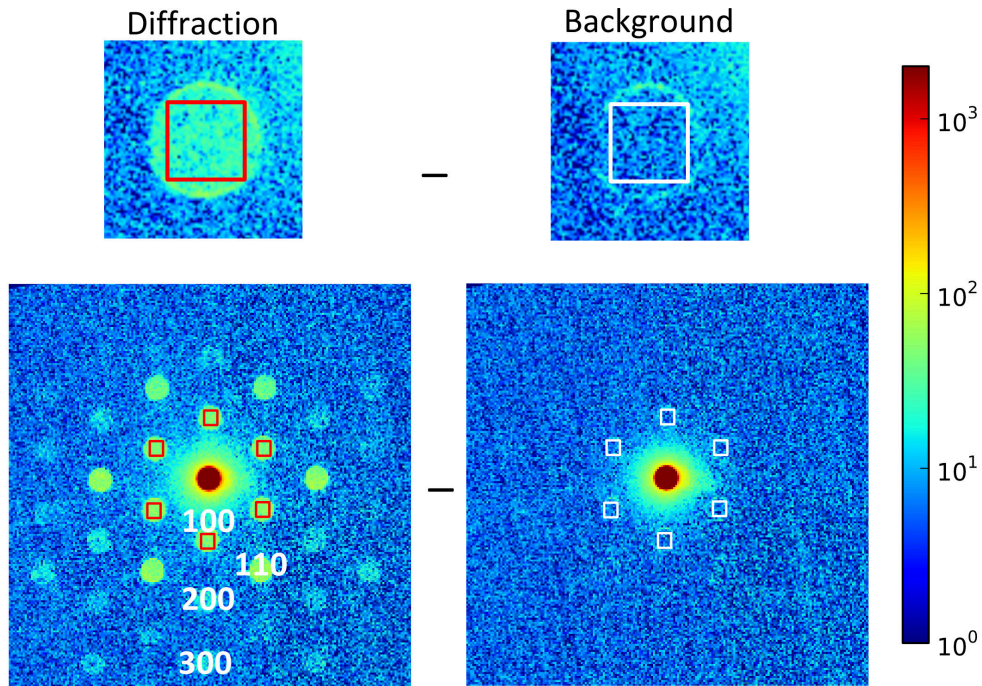


FIGURE C.II.7 – Extraction of the  $MoS_2$  experimental diffraction spot intensities. The intensity of one spot is the average of the square inside the spot minus the corresponding one in the background. The intensities of the 6 averaged equivalent spots are mapped in log color scale.

simulated spots in figure C.II.6 , so we can suppose that when the transmitted spot is minimum, we are around 12-14 layers (this will be quantified in the next section).

As for PACBED pattern, the beam is slightly tilted to center the diffraction pattern.

### C.II.1.4.3 Thickness results

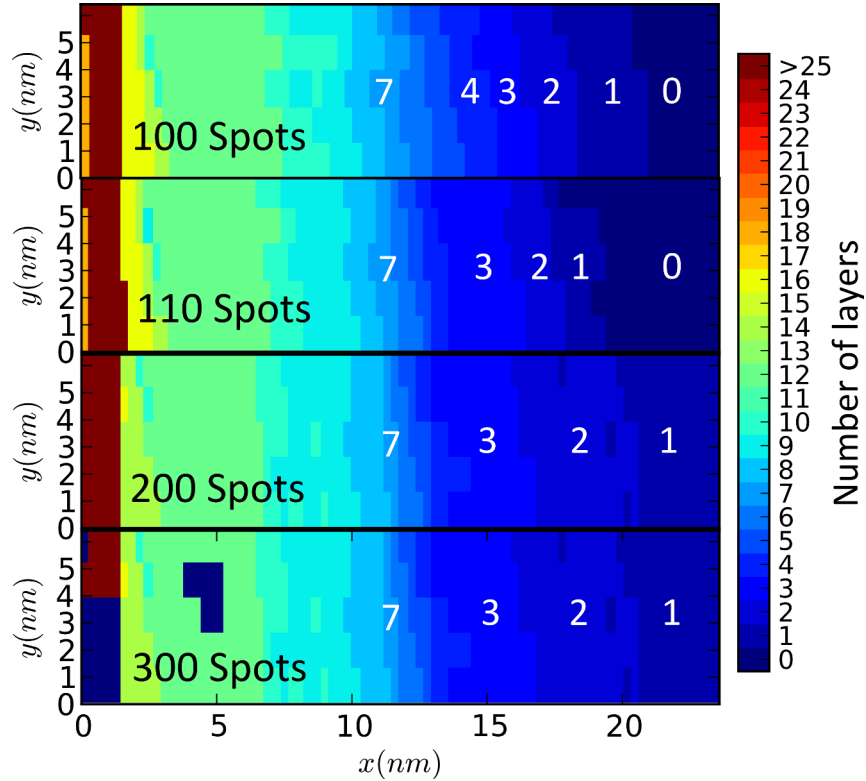


FIGURE C.II.8 – Map of the retrieved  $\text{MoS}_2$  thickness using the spots intensities given in figure C.II.7. The (100) spot gives the best fit of the thickness.

The thickness retrieved from intensity maps of figure C.II.7 is given in figure C.II.8. The thickness retrieval has been done using the intensity of the diffracted spots (100), (110), (200), (300), relative to the transmitted beam intensity.

To retrieve the thickness, the experimental intensity is compared to the simulated ones and the closest value is chosen. But as stated in figure C.II.6, the intensity is not linear with the thickness and its slope changes at 12, 22 and 34 layers. That is why the retrieval in figure C.II.8 has been made from right to left and when the thickness goes over 12, it can't go down (we supposed an increasing sample in thickness from right to left, as told by the STEM signal).

The retrieval is precise to a mono-layer when using the (100) spots. The (110) spots gives a similar thickness but fails to reproduce the thickness in mono-, bi- and tri-layers (there is nearly a shift of one monolayer). The (200) and (300) are very weak spots and are not reliable to give information on the thickness. The mono-layer intensity of these spots is so low that the noise of the CCD camera is enough for the algorithm to measure one monolayer in the vacuum signal.

From the simulated intensity, we know that the precision on the thickness will be low around 20-25 nanometers, and therefore the thickest zones in the retrieval may be wrong. It is interesting to compare this technique to PACBED and Quantitative STEM to be sure the results are correct.

### C.II.1.5 Comparison of the techniques

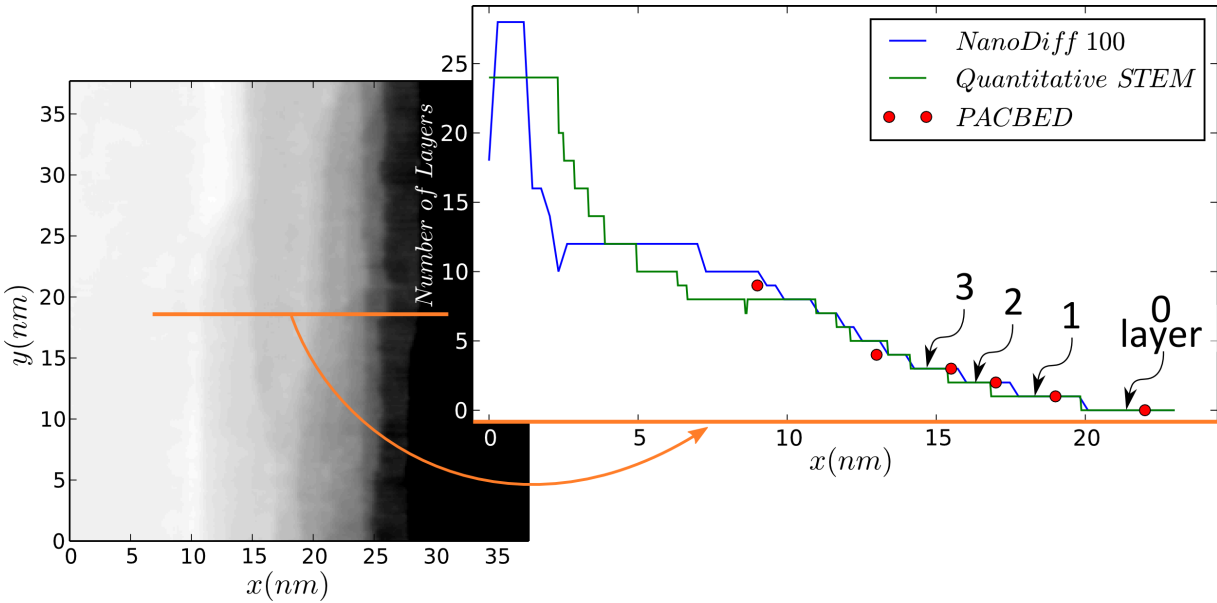


FIGURE C.II.9 – Comparison of the PACBED, Quantitative STEM and Quantitative nanodiffraction techniques to measure the  $MoS_2$  sample thickness. Thicknesses from nanodiffraction are given for the (100) spot (the more precise in thin zones). The thickness is in good agreement for all 3 techniques for very thin zones.

Figure C.II.9 gives the result of the measured thickness on a profile perpendicular to an exfoliated 2H- $MoS_2$  sheet. PACBED, Quantitative STEM and Nanodiffraction from (100) spots are in perfect agreement for in very thin zones (less 10 layers, meaning less 6 nm).

Regarding the spatial resolution of the techniques, the higher spatial resolution is for the Quantitative STEM that have sub-angstrom probe (it can image high resolution). The nanobeam probe size can be estimated by the Rayleigh criterion  $1.22\lambda/\alpha_{cv}$  to about 2 nm and the PACBED spatial resolution is the scanned area, here a square of about 1.5 nm.

Over 10 layers, PACBED diffraction has not been taken, so it is only possible to compare Quantitative STEM and Nanodiffraction. We can see that whereas the Quantitative STEM thickness is going regularly from 10 to 25 layers, the nanodiffraction retrieved thickness is more chaotic. This is due to the lack of precision around 20 layers because of the low variation of intensity in these zones. This low variation of intensity is the same in the simulated PACBED patterns and one should have the same difficulties to quantify the PACBED patterns in these thicknesses.

## C.II.2 Thickness measurement of few-layered Boron Nitride (BN)

The three previous measurement techniques have been applied to mechanically exfoliated Boron Nitride. Figure C.II.10 illustrates the differences between MoS<sub>2</sub> and BN diffraction. BN being a lightest atom, its diffraction is weaker and therefore more difficult to detect. Nevertheless, it is possible to see a monolayered diffraction of Boron Nitride on the CCD camera.

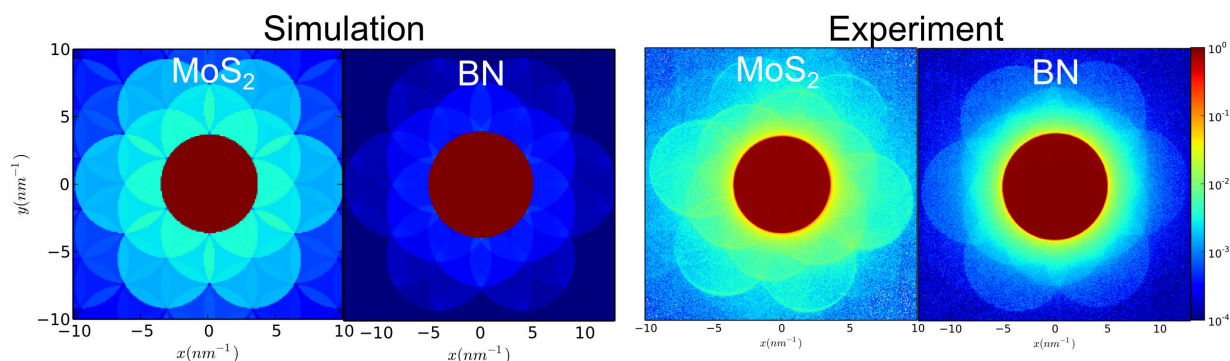


FIGURE C.II.10 – Simulated and experimental diffractions of MoS<sub>2</sub> and BN monolayers. BN having a smaller  $Z$  number, the diffraction is clearly weaker.

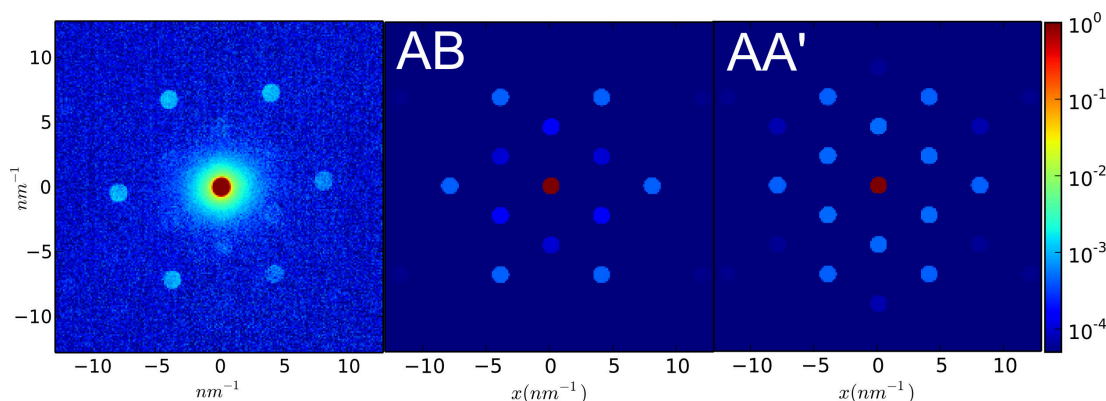


FIGURE C.II.11 – Structure determination of bi-layered BN crystal. Here, only the most stable stackings (AB and AA' ) have been simulated. AA, A'B,AB' have not been simulated because they are unlikely to be observed in experiments. Our exfoliated BN layer is in AB stacking.

Prior to simulate the diffraction necessary for the thickness determination, the crystal structure must be known. Figure C.II.11 compares experimental and simulated diffraction of bi-layered BN. We compare the experimental diffraction to the two most stable stackings, AB and AA'. The others stackings (AA, A'B,AB') being less stable and unlikely to be observed in experiments on clean samples. (Constantinescu et al., 2013).

As with MoS<sub>2</sub>, the first spot (100) intensity allows to choose between the two structures. The first spot being much weaker in the experimental pattern and for AB stacking, we can conclude that our exfoliated Boron Nitride has an AB stacking.

## C.II.2.1 Comparative Quantitative STEM and Nanodiffraction study

### C.II.2.1.1 Experimental data

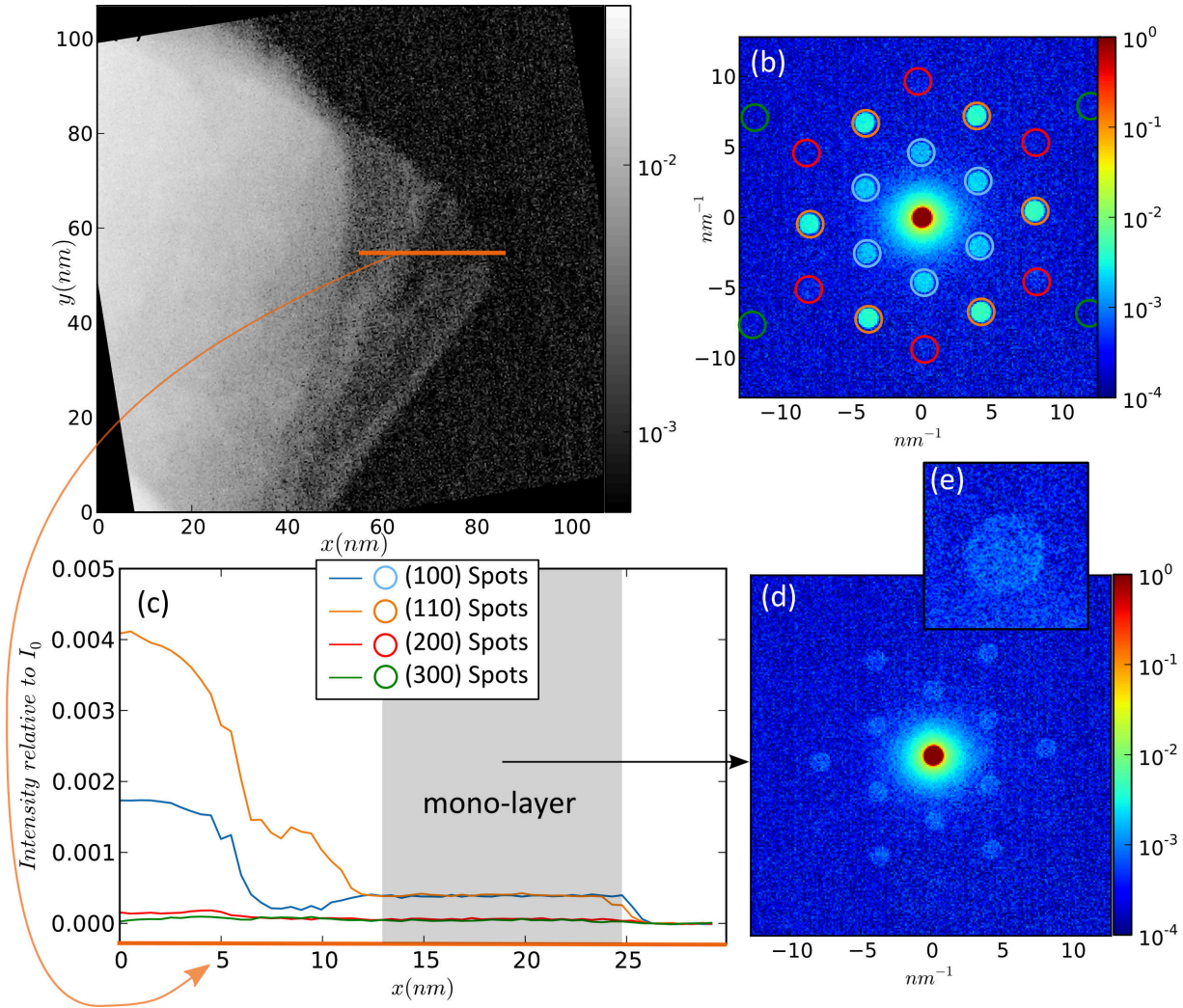


FIGURE C.II.12 – (a) Normalized STEM image and (b) Nano-beam diffraction of BN plotted in log scale. (c) Average intensity of diffracted spots for diffraction taken along the orange line, grey overlay correspond to a mono-layer diffraction. (d) diffraction from the 5-15 nm zone where (100) and (110) spots are of the same intensity, i.e. mono-layered BN (e) diffraction spot with no bright disk around.

In this section the thickness measurement of BN using Quantitative STEM and Nanodiffraction is compared. The experimental data were taken using the FEI Titan Ultimate at 80kV, with a convergence angle of 21 mrad for STEM and 2.8 mrad for Nanodiffraction. The camera length was 320 mm in both cases. With this camera length the DF2 detector inner-radius for the STEM image was 57.84 mrad and the outer-radius taken by the STEM simulations is 300 mrad.

Given the very low contrast of BN in the STEM image, we preferred to use an averaged stack of ten acquisition STEM images of 5 seconds (meaning a total acquisition time of 50 seconds) rather than a one minute acquisition. The average of the 5 seconds acquisition was indeed less noisy and contains much less scanning errors. The sample was stable enough to sum these acquisitions without re-aligning them. Figure C.II.12 (a) gives the resulting normalized STEM image. The detector used for taking the STEM image has been calibrated using the same procedure as the one described in the upper MoS<sub>2</sub> study.

Nanodiffraction patterns have been taken along a line in the STEM image and the intensities of the diffracted spots are given in C.II.12 (c). As for the MoS<sub>2</sub>, the spot intensity is the average of the 6 equivalent spots in the diffraction pattern. The beam being slightly tilted to center the diffraction pattern, the pattern is quite symmetric and the average is here only to give a better signal to noise ratio. Spots (200) and (300) are too dark to see any change of their intensity on this acquisition, that is why only (100) and (110) spots will be used in the later results. Another point compared to MoS<sub>2</sub> is that there are no bright disks around the spot due to the Airy shaped probe. There is certainly one, but it is not detected by the camera because too low in intensity.

### C.II.2.1.2 Simulation data

Figure C.II.13 shows the (100) and (110) spots intensity relative to the transmitted intensity for AA' and AB stacking. The intensity ratios are drastically different for the two stacking, it is therefore compulsory to know the crystal structure before any attempt of measuring the thickness. If the crystal structure is wrong, the result could be difficult to interpret, or worse, the retrieved thickness could be wrong too.

When the (100) spot is as intense as the (110) spot, the thickness is either 1, either 12 layers. It is therefore (as for the graphene case) very easy to identify mono-layer BN by looking at the ratio of the two first spots. In figure C.II.12 (c) the thickness from 5 to 15 nm is typically a mono-layer because the intensity of the two spots are the same.

The STEM signal simulation presented in figure C.II.14 shows less difference between the two structures. In the Quantitative STEM case, knowing the structure is less critical as it will influence only a few on the resulting thickness measurement (the difference here is less than a mono-layer).

### C.II.2.1.3 Comparison of the results

Figure C.II.15 shows the results of Quantitative STEM and Nanodiffraction thickness determination. Both quantitative STEM and Nanodiffraction can be sensitive to the mono-layer in Boron Nitride but this sensitivity is very limited and the experimental data has to be corrected in order to obtain accurate results. In Quantitative STEM, the vacuum intensity  $I_{vac}$  was well measured in both detector scan and STEM image vacuum region. With  $I_{vac}^{STEM} = 9971$  and  $I_{vac}^{DScan} = 9970$ . But the standard deviation of the noise in the vacuum STEM image was  $\Delta I_{vac} = 40$ . This noise is important compared to the signal of a mono-layer BN that is  $I_{mono}^{BN} = 11$  and even for the bi-layer signal  $I_{bi}^{BN} = 22$ . By averaging the STEM signal over 5 pixels, the standard deviation falls to  $\Delta I_{vac}^{averaged} = 8$ . By doing so, we reduced the spacial resolution, but the STEM image is less noisy and now sensitive to BN mono-layer. Nevertheless, we were faced to a

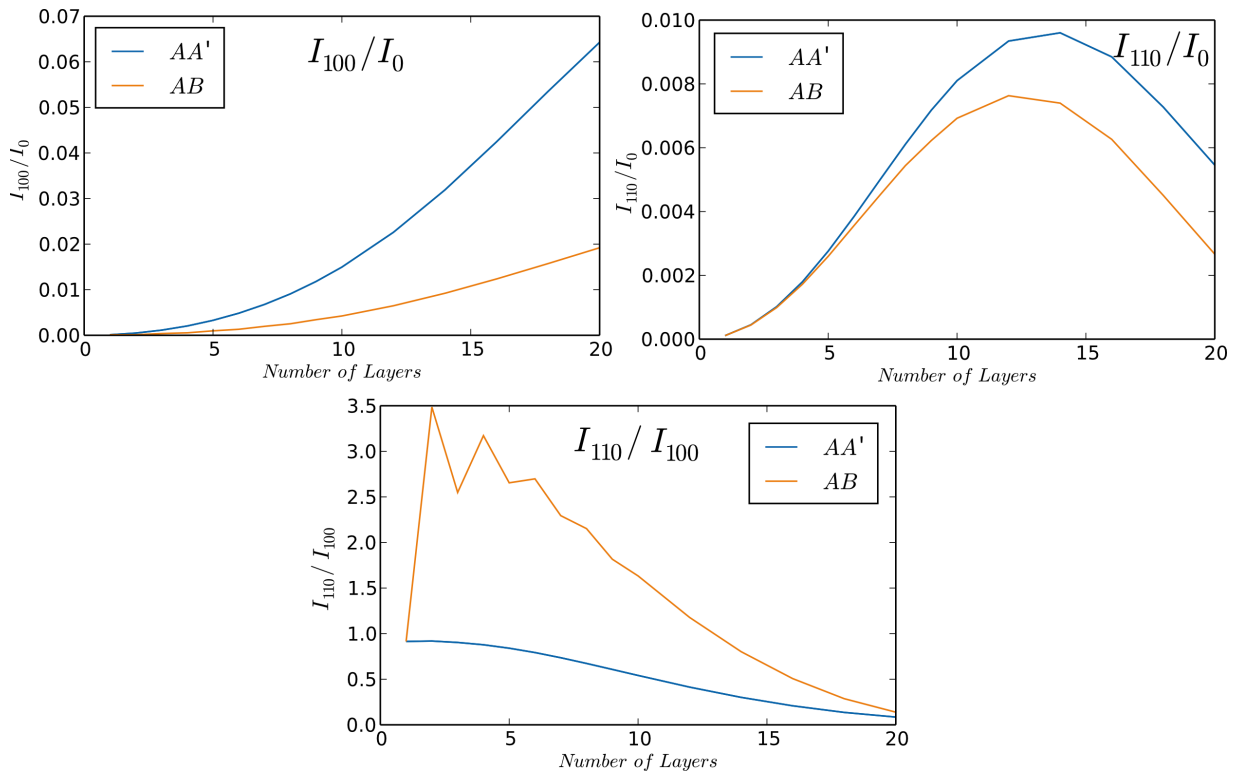


FIGURE C.II.13 – (100) and (110) spot intensities extracted from Boron Nitride simulations at 80kV. AA' and AB stackings have been simulated. It shows the importance of knowing the crystal structure for the thickness measurement.

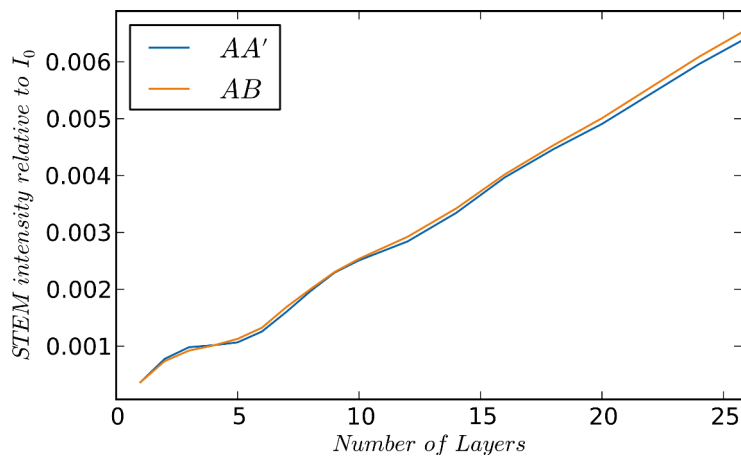


FIGURE C.II.14 – Simulation of the STEM signal relative to the beam intensity, using a inner detector radius of 57.84 mrad and a outer radius of 300mrad. AB and AA' stackings give nearly the same results with a slight oscillation of the intensity for AA' structure.

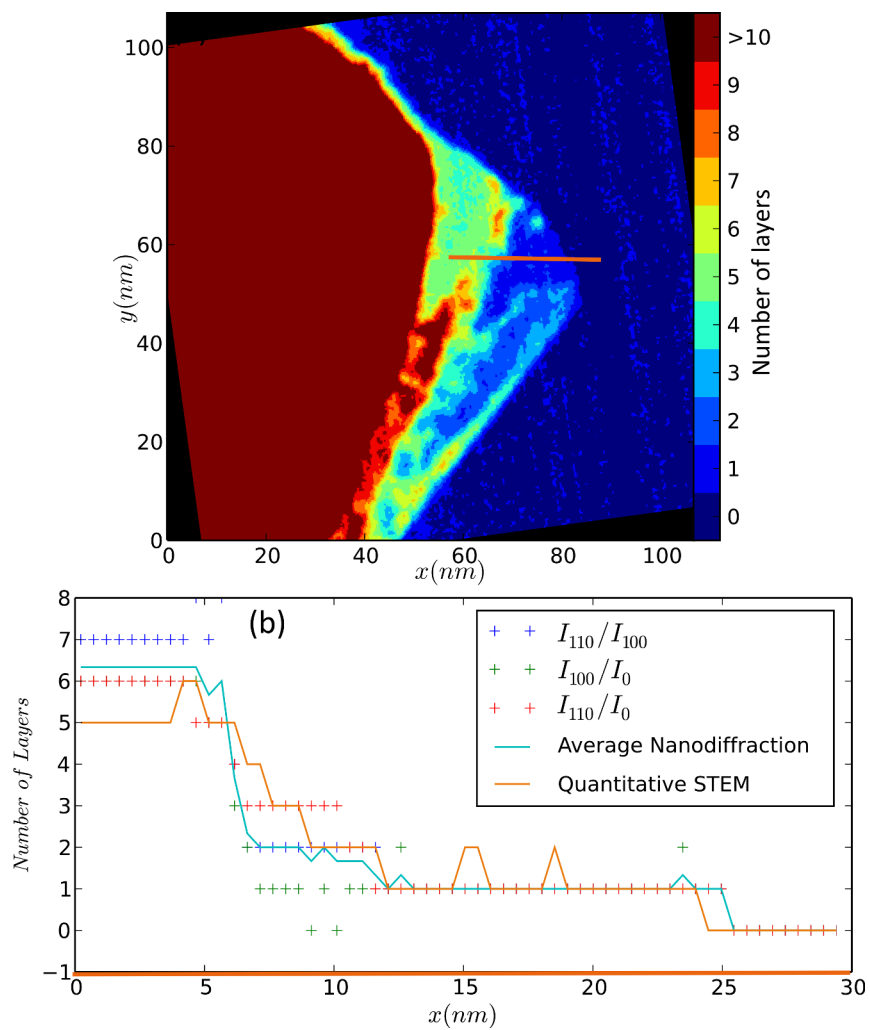


FIGURE C.II.15 – (a) Thickness map of BN sample by Quantitative STEM, Gaussian blur was applied on the image to remove the unwanted noise. (b) Comparison of thickness determination between nanodiffraction and Quantitative STEM (not blurred)

### C.II.2.1. Comparative Quantitative STEM and Nanodiffraction study

vacuum reference problem, because half of the vacuum was measured to be a mono-layer when using  $I_{vac}^{STEM}$  or  $I_{vac}^{DScan}$ .

In nanodiffraction, the signal of the mono-layer is so low that it is only visible in a log plot. But the strength of the Nanodiffraction is that mono-layer diffractions are completely different from the bi-layers ones, and therefore it is straightforward to determine if the area is mono-layered. This information has been used to calibrate the STEM signal by fitting the mono-layer areas in the nanodiffractions to the corresponding areas in the STEM image. To do so, we increase the vacuum level to  $I_{vac}^{corrected} = 9998$ . Mono-layered areas were of course measured as mono-layers and now 75% of the vacuum is measured as vacuum (25% only as a mono-layer due to the noise).

Concerning nanodiffraction quantification, the very low signal reaches the limit of the CCD camera and we do not know if the camera is linear in this regime. The experimental intensity of the spots was under the simulated ones (by about 11 count, i.e. 0.02%). We were therefore forced to calibrate the signal by identifying the mono-layered area and aligning the experimental intensity levels to the simulated one. This has been done by lowering the intensities by 11 counts.

After doing these corrections, the thicknesses retrieved by the two methods (figure C.II.15 (b)) are very close. The precision can reach the mono-layer.

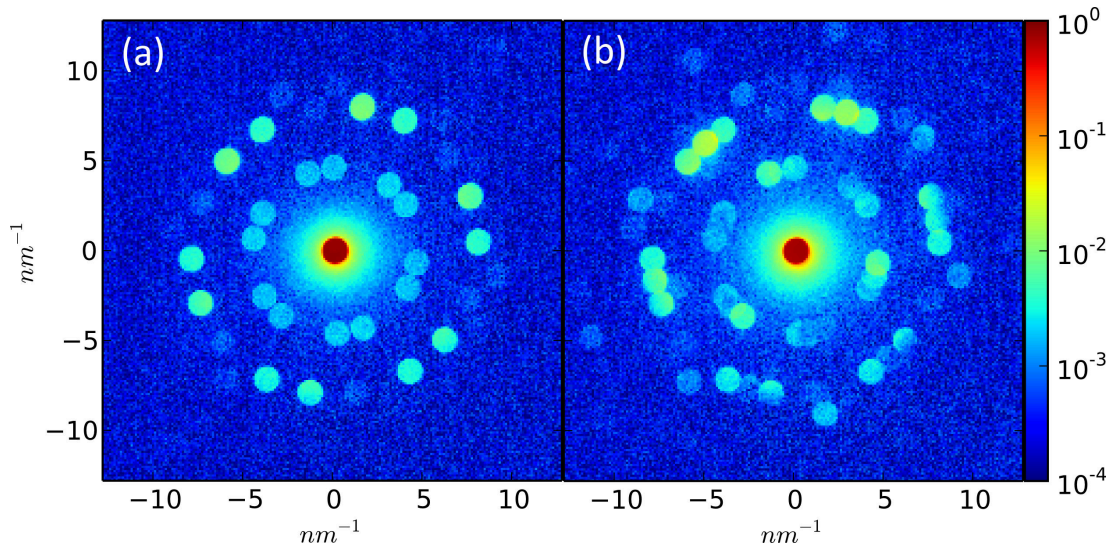


FIGURE C.II.16 – Diffraction from (a) 15 nm (b) 32 nm thick BN crystals. The thickness was determined with Quantitative STEM

We tried to apply this method on thicker zones of the sample but our exfoliated boron nitride was made of stacks of few-layered (<10 layers) AB stacking crystals. So on thicker zone the diffraction was made of several spots (see figure C.II.16) from different crystals organized in layers. On this particular case, it would be possible to use the Quantitative NanoDiffraction method, but it would need to implement an algorithm that takes the rotational average, and as the intensity is not linear versus the thickness, the number of diffracting crystals should be known.

### C.II.3 Discussion

All the thickness measurement methods worked well on MoS<sub>2</sub> and BN with a precision of one mono-layer on samples thinner than 10 layers. Each technique has its own advantages and drawbacks. Some points are discussed in order to compare the three techniques:

#### Experimental setup

Quantitative STEM is really convenient to set-up when doing STEM experiments, nevertheless, the detector has to be calibrated and the diffraction carefully centered on the detector before acquiring a STEM image. Each STEM image that is then taken can be analyzed, considering that the intensity of the incoming beam does not change during the experiment. PACBED is also straightforward to acquire because it only need to scan the beam over a small area. For Quantitative Nanobeam diffractions, only the C2 aperture has to be changed in order to make the beam less convergent. In addition, STEM coils can also be used to automatize the Nanobeam diffractions acquisition.

#### Data analysis

PACBED gives diffractions that can directly be compared to simulation, even during a microscope session. STEM images are straightforward to analysis but care has to be taken when choosing the vacuum intensity  $I_{vac}$  and Quantitative Nanodiffraction main drawback is the long data treatment needed to extract the intensities of the spots.

#### Spatial resolution

The spatial resolution of PACBED and Nanobeam are comparable and around 1-2 nm, and the spatial resolution of Quantitative STEM is much better because the STEM probe can resolve atoms. Nevertheless, we showed that for light material such as Boron Nitride, it was necessary to average the STEM image to lower the noise, deteriorating the spatial resolution.

#### Stacking structure determination

Only PACBED and Nanodiffraction can be used to determine the stacking structure, STEM being only a Z-contrast signal, there is no information on the stacking structure.

#### Precision in measurement

The case of Boron Nitride showed the big advantage of the diffraction techniques (PACBED and Nanodiffraction). The intensity ratio of diffraction spots are different for mono-layered and bi-layered BN, and it is therefore possible to distinguish mono or bi-layers by a simple qualitative observation. The diffracted signal being so low, there is no proof that we are in the CCD camera and STEM detector linear regime. In our case, a correction had to be applied to the vacuum intensity by identifying the mono-layer intensity in the experimental image to the simulated image. Doing such a correction, STEM and Nanodiffraction methods gave similar results for the thickness measurement of Boron Nitride layers.

---

On MoS<sub>2</sub>, the intensity being much higher, the three methods gave similar results for thin (<10 layers) areas. Nevertheless, for thicker areas (around 20 layers), the calculated spot intensities does not vary much and the measurement is not precise both for PACBED and Nanodiffraction methods. Quantitative STEM does not suffer from this lack of precision in given thicknesses as it relies on high-angle diffracted electrons whose signal is more linear with respect to the thickness.

To conclude, the sensitivity of the three techniques are comparable and these techniques are really complementary to study various materials and various thicknesses range. Using two or even three of the techniques together is a way to accurately measure the thickness and to minimize the measurement errors, for example PACBED or Nanobeam diffractions can often distinguish a monolayered and a bilayered material from the intensity ratio between diffraction spots, and this information can be used to calibrate the Quantitative STEM signal.

---

## Conclusion

---

In this thesis work, the development of Transmission Electron Microscopy techniques for the study of bulk and two-dimensional materials has been discussed. The TEM is an ideal characterization tool for two-dimensional materials providing high resolution local analysis together with large scale imaging. Aberration correctors and monochromators implemented in the latest generation electron microscopes allow to image two-dimensional materials with atomic resolution. The contrast of these images can be very tricky to interpret. It is dependent on numerous factors, such as the number of layers, the defocus, the aberrations etc. In this thesis, we showed the effect of three-fold astigmatism and sample tilt on the contrast of graphene HR-TEM images. A diffraction based study of the orientation of two-dimensional materials has also been done. It was possible to quantify the tilt of a few-layered Molybdenum disulfide sample by looking at the projection effect due to the inclination of the relrods.

Sample thickness of few-layered Molybdenum disulfide and Boron Nitride have been compared using three different techniques: Quantitative STEM, PACBED and Quantitative Nanodiffraction. Despite of the low intensity of diffracted beams due to the thin samples, all the thickness measurement techniques reaches a mono-layer precision. Each technique has its own advantages and drawbacks and they can be used in a complementary way to minimize the errors in the measurement.

The other part of this thesis is focused on Convergent Beam Electron Diffraction. A technique for the measurement of sample thickness, direction of observation, acceleration voltage and camera length has been presented. This technique relies on the on a reference perfect crystal CBED pattern and have been applied to a silicon sample for a proof of concept.

CBED patterns also contain information on the displacement field (i.e. strain and rotation state). The electron diffraction pattern on the CCD camera being a two-dimensional projection of a three-dimensional sample, there can be ambiguities on the strain measurement. In this thesis, a new method based on the study of the positions and angles of both excess and deficient HOLZ lines in CBED patterns allowed to reduce these ambiguities. From an unique direction of orientation, it was possible to retrieve the three diagonal terms of the deformation gradient tensor and therefore to retrieve the volume of the crystal cell.

By studying the splitting or broadening of the CBED excess HOLZ lines, it was also possible to retrieve the displacement along the electron beam direction. A Monte Carlo minimization algorithm has been built in order to retrieve this displacement from excess HOLZ lines profiles. This method has been tested on a sample consisting of silicon-germanium layers in a Silicon

---

matrix, and although the retrieved displacement was qualitatively correct, there was a slight difference compared to finite-element simulations results.

This Convergent Beam Electron Diffraction study gives a new insight into three-dimensional strain measurement at the nanoscale. A ultimate development of this technique would be to study both excess and deficient HOLZ lines positions, angles, and profiles and to develop a retrieval algorithm that might be able to fully characterize the three-dimensional displacement in the sample from these information.

With the improvement of instrumental techniques and the increasing need of material characterization at the nanoscale, continuing the development of TEM techniques is important to have a better understanding of nanomaterials unique properties.

# Appendix



---

## Appendix A: Strain formalism, the deformation gradient tensor **F**

---

The usual formalism to describe strain comes from the elastic theory. The strain is usually represented by the infinitesimal strain tensor  $\varepsilon$ , that is the symmetric part of the gradient displacement field :

$$\varepsilon = \begin{pmatrix} \varepsilon_{xx} & \varepsilon_{xy} & \varepsilon_{xz} \\ \varepsilon_{yx} & \varepsilon_{yy} & \varepsilon_{yz} \\ \varepsilon_{zx} & \varepsilon_{zy} & \varepsilon_{zz} \end{pmatrix} = \begin{pmatrix} \frac{\partial u_x}{\partial x} & \frac{1}{2} \left( \frac{\partial u_x}{\partial y} + \frac{\partial u_y}{\partial x} \right) & \frac{1}{2} \left( \frac{\partial u_x}{\partial z} + \frac{\partial u_z}{\partial x} \right) \\ \frac{1}{2} \left( \frac{\partial u_y}{\partial x} + \frac{\partial u_x}{\partial y} \right) & \frac{\partial u_y}{\partial y} & \frac{1}{2} \left( \frac{\partial u_y}{\partial z} + \frac{\partial u_z}{\partial y} \right) \\ \frac{1}{2} \left( \frac{\partial u_z}{\partial x} + \frac{\partial u_x}{\partial z} \right) & \frac{1}{2} \left( \frac{\partial u_z}{\partial y} + \frac{\partial u_y}{\partial z} \right) & \frac{\partial u_z}{\partial z} \end{pmatrix}$$

Where  $\mathbf{u}$  is the displacement field.

This infinitesimal strain tensor being only the symmetric part of the gradient displacement field, it does not reflect the possible rotation that can occur in response to stress in the sample. However, this rotation is essential to understand the whole deformation, that is why, in the scope of this thesis, the deformation gradient tensor has been chosen to describe the strain state of the samples. This deformation gradient tensor is linked to the gradient of the displacement field by :

$$\mathbf{F} = \begin{pmatrix} 1 + \frac{\partial u_x}{\partial x} & \frac{\partial u_x}{\partial y} & \frac{\partial u_x}{\partial z} \\ \frac{\partial u_y}{\partial x} & 1 + \frac{\partial u_y}{\partial y} & \frac{\partial u_y}{\partial z} \\ \frac{\partial u_z}{\partial x} & \frac{\partial u_z}{\partial y} & 1 + \frac{\partial u_z}{\partial z} \end{pmatrix} = \nabla \mathbf{u} + \mathbf{I}$$

$\mathbf{I}$  being the identity matrix,  $\mathbf{F}$  the deformation gradient tensor.

The  $\mathbf{F}$  tensor can be easily linked to the crystal lattice parameters. A given crystal lattice is characterized by its 3 lattice vectors  $\mathbf{a}$ ,  $\mathbf{b}$  and  $\mathbf{c}$ . In a given orthogonal basis  $(O, x, y, z)$  the coordinates of these 3 vectors can be put in a matrix  $\mathbf{A}$  that completely characterizes the crystal lattice:

$$\mathbf{A} = \begin{pmatrix} a_x & b_x & c_x \\ a_y & b_y & c_y \\ a_z & b_z & c_z \end{pmatrix} \tag{C.II.1}$$

To study the deformation of the crystal, it is necessary to compare an undeformed crystal characterized by its matrix  $\mathbf{A}_0$  to some deformed crystal characterized by its matrix  $\mathbf{A}$ . If  $\mathbf{A}_0$

---

is the matrix describing the perfect crystal and  $\mathbf{A}$  the one for the deformed crystal, then the deformation gradient tensor is given by (Rouviere and Sarigiannidou, 2005):

$$\mathbf{F} = \mathbf{A}\mathbf{A}_0^{-1} = \begin{pmatrix} f_{xx} & f_{xy} & f_{xz} \\ f_{yx} & f_{yy} & f_{yz} \\ f_{zx} & f_{zy} & f_{zz} \end{pmatrix} \quad (\text{C.II.2})$$

This  $\mathbf{F}$  tensor can be split into two parts, rotation and strain.

When dealing with small rotation and small strains, the symmetric part of  $\mathbf{F}$  corresponds to the strain tensor  $\epsilon$ , and the antisymmetric part to the pure rotation  $\mathbf{R}$ .

$$\mathbf{F} = \mathbf{R} + \epsilon \quad (\text{C.II.3})$$

where

$$\epsilon = \frac{1}{2} (\mathbf{F} + \mathbf{F}^T) - \mathbf{I} \quad (\text{C.II.4})$$

$$\mathbf{R} = \frac{1}{2} (\mathbf{F} - \mathbf{F}^T) + \mathbf{I} \quad (\text{C.II.5})$$

The volume of the lattice is given by the trace of the  $\epsilon$  tensor :

$$V = Tr(\epsilon) = Tr(\mathbf{F}) \quad (\text{C.II.6})$$

The infinitesimal regime breaks down when dealing with significant rotation. For instance, a one degree rotation induces a  $10^{-4}$  error on the stretch tensor. The polar decomposition of the  $\mathbf{F}$  tensor should then be used (Maurice et al., 2012):

$$\mathbf{F} = \mathbf{R}\mathbf{U} \quad (\text{C.II.7})$$

where  $\mathbf{R}$  is again the pure rotation and  $\mathbf{U}$  the right stretch tensor. To find the polar decomposition, the property of the rotation ( $\mathbf{R}^T\mathbf{R} = \mathbf{I}$ ) is used :

$$\mathbf{F}^T\mathbf{F} = \mathbf{U}^T\mathbf{R}^T\mathbf{R}\mathbf{U} = \mathbf{U}^T\mathbf{U} = \mathbf{U}^2 \quad (\text{C.II.8})$$

Since  $\mathbf{F}^T\mathbf{F}$  is a positive-semidefinite Hermitian matrix, the right stretch tensor  $\mathbf{U}$  has an unique expression given by :

$$\mathbf{U} = \sqrt{\mathbf{F}^T\mathbf{F}} \quad (\text{C.II.9})$$

and the rotation matrix is then given by :

$$\mathbf{R} = \mathbf{F}\mathbf{U}^{-1} \quad (\text{C.II.10})$$

From this decomposition, the Biot strain tensor  $\epsilon$  can be retrieved :

$$\epsilon = \mathbf{U} - \mathbf{I} = \sqrt{\mathbf{F}^T\mathbf{F}} - \mathbf{I} \quad (\text{C.II.11})$$

Such equation shows that the  $\mathbf{F}$  tensor is an important tensor from which all the physical parameters can be recovered. This is why the deformation gradient tensor  $\mathbf{F}$  has been chosen to describe the local stress and the local rotation of the sample.

---

## Appendix B: List of python programs

---

### 3D CBED GUI

Deformation gradient tensor retrieval in the case of uniformly deformed sample ([Chapter 2 of Part II](#)).

*Main\_3DCBED\_multiProc.py*

The Graphical User Interface inputs all the CBED experimental data, finds the positions of HOLZ lines by template matching, and retrieves the  $\mathbf{F}$  tensor components.

*fileData.py*

Contains all the data and variable useful for the GUI.

*commandes\_plot.py*

Line commands to plot the results.

### CBED Rocking Curves

Displacement variation along the beam direction retrieval ([Chapter 3 of Part II](#))

*DefinitionLines.py*

Define HOLZ lines profiles from experimental image (manual definition)

*DeScan.py*

Returns the descscan table from an experimental dataset.

*ExtractLines\_Descanned.py*

Extract HOLZ lines profiles defined by *DefinitionLines.py* and correct the descscan using the descscan table from *DeScan.py*.

*MC\_Global\_Exp\_MultiProc\_2Axis\_2.py*

Monte Carlo minimisation on the HOLZ lines profiles.

*MC\_Multi\_2Axis2\_plot\_result.py*

Plot of the results.

### CBED Thickness Dellile

Thickness measurement using [Delille et al. \(2000\)](#) method.

*Dellile2.py*

---

## Experimental Parameter Retrieval

Experimental parameters retrieval ( $t, E, \alpha_{cv}, u, v$ ) from [Chapter 1 of Part II](#).

[fitEandtanduvw\\_Transmis\\_WORKINGSAVE.py](#)

From an experimental reference pattern

[fitEandtanduvw\\_ExpZA1Transmis-b-WORKINGSsave.py](#)

From an experimental reference pattern

## Dynamic simulations

Many-Beams dynamic Bloch wave CBED simulations ([Chapter 3 of Part I](#))

[MultiProc\\_AllF.py](#)

## Graphene Tilt

Study of the projection effect ([Chapter 1 of Part III](#))

[GrapheneTilt2.py](#) and [GrapheneTilt2beta.py](#)

Spot positions analysis for alpha and beta experimental tilts.

[Plot\\_Results.py](#) and [Plot\\_Resultsbeta.py](#)

Plot the experimental projection factor.

## Kirkland automation

Python automation of [Kirkland \(2010\)](#) simulation code for multislice simulation of Nano-diffraction, PACBED and quantitative STEM.

[Simulate\\_Autostem\\_—.py](#)

## Thickness Measurement

Thickness measurement from [Chapter 2 of Part III](#) of BN or MoS<sub>2</sub> with PACBED, Nano-diffraction and Quantitative STEM.

[BN or MoS2-Ultimate-PACBED or Nanodiff or QuantiSTEM.py](#)

## MoS<sub>2</sub> Tilt Study

Tilt study of MoS<sub>2</sub> from [Chapter 1 of Part III](#)

[MoS2-Ultimate-s7Ripples.py](#)

### Abbreviations

CBED	Convergent Beam Electron Diffraction
CCD	Charge-Coupled Device
CL	Camera Length
EBSD	Electron Back Scattered Diffraction
FEG	Field Emission Gun
FIB	Focused Ion Beam
FLG	Few Layers Graphene
FOLZ	First Order Laue Zone
GPA	Geometrical Phase Analysis
HOLZ	High Order Laue Zone
LACBED	Large Angle Convergent Beam Electron Diffraction
MTF	Modulation Transfer Function
NBED	Nano Beam Electron Diffraction
PACBED	Position Averaged Convergent Beam Electron Diffraction
PED	Precession Electron Diffraction
SAED	Selected Area Electron Diffraction
SEM	Scanning Electron Microscope
SLG	Single Layer Graphene
STEM	Scanning Transmission Electron Microscopy

---

TEM            Transmission Electron Microscope

ZOLZ           Zero Order Laue Zone

### Symbols

$\alpha_c v$             Convergence semi-angle

$\chi$                 Aberration function

$\Delta E$             Band Gap

$\Delta f$             Defocus

$\lambda$                 Electron wavelength

$\mathbf{F}$                 Deformation gradient tensor

$\mathbf{g}_{eff}$             Effective diffraction vector

$\mathbf{g}_{hkl}$             (h,k,l) planes diffraction vector

$\mathbf{k}'$                 Diffracted wave vector

$\mathbf{k}_0$                 Electron wave vector

$\mathbf{k}_0$                 Incident wave vector

$\theta_B$                 Bragg angle

$\theta_{B,eff}$            Effective Bragg angle

$\varepsilon$                 Strain tensor

$\xi_g$                 Extinction distance

$a, b, c, \alpha, \beta, \gamma$  Crystal lattice constants

$A_1$                 Two-fold astigmatism

$A_2$                 Three-fold astigmatism

$B_2$                 Coma

$c$                  Speed of light

$C_3$                 Third-order spherical aberration

$C_5$                 Fifth-order spherical aberration

$C_c$                 Chromatic aberration

$C_g$                 Bloch wave coefficient

$d_{hkl}$	(h,k,l) planes spacing
$E$	High Tension
$e$	Electron charge
$f_e$	Electron scattering factor
$F_g$	Structure factor
$h$	Planck's constant
$I_{det}$	STEM Detector intensity
$I_g(sg)$	HOLZ line intensity profile
$I_{norm}$	Normalized STEM intensity
$I_{raw}$	Raw STEM intensity
$I_{vac}$	STEM detector noise
$m_0$	Electron mass
$S_g$	Deviation from exact Bragg condition
$s_g$	Deviation parameter
$V_0$	Crystal potential
T	Temperature
t	Sample thickness
Z	Atomic number



---

## Bibliography

---

- Alfonso, C., Alexandre, L., Leroux, C., Jurczak, G., Saikaly, W., Charai, A., Thibault-Penissou, J., Mar. 2010. HOLZ lines splitting on SiGe/si relaxed samples. analytical solutions for the kinematical equation. *Ultramicroscopy* 110 (4), 285–296.  
URL <http://dx.doi.org/10.1016/j.ultramic.2009.12.005>
- Alloyeau, D., Ricolleau, C., Oikawa, T., Langlois, C., Le Bouar, Y., Loiseau, A., Jun. 2008. STEM nanodiffraction technique for structural analysis of CoPt nanoparticles. *Ultramicroscopy* 108 (7), 656–662.  
URL <http://dx.doi.org/10.1016/j.ultramic.2007.10.006>
- AMCSD, 2014. American mineralogist crystal structure database.  
URL <http://rruff.geo.arizona.edu/AMS/minerals/Molybdenite>
- Anastassakis, E., Pinczuk, A., Burstein, E., Pollak, F. H., Cardona, M., Jan. 1970. Effect of static uniaxial stress on the raman spectrum of silicon. *Solid State Communications* 8 (2), 133–138.  
URL [http://dx.doi.org/10.1016/0038-1098\(70\)90588-0](http://dx.doi.org/10.1016/0038-1098(70)90588-0)
- Avouris, P., Dimitrakopoulos, C., Mar. 2012. Graphene: synthesis and applications. *Materials Today* 15 (3), 86–97.  
URL [http://dx.doi.org/10.1016/S1369-7021\(12\)70044-5](http://dx.doi.org/10.1016/S1369-7021(12)70044-5)
- Ayache, J., Beaunier, L., Boumendil, J., Ehret, G., Laub, D., 2010. Sample preparation handbook for transmission electron microscopy. Springer.  
URL <http://www.springer.com/materials/characterization+%26+evaluation/book/978-1-4419-6087-0>
- Beche, A., Oct. 2009. Mesure de deformation a l'échelle nanometrique par microscopie electronique en transmission. Ph.D. thesis, Institut National Polytechnique de Grenoble - INPG.  
URL <http://tel.archives-ouvertes.fr/tel-00489867>
- Beche, A., Rouviere, J. L., Barnes, J. P., Cooper, D., Aug. 2013. Strain measurement at the nanoscale: Comparison between convergent beam electron diffraction, nano-beam electron diffraction, high resolution imaging and dark field electron holography. *Ultramicroscopy* 131, 10–23.  
URL <http://dx.doi.org/10.1016/j.ultramic.2013.03.014>

## BIBLIOGRAPHY

---

- Beche, A., Rouviere, J.-L., Clement, L., Hartmann, J. M., Sep. 2009. Improved precision in strain measurement using nanobeam electron diffraction. *Applied Physics Letters* 95 (12), 123114–123114–3.  
URL <http://dx.doi.org/10.1063/1.3224886>
- Benameur, M. M., Radisavljevic, B., Heron, J. S., Sahoo, S., Berger, H., Kis, A., Mar. 2011. Visibility of dichalcogenide nanolayers. *Nanotechnology* 22 (12), 125706.  
URL <http://dx.doi.org/10.1088/0957-4484/22/12/125706>
- Benedetti, A., Bender, H., Cullis, A. G., Midgley, P. A., 2008. On the asymmetric splitting of CBED HOLZ lines under the gate of recessed SiGe source/drain transistors. In: *Microscopy of Semiconducting Materials 2007*. No. 120 in Springer Proceedings in Physics. pp. 411–414.  
URL [http://dx.doi.org/10.1007/978-1-4020-8615-1\\_89](http://dx.doi.org/10.1007/978-1-4020-8615-1_89)
- Bethe, H., Jan. 1928. Theorie der beugung von elektronen an kristallen. *Annalen der Physik* 392 (17), 55–129.  
URL <http://dx.doi.org/10.1002/andp.19283921704>
- Bierwolf, R., Hohenstein, M., Phillipp, F., Brandt, O., Crook, G. E., Ploog, K., Feb. 1993. Direct measurement of local lattice distortions in strained layer structures by HREM. *Ultramicroscopy* 49 (1-4), 273–285.  
URL [http://dx.doi.org/10.1016/0304-3991\(93\)90234-0](http://dx.doi.org/10.1016/0304-3991(93)90234-0)
- Boneschanscher, M. P., van der Lit, J., Sun, Z., Swart, I., Liljeroth, P., Vanmaekelbergh, D., Nov. 2012. Quantitative atomic resolution force imaging on epitaxial graphene with reactive and nonreactive AFM probes. *ACS Nano* 6 (11), 10216–10221.  
URL <http://dx.doi.org/10.1021/nm3040155>
- Bradski, G., Nov. 2000. The OpenCV library. *Dr Dobbs Journal* 25 (11), 120–+, WOS:000089917100022.  
URL <http://www.drdobbs.com/open-source/the-opencv-library/184404319>
- Brunetti, G., Bouzy, E., Fundenberger, J. J., Morawiec, A., Tidu, A., Mar. 2010. Determination of lattice parameters from multiple CBED patterns: A statistical approach. *Ultramicroscopy* 110 (4), 269–277.  
URL <http://dx.doi.org/10.1016/j.ultramic.2009.11.004>
- Byrd, R. H., Lu, P., Nocedal, J., Zhu, C., Sep. 1995. A limited memory algorithm for bound constrained optimization. *SIAM Journal on Scientific Computing* 16 (5), 1190–1208.  
URL <http://dx.doi.org/10.1137/0916069>
- Cancado, L. G., Jorio, A., Ferreira, E. H. M., Stavale, F., Achete, C. A., Capaz, R. B., Moutinho, M. V. O., Lombardo, A., Kulmala, T. S., Ferrari, A. C., Aug. 2011. Quantifying defects in graphene via raman spectroscopy at different excitation energies. *Nano Letters* 11 (8), 3190–3196.  
URL <http://dx.doi.org/10.1021/nl201432g>

- Castro Neto, A. H., Guinea, F., Peres, N. M. R., Novoselov, K. S., Geim, A. K., Jan. 2009. The electronic properties of graphene. *Reviews of Modern Physics* 81 (1), 109–162.  
URL <http://dx.doi.org/10.1103/RevModPhys.81.109>
- Chang, L. Y., Kirkland, A. I., Titchmarsh, J. M., Mar. 2006. On the importance of fifth-order spherical aberration for a fully corrected electron microscope. *Ultramicroscopy* 106 (4-5), 301–306.  
URL <http://dx.doi.org/10.1016/j.ultramicro.2005.09.004>
- Clement, L., Pantel, R., Kwakman, L. F. T., Rouviere, J. L., Jul. 2004. Strain measurements by convergent-beam electron diffraction: The importance of stress relaxation in lamella preparations. *Applied Physics Letters* 85 (4), 651–653, WOS:000222855400047.  
URL <http://dx.doi.org/10.1063/1.1774275>
- Constantinescu, G., Kuc, A., Heine, T., Jul. 2013. Stacking in bulk and bilayer hexagonal boron nitride. *Physical Review Letters* 111 (3), 036104.  
URL <http://dx.doi.org/10.1103/PhysRevLett.111.036104>
- Cooper, D., Beche, A., Hartmann, J.-M., Carron, V., Rouviere, J.-L., Mar. 2010. Strain evolution during the silicidation of nanometer-scale SiGe semiconductor devices studied by dark field electron holography. *Applied Physics Letters* 96 (11), 113508.  
URL <http://dx.doi.org/10.1063/1.3358149>
- Cooper, D., Rouviere, J.-L., Beche, A., Kadkhodazadeh, S., Semenova, E. S., Yvind, K., Dunin-Borkowski, R., Dec. 2011. Quantitative strain mapping of InAs/InP quantum dots with 1 nm spatial resolution using dark field electron holography. *Applied Physics Letters* 99 (26), 261911.  
URL <http://dx.doi.org/10.1063/1.3672194>
- Coraux, J., NDiaye, A. T., Busse, C., Michely, T., Feb. 2008. Structural coherency of graphene on ir(111). *Nano Letters* 8 (2), 565–570.  
URL <http://dx.doi.org/10.1021/nl0728874>
- de Broglie, L., Nov. 1924. *Recherches sur la theorie des quanta*. Ph.D. thesis.  
URL <http://tel.archives-ouvertes.fr/tel-00006807>
- De Graef, M., Apr. 2003. *Introduction Conventional Transmission Electron Microscopy*. Cambridge University Press.  
URL <http://www.cambridge.org/us/academic/subjects/engineering/materials-science/introduction-conventional-transmission-electron-microscopy>
- Dean, C. R., Young, A. F., Meric, I., Lee, C., Wang, L., Sorgenfrei, S., Watanabe, K., Taniguchi, T., Kim, P., Shepard, K. L., Hone, J., Oct. 2010. Boron nitride substrates for high-quality graphene electronics. *Nature Nanotechnology* 5 (10), 722–726.  
URL <http://dx.doi.org/10.1038/nnano.2010.172>
- Delille, D., Pantel, R., Van Cappellen, E., 2000. Crystal thickness and extinction distance determination using energy filtered CBED pattern intensity measurement and dynamical diffraction

## BIBLIOGRAPHY

---

- theory fitting. *Ultramicroscopy* 87, 5–18.  
URL [http://dx.doi.org/10.1016/S0304-3991\(00\)00067-X](http://dx.doi.org/10.1016/S0304-3991(00)00067-X)
- Denton, A. R., Ashcroft, N. W., Mar. 1991. Vegards law. *Physical Review A* 43 (6), 3161–3164.  
URL <http://dx.doi.org/10.1103/PhysRevA.43.3161>
- Di Fonzo, S., Jark, W., Lagomarsino, S., Giannini, C., De Caro, L., Cedola, A., Muller, M., Feb. 2000. Non-destructive determination of local strain with 100-nanometre spatial resolution. *Nature* 403 (6770), 638–640.  
URL <http://dx.doi.org/10.1038/35001035>
- Dismukes, J. P., Ekstrom, L., Steigmeier, E. F., Kudman, I., Beers, D. S., Oct. 1964. Thermal and electrical properties of heavily doped GeSi alloys up to 1300k. *Journal of Applied Physics* 35 (10), 2899–2907.  
URL <http://dx.doi.org/10.1063/1.1713126>
- Doyle, P. A., Turner, P. S., May 1968. Relativistic hartree-fock x-ray and electron scattering factors. *Acta Crystallographica Section A* 24 (3), 390–397.  
URL <http://dx.doi.org/10.1107/S0567739468000756>
- Dyck, D. V., May 1980. Fast computational procedures for the simulation of structure images in complex or disordered crystals: a new approach. *Journal of Microscopy* 119 (1), 141–152.  
URL <http://dx.doi.org/10.1111/j.1365-2818.1980.tb04084.x>
- Ecob, R. C., Jul. 1986. Comments on the measurement of foil thickness by convergent beam electron diffraction. *Scripta Metallurgica* 20 (7), 1001–1006.  
URL [http://dx.doi.org/10.1016/0036-9748\(86\)90424-2](http://dx.doi.org/10.1016/0036-9748(86)90424-2)
- Eda, G., Fujita, T., Yamaguchi, H., Voiry, D., Chen, M., Chhowalla, M., 2012. Coherent atomic and electronic heterostructures of single-layer MoS<sub>2</sub>. *ACS Nano* 6 (8), 7311–7317.  
URL <http://dx.doi.org/10.1021/nn302422x>
- Egerton, R., Jan. 1986. *Electron energy-loss spectroscopy in the electron microscope*. Springer.
- Ferrari, A. C., Jul. 2007. Raman spectroscopy of graphene and graphite. disorder, electron phonon coupling, doping and nonadiabatic effects. *Solid State Communications* 143, 47–57.  
URL <http://dx.doi.org/10.1016/j.ssc.2007.03.052>
- Gailhanou, M., Loubens, A., Micha, J.-S., Charlet, B., Minkevich, A. A., Fortunier, R., Thomas, O., Mar. 2007. Strain field in silicon on insulator lines using high resolution x-ray diffraction. *Applied Physics Letters* 90 (11), 111914.  
URL <http://dx.doi.org/10.1063/1.2713335>
- Galindo, P. L., Kret, S., Sanchez, A. M., Laval, J.-Y., Yanez, A., Pizarro, J., Guerrero, E., Ben, T., Molina, S. I., Nov. 2007. The peak pairs algorithm for strain mapping from HRTEM images. *Ultramicroscopy* 107 (12), 1186–1193.  
URL <http://dx.doi.org/10.1016/j.ultramicro.2007.01.019>

- Gao, H. X., Peng, L.-M., Sep. 1999. Parameterization of the temperature dependence of the debye waller factors. *Acta Crystallographica Section A Foundations of Crystallography* 55 (5), 926–932.  
URL <http://dx.doi.org/10.1107/S0108767399005176>
- Gao, L., Guest, J. R., Guisinger, N. P., Sep. 2010. Epitaxial graphene on cu(111). *Nano Letters* 10 (9), 3512–3516.  
URL <http://dx.doi.org/10.1021/nl1016706>
- Georgiou, T., Jalil, R., Belle, B. D., Britnell, L., Gorbachev, R. V., Morozov, S. V., Kim, Y.-J., Gholinia, A., Haigh, S. J., Makarovskiy, O., Eaves, L., Ponomarenko, L. A., Geim, A. K., Novoselov, K. S., Mishchenko, A., Feb. 2013. Vertical field-effect transistor based on graphene-WS<sub>2</sub> heterostructures for flexible and transparent electronics. *Nature Nanotechnology* 8 (2), 100–103.  
URL <http://dx.doi.org/10.1038/nnano.2012.224>
- Hartmann, J. M., Papon, A. M., Destefanis, V., Billon, T., Dec. 2008. Reduced pressure chemical vapor deposition of ge thick layers on si. *Journal of Crystal Growth* 310 (24), 5287–5296.  
URL <http://dx.doi.org/10.1016/j.jcrysgro.2008.08.062>
- Hohenberg, P., Kohn, W., Nov. 1964. Inhomogeneous electron gas. *Physical Review* 136 (3B), B864–B871.  
URL <http://dx.doi.org/10.1103/PhysRev.136.B864>
- Houdellier, F., Roucau, C., Clement, L., Rouviere, J. L., Casanove, M. J., Aug. 2006. Quantitative analysis of HOLZ line splitting in CBED patterns of epitaxially strained layers. *Ultramicroscopy* 106 (10), 951–959.  
URL <http://dx.doi.org/10.1016/j.ultramic.2006.04.011>
- Huang, P. Y., Ruiz-Vargas, C. S., van der Zande, A. M., Whitney, W. S., Levendorf, M. P., Kevek, J. W., Garg, S., Alden, J. S., Hustedt, C. J., Zhu, Y., Park, J., McEuen, P. L., Muller, D. A., Jan. 2011. Grains and grain boundaries in single-layer graphene atomic patchwork quilts. *Nature* 469 (7330), 389–392.  
URL <http://dx.doi.org/10.1038/nature09718>
- Hytch, M., Houdellier, F., Hue, F., Snoeck, E., Jun. 2008. Nanoscale holographic interferometry for strain measurements in electronic devices. *Nature* 453 (7198), 1086–1089.  
URL <http://dx.doi.org/10.1038/nature07049>
- Hytch, M. J., Houdellier, F., Hue, F., Snoeck, E., Jul. 2011. Dark-field electron holography for the measurement of geometric phase. *Ultramicroscopy* 111 (8), 1328–1337.  
URL <http://dx.doi.org/10.1016/j.ultramic.2011.04.008>
- Hytch, M. J., Putaux, J.-L., Penisson, J.-M., May 2003. Measurement of the displacement field of dislocations to 0.03a by electron microscopy. *Nature* 423 (6937), 270–273.  
URL <http://dx.doi.org/10.1038/nature01638>

## BIBLIOGRAPHY

---

- international tables for crystallography, 2006. Volume A-G.  
URL <http://dx.doi.org/10.1107/97809553602060000001>
- Jones, P. M., Rackham, G. M., Steeds, J. W., May 1977. Higher order laue zone effects in electron diffraction and their use in lattice parameter determination. Proceedings of the Royal Society of London. A. Mathematical and Physical Sciences 354 (1677), 197–222.  
URL <http://dx.doi.org/10.1098/rspa.1977.0064>
- Kaiser, U., Biskupek, J., Meyer, J. C., Leschner, J., Lechner, L., Rose, H., Stoger-Pollach, M., Khlobystov, A. N., Hartel, P., Muller, H., Haider, M., Eyhusen, S., Benner, G., Jul. 2011. Transmission electron microscopy at 20kv for imaging and spectroscopy. Ultramicroscopy 111 (8), 1239–1246.  
URL <http://dx.doi.org/10.1016/j.ultramic.2011.03.012>
- Katsnelson, M. I., Novoselov, K. S., Geim, A. K., Sep. 2006. Chiral tunnelling and the klein paradox in graphene. Nature Physics 2 (9), 620–625.  
URL <http://dx.doi.org/10.1038/nphys384>
- Kelly, P., Jostsons, A., Blake, R., Napier, J., 1975. Determination of foil thickness by scanning-transmission electron-microscopy. Physica Status Solidi a-Applied Research 31 (2), 771–780.  
URL <http://dx.doi.org/10.1002/pssa.2210310251>
- Kirkland, E. J., 2010. Advanced Computing in Electron Microscopy, 2nd Edition. Springer.  
URL <http://www.springer.com/physics/optics+%26+lasers/book/978-1-4419-6532-5>
- Koch, C. T., Jun. 2011. Aberration-compensated large-angle rocking-beam electron diffraction. Ultramicroscopy 111 (7), 828–840.  
URL <http://dx.doi.org/10.1016/j.ultramic.2010.12.014>
- Kramer, Mayer, Apr. 1999. Using the hough transform for HOLZ line identification in convergent beam electron diffraction. Journal of Microscopy 194 (1), 02–11.  
URL <http://dx.doi.org/10.1046/j.1365-2818.1999.00475.x>
- Kramer, M. J., Mayer, J., Witt, C., Weickenmeier, A., Ruhle, M., 2000. Analysis of local strain in aluminium interconnects by energy filtered CBED. Ultramicroscopy 81, 245–262.  
URL [http://dx.doi.org/10.1016/S0304-3991\(99\)00191-6](http://dx.doi.org/10.1016/S0304-3991(99)00191-6)
- Krishnamurthy, S., Sher, A., Chen, A.-B., Jul. 1985. Generalized brooks formula and the electron mobility in SixGe1-x alloys. Applied Physics Letters 47 (2), 160–162.  
URL <http://dx.doi.org/10.1063/1.96248>
- Krivanek, O. L., Chisholm, M. F., Nicolosi, V., Pennycook, T. J., Corbin, G. J., Dellby, N., Murfitt, M. F., Own, C. S., Szilagy, Z. S., Oxley, M. P., Pantelides, S. T., Pennycook, S. J., Mar. 2010. Atom-by-atom structural and chemical analysis by annular dark-field electron microscopy. Nature 464 (7288), 571–574.  
URL <http://dx.doi.org/10.1038/nature08879>

- LeBeau, J., Findlay, S., Allen, L., Stemmer, S., 2009. Position averaged convergent beam electron diffraction. *Microscopy and Microanalysis* 15 (Supplement S2), 494–495.  
URL <http://dx.doi.org/10.1017/S1431927609096743>
- LeBeau, J. M., Findlay, S. D., Allen, L. J., Stemmer, S., May 2008. Quantitative atomic resolution scanning transmission electron microscopy. *Physical Review Letters* 100 (20), 206101.  
URL <http://dx.doi.org/10.1103/PhysRevLett.100.206101>
- LeBeau, J. M., Findlay, S. D., Allen, L. J., Stemmer, S., Jan. 2010. Position averaged convergent beam electron diffraction, theory and applications. *Ultramicroscopy* 110 (2), 118–125.  
URL <http://dx.doi.org/10.1016/j.ultramicro.2009.10.001>
- LeBeau, J. M., Stemmer, S., Nov. 2008. Experimental quantification of annular dark-field images in scanning transmission electron microscopy. *Ultramicroscopy* 108 (12), 1653–1658.  
URL <http://dx.doi.org/10.1016/j.ultramicro.2008.07.001>
- Lee, C., Wei, X., Kysar, J. W., Hone, J., Jul. 2008. Measurement of the elastic properties and intrinsic strength of monolayer graphene. *Science* 321 (5887), 385–388.  
URL <http://dx.doi.org/10.1126/science.1157996>
- Lee, Z., Meyer, J. C., Rose, H., Kaiser, U., Jan. 2012. Optimum HRTEM image contrast at 20kv and 80kv-exemplified by graphene. *Ultramicroscopy* 112 (1), 39–46.  
URL <http://dx.doi.org/10.1016/j.ultramicro.2011.10.009>
- Li, X., Cai, W., An, J., Kim, S., Nah, J., Yang, D., Piner, R., Velamakanni, A., Jung, I., Tutuc, E., Banerjee, S. K., Colombo, L., Ruoff, R. S., Jun. 2009. Large-area synthesis of high-quality and uniform graphene films on copper foils. *Science* 324 (5932), 1312–1314.  
URL <http://dx.doi.org/10.1126/science.1171245>
- Liarokapis, E., Papadimitriou, D., Rumberg, J., Richter, W., Jan. 1999. Raman and RAS measurements on uniaxially strained thin semiconductor layers. *physica status solidi (b)* 211 (1), 309–316.  
URL [http://onlinelibrary.wiley.com/doi/10.1002/\(SICI\)1521-3951\(199901\)211:1%3C309::AID-PSSB309%3E3.0.CO;2-W/abstract](http://onlinelibrary.wiley.com/doi/10.1002/(SICI)1521-3951(199901)211:1%3C309::AID-PSSB309%3E3.0.CO;2-W/abstract)
- Lin, Y.-C., Dumcenco, D. O., Huang, Y.-S., Suenaga, K., May 2014. Atomic mechanism of the semiconducting-to-metallic phase transition in single-layered MoS<sub>2</sub>. *Nature Nanotechnology* 9 (5), 391–396.  
URL <http://dx.doi.org/10.1038/nnano.2014.64>
- Lin, Y. P., Bird, D. M., Vincent, R., Apr. 1989. Errors and correction term for holz line simulations. *Ultramicroscopy* 27 (3), 233–239.  
URL [http://dx.doi.org/10.1016/0304-3991\(89\)90016-8](http://dx.doi.org/10.1016/0304-3991(89)90016-8)
- Liu, J. P., Li, K., Pandey, S. M., Benistant, F. L., See, A., Zhou, M. S., Hsia, L. C., Schampers, R., Klenov, D. O., Dec. 2008. Strain relaxation in transistor channels with embedded epitaxial silicon germanium source/drain. *Applied Physics Letters* 93 (22), 221912.  
URL <http://dx.doi.org/10.1063/1.3040323>

## BIBLIOGRAPHY

---

- Loane, R. F., Xu, P., Silcox, J., May 1991. Thermal vibrations in convergent-beam electron diffraction. *Acta Crystallographica Section A* 47 (3), 267–278.  
URL <http://dx.doi.org/10.1107/S0108767391000375>
- Lu, Z., Pyczak, F., Kramer, S., Biermann, H., Mughrabi, H., 2003. Fast and reliable evaluation of lattice distortions from convergent-beam electron diffraction patterns. *Philosophical Magazine* 83 (20), 2383–2397.  
URL <http://dx.doi.org/10.1080/0141861031000109573>
- Luy, J.-F., Russer, P., 1994. *Silicon-Based Millimeter-Wave Devices*. Springer Series in Electronics and Photonics. Springer.  
URL <http://www.springer.com/materials/optical+%26+electronic+materials/book/978-3-642-79033-1>
- Maier, H. J., Keller, R. R., Renner, H., Mughrabi, H., Preston, A., 1996. On the unique evaluation of local lattice parameters by convergent-beam electron diffraction. *Philosophical Magazine A* 74 (1), 23–43.  
URL <http://dx.doi.org/10.1080/01418619608239688>
- Mak, K. F., Lee, C., Hone, J., Shan, J., Heinz, T. F., Sep. 2010. Atomically thin MoS<sub>2</sub>: A new direct-gap semiconductor. *Physical Review Letters* 105 (13), 136805.  
URL <http://dx.doi.org/10.1103/PhysRevLett.105.136805>
- Maurice, C., Driver, J. H., Fortunier, R., Feb. 2012. On solving the orientation gradient dependency of high angular resolution EBSD. *Ultramicroscopy* 113, 171–181.  
URL <http://dx.doi.org/10.1016/j.ultramicro.2011.10.013>
- Meyer, J. C., Geim, A. K., Katsnelson, M. I., Novoselov, K. S., Obergfell, D., Roth, S., Girit, C., Zettl, A., Jul. 2007. On the roughness of single and bilayer graphene membranes. *Solid State Communications* 143 (1-2), 101–109.  
URL <http://dx.doi.org/10.1016/j.ssc.2007.02.047>
- Meyer, J. C., Kisielowski, C., Erni, R., Rossell, M. D., Crommie, M. F., Zettl, A., Nov. 2008. Direct imaging of lattice atoms and topological defects in graphene membranes. *Nano Letters* 8 (11), 3582–3586.  
URL <http://dx.doi.org/10.1021/nl801386m>
- Meyer, J. C., Kurasch, S., Park, H. J., Skakalova, V., Kunzel, D., Gross, A., Chuvilin, A., Algara-Siller, G., Roth, S., Iwasaki, T., Starke, U., Smet, J. H., Kaiser, U., Mar. 2011. Experimental analysis of charge redistribution due to chemical bonding by high-resolution transmission electron microscopy. *Nature Materials* 10 (3), 209–215.  
URL <http://dx.doi.org/10.1038/nmat2941>
- Michael, J. R., Williams, D. B., Sep. 1987. A consistent definition of probe size and spatial resolution in the analytical electron microscope. *Journal of Microscopy* 147 (3), 289–303.  
URL <http://dx.doi.org/10.1111/j.1365-2818.1987.tb02840.x>

- Mkhoyan, K. A., Babinec, T., Maccagnano, S. E., Kirkland, E. J., Silcox, J., Apr. 2007. Separation of bulk and surface losses in low loss EELS measurements in STEM. *Ultramicroscopy* 107 (4,5), 345–355.  
URL <http://dx.doi.org/10.1016/j.ultramic.2006.09.003>
- Momma, K., Izumi, F., Dec. 2011. VESTA 3 for three-dimensional visualization of crystal, volumetric and morphology data. *Journal of Applied Crystallography* 44 (6), 1272–1276.  
URL <http://dx.doi.org/10.1107/S0021889811038970>
- Morawiec, A., 2005. Formal conditions for unambiguous residual strain determination by CBED. *Philosophical Magazine* 85 (15), 1611–1623.  
URL <http://dx.doi.org/10.1080/09500830500041146>
- Morawiec, A., 2007a. An algorithm for refinement of lattice parameters using CBED patterns. *Ultramicroscopy* 107 (4-5), 390–395.  
URL <http://dx.doi.org/10.1016/j.ultramic.2006.10.003>
- Morawiec, A., Jun. 2007b. A program for refinement of lattice parameters based on multiple convergent-beam electron diffraction patterns. *Journal of Applied Crystallography* 40 (3), 618–622.  
URL <http://dx.doi.org/10.1107/S0021889807018262>
- Morniroli, J. P., Ji, G., Jacob, D., Oct. 2012. A systematic method to identify the space group from PED and CBED patterns part i - theory. *Ultramicroscopy* 121, 42–60.  
URL <http://dx.doi.org/10.1016/j.ultramic.2012.04.008>
- Mott, N. F., Jun. 1930. The scattering of electrons by atoms. *Proceedings of the Royal Society of London. Series A* 127 (806), 658–665.  
URL <http://dx.doi.org/10.1098/rspa.1930.0082>
- Nelder, J. A., Mead, R., Jan. 1965. A simplex method for function minimization. *The Computer Journal* 7 (4), 308–313.  
URL <http://dx.doi.org/10.1093/comjnl/7.4.308>
- Ning Lu, Guo, H., Lu Wang, Xiaojun Wu, Xiao Cheng Zeng, Apr. 2014. van der waals trilayers and superlattices: modification of electronic structures of MoS2 by intercalation - nanoscale (RSC publishing). *Nanoscale* (9), 4566.  
URL <http://dx.doi.org/10.1039/c4nr00783b>
- Novoselov, K. S., Geim, A. K., Morozov, S. V., Jiang, D., Katsnelson, M. I., Grigorieva, I. V., Dubonos, S. V., Firsov, A. A., Nov. 2005. Two-dimensional gas of massless dirac fermions in graphene. *Nature* 438 (7065), 197–200.  
URL <http://dx.doi.org/10.1038/nature04233>
- Novoselov, K. S., Geim, A. K., Morozov, S. V., Jiang, D., Zhang, Y., Dubonos, S. V., Grigorieva, I. V., Firsov, A. A., Oct. 2004. Electric field effect in atomically thin carbon films. *Science* 306 (5696), 666–669.  
URL <http://dx.doi.org/10.1126/science.1102896>

## BIBLIOGRAPHY

---

- Peng, L. M., Cowley, J. M., Jan. 1988. Errors arising from numerical use of the mott formula in electron image simulation. *Acta Crystallographica Section A Foundations of Crystallography* 44 (1), 1–6.  
URL <http://dx.doi.org/10.1107/S0108767387006858>
- Quhe, R., Zheng, J., Luo, G., Liu, Q., Qin, R., Zhou, J., Yu, D., Nagase, S., Mei, W.-N., Gao, Z., Lu, J., Feb. 2012. Tunable and sizable band gap of single-layer graphene sandwiched between hexagonal boron nitride. *NPG Asia Materials* 4 (2), e6.  
URL <http://dx.doi.org/10.1038/am.2012.10>
- Radisavljevic, B., Whitwick, M. B., Kis, A., Dec. 2011. Integrated circuits and logic operations based on single-layer MoS<sub>2</sub>. *ACS Nano* 5 (12), 9934–9938.  
URL <http://dx.doi.org/10.1021/nm203715c>
- Radisavljevic, B., Whitwick, M. B., Kis, A., Jul. 2012. Small-signal amplifier based on single-layer MoS<sub>2</sub>. *Applied Physics Letters* 101 (4), 043103.  
URL <http://dx.doi.org/10.1063/1.4738986>
- Reimer, L., Kohl, H., 2008. *Transmission Electron Microscopy - Physics of Image Formation*, 5th Edition. Springer.  
URL <http://www.springer.com/materials/book/978-0-387-40093-8>
- Reina, A., Thiele, S., Jia, X., Bhaviripudi, S., Dresselhaus, M. S., Schaefer, J. A., Kong, J., Jun. 2009. Growth of large-area single- and bi-layer graphene by controlled carbon precipitation on polycrystalline ni surfaces. *Nano Research* 2 (6), 509–516.  
URL <http://dx.doi.org/10.1007/s12274-009-9059-y>
- Rosenauer, A., Gerthsen, D., 1999. Atomic scale strain and composition evaluation from high-resolution transmission electron microscopy images. In: Peter W. Hawkes (Ed.), *Advances in Imaging and Electron Physics*. Vol. Volume 107. Elsevier, pp. 121–230.  
URL [dx.doi.org/10.1016/S1076-5670\(08\)70187-3](http://dx.doi.org/10.1016/S1076-5670(08)70187-3)
- Rosenauer, A., Gries, K., Muller, K., Pretorius, A., Schowalter, M., Avramescu, A., Engl, K., Lutgen, S., 2009. Measurement of specimen thickness and composition in using high-angle annular dark field images. *Ultramicroscopy* 109 (9), 1171–1182.  
URL <http://dx.doi.org/10.1016/j.ultramicro.2009.05.003>
- Rouviere, J.-L., Jan. 2008. The use of the geometrical phase analysis to measure strain in nearly periodic images. In: Cullis, A. G., Midgley, P. A. (Eds.), *Microscopy of Semiconducting Materials 2007*. No. 120 in *Springer Proceedings in Physics*. Springer, pp. 199–202.  
URL [http://link.springer.com/chapter/10.1007/978-1-4020-8615-1\\_43](http://link.springer.com/chapter/10.1007/978-1-4020-8615-1_43)
- Rouviere, J.-L., Beche, A., Martin, Y., Denneulin, T., Cooper, D., Dec. 2013. Improved strain precision with high spatial resolution using nanobeam precession electron diffraction. *Applied Physics Letters* 103 (24), 241913.  
URL <http://dx.doi.org/10.1063/1.4829154>

- Rouviere, J. L., Sarigiannidou, E., Dec. 2005. Theoretical discussions on the geometrical phase analysis. *Ultramicroscopy* 106 (1), 1–17.  
URL <http://dx.doi.org/10.1016/j.ultramic.2005.06.001>
- Rusin, T. M., Zawadzki, W., Jul. 2009. Theory of electron zitterbewegung in graphene probed by femtosecond laser pulses. *Physical Review B* 80 (4), 045416.  
URL <http://dx.doi.org/10.1103/PhysRevB.80.045416>
- Ruska, E., Knoll, M., Jun. 1932. Das electronenmikroskop.  
URL <http://ernstruska.digilibrary.de/bibliographie/q006/q006.pdf>
- Schaffler, F., Dec. 1997. High-mobility si and ge structures. *Semiconductor Science and Technology* 12 (12), 1515.  
URL <http://dx.doi.org/10.1088/0268-1242/12/12/001>
- Schonfeld, B., Huang, J. J., Moss, S. C., Aug. 1983. Anisotropic mean-square displacements (MSD) in single-crystals of 2h- and 3r-MoS<sub>2</sub>. *Acta Crystallographica Section B Structural Science* 39 (4), 404–407.  
URL <http://dx.doi.org/10.1107/S0108768183002645>
- Slawinska, J., Zasada, I., Klusek, Z., Apr. 2010. Energy gap tuning in graphene on hexagonal boron nitride bilayer system. *Physical Review B* 81 (15), 155433.  
URL <http://dx.doi.org/10.1103/PhysRevB.81.155433>
- Soler, J. M., Artacho, E., Gale, J. D., Garcia, A., Junquera, J., Ordejon, P., Sanchez-Portal, D., Mar. 2002. The SIESTA method for ab initio order-n materials simulation. *Journal of Physics: Condensed Matter* 14 (11), 2745.  
URL <http://dx.doi.org/10.1088/0953-8984/14/11/302>
- Spence, J. C. H., Zuo, J. M., 1992. *Electron microdiffraction*. Springer.  
URL <http://dx.doi.org/10.1007/978-1-4899-2353-0>
- Spessot, A., Frabboni, S., Balboni, R., Armigliato, A., May 2007. Method for determination of the displacement field in patterned nanostructures by TEM/CBED analysis of split high-order laue zone line profiles. *Journal of microscopy* 226 (Pt 2), 140–155.  
URL <http://dx.doi.org/10.1111/j.1365-2818.2007.01760.x>
- Splendiani, A., Sun, L., Zhang, Y., Li, T., Kim, J., Chim, C.-Y., Galli, G., Wang, F., Apr. 2010. Emerging photoluminescence in monolayer MoS<sub>2</sub>. *Nano Letters* 10 (4), 1271–1275.  
URL <http://dx.doi.org/10.1021/nl903868w>
- Stadelmann, P. A., 1987. EMS - a software package for electron diffraction analysis and HREM image simulation in materials science. *Ultramicroscopy* 21 (2), 131–145.  
URL [http://dx.doi.org/10.1016/0304-3991\(87\)90080-5](http://dx.doi.org/10.1016/0304-3991(87)90080-5)
- Sutter, P. W., Flege, J.-I., Sutter, E. A., May 2008. Epitaxial graphene on ruthenium. *Nature Materials* 7 (5), 406–411.  
URL <http://dx.doi.org/10.1038/nmat2166>

## BIBLIOGRAPHY

---

- Takeda, M., Suzuki, J., Jul. 1996. Crystallographic heterodyne phase detection for highly sensitive lattice-distortion measurements. *Journal of the Optical Society of America A* 13 (7), 1495–1500.  
URL <http://dx.doi.org/10.1364/JOSAA.13.001495>
- Tanaka, M., Tsuda, K., Aug. 2011. Convergent-beam electron diffraction. *Journal of Electron Microscopy* 60 (supplement 1), S245–S267.  
URL <http://dx.doi.org/10.1093/jmicro/dfr038>
- Terrones, M., Botello-Mendez, A. R., Campos-Delgado, J., Lopez-Urias, F., Vega-Cantu, Y. I., Rodriguez-Macias, F. J., Elias, A. L., Munoz-Sandoval, E., Cano-Marquez, A. G., Jean-Christophe Charlier, Terrones, H., Aug. 2010. Graphene and graphite nanoribbons: Morphology, properties, synthesis, defects and applications. *Nano Today* 5 (4), 351–372.  
URL <http://dx.doi.org/10.1016/j.nantod.2010.06.010>
- Toda, A., Ikarashi, N., Ono, H., Mar. 2000. Local lattice strain measurements in semiconductor devices by using convergent-beam electron diffraction. *Journal of Crystal Growth* 210 (1-3), 341–345.  
URL [http://dx.doi.org/10.1016/S0022-0248\(99\)00707-1](http://dx.doi.org/10.1016/S0022-0248(99)00707-1)
- Usuda, K., Mizuno, T., Tezuka, T., Sugiyama, N., Moriyama, Y., Nakaharai, S., Takagi, S.-i., Mar. 2004. Strain relaxation of strained-si layers on SiGe-on-insulator (SGOI) structures after mesa isolation. *Applied Surface Science* 224 (1-4), 113–116.  
URL <http://dx.doi.org/10.1016/j.apsusc.2003.11.058>
- Usuda, K., Numata, T., Tezuka, T., Sugiyama, N., Moriyama, Y., Nakaharai, S., Takagi, S., Sep. 2003. Strain evaluation for thin strained-si on SGOI and strained-si on nothing (SSON) structures using nano-beam electron diffraction (NBD). In: *SOI Conference, 2003. IEEE International*. pp. 138–139.  
URL <http://dx.doi.org/10.1109/SOI.2003.1242928>
- Vincent, R., Preston, A., King, M., 1988. Measurement of strain in silver halide particles by convergent beam electron diffraction. *Ultramicroscopy* 24 (4), 409–419.  
URL [http://dx.doi.org/10.1016/0304-3991\(88\)90131-3](http://dx.doi.org/10.1016/0304-3991(88)90131-3)
- Vincent, R., Walsh, T., Pozzi, M., Jan. 1999. Iterative phase retrieval from kinematic rocking curves in CBED patterns. *Ultramicroscopy* 76 (3), 125–137.  
URL [http://dx.doi.org/10.1016/S0304-3991\(98\)00076-X](http://dx.doi.org/10.1016/S0304-3991(98)00076-X)
- Voloshina, E. N., Fertitta, E., Garhofer, A., Mittendorfer, F., Fonin, M., Thissen, A., Dedkov, Y. S., Jan. 2013. Electronic structure and imaging contrast of graphene moire on metals. *Scientific Reports* 3.  
URL <http://dx.doi.org/10.1038/srep01072>
- Wang, H., Wang, Q., Cheng, Y., Li, K., Yao, Y., Zhang, Q., Dong, C., Wang, P., Schwingenschlogl, U., Yang, W., Zhang, X. X., Jan. 2012a. Doping monolayer graphene with single atom substitutions. *Nano Letters* 12 (1), 141–144.  
URL <http://dx.doi.org/10.1021/nl2031629>

- Wang, Q. H., Kalantar-Zadeh, K., Kis, A., Coleman, J. N., Strano, M. S., Nov. 2012b. Electronics and optoelectronics of two-dimensional transition metal dichalcogenides. *Nature Nanotechnology* 7 (11), 699–712.  
URL <http://dx.doi.org/10.1038/nnano.2012.193>
- Wang, W. L., Bhandari, S., Yi, W., Bell, D. C., Westervelt, R., Kaxiras, E., 2012c. Direct imaging of atomic-scale ripples in few-layer graphene. *Nano Letters* 12 (5), 2278–2282.  
URL <http://dx.doi.org/10.1021/nl300071y>
- Watanabe, M., Williams, D. B., Feb. 2006. The quantitative analysis of thin specimens: a review of progress from the cliff-lorimer to the new zeta-factor methods. *Journal of Microscopy* 221 (2), 89–109.  
URL <http://dx.doi.org/10.1111/j.1365-2818.2006.01549.x>
- Weickenmeier, A., Kohl, H., Sep. 1991. Computation of absorptive form factors for high-energy electron diffraction. *Acta Crystallographica Section A Foundations of Crystallography* 47 (5), 590–597.  
URL <http://dx.doi.org/10.1107/S0108767391004804>
- White, T. A., Eggeman, A. S., Midgley, P. A., Jun. 2010. Is precession electron diffraction kinematical-part i-phase-scrambling multislice simulations. *Ultramicroscopy* 110 (7), 763–770.  
URL <http://dx.doi.org/10.1016/j.ultramic.2009.10.013>
- William, D. B., Carter, C. B., 2009. *Transmission Electron Microscopy*, 2nd Edition. Springer.  
URL <http://www.springer.com/materials/characterization+%26+evaluation/book/978-0-387-76500-6>
- Wittmann, R., Parzinger, C., Gerthsen, D., Jan. 1998. Quantitative determination of lattice parameters from CBED patterns: accuracy and performance. *Ultramicroscopy* 70 (3), 145–159.  
URL [http://dx.doi.org/10.1016/S0304-3991\(97\)00107-1](http://dx.doi.org/10.1016/S0304-3991(97)00107-1)
- Wypych, F., Solenthaler, C., Prins, R., Weber, T., May 1999. Electron diffraction study of intercalation compounds derived from 1t-MoS<sub>2</sub>. *Journal of Solid State Chemistry* 144 (2), 430–436.  
URL <http://dx.doi.org/10.1006/jssc.1999.8193>
- Zuo, J. M., Apr. 1992. Automated lattice parameter measurement from HOLZ lines and their use for the measurement of oxygen content in YBa<sub>2</sub>Cu<sub>3</sub>O<sub>7</sub> from nanometer-sized region. *Ultramicroscopy* 41, 211–223.  
URL [http://dx.doi.org/10.1016/0304-3991\(92\)90110-6](http://dx.doi.org/10.1016/0304-3991(92)90110-6)
- Zuo, J. M., Spence, J. C. H., Jun. 1991. Automated structure factor refinement from convergent-beam patterns. *Ultramicroscopy* 35, 185–196.  
URL [http://dx.doi.org/10.1016/0304-3991\(91\)90071-D](http://dx.doi.org/10.1016/0304-3991(91)90071-D)



---

## List of Figures

---

1	Number of research articles containing the word “nanomaterials” or “graphene” published each year. Source : Scopus . . . . .	1
A.I.1	Illustration of the Bragg Law in the direct space.. . . . .	7
A.I.2	Bragg Law in reciprocal space. . . . .	8
A.I.3	Typical NBED and CBED patterns. . . . .	9
A.I.4	Schematic view of the formation of the CBED diffraction pattern.. . . . .	10
A.I.5	Precession Electron Diffraction . . . . .	11
A.I.6	MoS <sub>2</sub> PACBED patterns. . . . .	12
A.I.7	Schematic ray diagram of BF- DF- and HR-TEM. . . . .	13
A.I.8	Ray-Diagram illustrating the use of the monochromator. . . . .	15
A.I.9	Illustration of the convergent probe scanning for the formation of the STEM image. . . . .	16
A.I.10	Detector centering for Quantitative STEM. . . . .	17
A.II.1	STEM image and SIMS profile of multi-layered Si-SiGe specimen. . . . .	20
A.II.2	Si and SiGe structure and lattice constant. . . . .	20
A.II.3	Band gap variation of $Si_{1-x}Ge_x$ alloys with respect to the Ge concentration. . . . .	21
A.II.4	Schematic view of a wedge tripod polished sample. . . . .	22
A.II.5	Crystal structure of graphene and graphite. . . . .	23
A.II.6	Band structure of Graphene. . . . .	24
A.II.7	MoS <sub>2</sub> crystal structure.. . . . .	26
A.II.8	h-BN crystal structure.. . . . .	27
A.II.9	TEM sample preparation of exfoliated MoS <sub>2</sub> . . . . .	28
A.II.10	Comparison between Peak-Finding and GPA techniques. . . . .	29
A.II.11	Dark-Field Holography. . . . .	30
A.II.12	Evolution of Raman G peak as a function of number of graphene layers. . . . .	31
A.II.13	Color-coded images of graphene grains regions using several different aperture locations.. . . . .	32
A.II.14	BN monolayer ADF-STEM image and simulation. . . . .	33
A.III.1	Schematic representation of excitation error ( $S_g$ ). . . . .	36
A.III.2	The projection effect observed when tilting a mono-layered sample. . . . .	38

LIST OF FIGURES

---

A.III.3	Projection factor as a function of the sample tilt angle. . . . .	39
A.III.4	Illustration of the Multislice simulation. . . . .	44
B.I.1	Unfiltered and filtered (using 10eV slit) CBED pattern. . . . .	50
B.I.2	0°C and -150°C filtered CBED pattern, from perfect Silicon. . . . .	51
B.I.3	Effect of cooling on the profile of [1,-1,-5] HOLZ line. . . . .	51
B.I.4	Calibration of the camera length using deficient and excess silicon (004) HOLZ line. . . . .	52
B.I.5	Profile of 004 silicon excess HOLZ line at 200kV. . . . .	53
B.I.6	Results of the CBED thickness and structure factor measurement using Delille et al. (2000) method. . . . .	54
B.I.7	Comparison of results between CBED thickness measurement from [sub:Thickness-Application-Si] and EDS measurement in a SEM. . . . .	55
B.I.8	Description of the experimental parameters retrieval algorithm. . . . .	57
B.I.9	Fit of the experimental parameters of Silicon . . . . .	60
B.I.10	Example of interactions between excess lines that are not visible in the simulation. . . . .	61
B.II.1	CBED Ambiguity : difference between the reference CBED pattern and a deformed silicon pattern. . . . .	64
B.II.2	CBED Ambiguity : additional information carried by the excess HOLZ lines. . . . .	65
B.II.3	(a) on-axis [1,1,0] or (b) off- axis[651,441,31] reciprocal space of Silicon, showing the diffracting planes in CBED condition (inner and outer Ewald spheres limits are plotted here). On the right, two experimental Silicon patterns from a low and high index zone axis. . . . .	67
B.II.4	Dynamically simulated CBED disks using the Bloch Waves method. . . . .	68
B.II.5	Comparison between Kinematic and Dynamic simulation. . . . .	70
B.II.6	Templates used for fitting transmitted and excess HOLZ lines. . . . .	72
B.II.7	Schematic view of the $\mathbf{F}$ -tensor retrieval. . . . .	75
B.II.8	Scatter plot of 20 independent retrievals of the same deformation state. . . . .	77
B.II.9	Algorithm retrieval results obtained from 20 dynamically simulated patterns, with different strains and rotation state. . . . .	78
B.II.10	Results obtained from dynamic simulations, with two zone axes : [651,441,31] and [441,651,31]. . . . .	79
B.III.1	Schematic view of the Monte Carlo algorithm displacement retrieval. . . . .	83
B.III.2	$\mathbf{u}(z)$ displacement retrieval by the Monte Carlo algorithm. . . . .	85
B.III.3	Extraction of experimental HOLZ line profiles. . . . .	86
B.III.4	Numerical descant correction. . . . .	87
B.III.5	Experimental and best simulated HOLZ lines profiles. . . . .	89
B.III.6	Projected retrieved displacement on the (x,z) plane. . . . .	90
B.III.7	Retrieved $u_{x,y,z}(x, z)$ displacement. . . . .	91
B.III.8	Derivative of the $\mathbf{u}(z)$ displacement with respect to z. . . . .	92
C.I.1	Calculated HRTEM images of graphene at 80 kV. . . . .	100

C.I.2	Step from a single-layer (SLG) to a bi-layer (BLG). . . . .	101
C.I.3	Reconstruction of the surface topography of few-layered graphene. . . . .	102
C.I.4	Filtered HR-TEM images of untilted, 10°, and 30° tilted graphene mono-layer. . . . .	103
C.I.5	HR-TEM image of graphene grain boundary at 80kV. . . . .	104
C.I.6	Experimental and simulated flower defect in graphene. . . . .	105
C.I.7	Illustration of the reciprocal space of single- and double-layer graphene. . . . .	106
C.I.8	Measurement of the projection effect in graphene. . . . .	108
C.I.9	TEM image of the sample used to evidence the projection effect. . . . .	109
C.I.10	Experimental broadening with tilt amplitude of a diffraction spot. . . . .	110
C.I.11	Broadening of the (100) graphene diffraction spot with sample tilt. . . . .	111
C.I.12	STEM image and diffraction of the few-layered MoS <sub>2</sub> . . . . .	112
C.I.13	Template matching to determine the spot positions. . . . .	113
C.I.14	Average stretching coefficient of the MoS <sub>2</sub> (100) <sub>0</sub> , (100) <sub>60</sub> , (100) <sub>120</sub> spots. . . . .	113
C.I.15	Effect of the alpha tilt on a HR-TEM image of graphene. . . . .	115
C.II.1	Determination of MoS <sub>2</sub> crystal structure from PACBED and NBED diffraction patterns. . . . .	118
C.II.2	Normalized sensitivity of FEI Titan Ultimate DF2 detector. . . . .	119
C.II.3	Simulated normalized intensity on the DF2 detector of few-layered 2H-MoS <sub>2</sub> . . . . .	120
C.II.4	Normalized DF2 HR-STEM image of exfoliated 2H-MoS <sub>2</sub> and retrieved thickness. . . . .	121
C.II.5	Experimental PACBED pattern and their corresponding simulated patterns. . . . .	123
C.II.6	Transmitted and diffracted spots intensities in as a function of the sample thickness for 2H-MoS <sub>2</sub> . . . . .	125
C.II.7	Extraction of the MoS <sub>2</sub> experimental diffraction spot intensities. . . . .	126
C.II.8	Map of the retrieved MoS <sub>2</sub> thickness using the spots intensities given in figure C.II.7. . . . .	127
C.II.9	Comparison of the PACBED, Quantitative STEM and Quantitative nanodiffraction techniques to measure the MoS <sub>2</sub> sample thickness. . . . .	128
C.II.10	Simulated and experimental diffractions of MoS <sub>2</sub> and BN monolayers. . . . .	129
C.II.11	Structure determination of bi-layered BN crystal. . . . .	129
C.II.12	Normalized STEM image and Nano-beam diffraction of BN plotted in log scale. . . . .	130
C.II.13	(100) and (110) spot intensities extracted from Boron Nitride simulation. . . . .	132
C.II.14	Simulation of the STEM signal relative to the beam intensity, using a inner detector radius of 57.84 mrad and a outer radius of 300mrad. AB and AA' stackings give nearly the same results with a slight oscillation of the intensity for AA' structure. . . . .	132
C.II.15	Comparison of thickness determination between nanodiffraction and Quantitative STEM. . . . .	133
C.II.16	Diffraction from 15nm and 32nm thick BN crystals . . . . .	134



---

## List of Tables

---

B.II.1	HOLZ line weight ( $w^g$ ) and dynamic shifts ( $DS^g$ ) fitted on a reference dynamic simulation pattern. . . . .	74
B.III.1	Direction of observation and diffracting planes used for the simulation of silicon rocking curves. . . . .	84





## Abstract

The small dimensions of nanomaterials give them remarkable properties attracting the scientific community. In order to understand and control these properties, it is essential to characterize them at the nanometer scale. This thesis work is based on the development of electron microscopy diffraction techniques for the study of two and three dimensional materials.

Convergent Beam Electron Diffraction patterns contain large amount of information on the sample geometry. This information, carried by HOLZ lines, allows to determine the sample thickness, the structure factor, the direction of observation, the electron acceleration voltage and the camera length. Ambiguities in strain measurement arise from the experimental two-dimensional projection of three-dimensional information. During this thesis, it has been possible to reduce these ambiguities and therefore to measure the diagonal components of the deformation gradient tensor from one direction of observation only. By studying the HOLZ lines broadening, due to a non-uniform strain along the electron beam direction, it has been possible to retrieve the displacement field along the beam direction.

The second part of this thesis is focused on the study of two-dimensional materials such as Graphene, Boron Nitride (BN) or Molybdenum disulfide (MoS<sub>2</sub>). The delicate interpretation of the contrast of high-resolution transmission electron microscopy images and especially the importance of aberrations and sample tilt on this contrast is discussed. A method to quantify two-dimensional sample orientation using diffraction spots projection effect is presented. Finally, three thickness measurement techniques are compared by applying them to few-layered MoS<sub>2</sub> et BN.

Keywords: Transmission Electron Microscopy (TEM), Convergent Beam Electron Diffraction (CBED), Nanodiffraction (NBED), Deformation, Graphene, Thickness measurement

## Résumé

De par leurs propriétés physico-chimiques spécifiques, les nanomatériaux attirent de plus en plus la communauté scientifique. Dans ce contexte, il est important d'améliorer les techniques de caractérisation à l'échelle nanométrique. Ce travail de thèse est basé sur le développement de techniques de diffraction électronique pour l'étude de matériaux bi-dimensionnels et tri-dimensionnels.

La diffraction électronique en faisceau convergent contient de nombreuses informations sur la structure l'échantillon. Ces informations, portées par les lignes de HOLZ, permettent de déterminer l'épaisseur de l'échantillon, le facteur de structure, la direction d'observation, la tension d'accélération des électrons, ainsi que la longueur de caméra. Des ambiguïtés existent dans la détermination de l'état de contraintes car un cliché expérimental est une projection bi-dimensionnelle d'une information tri-dimensionnelle. Il a été possible au cours de cette thèse de réduire ces ambiguïtés et de déterminer ainsi les composantes diagonales du tenseur de déformation à partir d'une seule direction d'observation. En étudiant l'élargissement des lignes de HOLZ, dû à une déformation non uniforme dans le sens de propagation des électrons, il a été possible de remonter au champ de déplacement suivant l'axe du faisceau d'électrons.

La seconde partie de cette thèse s'intéresse aux matériaux bi-dimensionnels comme le Graphène, le Nitrure de Bore (BN) et le disulfure de Molybdène (MoS<sub>2</sub>). L'interprétation du contraste d'une image de microscopie électronique en transmission haute résolution est discutée, notamment sur l'importance de l'orientation de l'échantillon et des aberrations. Une méthode de mesure de l'orientation d'un échantillon bi-dimensionnel basée sur la projection des tâches de diffraction est présentée. Enfin, trois techniques de mesure d'épaisseur sont comparées en les appliquant à quelques couches atomique de MoS<sub>2</sub> et BN.

Mots clés : Microscopie Électronique en Transmission (MET), Diffraction en faisceau convergent (CBED), Nano-diffraction (NBED), Déformation, Graphène, Mesure d'épaisseur